SYNTHESIS, STRUCTURAL AND MAGNETIC PROPERTIES OF BULK AND NANOSIZED $(Zn, Cd, Cu)_{0.5}Ni_{0.5}Fe_2O_4$ AND $NiFe_2O_4$ FERRITES

by

Justice Zakhele Msomi

BSc, BSc(Hons) (UDW), MSc (UND)

This thesis is submitted to the University of KwaZulu–Natal in fulfilment of the academic requirements for the degree of Doctor of Philosophy.

February 2007

Acknowledgments

I would like to thank the following people for their contributions and sacrifices as indicated below to make this work a success:

- Dr T. Moyo for invaluable supervision, guidance and encouragement throughout the period of this work.

- Prof T. B. Doyle and Prof K. Bharuth–Ram for many ideas and inputs throughout the period of this work.

- Staff members in the Physics Workshop at Howard College campus for their prompt attention to all aspects of designing and maintenance of the experimental apparatus used in this work and my fellow research students in the School of Physics for their encouragement and support at all times.

- Prof H. C. Swart at the University of The Free State Department of Physics for constant encouragement and support.

My final thanks are reserved for members of my family for their encouragement, support and understanding.

Dedication

I dedicate this thesis to my mother, Regina Msomi, and the rest of my family.

Declaration

The candidate wishes to confirm that work described in this thesis was carried out by the author in the School of Physics at University of KwaZulu–Natal. This is original work by the author and has not been submitted in any form to another University or Institution. Credit has been given where use of the work of others is made.

J. Z. Msomi

February 2007

Abstract

We present a study of the synthesis, structural and magnetic properties of bulk and nanosized (Zn, Cd, Cu)$_{0.5}$Ni$_{0.5}$Fe$_2$O$_4$ and NiFe$_2$O$_4$ compounds. The effects of electronic configuration and atomic sizes of Zn, Cd, Cu and Ni on the magnetic properties of the ferrites are the primary focus of the study. Different synthesis routes, preparation conditions and how they affect single phase formation are explored.

The synthesis was undertaken by solid–state reaction, combustion, hydrothermal and glycothermal techniques. The structure determination was by X-ray diffraction. The magnetic measurements were performed using Mössbauer spectroscopy (from 79 K to about 850 K) and a vibrating sample magnetometer (at about 300 K). The bulk densities of the sintered pellets were deduced by Archimedes principle. The bulk oxides were produced by solid–state reaction and combustion techniques. Fine powders with grain sizes of about 10 nm were produced from bulk compounds by a Retsch planetary ball mill and by the hydrothermal and glycothermal processes. The effects of the applied pressure used to make pellets (related to green density of the raw pellets) and the sintering temperature on the properties were investigated.

An anomalous variation of bulk densities of (Zn, Cd)$_{0.5}$Ni$_{0.5}$Fe$_2$O$_4$ oxides with increase in pelletizing pressure was observed which appears to suggest evidence for trapped porosity. Different states of pelletizing the samples appear to be related to a systematic change of the hyperfine field distributions derived from the Mössbauer spectra. The temperature dependence of the magnetic hyperfine fields at tetrahedral (A) and octahedral (B) sites were observed to vary with temperature according to the equations $B_{hf}(T) = B_{hf}(0)[1 - (T/T_C)^n]^{\beta_n}$ where $n = 1$ (based on the Landau–Ginzburg theory) and $n = 2$ (based on the Stoner theory). The equation $B_{hf}(T) = B_{hf}(0)[1-(T/T_C)^2]^{\beta_2}$ appears to fit the hyperfine field data over a wider temperature range. The Zn– and Cd–based oxides were found to be ferrimagnetic with Curie temperature $T_C = 548 \pm 3$ K

(measured by zero velocity technique). The Cu–based compound exhibited antiferromagnetic behavior with a magnetic transition temperature of 825 ± 3 K. The difference in behavior between Zn–, Cd– and Cu–based compounds is due to difference in electronic configuration and atomic or ionic sizes. The stronger magnetic coupling between spins in the Cu–based sample can be explained by the presence of RKKY interactions in addition to superexchange interactions. The larger ionic size for Cd appears to favour smaller grain sizes in Cd–based oxides. An anomalous increase in T_C is obtained in the $Zn_{0.5}Ni_{0.5}Fe_2O_4$ compound with reduction in grain size. This increase in T_C is attributed to a distribution of Zn ions on both A and B sites.

The Mössbauer spectra of the milled nanosized samples show a combination of ferrimagnetic and paramagnetic behavior. The coercive field (H_C) at room temperature was found to increase with reduction in grain size (G) according to the equation $H_C = a_m + b_m/G$, which is consistent with multidomain particles. With further reduction in grain sizes, the coercive field reduced according to the equation $H_C = a_s - b_s/G^2$. This equation is associated with the onset of single domain particles. The samples produced by hydrothermal and glycothermal processes show evidence of transformation from single domain to multidomain structure with increasing sintering temperature.

The ease of single–phase formation in the compounds studied is shown to depend on the technique used to prepare the samples. Single phase formation of the spinel structure was easier to achieve in samples prepared by wet chemical methods because lower sintering temperatures ($T < 1000\ ^oC$) were required.

Publications based on the current work

1. Mössbauer studies on (Zn, Cd, Cu)$_{0.5}$Ni$_{0.5}$Fe$_2$O$_4$ oxides, J. Z. Msomi, K. Bharuth-Ram, V. V. Naicker and T. Moyo, Hyperfine Interactions 158 (2004) 151.

2. Magnetic properties of bulk and nanosized (Zn, Cd, Cu)$_{0.5}$Ni$_{0.5}$Fe$_2$O$_4$ ferrites, J. Z. Msomi, T. Moyo and T. B. Doyle, J. Magn. Magn. Mater. 310 (2007) 2534 (presented at the International Conference on Magnetism, Kyoto Japan, August 20–25 2006).

3. Synthesis of Cu$_{0.5}$Ni$_{0.5}$Fe$_2$O$_4$ nanoparticles, J. Z. Msomi and T. Moyo, J. African Phys. Rev. (submitted for publication 2007, presented at the EBASI International Conference, Western Cape, South Africa, January 24–26 2007).

4. Green density effects on the structural and magnetic properties of (Zn, Cd)$_{0.5}$Ni$_{0.5}$Fe$_2$O$_4$ ferrites produced by combustion technique, T. Moyo, P. R. Silva, H. Saitovitch and J. Z. Msomi, J. African Phys. Rev. (submitted for publication 2007, presented at EBASI International Conference, Western Cape, South Africa, January 24–26 2007).

5. Effect of domain transformation on the magnetic properties of Cu$_x$Ni$_{1-x}$Fe$_2$O$_4$ oxides, J. Z. Msomi and T. Moyo, NSTI–Nanotech 2007, Technical Proceedings 4 (2007) 397. (presented at the Nanotechnology Conference, Santa Clara, USA, May 20–24 2007).

6. Temperature dependence of hyperfine fields of (Ni, Cu)Fe$_2$O$_4$ oxides (to be presented at the XIV International conference on Hyperfine Interactions, Iguazu Falls, Brazil, August 5–10 2007).

Contents

List of Figures

List of Tables

Chapter 1

Introduction to ferrites

Ferrites are a group of oxides that have a general chemical formula $M\mathrm{Fe_2O_4}$ where M is a divalent metal ion such as Zn, Cd, Cu, Ni, Co, Mg or Fe [1]. Mixed ferrites can be produced by mixing two or more kinds of M ions [2]. $\mathrm{Zn_{0.5}Ni_{0.5}Fe_2O_4}$ is an example of a mixed ferrite and is one of the compounds studied in the current work. Ferrites exhibit a variety of useful and interesting properties. In this chapter we discuss briefly the synthesis, structure, magnetic properties and applications of ferrites. A brief account for the motivation of the current work is also given.

1.1 Synthesis of ferrites

Ferrites in bulk form are generally made by using solid state reaction [3–14]. The starting materials in this technique are high purity oxides. This requires two stages of grinding and prolonged heat treatments at high temperatures (900 ^{o} C to 1400 ^{o} C [15]). Ferrite materials can also be made by mechanical milling. In this method the correct proportions of high purity oxides required to form a desired compound are weighed and poured into agate or hardened steel jars with agate or stainless steel balls respectively. The mixture is milled for several hours (depending on milling conditions such as grinding ball to sample mass ratio and speed at which the jars are rotated) until the desired

phase is formed.

Besides being cumbersome, solid state reactions require high temperature heat treatments which can cause evaporation of some of the constituent metal oxides or phase changes e.g. Fe_3O_4 to α–Fe_2O_3 or γ–Fe_2O_3 [16]. This can result in the final products having modified stoichiometric composition or samples with unreproducible characteristics. The milling process may also cause loss of sample due to adhesion of sample to grinding surfaces. This can lead to possible changes in the stoichiometry of the desired compounds. Furthermore, during traditional solid state mixing or milling contamination or introduction of impurities to the sample from grinding surfaces may be unavoidable.

Other methods of producing ferrites have been introduced and are still currently being developed. Many papers have appeared in literature recently associated with wet chemical methods such as sol–gel [17], hydrothermal [18–24], glycothermal [25], citrate precursor [16, 26, 27] and combustion [15, 29, 30] which seek to produce better quality ferrites. In wet chemical methods the salt solutions of desired compositions are mixed thoroughly to ensure molecular level of mixing. A base such as KOH or ignitor such as urea is added to the mixture. The final mixture is then heated in order to form the desired ferrite powder. The sintering temperature of the final product that ensures single phase formation tends to be much lower than for samples produced by solid state reaction. The incorporation of unwanted impurities and sample losses are much reduced in samples produced by wet chemical methods.

In order to investigate the effect of different production techniques on the properties of ferrites, samples were produced by solid state reaction, combustion, hydrothermal and glycothemal methods and studied in the current work.

1.2 Crystal structure of ferrites

The crystal structure of MFe_2O_4 is that of a cubic spinel ($MgAl_2O_4$) [31]. It consists of two interstitial sites called A and B occupied by metal ions.

The position of the A site is half way between the corner and center of the cube diagonal and that of B site is at the center of the edge of a cube as shown in Figure 1.1. The occupied B sites form rows parallel to face diagonals (see Figure 1.2). The A sites that are occupied are those with empty nearest neighbor B sites [2]. The A site ions have four neighboring oxygen ions forming a tetrahedron, while the B site ions are surrounded by six oxygen ions forming an octahedron [31]. We therefore speak of tetrahedral (A) and octahedral (B) sites. Ferrites can therefore be represented by the chemical formula AB_2O_4 where A and B represent metal cations on the tetrahedral (A) and octahedral (B) sites respectively.

The spinel structure can be 'normal' or 'inverse' depending on the distribution of cations on the interstitial sites. In a normal spinel all the tetrahedral (A) sites are occupied by divalent ions and the octahedral (B) sites by trivalent ions. Cadmium ($CdFe_2O_4$) and zinc ($ZnFe_2O_4$) ferrites are examples of normal spinels [24, 32, 33] where all the Cd^{2+} and Zn^{2+} ions are distributed on A sites and the Fe^{3+} ions occupy B sites. In an inverse spinel the trivalent ions are distributed equally between A and B sites and all the divalent ions occupy B sites. Copper ($CuFe_2O_4$) and nickel ($NiFe_2O_4$) ferrites are examples of inverse spinel [14, 34]. Half of the Fe^{3+} ions occupy A sites and the other half occupy B sites with Cu^{2+} or Ni^{2+} cations. Since the magnetic moments of the ions on A sites are antiparallel to those on B sites in ferrites, the magnetization of an inverse spinel is due to divalent M ions [2]. Most ferrites are partly normal or partly inverse [2]. The degree of inversion appears to have a remarkable effect on the magnetic properties. This is influenced by sample preparation methodology [14] and sintering temperature [2, 3]. Cations also have site preferences for A or B sites depending on their size and electronic configuration. Those with smaller size prefer to occupy the smaller tetrahedral (A) sites while larger cations have more preference for roomier octahedral (B) sites [2, 31]. Zn^{2+} and Cd^{2+} ions have been observed to show more preference for A sites where their 4s,p and 5s,p electrons respectively form covalent bonds with six 2p electrons

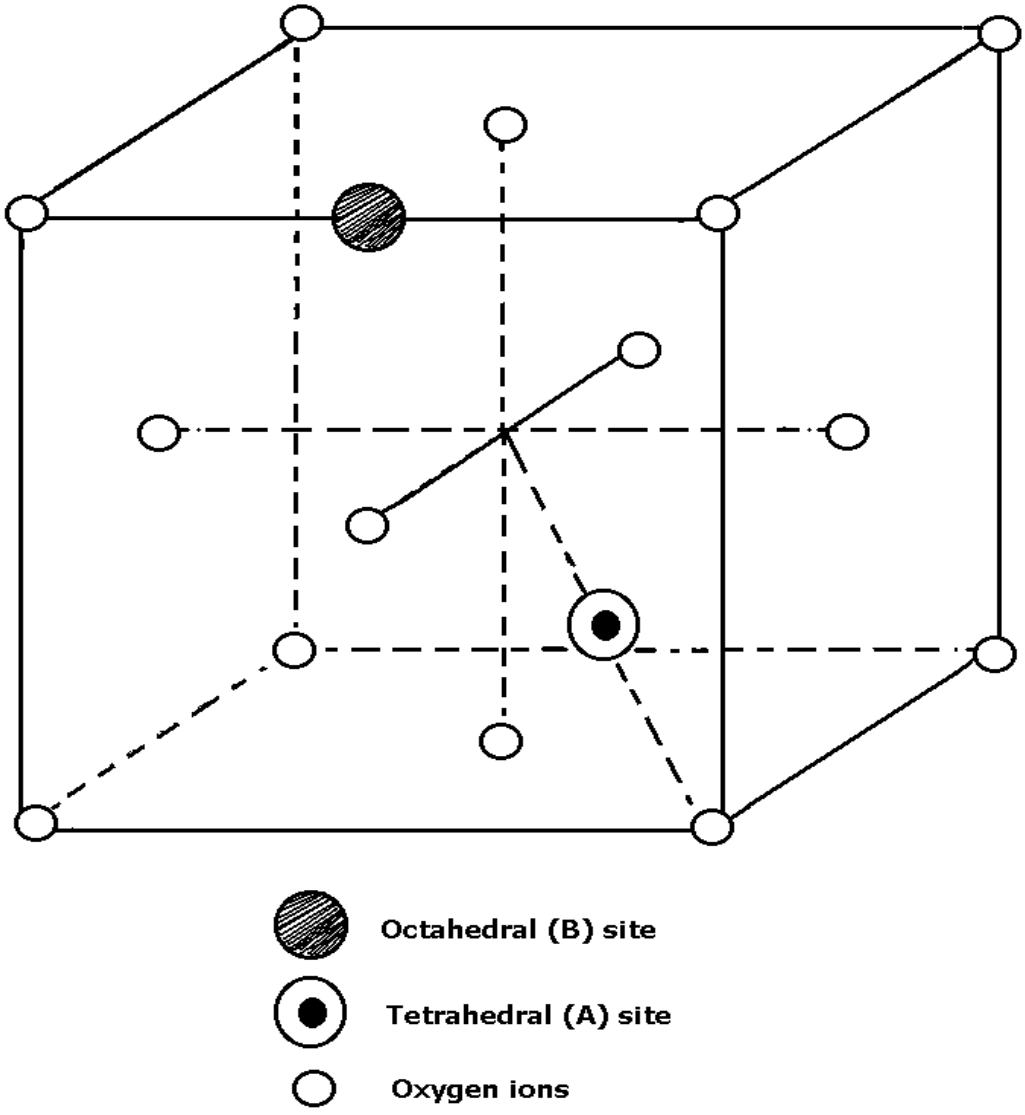

Figure 1.1: Schematic diagram of one eighth of the unit cell of the spinel structure [2].

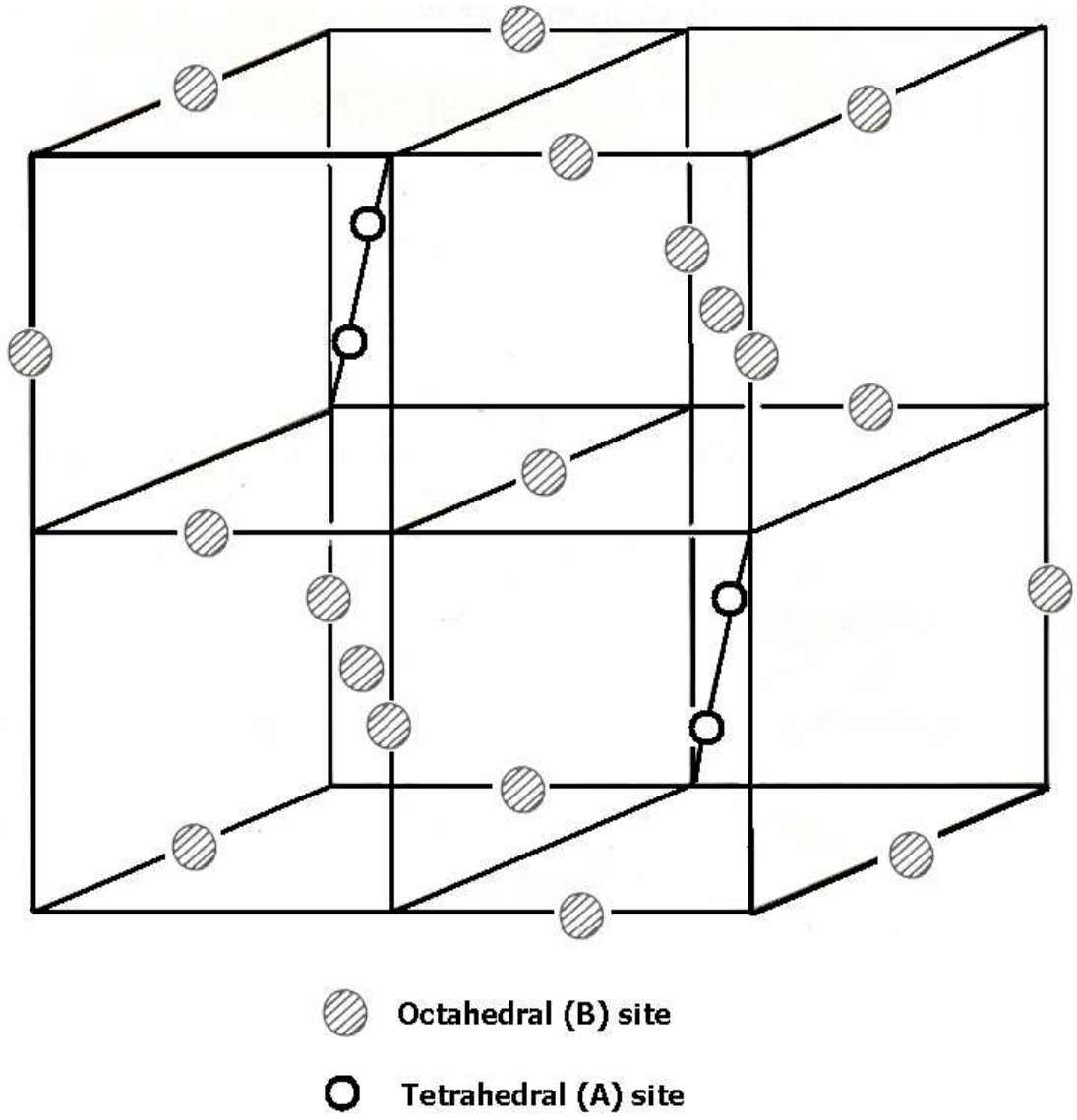

Figure 1.2: Occupation of tetrahedral (A) and octahedral (B) sites in a spinel [2].

of oxygen ions [7, 31]. The Ni [34] and Cu [6, 35] ions prefer B sites.

In the present work, formation of single phase structure of the compounds produced was confirmed by x–ray diffraction measurements and analysis.

1.3 Magnetic properties of ferrites

Ferrites are essentially a dilute system of metal ions interspaced between oxygen ions. The oxygen ions play a role of mediating the magnetic interaction between the metal ions [1, 31]. The oxygen ions also insulate metal ions from each other. This is the basis of much increased resistivity of ferrites. Magnetic properties of ferrites are the primary concern of this thesis. The origin of this magnetism is due to magnetic moments at the metal ions. The interaction of these magnetic moments through the intervening O^{2-} ions is responsible for the observed magnetic order. This interaction is called superexchange interaction [1, 31].

The magnetic behavior in ferrites is similar to that of ferromagnetic materials. As the temperature of the sample is decreased below the Curie point, magnetization rapidly increases at first and then slowly rises to maximum at absolute zero. The magnetic properties are also characterized by a non–linear variation of magnetization with an applied field. When the temperature is increased above the Curie point a paramagnetic state is obtained. During Mössbauer and magnetization measurements this can, respectively, be seen by the collapse of the six line Mössbauer spectrum to a doublet and the onset of zero saturation magnetization.

The magnetism in ferrites is a special case of antiferromagnetism where the spins that are aligned antiparallel are unequal in size. Unlike antiferromagnets, a resultant magnetization is observed due to the differences in the magnitude of the magnetic moments between sublattices.

1.4 Applications of ferrites

Ferrite materials have wide range of applications. In general these are based on their favorable magnetic, electrical, mechanical or chemical properties. Sometimes two or more of the above properties are critical for certain applications. Ni–Zn substituted mixed ferrites are soft ferrimagnetic materials with low coercivity, high resistivity values and little eddy current losses [15, 36]. These properties make them excellent core materials for power transformers in electrical and telecommunication applications. They are also used in high frequency devices for radio frequency applications [17, 18].

Manganese ferrites are widely used in electronic applications such as transformers, choke coils, noise filters and recording media [19]. They are also used as catalyst and humidity sensors [22]. Multilayer chip inductors can also be made from ferrites. These are useful as surface mounting devices for miniaturization of electronic devices such as cellular phones and video cameras [37]. The use of small and compact power supplies for computers, microprocessors and video cassette recorders has also led to a increased demand for ferrites with high switching frequencies and better material performance [38].

Recently, there has been a renewed interest in the study of nanosized ferrites. The reasons for this are potential applications in nanoscience and technology [39]. This has also been driven by the quest for new products and fundamental understanding of material properties when the particle size approaches atomic scale. Cobalt ferrite ($CoFe_2O_4$) has high coercivity and moderate magnetization [40]. These properties along with its physical stability make $CoFe_2O_4$ nanoparticles suitable for magnetic recording applications such as audio, videotape and high density recording disks [41]. Magnetic nanoparticles are also relevant to modern technologies such as contrast enhancement of magnetic resonance imaging and high-density data storage. Nanoparticles can also be used as magnetic carriers for delivery of medicine to specific parts of the body [16, 25]. The drug capsules can be thermally opened at a predetermined site

within the body. The heating effect of nanomagnetic particles in response to alternating magnetic fields may also be useful at destroying tumor cells [42]. Therefore any systematic study of nanosized magnetic materials is important.

1.5 Motivation for current work

The properties of ferrites are dependent on the distribution of cations amongst A and B sites. As observed earlier, different types of cations have different site preferences. The highly stable spinel structure allows the possibility of introducing a variety of magnetic disorder and frustrations [3, 8]. This accounts for a variety of electrical and magnetic properties of ferrites. Making suitable substitutions on A or B sites can improve the properties. As an example Ni ferrites have high resistivity and thus low conductivity making them useful for microwave applications [43]. Zn–Ni substituted ferrite are also amongst some of the well–studied and used high resistivity ferrites. The desired phase is easy to form [15] and materials produced have the advantage of high stability and low cost. This accounts for the wide use of Zn–Ni ferrites in the electronic industry.

The magnetic properties of ferrites in bulk form have also been observed to be drastically different from those of nanosized ferrites [37–47]. As an example, the enhancement of the magnetic transition temperature of nanosized $ZnFe_2O_4$ oxide due to milling was attributed to the distribution of Zn ions on both A and B sites [44, 45]. This is interesting because Zn ions are known to occupy A sites only in bulk compounds [7, 8].

In this thesis we present a systematic study of the effect of cation distributions between the tetrahedral (A) and octahedral (B) sites on the magnetic properties of ferrites. In order to achieve this we made bulk (Zn, Cd, $Cu)_{0.5}Ni_{0.5}Fe_2O_4$ and $NiFe_2O_4$ samples by solid state reaction and systematically reduced their grain sizes to about 10 nm scale using a Retsch high energy ball miller. In the preliminary work [4, 5] we have investigated the effect of

atomic size difference between Cd and Zn ions on the magnetic properties of (Zn, Cd)$_x$Co$_{1-x}$Fe$_{2-x}$Al$_x$O$_4$ and (Cd, Zn)$_x$Co$_{0.9}$Fe$_{1.7-x}$Ti$_{0.4}$O$_4$ using Mössbauer spectroscopy at about 300 K. Mössbauer spectra did not indicate significant changes associated with size difference of atoms involved. The aim of the current work is to investigate the effect of replacing Zn by Cd or Cu in the Zn–Ni substituted ferrites. Cd ion has larger ionic size (0.097 nm) than Zn (0.074 nm) and Cu (0.072 nm) is slightly smaller. While Zn and Cd atoms have full outer s orbital electrons, Cu has an unpaired electron in its outer orbital. In this work we have characterized the samples by both Mössbauer (79 K to 900 K) and magnetization measurements (at about 300 K) in order to investigate the effects of atomic size and electronic configuration differences.

Apart from the type and particle size, cation distribution in ferrites also depends on heat treatment during preparation [3, 14, 31]. We therefore made some of the samples by using combustion, hydrothermal and glycothermal techniques in order to compare the properties. The samples made by these wet chemical methods were sintered at different temperatures until the complete single phase spinel structure was formed.

In summary the main objectives of the current work are to investigate the effects of cation distribution due to:

1. atomic size, electronic configuration differences and particle size

2. heat treatments during sample preparation method

on the magnetic properties of ferrites. In chapter 2 some details on the magnetism of magnetic materials are presented. Mössbauer spectroscopy has been used extensively in this work. The basic principles of this technique are reviewed in chapter 3. The experimental details are presented in chapter 4. In chapters 5, 6, 7 and 8 we present the results and discussions and general conclusions are provided in chapter 9.

Chapter 2

Magnetism in magnetic materials

2.1 Origins of magnetic moments

Magnetism in magnetic materials arises due to the presence of permanent and induced magnetic moments at constituent atoms and their mutual interaction. The origin of magnetic moments is due to electronic motions and intrinsic spin of electrons [1, 48, 49]. To demonstrate this we consider an electron of mass m_e and charge $-e$ moving in a closed circular orbit of radius r. The circulating current I is associated with a magnetic moment $\mu = IA$ where $A = \pi r^2$ is the area of the closed loop. If the electron is moving at frequency f (with angular frequency $\omega = 2\pi f$) the current $I = -ef$. Hence

$$\mu = -ef\pi r^2 = -\frac{1}{2}e\omega r^2 = -\frac{1}{2m_e}l_z \tag{2.1.1}$$

where $l_z = m_e\omega r^2$ is the orbital angular momentum. Since l_z is quantized ($l_z = m_l\hbar$ where $m_l = 0, 1, 2, 3 \ldots$)

$$\mu_l = -\left(\frac{e\hbar}{2m_e}\right)m_l = -\mu_B m_l. \tag{2.1.2}$$

The quantity $\mu_B = e\hbar/2m_e = 9.274 \times 10^{-24}$ J/T is the Bohr magneton and is the fundamental unit of magnetic moment.

Equation (2.1.1) shows that the electron magnetic moment is proportional to its orbital angular momentum. Since an electron has also got intrinsic spin angular momentum its total magnetic moment is therefore proportional to the total angular momentum ($\overrightarrow{j}$) due to both orbital ($\overrightarrow{l}$) and spin ($\overrightarrow{s}$) angular momenta, i.e.,

$$\overrightarrow{\mu} = \gamma \overrightarrow{j} = \gamma(\overrightarrow{l} + \overrightarrow{s}) \tag{2.1.3}$$

where γ is called the magnetomechanical ratio. In general the hamiltonian for an electron at position $\overrightarrow{r} = (x_i, y_i, z_i)$ in a steady electric ($\overrightarrow{E}$) and magnetic ($\overrightarrow{B}$) field can be shown to be

$$H_e = \frac{p^2}{2m_e} + \frac{\mu_B}{\hbar}\overrightarrow{B} \cdot \overrightarrow{l} + \frac{e^2}{8m_e}(\overrightarrow{B} \times \overrightarrow{r})^2 - e\phi \tag{2.1.4}$$

where ϕ is the static electric potential due to the electric field. This hamiltonian can be rewritten in the form $H_e = H_0 + \delta H(B)$ where $\delta H(B)$ can be considered as a field dependent perturbation. The eigen values can be obtained by solving the eigen value equation

$$H_e\psi_n = E_n\psi_n \tag{2.1.5}$$

where ψ_n is an eigen function. Using perturbation theory to second order the energy eigen values can be shown [50] to be

$$E_n = E_0 + \frac{\mu_B}{\hbar}(\overrightarrow{B} \cdot < n|\overrightarrow{l} + 2\overrightarrow{s}|n >) + \frac{e^2B^2}{8m_e}(< n|\sum_i (x_i^2 + y_i^2)|n >) + \sum_{n \neq n'} \left(\frac{\left| < n|\frac{\mu_B B}{\hbar}(\overrightarrow{l} + 2\overrightarrow{s})|n' > \right|^2}{E_n - E'_n} \right) + \ldots \tag{2.1.6}$$

The magnetic moment is

$$\mu = -\frac{\partial E_n}{\partial B}. \tag{2.1.7}$$

This gives

$$\overrightarrow{\mu} = -\frac{\mu_B}{\hbar} < n|(\overrightarrow{l} + 2\overrightarrow{s})|n > -\frac{e^2B}{4m_e}(< n|\sum_i (x_i^2 + y_i^2)|n >) - 2B \sum_{n \neq n'} \left(\frac{\left| < n|\frac{\mu_B}{\hbar}(\overrightarrow{l} + 2\overrightarrow{s})|n' > \right|^2}{E_n - E'_n} \right) + \ldots . \tag{2.1.8}$$

The first term in equation (2.1.8) is the permanent magnetic moment of an electron. This is due to orbital and spin angular momentum. It gives rise to paramagnetism, ferromagnetism, antiferromagnetism and ferrimagnetism. The second term is the induced magnetic moment and gives rise to diamagnetism. While the third term is the induced paramagnetic moment.

The magnetic moment of an atom is determined by contributions from all the electrons. According to Russell–Saunders coupling [50–52] in an atom, the angular momenta of all its electrons couple to give a total orbital angular momentum ($\overrightarrow{L} = \sum \overrightarrow{l}_i$). The electron spin momenta also couple to give rise to the resultant spin angular momentum ($\overrightarrow{S} = \sum \overrightarrow{s}_i$). $\overrightarrow{L}$ and $\overrightarrow{S}$ then couple to form the total angular momentum $\overrightarrow{J}$ according to Hund's rules [48, 50]. The magnitude of the average atomic magnetic moment (μ_J) can be calculated from its total angular momentum by using the equation [52]

$$\mu_J = \mu_B g \sqrt{J(J+1)} \tag{2.1.9}$$

where the Landé factor g is given by

$$g = 1 + \frac{J(J+1) + S(S+1) - L(L+1)}{2J(J+1)}. \tag{2.1.10}$$

2.2 Magnetization and susceptibility

The total magnetic moment per unit volume of the sample is called magnetization, $\overrightarrow{M}$. This is defined as

$$\overrightarrow{M} = \frac{\sum \overrightarrow{\mu}_i}{V} \tag{2.2.1}$$

where V is the volume of a sample of mass m. The magnetization depends on temperature and on how the magnetic moments are coupled together.

Experimentally it is more convenient to define the magnetization per unit mass of substance as

$$\overrightarrow{\sigma} = \frac{\sum \overrightarrow{\mu}_i}{m}. \tag{2.2.2}$$

It is easier to measure the mass of the sample than its volume. The volume of the sample may also change as a function of temperature (thermal expansion) or applied magnetic field (magnetostriction). Hence it is better to define the magnetization in terms of $\overrightarrow{\sigma}$. From equations (2.2.1) and (2.2.2) we can show that

$$\overrightarrow{\sigma} = \frac{\overrightarrow{M}}{\rho} \tag{2.2.3}$$

where ρ is the density of the sample. Experimentally the magnetization is determined under the influence of an applied magnetic field, H_0. It is assumed in this work that $B_0 = \mu_0 H_0$ where B_0 is the magnetic induction and μ_0 is the permeability of free space. The response function of the magnetization under the effect of magnetic field is called susceptibility χ which can be defined (in the Systm̀e International d'Unitś (SI)) as [49, 53]

$$\chi = \frac{\mu_0 M}{B_0}. \tag{2.2.4}$$

Induced moments give rise to a negative susceptibility ($\chi < 0$) associated with diamagnetism. Materials with permanent magnetic moments have positive susceptibilities ($\chi > 0$). Analysis and measurement of susceptibility can be used to distinguish the magnetic behavior of different materials.

In magnetism there are essentially two systems of units of expressing magnetic quantities, namely the Systm̀e International d'Unitś (SI) and centimeter–gram–second (CGS) systems. The conversion from one system to another is usually given in introductory text books in Condensed Matter Physics [48, 53]. The conversion tables are also available in the literature [20]. The magnetization per unit mass can be expressed in Ampere meter squared per kilogram (A m^2/kg) in SI units and in electromagnetic units per gram (emu/g) in CGS units. The magnetic field in SI units is expressed in Tesla (T) and in Oersted (Oe) or Gauss (G). In the present study all experimental values of magnetization and magnetic fields are expressed in CGS units.

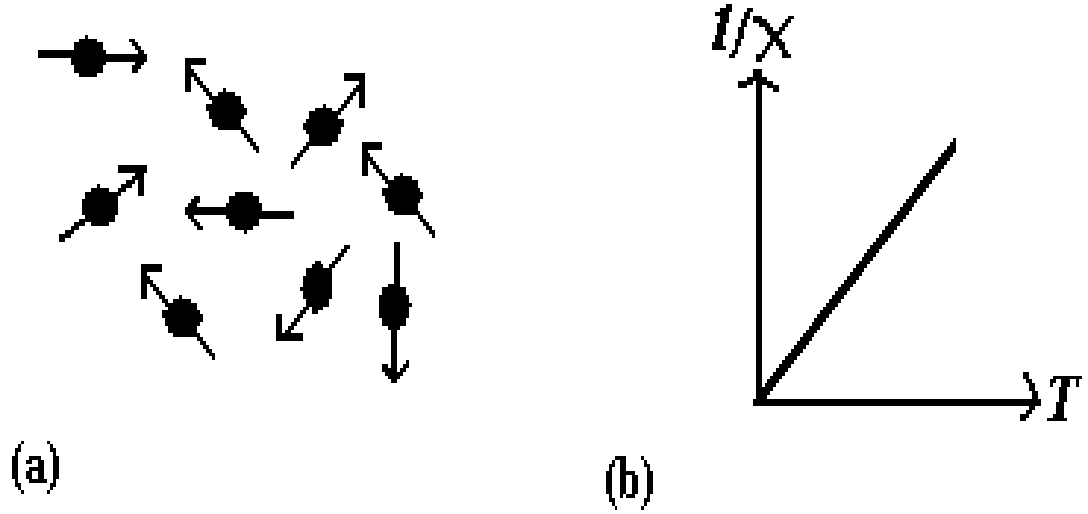

Figure 2.1: (a) Magnetic structure and (b) variation of $1/\chi$ with temperature in a paramagnet [52].

2.3 Magnetic order in solids

In this section we present a discussion of different types of magnetic order in solids which are more relevant to the present work. These are paramagnetism, ferromagnetism, antiferromagnetism and ferrimagnetism. The diamagnetic effect is present in all materials, but for the materials studied here this contributes a negligible amount to the total magnetic behavior. Other types of more complex magnetic structures also exist [54].

2.3.1 Paramagnetism

Paramagnetic materials are characterized by a random distribution of magnetic moments as shown in Figure 2.1 (a). Paramagnetism occurs in a system with non–interacting or weakly interacting magnetic moments. The behavior is characterized by a positive susceptibility which is temperature dependent as shown in Figure 2.1 (b). In the presence of magnetic field B_0 magnetic moments will orient themselves in particular directions with possible energies

$$E_J = -\overrightarrow{\mu}_J.\overrightarrow{B}_0 = -g\mu_B m_J B_0 \tag{2.3.1}$$

where m_J = -J, -J + 1, ..., J - 1, J. From statistical mechanics, the average magnetic moment of an atom in the field direction is given by

$$< \mu_J >= \sum g m_J P(E_J) \mu_B \tag{2.3.2}$$

where $P(E_J)$ is the Maxwell–Boltzmann distribution which specifies the probability that the state with energy E_J is occupied. Since

$$P(E_J) = \frac{e^{-g\mu_B m_J B_0/k_B T}}{\sum e^{-g\mu_B m_J B_0/k_B T}} \tag{2.3.3}$$

we can show that

$$< \mu_J >= J g \mu_B F(J, y). \tag{2.3.4}$$

The Brillouin function $F(J, y)$ is given by [1, 50]

$$F(J, y) = \left(1 + \frac{1}{2J}\right) coth \left[\left(1 + \frac{1}{2}\right) y\right] - \frac{1}{2J} coth \left[\frac{y}{2J}\right] \tag{2.3.5}$$

where

$$y = \frac{J g \mu_B B_0}{k_B T}. \tag{2.3.6}$$

For small values of y corresponding to high temperature and small magnetic field (B_0) the Brillouin function is approximately given by [50]

$$F(J, y) \simeq \frac{y(J+1)}{3J}. \tag{2.3.7}$$

From equations (2.3.4) and (2.3.7) the magnetization for N non–interacting magnetic moments per unit volume is given by

$$M = \frac{N < \mu_J >}{V} = \frac{N J g \mu_B F(y, J)}{V} = \frac{N g^2 \mu_B^2 J(J+1) B_0}{3 V k_B T} \tag{2.3.8}$$

where V is the volume of the sample. The susceptibility of the sample can be deduced to be

$$\chi = \frac{\mu_0 M}{B_0} = \frac{\mu_0 N g^2 \mu_B^2 J(J+1)}{3 V k_B T} = \frac{C}{T}, \tag{2.3.9}$$

where

$$C = \frac{\mu_0 N g^2 \mu_B^2 J(J+1)}{3 V K_B} \tag{2.3.10}$$

is referred to as the Curie constant. This temperature dependence of paramagnetic susceptibility was discovered by P. Curie in 1895 and hence is known as the Curie law [52]. The Curie law holds very well in many paramagnetic crystals but the law often observed experimentally is [1, 50, 52]

$$\chi = \frac{C}{T - \theta_p} \tag{2.3.11}$$

where θ_p has a value close to the paramagnetic Curie temperature. This result is known as Curie–Weiss law which arises due to interactions between magnetic moments.

2.3.2 Ferromagnetism

Fe, Ni and Co are classical ferromagnetic materials. These elements have atoms with permanent magnetic moments which spontaneously align themselves parallel to each other below some critical temperature called the Curie temperature, T_C. Below T_C ferromagnets exhibit a net spontaneous magnetization even in zero field. At absolute zero temperature the magnetic order would be perfect as shown in Figure 2.2 (a). With increasing temperature some of the spins begin to disorder due to thermal agitation. At T_C the disorder is complete. Above T_C ferromagnetic materials exhibit a paramagnetic behavior. The susceptibility that follows the Curie–Weiss law is given by equation (2.3.11). However, this law fails in the vicinity of the Curie point, T_C.

The variation of magnetization with temperature in ferromagnetic materials was first explained by the Weiss mean–field theory (1907). This theory is based on the assumption that each magnetic moment in a ferromagnet is acted upon by an intense internal magnetic field (B_{in}) that is proportional to the magnetization (M_S) of the sample [1, 48, 49, 53] i.e.,

$$B_{in} = \lambda M_S \tag{2.3.12}$$

where λ is molecular field coefficient. B_{in} is much larger than the fields which can be produced due to dipole fields of a permanent magnet. The origin of

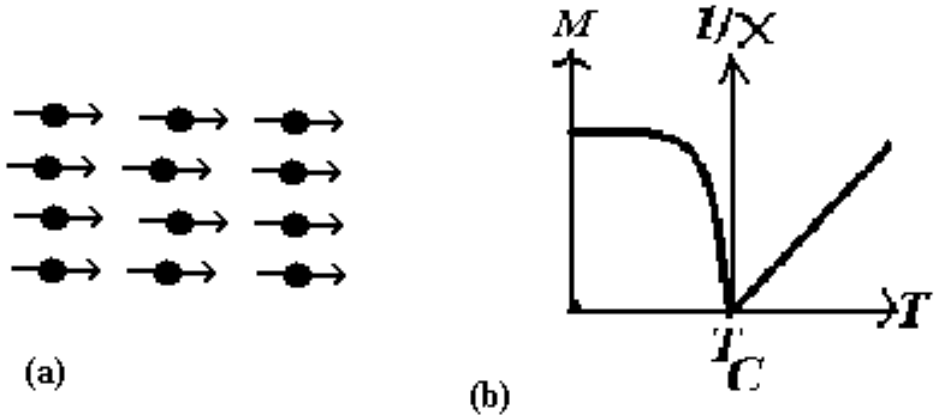

Figure 2.2: (a) Magnetic structure and (b) variation of $1/\chi$ with temperature in a ferromagnet [52].

B_{in} is now known to be due to exchange interactions. The justification of $B_{in} = \lambda M_S$ is in the fact that the driving force that tends to align atomic moments in the same direction is proportional to the magnetic moments that are already aligned. If an additional external magnetic field (B_0) is applied to the sample the effective field will thus be

$$B_e = B_0 + B_{in} = B_0 + \lambda M_S. \tag{2.3.13}$$

From equation (2.3.8) the magnetization of a ferromagnetic sample can be assumed to be

$$M_S = \frac{NJg\mu_B F(J, y')}{V} \tag{2.3.14}$$

where

$$y' = \frac{Jg\mu_B(B_0 + \lambda M_S)}{k_B T}. \tag{2.3.15}$$

Usually $B_{in} >> B_0$ hence M_S is still finite even for $B_0 = 0$. Since the Brillouin function $F(J, y')$ approaches 1 with increasing y' [1, 51], equation (2.3.14) therefore shows that spontaneous magnetization saturates to

$$M_S(0, 0) = \frac{NJg\mu_B}{V} \tag{2.3.16}$$

at 0 K. This implies that magnetic moments are in perfect alignment. At $T >$ 0 K and $B_0 = 0$, the spontaneous magnetization given by equation (2.3.14) can

be expressed as

$$M_S(0,T) = M_S(0,0)F(J,y') \tag{2.3.17}$$

where

$$y' = \frac{g\mu_B J\lambda M_S(0,T)}{k_B T}. \tag{2.3.18}$$

The form of equation (2.3.18) indicates that y' approaches zero with increasing temperature. Since the Brillouin function $F(J,y')$ approaches zero with decrease in y' [51], equation (2.3.17) indicates that the spontaneous magnetization will vanish with increase in temperature. This is in agreement with the experimental behaviour of magnetization with temperature as shown in Figure 2.2 (b). The Weiss theory therefore successfully predicts the temperature dependence and its collapse at finite temperature T_C. Equation (2.3.17) can be rewritten in the form

$$\frac{M_S(0,T)}{M_S(0,0)} = F(J,y'). \tag{2.3.19}$$

By dividing equation (2.3.18) by equation (2.3.16) we get

$$\frac{M_S(0,T)}{M_S(0,0)} = \left(\frac{k_B T}{NJ^2 g^2 \mu_B^2 \lambda}\right) y'. \tag{2.3.20}$$

The equations (2.3.19) and (2.3.20) can be represented graphically by curves C1 and C2 respectively as shown in Figure 2.3. The magnetic state of a ferromagnet is obtained by satisfying simultaneously both equations (2.3.19) and (2.3.20). In the vicinity of the Curie temperature ($T < T_C$) the spontaneous magnetization $M_S(0,T)$ is small. From the form of equation (2.3.18) y' approaches zero for small values of $M_S(0,T)$. From equations (2.3.7), (2.3.19) and (2.3.20) we can show that the Curie temperature is given by [50]

$$T_C = \frac{Ng^2\mu_B^2 g^2 \lambda J(J+1)}{3Vk_B}. \tag{2.3.21}$$

A better approaximation of the Brillouin function near T_C (for $T \leq T_C$ and $y' \ll 1$) is given by

$$F(J,y) = \frac{y'(J+1)}{3J} - \frac{y'^4(2J+1)}{3(2J)^4 35} + \ldots \tag{2.3.22}$$

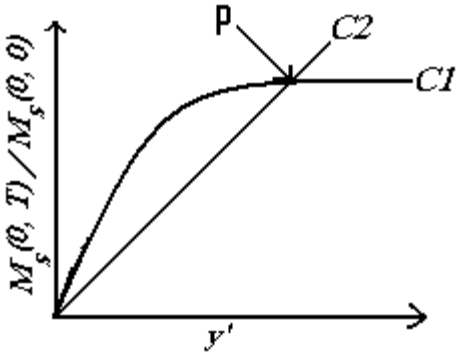

Figure 2.3: Graphical representation of equations (2.3.19) and (2.3.20) [1, 51].

Hence we can show that

$$M_S(0,T) \propto (T_c - T)^{1/2}\,. \tag{2.3.23}$$

However, experiments show spontaneous magnetization to vary as [50]

$$M_S(0,T) \propto (T_c - T)^{1/3}\,. \tag{2.3.24}$$

A proper treatment of this problem is discussed in the theory of critical phenomena [55, 56] which is not the subject of this study.

Above T_C the sample is in paramagnetic state. Its magnetization is small and depends on the applied field. The assumption that $B_{in} >> B_0$ is no longer valid. Based on equations (2.3.7), (2.3.14) and (2.3.15)

$$M = \frac{NJ^2g^2\mu_B^2J^2(J+1)(B_0+\lambda M)}{3Vk_BT}. \tag{2.3.25}$$

This leads to the Curie–Weiss law for the paramagnetic susceptibility

$$\chi = \frac{C}{T-\theta_p} \tag{2.3.26}$$

where C is the Curie constant and θ_p is the paramagnetic Curie point. Experimental results tend to show that $\theta_p \geq T_C$ [57].

The form of equation (2.3.18) indicates that as T approaches 0 K $y' >> 1$. In this case the Brillouin function is [48]

$$F(J,y') \simeq 1 - \frac{exp(-y')}{J}. \tag{2.3.27}$$

The predicted variation of $M_S(0,T)$ at low temperature in the Weiss model is therefore

$$M_S(0,T) = M_S(0,0)\left(1 - \frac{exp\left(-\frac{T_C}{(J+1)T}\right)}{J}\right). \tag{2.3.28}$$

Due to the effect of spin wave excitation what is observed is a magnetization which is given by an expression of the form

$$M_S(0,T) = M_S(0,0)\left(1 - AT^{3/2} + \ldots\right). \tag{2.3.29}$$

In the Stoner theory of itenerant electron magnetism, the temperature dependence of magnetization is given by [58]

$$M(T) = M(0)\left[1 - \left(\frac{T}{T_C}\right)^2\right]^{1/2}. \tag{2.3.30}$$

Such a temperature dependence suggests that single particle excitations may be responsible for the collapse of magnetization with increasing temperature.

2.3.3 Antiferromagnetism

In antiferromagnets magnetic moments are aligned in a self compensatory manner so that the overall spontaneous magnetization is zero (see Figure 2.4 (a)). This kind of antiparallel alignment is due to negative exchange interaction between magnetic moments. An antiferromagnet has a critical temperature called the Néel temperature, T_N. Below T_N the moments are aligned antiparallel giving rise to zero net magnetization. If the temperature is increased above T_N, magnetic moments become randomly oriented and paramagnetic behavior is thus observed.

In the simplest form of antiferromagnetism, a crystal can be divided into two sublattices A and B as shown in Figure 2.5. The spins in one sublattice point one way and in the other point in the opposite direction. The mean–field theory can be used to deduce the magnetization of each sublattice. In this model the internal fields acting on moments on A and B sub lattices can be written as [1, 14, 48]

$$B_{in}^A = \lambda_{AA} M_A + \lambda_{AB} M_B \tag{2.3.31}$$

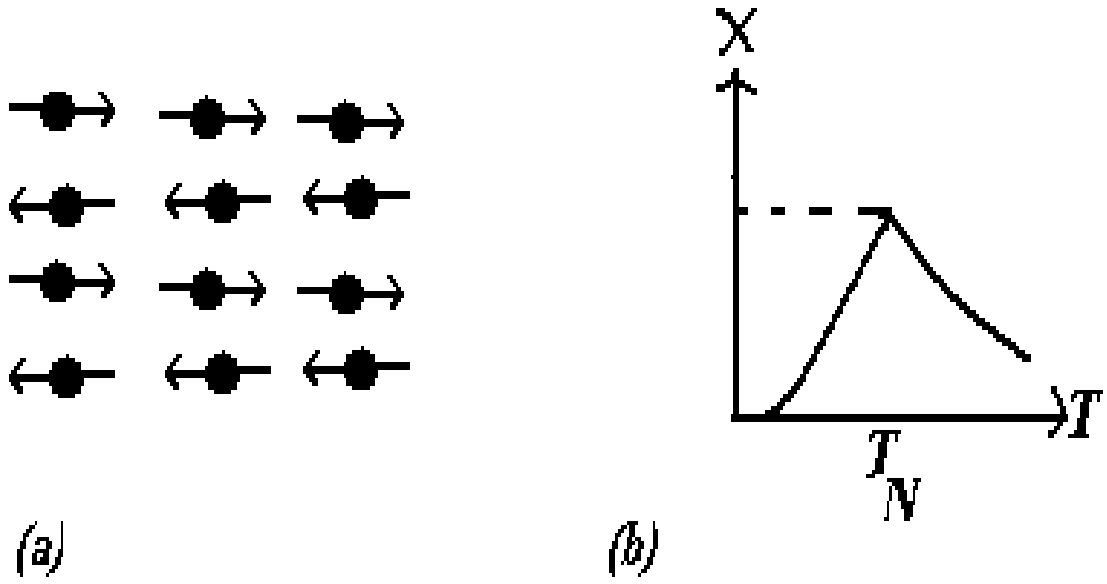

Figure 2.4: (a) Magnetic structure and (b) variation of $1/\chi$ with temperature in an antiferromagnet [57].

and

$$B_{in}^{B} = \lambda_{BA} M_A + \lambda_{BB} M_B. \tag{2.3.32}$$

For $\lambda_{AB} = \lambda_{BA} = -\lambda_1$ (nearest neighbors) and $\lambda_{AA} = \lambda_{BB} = -\lambda_2$ (next nearest neighbors), where λ_1 and λ_2 are both positive. The equations (2.3.31) and (2.3.32) can be rewritten in the forms

$$B_{in}^{A} = M_A(\lambda_1 - \lambda_2) \tag{2.3.33}$$

and

$$B_{in}^{B} = M_B(\lambda_1 - \lambda_2) \tag{2.3.34}$$

respectively. Assuming the average magnetizations on A and B sublattices are $M_A = \frac{N<\mu_A>}{2V}$ and $M_B = \frac{N<\mu_B>}{2V}$, equation (2.3.4) gives

$$M_A = \frac{NJg\mu_B F(J, y_A)}{2V} \tag{2.3.35}$$

and

$$M_B = \frac{NJg\mu_B F(J, y_B)}{2V} \tag{2.3.36}$$

where

$$y_A = \frac{Jg\mu_B B_{in}^A}{k_B T} = \frac{Jg\mu_B M_A(\lambda_1 - \lambda_2)}{k_B T} \tag{2.3.37}$$

and

$$y_B = \frac{Jg\mu_B B_{in}^B}{k_B T} = \frac{Jg\mu_B M_B(\lambda_1 - \lambda_2)}{k_B T} \tag{2.3.38}$$

as defined by equation (2.3.6). If magnetization on the two sublattices are the same ($M_A = M_B = M$) we get

$$M = \frac{NJg\mu_B F(y, J)}{2V} \tag{2.3.39}$$

where

$$y = \frac{Jg\mu_B M(\lambda_1 - \lambda_2)}{k_B T}. \tag{2.3.40}$$

The Néel temperature can be shown to be

$$T_N = \frac{\lambda_1 - \lambda_2}{2\mu_0} C \tag{2.3.41}$$

where C is the Curie constant. In the presence of the applied field B_0 and above the Néel point, the effective field acting on a magnetic moment on A and B sublattices are

$$B_e^A = B_0 + B_{in}^A = B_0 - \lambda_2 M_A - \lambda_1 M_B \tag{2.3.42}$$

and

$$B_e^B = B_0 + B_{in}^B = B_0 - \lambda_1 M_A - \lambda_2 M_B. \tag{2.3.43}$$

Hence from equations (2.3.7), (2.3.34) and (2.3.35) we get

$$M_A = \frac{Ng^2\mu_B^2 J(J+1)(B_0 - \lambda_2 M_A - \lambda_1 M_B)}{6Vk_B T} \tag{2.3.44}$$

and

$$M_B = \frac{Ng^2\mu_B^2 J(J+1)(B_0 - \lambda_1 M_A - \lambda_2 M_B)}{6Vk_B T}. \tag{2.3.45}$$

Adding equations (2.3.44) and (2.3.45) we can show that the susceptibility above T_N is

$$\chi = \frac{C}{T - \theta_P} \tag{2.3.46}$$

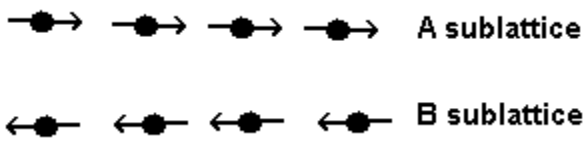

Figure 2.5: A and B sublattices (simple form of antiferromagnetism).

where

$$\theta_P = \frac{C(\lambda_1 + \lambda_2)}{2\mu_0}. \tag{2.3.47}$$

θ_P is related to the Néel temperature T_N as follows:

$$\theta_P = \frac{\lambda_1 + \lambda_2}{\lambda_1 - \lambda_2} T_N. \tag{2.3.48}$$

An antiferromagnet will register a magnetic response when subjected to an applied field B_0 below T_N. The bulk magnetization $M(B_0)$ depends on whether the field is applied perpendicular or parallel to the alignment of the magnetic moments. This leads to perpendicular $\chi_\perp$ and parallel $\chi_{||}$ susceptibilities [50]. If a large enough field is applied parallel to magnetic moments, susceptibility $\chi_{||}$ increases with temperature as [57]

$$\chi_{||} \simeq \frac{\mu_0 g^2 \mu_B^2 N}{4 V k_B T} e^{-2T_N/T} \tag{2.3.49}$$

for $T \ll T_N$. While for a the field applied perpendicular to spin axis the susceptibility $\chi_\perp$ is [57]

$$\chi_\perp = -\frac{g^2 \mu_B^2 N}{2\nu J_{ex} V k_B T} \tag{2.3.50}$$

where the exchange integral $J_{ex} < 0$, ν is the number of nearest neighbors and the quantity νJ_{ex} is the energy required to reverse a spin. This does not change with temperature because in this case magnetization is due to rotation of each spin from its axis. Above Néel temperature the susceptibility decrease with

increasing temperature as [57]

$$\chi = \frac{\mu_0 g^2 \mu_B^2 N}{4V k_B T} \frac{1}{T + T_N}. \tag{2.3.51}$$

The variation of the susceptibility in an antiferromagnet with temperature is shown in Figure 2.4 (b).

2.3.4 Ferrimagnetism

Ferrimagnetism occurs in ferrites. It is a special case of antiferromagnetism. In ferrimagnets spins are ordered antiferromagnetically. However, the spins on adjacent sublattices are unequal and anti–parallel as shown in Figure 2.6 (a). The resultant magnetization occurs due to a difference in the magnitude of magnetic moments. A Curie temperature exists. Above T_C a paramagnetic behavior is observed and below T_C ferrimagnets have spontaneous magnetization.

Ferrimagnetism can be described using a two sublattice model introduced by Néel in 1948. The magnetization of the sublattices oppose each other and the total magnetization can be written as

$$M = \lambda M_1 - (1 - \lambda) M_2. \tag{2.3.52}$$

If $\lambda = 1$ or 0 equation (2.3.52) implies ferromagnetism. If $\lambda = 1/2$ we have antiferromagnetism. Ferrimagnetism occurs if $\lambda \neq 0$, 1/2 or 1. The susceptibility of a ferrimagnet shows a hyperbolic dependence on temperature as shown in Figure 2.6 (b). The combination of the two–sublattice theory with Mean–field theory yields a susceptibility that varies with temperature as [48]

$$\frac{1}{\chi} = \frac{T}{C} + \frac{1}{\chi_0} + \frac{A}{T - \theta}. \tag{2.3.53}$$

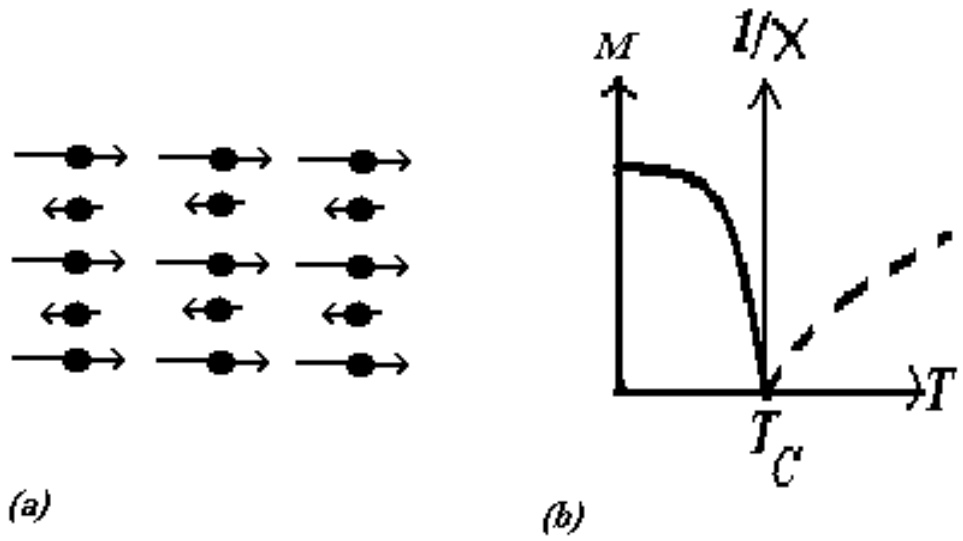

Figure 2.6: (a) Magnetic structure and (b) variation of $1/\chi$ with temperature in a ferrimagnet [52].

2.4 Magnetic interactions

There are two basic interactions between magnetic moments in a solid namely dipole–dipole and exchange interactions. Dipole–dipole interactions are known not to contribute to spontaneous magnetization (Weiss (1907)). Exchange interactions account for the observed magnetic order. Exchange interaction has a quantum mechanical origin and is closely related to the effects of the Pauli exclusion principle.

Magnetic moments that are so close that their wavefunctions overlap, interact through direct exchange interaction. This is a strong and short range interaction which for two spins $\overrightarrow{S}_i$ and $\overrightarrow{S}_j$ is expressed by the Heisenberg hamiltonian [52]

$$H_e = -J_{ij}\,\overrightarrow{S}_i \cdot \overrightarrow{S}_j \tag{2.4.1}$$

where J_{ij} is an exchange integral. J_{ij} is positive for ferromagnetism (or parallel spin arrangement) and is negative for antiferromagnetism (or antiparallel spin arrangement). The interaction of magnetic moments that are far from each other occurs through an intermediary. This is known as indirect exchange

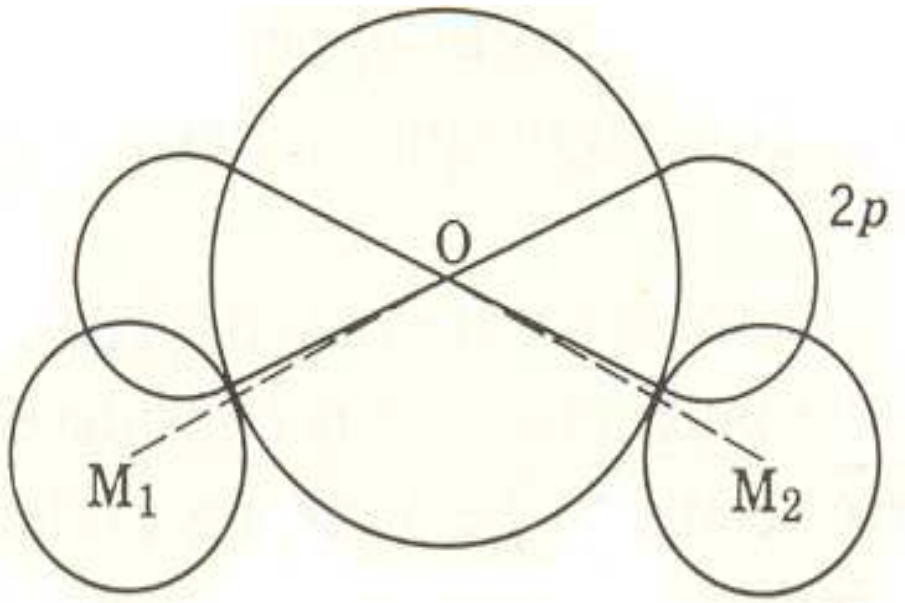

Figure 2.7: 2 p orbital of oxygen ion overlapping orbitals of metal ions M_1 and M_2 [2].

interaction. In metallic systems magnetic moments interact through the polarization of conduction electrons. This type of interaction is called RKKY interactions. In magnetic insulators such as the present compounds under study, magnetic moments interact through a non–magnetic ion. This is known as superexchange interaction. In ferrites there are strong exchange interactions between neighboring magnetic moments that take place via the intervening closed shells of oxygen ions. This indirect exchange can be explained by considering two metal ions M_1 and M_2 separated by an oxygen ion where there is an extensive overlapping between orbitals of the oxygen and metal ions as shown in Figure 2.7. This results in spin information from one metal atom being transferred to another metal atom.

2.5 Domain magnetism

A piece of iron does not show an apparent magnetic order at room temperature even though its Curie temperature is about 1043 K. However, when it is subjected to a small magnetic field it becomes easily magnetized. On the other hand an assembly of free magnetic moments requires about $\approx 3 \times 10^7$ Oe in order to be magnetized to saturation [1]. The relative ease to magnetize a ferromagnetic sample is due to domain structure formation. A ferromagnetic sample is subdivided into small regions called domains. The domain size depends on the size and shape of the crystal, internal strains, applied magnetic fields and magnetocrystalline anisotropy. Within each domain there are strong positive interactions between neighboring magnetic moments favoring parallel alignment. The individual domains therefore have spontaneous magnetization. The magnetizations of different domains point in different directions. This results in zero net magnetization in the absence of an external field. The effect of the applied field is not to induce magnetization at atomic level, but merely to align the magnetizations of different domains in the field direction.

The state in which all magnetic moments point in one direction has higher energy than the demagnetized state. Domains form in order to minimize the magnetostatic energy in both inside and outside of the specimen. In order to show a reduction in magnetostatic energy, initially consider a single domain (with magnetization M) in a magnetic field B_0 as shown in Figure 2.8. The discontinuity of the normal component of the magnetization creates 'free poles' which leads to a demagnetizing field DM. D is called the demagnetizing factor and depends on the shape of the specimen [49]. The internal field that produces magnetization is therefore

$$\overrightarrow{B}_{0i} = \overrightarrow{B}_0 - D\overrightarrow{M}. \tag{2.5.1}$$

This field is associated with magnetic energy [49]

$$U_m = -\frac{1}{2}\overrightarrow{B}_{0i} \cdot \overrightarrow{M} - \overrightarrow{B}_0 \cdot \overrightarrow{M}. \tag{2.5.2}$$

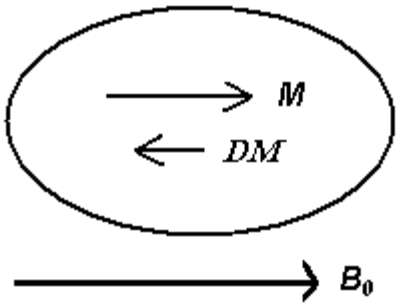

Figure 2.8: Magnetized single domain [49].

Even in the absence of the applied field a magnetic energy still exists called the magnetostatic self energy which is given by [49]

$$U_S = \frac{1}{2} DM^2. \tag{2.5.3}$$

This is the energy that needs to be minimized by domain formation. For domains of closure there are no 'surface poles' and hence no magnetic energy [53].

The transition from one domain to another involves spin reversal. This is associated with increase in exchange energy between spins. An abrupt change of spin direction increases the exchange energy by 4 $J_{ex}S^2$ per atom per boundary [48]. Allowing for gradual transition in N increments of π/N at each atom within the boundary increases the exchange energy by only [49]

$$U_{EW} = \left(-2J_{ex}S^2 cos(\frac{\pi}{N}) + 2J_{ex}S^2\right) N \simeq \frac{J_{ex}S^2\pi^2}{N} \ll 4J_{ex}S^2. \tag{2.5.4}$$

Crystals are also not isotropic in their behavior. Their properties tend to depend on crystal directions. This is typical of magnetization curves of many materials under the effect of an applied magnetic field. There are 'easy' and 'difficult' directions of magnetization. This is due to spin–orbit interaction. Spins rotating from their preferred directions require an additional energy called magnetocrystalline anisotropy energy. This energy is usually expressed in terms of empirical and anisotropy constants. The total free energy of a ferromagnetic crystal is therefore due to contributions from various sources such

as magnetostatic, wall, exchange and magnetocrystalline anisotropy energies. There is also a contribution due to imperfections (or defects) in the crystal. The domain structure that forms is that which minimizes the total free energy.

2.6 Magnetization processes

The state of magnetization of a sample is usually a complicated function of both external influences and internal microstructure. The magnetization characterizes the order of the spins in response to both applied and internal fields. The effect of temperature change is also critical. The principal measurements encountered here involve isothermal measurements of magnetization under the effect of an applied field and temperature dependence of the internal hyperfine field. For a typical ferromagnet below T_C, its isothermal magnetization may vary as shown in Figure 2.9 in response to positive and negative magnetic fields applied in a cyclic sequence. The hysteresis loop formed provides information about domain wall movements and hence ease of magnetization reversal processes. The initial magnetization curve along AB in Figure 2.6 proceeds by reversible domain wall movements in low fields. The approach to saturation at high fields occurs through irreversible domain wall movements and rotations of the individual magnetic moments. When the applied field is reduced to zero the residue magnetization is called remanence, M_R. The reverse field required to reduce the magnetization to zero is called the coercive field (or coercivity), H_C. The evolution of H_C with grain size is particularly important in the present work. Magnetization measurements in the vicinity of the Curie point can provide information about critical exponents and also T_C determination itself. The magnetic state of a sample can be investigated in terms of the Landau expansion of free energy in powers of the magnetization of the sample. The free energy is expressed as

$$F(M) = \frac{1}{2}a_1M^2 + \frac{1}{4}a_3M^4 + \frac{1}{6}a_5M^6 + \ldots - \overrightarrow{M} \cdot \overrightarrow{B}_0 \qquad (2.6.1)$$

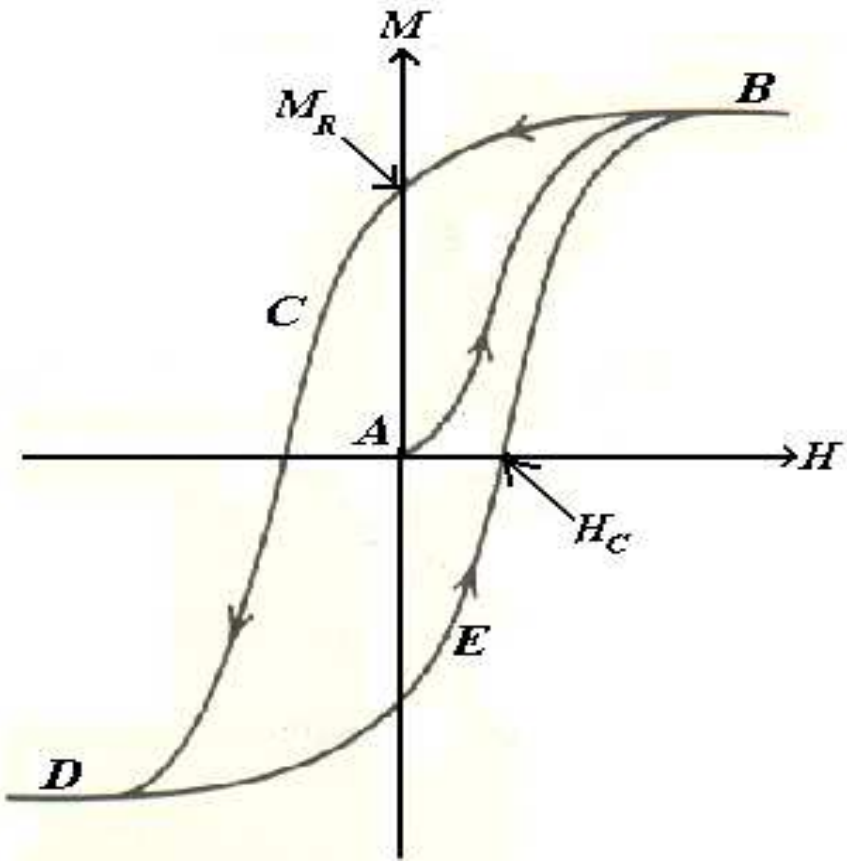

Figure 2.9: Variation of magnetization with applied field in a ferromagnet [2].

where the coefficients a_n are function of temperature and composition. The analysis of equation (2.6.1) is helpful in the understanding of the properties of a diverse range of materials.

Chapter 3

Mössbauer spectroscopy

In 1957 Rudolf L. Mössbauer discovered recoilless emission and absorption of 129 keV γ–rays of ^{191}Ir. He was awarded the Nobel prize for Physics in 1961. Mössbauer spectroscopy so named in his honour leads to a very accurate and sensitive way of obtaining information about chemical systems. It provides information on magnetic, structural, bonding, time dependent and other dynamical properties of materials. This is critically dependent on the availability of monochromatic electromagnetic radiation with a very narrow energy spectrum that can be used to detect small variations in the interaction energy between the nucleus and the extra–nuclear electrons. Mössbauer spectroscopy is now a well established experimental technique in the investigation of solids. In this chapter we present some of the basic principles of the technique.

3.1 Mössbauer effect

The Mössbauer effect is the recoilless emission and absorption of γ–rays by identical nuclei in a γ–ray source and absorber respectively. Nuclei have excited states that can be accessed from the ground state by absorption of photons with energies that are equal to the energy difference between the excited state and the ground state. If a nucleus within a radioactive source were to emit a photon without recoiling, an identical nucleus in another sample can absorb

the photon. However, due to nuclear recoil, emitted photons will not have the initial full transition energy and thus resonant absorption will be impossible. This can be seen by considering a free nucleus at rest in an excited state with energy E above the ground state emitting a photon of energy $E_\gamma = p_\gamma c$. The nucleus recoils with momentum $-p_\gamma$ and energy [59]

$$E_R = \frac{E_\gamma^2}{2mc^2} \tag{3.1.1}$$

where m is the nuclear mass and c is the speed of light. By conservation of energy the emitted photon energy is $E_\gamma = E - E_R$. Similarly in an absorption process a photon with energy $E_\gamma = E + E_R$ is required to excite an identical nucleus from the ground state to energy E. The effect of recoil is to cause a deficit in the energy of $2E_R$ between the emission and absorption lines as shown in Figure 3.1. The recoil energy E_R must be smaller than the natural line width (Γ) of the emission line for resonance to occur.

The excited state of ^{57}Fe nucleus used in Mössbauer experiment has energy $E = 14.41$ keV. The natural line width determined by its life time (1.4×10^{-7} s) is 4.6×10^{-9} eV [51, 59]. This is much smaller than the recoil energy $E_R \approx 1.95 \times 10^{-3}$ eV [59]. Resonant absorption of γ–rays emitted by free nuclei is therefore virtually impossible. When an emitting nucleus is embedded in a solid crystal the recoil energy will tend to be much less. This is because the recoil momentum is to a large extent taken up by the crystal as a whole. The nuclear mass m in equation (3.1.1) can be replaced by the mass M of the whole crystal. The recoil energy thus becomes

$$E_R = \frac{E_\gamma^2}{2Mc^2}. \tag{3.1.2}$$

In a typical crystallite there are at least 10^{15} atoms [59]. The recoil energy is therefore very much reduced. However, nuclei are not completely rigidly bound in the crystal lattice and are free to vibrate. If the recoil energy is not taken up by the whole sample, it will be transferred to the lattice by increasing its vibrational energy. The recoil energy is only transferred to lattice vibrations

if it corresponds closely with allowed increments (0, $\pm\hbar\omega, \pm 2\hbar\omega, \pm\hbar\omega$ etc.). If $E_R < \hbar\omega$ either zero or $\hbar\omega$ units of vibrational energy can be transferred to the lattice [59]. In order to achieve resonant absorption experimentally, the energy of the γ–rays needs to be Doppler shifted by introducing relative motion between the source and the absorber. Typical velocities of source relative to the absorber are of the order 10 mm/s. A plot of the transmitted γ–ray intensity through a sample as a function of velocity constitutes a Mössbauer spectrum.

3.2 Recoilless emissions

In terms of vibrational properties of the crystal lattice, the fraction of recoilless emissions of Mössbauer source can be expressed as [32]

$$f = exp\left(-\frac{E_\gamma^2 < x^2 >}{(\hbar c)^2}\right) \tag{3.2.1}$$

where $< x^2 >$ is the component of the mean-square vibrational amplitude of the emitting atom in the direction of the γ–rays. The form of equation (3.2.1) indicates that f will be large for a tightly bound nucleus (small mean-square displacements) with small γ–ray energies. $< x^2 >$ can be determined from the vibrational properties of the crystal lattice. In the Debye model, vibrational modes of atoms have frequencies up to a maximum value ω_D, called the Debye frequency. The Debye temperature (θ_D) is defined as

$$\theta_D = \frac{\hbar\omega_D}{k_B}. \tag{3.2.2}$$

In the Debye approximation equation (3.2.1) becomes [32]

$$f = exp\left[-\frac{6E_R}{k_B\theta_D}\left[\frac{1}{4} + \left(\frac{T}{\theta_D}\right)^2 \int_0^{\theta_D/T} \frac{xdx}{e^x - 1}\right]\right] \tag{3.2.3}$$

where $x = \hbar/k_BT$. The form of equation (3.2.3) indicates that f is large when θ_D is large, recoil energy is small and at low sample measuring temperature (T). These conditions place restrictions on the nuclei that can be suitable for Mössbauer spectroscopy. Typical nuclei showing Mössbauer effect are ^{57}Fe ,^{119}Sn, ^{127}I, ^{125}Te and ^{195}Pt [59].

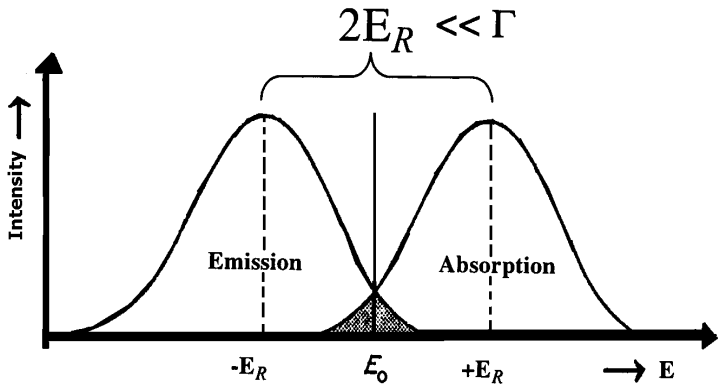

Figure 3.1: Emissions and absorption lines.

^{57}Fe Mössbauer isotope has strong recoilless absorption. Fe–based compounds were produced and studied in the current work. Hence ^{57}Fe Mössbauer spectroscopy was an obvious choice. The ^{57}Fe nucleus is produced by the radioactive decay of ^{57}Co nucleus as shown in Figure 3.2. The excited state energy (570 keV) of ^{57}Co has half life of 270 days. This decays by electron capture (EC) to the 137 keV excited energy state of ^{57}Fe ($I = 5/2$). About 9 % of all ^{57}Fe nuclei in this excited state decay to ground state ($I_g = 1/2$). 91 % decay to the 14.41 keV energy state ($I_e = 3/2$) by emitting γ–photons. The transition used in the Mössbauer experiment is between the 14.41 keV state and the ground energy state of ^{57}Fe.

3.3 Hyperfine interactions

In Mössbauer experiments very small energy shifts and splittings of the nuclear energy levels caused by electrostatic and magnetic interactions of the nucleus with its surroundings are measured. The electrostatic and magnetic interactions of the nucleus with its surroundings are together known as 'hyperfine interactions' and are reviewed in this section.

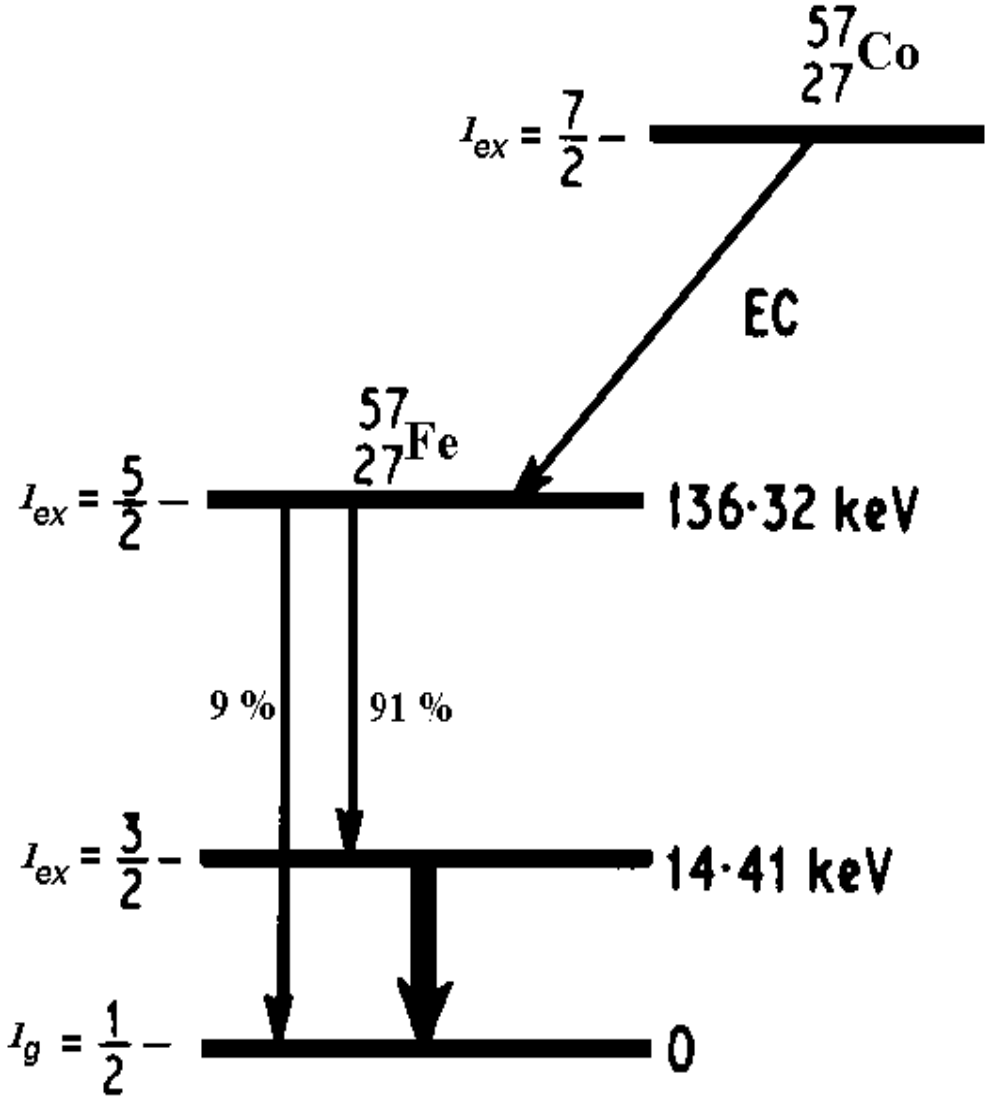

Figure 3.2: The energy levels of ^{57}Fe nucleus.

3.3.1 Isomer shift

The interaction of nuclear charge with extra–nuclear electron charge density causes a shift but not splitting in nuclear energies called isomer shift, chemical shift or center shift as shown in Figure 3.3 (a). This is seen as a shift in the centroid of the Mössbauer spectrum from zero velocity. The expression for the isomer shift is [51]

$$\delta = \left(\frac{2\pi Z e^2}{5}\right)\left[|\psi_S(0)|^2 - |\psi_A(0)|^2\right]\left(R_{ex}^2 - R_{gd}^2\right) \tag{3.3.1}$$

where Z is the atomic number, e is the electronic charge, $|\psi_S(0)|^2$ and $|\psi_A(0)|^2$ are s–electron densities at the nuclear sites of the source and absorber respectively. R_{ex} and R_{gd} are nuclear radii in the excited and ground states.

The change in nuclear radius ($\triangle R = R_{ex} - R_{gd}$) is constant for a particular Mössbauer transition. For a fixed Mössbauer source equation (3.3.1) can therefore be written as

$$\delta = K_0 - K|\psi_A(0)|^2 \tag{3.3.2}$$

where K_0 and K are constants. The form of equation (3.3.2) indicates that the isomer shift is a direct function of s electron density at the absorber nuclei. It is therefore sensitive to changes of orbital occupation in the valence shell of the absorber atom. Its most valuable application is in the classification of various compounds according to their oxidation state, degree of covalency and coordination number.

Different values of isomer shifts for Fe^{2+} and Fe^{3+} occur although these have the same s electrons. The difference between the isomer shift values for these ions is attributed to the extra d electron in Fe^{2+} ion which reduces the net attractive Coulomb potential for the 3s electrons. This causes their wave functions to expand slightly and hence reduce its charge density at the nucleus. For convenience the isomer shift is usually quoted in mm/s rather than in energy units. 1 mm/s is proportional to 4.8×10^{-8} keV for the ^{57}Fe isotope [59]. The difference between the isomer shift of Fe^{2+} and Fe^{3+} ions is

about 0.9 mm/s. This is larger than the natural line width and can therefore be measured in Mössbauer experiments.

3.3.2 Electric quadrupole and Magnetic hyperfine interactions

The energy transition used in the ^{57}Fe Mössbauer experiment is between the first excited state and ground state with spins $I = 3/2$ and $I = 1/2$ respectively. These energy levels split in the presence of a magnetic field into $(2I+1)$ levels. The $I = 3/2$ nuclear level splits into four nuclear levels corresponding to m_I = +3/2, +1/2, -1/2 and -3/2 and the $I = 1/2$ level splits into two levels corresponding to $m_I = +1/2$ and -1/2 as shown in Figure 3.3 (b). The energies of the nuclear levels are given by

$$E_m = -\frac{\mu B}{I} m_I = -g\mu_N B m_I \tag{3.3.3}$$

where m_I is the magnetic quantum number and takes values I, I-1, I-2 ...,-I. μ_N is the nuclear magneton, g is the nuclear g–factor and B is the magnetic field. B depends on the combination of both internal and applied magnetic fields. In the current work the Mössbauer measurements were performed in zero applied field. The magnetic splitting is therefore due to internal fields only. The transition between any two energy levels takes place whenever the selection rules $\triangle m_I = 0$ or $\pm$ 1 are satisfied.

The interaction of the nuclear quadrupole $\overrightarrow{Q}$ moment with the electric field gradient $\nabla\overrightarrow{E}$ of the crystal lattice causes splitting of the nuclear energy level $I = 3/2$. The energy eigen values for I =3/2 have solutions given by [32, 51]

$$E_Q = \frac{eV_{zz}Q}{4I(2I-1)} \frac{3m_I^2 - I(I+1)}{4I(2I-1)} \sqrt{\left(1 + \frac{\eta^2}{3}\right)}. \tag{3.3.4}$$

$\eta = [\partial^2 V/\partial x^2 - \partial^2 V/\partial y^2]/q$ is an asymmetry parameter and $V_{zz} = \partial^2 V/\partial z^2$ is the component of the electric field gradient tensor along the z axis. For nuclei with spin $I = 0$ or $I = 1/2$ the electric quadrupole moment is zero,

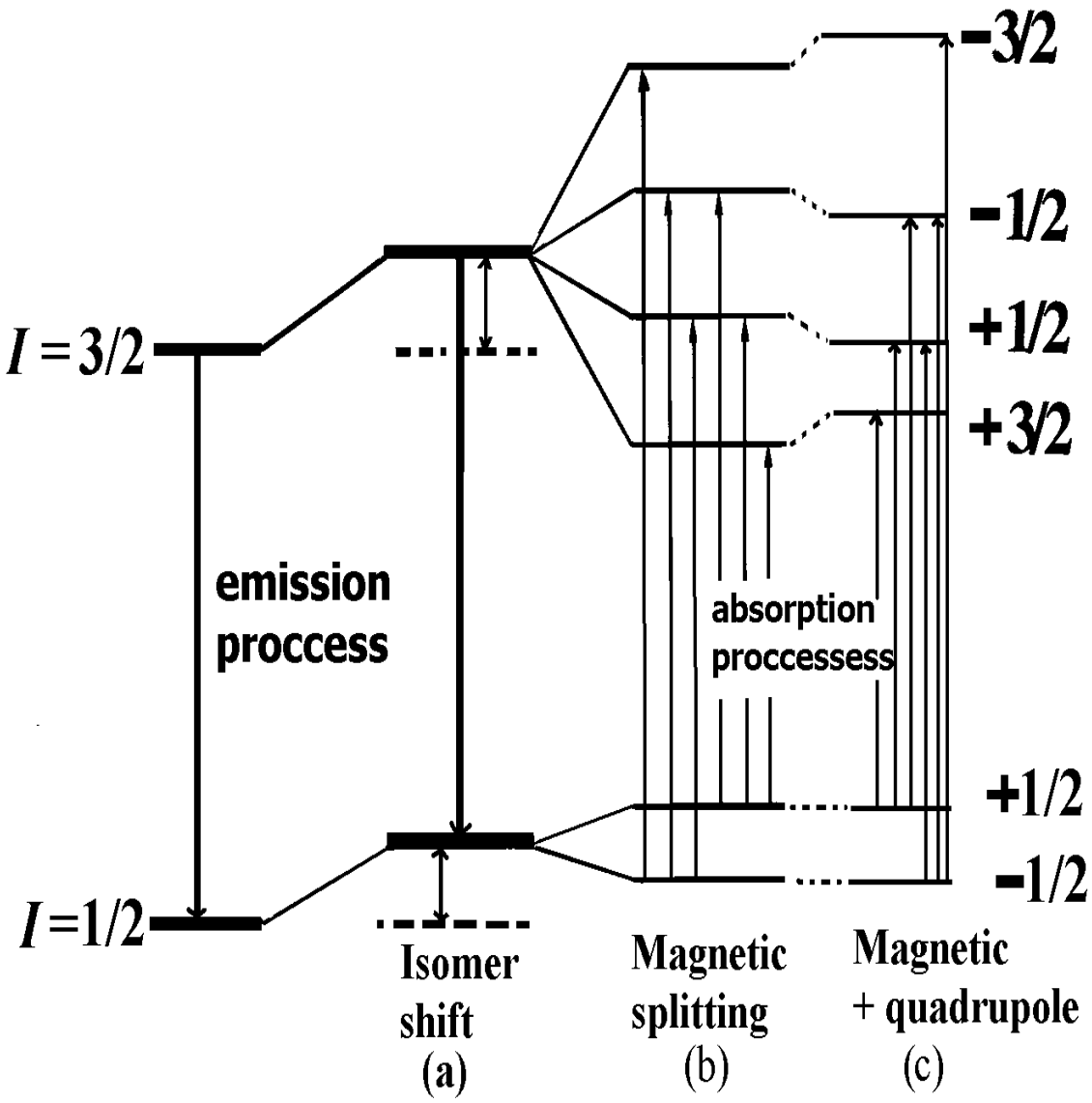

Figure 3.3: (a) Isomer shift, (b) magnetic splitting and (c) combined magnetic and quadrupole splittings.

hence the quadrupole interaction energy is zero. Quadrupole interaction does not affect the ground energy state of ^{57}Fe Mössbauer transition. The 14.41 keV excited energy state ($I = 3/2$) splits into two energy levels corresponding to $m_I = \pm 3/2$ and $m_I = \pm 1/2$. These appear as two absorption peaks in a Mössbauer spectrum with separation

$$\nabla = \frac{1}{2} e V_{zz} Q \tag{3.3.5}$$

called the quadrupole splitting.

If the nucleus experiences both quadrupole and magnetic interaction, the energy levels resulting from magnetic splitting are shifted by [32]

$$\epsilon = \frac{e^2 q Q}{4} \left(\frac{3cos^2\theta - 1}{2} \right) \tag{3.3.6}$$

as shown in Figure 3.3 (c) where θ is the angle between the magnetic axis and the major axis of the electric field gradient tensor. The energies of the nuclear energy levels due to effects of both magnetic field and crystal electric field gradient are given by [32]

$$E_{QM} = \frac{e^2 q Q}{4} \left((-1)^{|m_z|+1/2} \right) \left(\frac{3cos^2\theta - 1}{2} \right) - g\mu_N \overrightarrow{I} . \overrightarrow{B}. \tag{3.3.7}$$

The resulting ^{57}Fe Mössbauer spectrum has six lines but is not symmetrical about the centroid [32].

Chapter 4

Experimental techniques

4.1 Introduction

Spinel ferrites can be produced by solid state reaction and high energy ball milling from high purity oxides. Wet chemical methods such as sol–gel [17], hydrothermal [18–22], glycothermal [25], citrate precursor [16, 26, 27] and combustion methods [15, 29, 30] can also be used to produce better quality materials from salt solutions. The samples studied in the current work were made by using solid state reaction, combustion, hydrothermal and glycothermal techniques. One of the objectives of the study was to investigate the effect of sample preparation conditions and methods on the magnetic properties. High energy ball milling was used to produce nanosized powders from bulk samples. The single phase cubic spinel structure in all the synthesized ferrites was confirmed by X–ray diffraction. The bulk densities of the samples were measured on small solid fragments using Archimedes principle.

Magnetic measurements were performed by ^{57}Fe Mössbauer spectroscopy and vibrating sample magnetometer. The experimental procedures for synthesis and measurements of certain basic properties are presented in this chapter.

4.2 Sample preparation

4.2.1 Solid state reaction

The solid state reaction technique is generally referred to as the standard ceramic process. High purity oxides are mixed in the correct proportion and ground by an agate mortar and pestle. Samples of the $NiFe_2O_4$ and (Cu, Zn, Cd)$_{0.5}Ni_{0.5}Fe_2O_4$ compounds were prepared by this method. The starting materials were CdO (99 %), ZnO (99.99 %), CuO (99.99 %), NiO (99 %) and Fe_3O_4 (99.995 %)), supplied by Aldrich Chemical Company. As an example the stochiometric reaction of metal oxides to produce the $NiFe_2O_4$ ferrite would be

$$6NiO + 4Fe_3O_4 + O_2 \rightarrow 6NiFe_2O_4. \tag{4.2.1}$$

The chemical synthesis can be assumed [47] to proceed according to the reactions

$$3Fe_3O_4 + \frac{1}{2}O_2 \rightarrow 3(\alpha - Fe_2O_3) + Fe_3O_4 \tag{4.2.2}$$

and

$$(\alpha - Fe_2O_3) + NiO \rightarrow NiFe_2O_4. \tag{4.2.3}$$

The hematite phase $(\alpha - Fe_2O_3)$ oxidizes during heat treatment. The sample size of each starting oxide mixture was approximately 1 g. During the initial mixing process a small amount of ethanol or isopropanol was added to the mixture. This helps to homogenise the mixture and ensure that any spilage does not affect the stochiometry of the required compound. After grinding the sample for about 45 minutes (by hand), the dried mixed powder was pressed into a pellet. The pellets were initially fired in air at 950 ^{o}C for 32 hours after which the pellets were reground and repelletised. For the size of the die used to make pellets a pressure of approximately 400 MPa was applied for about two minutes in the formation of a pellet. Finally the pellets were sintered at 1100 ^{o}C. The heat treatments were done in air in a preheated furnace. After each heat treatment pruducts were allowed to cool slowly to room temperature.

The sample preparation technique employed above is also known as the double sintering method due to the two stages of heat treatment.

4.2.2 High energy ball milling

High energy ball milling can be used to mix powders uniformly, synthesize compounds and reduce bulk samples to nanosize. In this technique the required proportions of starting materials are mixed and sealed in hardened steel vials with steel balls. Agents like stearic acid or acetone may be added to the mixture [43, 60] or just dry milled [47]. The milling time required to form the sample depends on the ball to sample mass ratio, the speed at which the vials are rotated and ease of phase formation. Yu et al [47] made the $Zn_{0.5}Ni_{0.5}Fe_2O_4$ compound after 100 hours of milling. Zeng et al [60] investigated the influence of milling conditions such as ball to sample mass ratio, milling time and addition of process control agents on the magnetic properties. The high ball to powder mass ratio was found to reduce remanent magnetization and coercive fields. Addition of stearic acid did not improve the magnetic properties.

A Retsch planetary ball mill (type: PM 400) was used to grind bulk ferrites to nanometer scale. This facility has also the capability for mechanical alloying. Milling can be undertaken in air or inert gas atmosphere. The Retsch PM 400 has four grinding stations for simultaneous sample preparation. At present any two opposite stations can be used. The ball to sample mass ratio used was 20:1. The sample size in each vial was about 5 g. A typical grinding schedule was for a total time of at least 50 hours at a speed of 200 revolutions per minute. At conveniently selected times (for an example 1, 2, 4, 6, 12, 18, 24, 30, 40 and 50 hours) about 0.2 g of sample was removed in the study of the effect of grain size reduction.

4.2.3 Hydrothermal process

The starting materials in this sample preparation method can be nitrates or chlorides. The required stoichiometric amounts of metal nitrates solutions are mixed to obtain the desired composition. When nitrates are used, sodium or potasium hydroxide is slowly added to the mixture until a precipitate forms. When metal chlorides are used as starting materials aqueous ammonia is used as a precipitant. We have prepared (Cu, Cd)$_{0.5}$Ni$_{0.5}$Fe$_2$O$_4$ compounds by hydrothermal technique. The starting materials were Cu(NO$_3$)$_2$.3H$_2$O$_4$ (98 %), Cd(NO$_3$)$_2$.6H$_2$O$_4$ (99.999 %), Ni(NO$_3$)$_2$.6H$_2$O$_4$ (99.999 %), Fe(NO$_3$)$_3$.9H$_2$O$_4$ (99.99 %) and KOH.

The nitrates were mixed using a magnetic stirrer for about 40 minutes in 200 ml of deionised water. A concentration of 1 M solution of KOH was then slowly added to the nitrate mixture under rapid stirring until full precipitation was achieved. We assume that in order to make for instance the Cd$_{0.5}$Ni$_{0.5}$Fe$_2$O$_4$ oxide, the chemical reaction is as follows :

$$\frac{1}{2}\mathrm{Cd(NO_3)_2.6H_2O} + \frac{1}{2}\mathrm{Ni(NO_3)_2.6H_2O} + 2\mathrm{Fe(NO_3)_3.9H_2O} \\ +4\mathrm{KOH} \rightarrow \mathrm{Cd_{0.5}Ni_{0.5}Fe_2(OH)_4} + 4\mathrm{KNO_3} + \mathrm{H_2O}. \qquad (4.2.4)$$

The precipitate (Cd$_{0.5}$Ni$_{0.5}$Fe$_2$(OH)$_4$) was washed several times in deionised water and in ethanol to remove excess hydroxial ions. During the washing process the precipitate was filtered using ashless Glass microfibre filters (GF/F Whatman). Absence of excess hydroxide ions in the filtrate was confirmed by addition of phenolphthalein [18].

The precipitate was finally dispersed in about 200 ml of deionised water in a pressure vessel of a model 4842 PARR reactor. The sample was heated for six hours at 100 ^{o}C. The gauge pressure in the pressure vessel was maintained at 345 kPa. Another sample was prepared by hydrothermal technique in an open reflux system at atmospheric pressure (Figure 4.1). After the hydrothermal heat treatment the samples were washed several times in deionised water and then finally in ethanol. The synthesized oxides were dried under 250 W infra

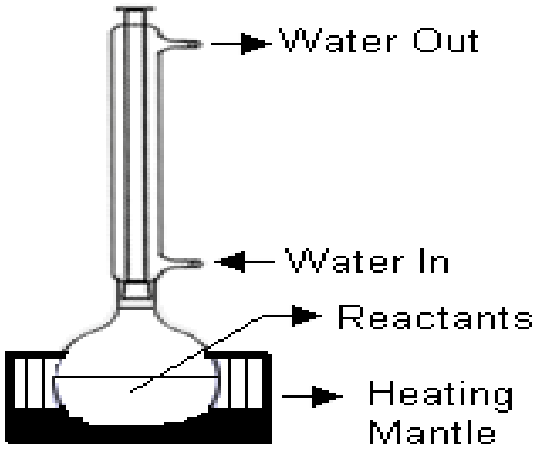

Figure 4.1: Diagram of reflux apparatus.

red light. The dried powders were homogenized using agate mortar and pestle and sintered at different temperatures until complete single phase formation was achieved.

4.2.4 Glycothermal process

This method is similar to the hydrothermal technique described in the previous section. The difference is that now the precipitate is heated in ethylene glycol solution instead of deionised water. This has an advantage of a higher boiling point (200 ^{o}C) compared to water (100 ^{o}C). The heat treatment was also performed at higher gauge pressure of 690 kPa. The $Cu_{0.5}Ni_{0.5}Fe_2O_4$ oxide was also made by glycothermal process. The starting materials in this case were $Cu(NO_3)_2.3H_2O_4$ (98 %), $Ni(NO_3)_2.6H_2O_4$ and $Fe(NO_3)_3.9H_2O_4$ and KOH. A 0.1 M solution of KOH was then slowly added to the mixture of nitrate solutions until the precipitate formed.

4.2.5 Combustion method

The starting materials in this method are metal nitrates and fuel (urea). The nitrates and urea respectively act as oxidizing and reducing reactants. The (Zn,

$Cd)_{0.5}Ni_{0.5}Fe_2O_4$ compounds were also made using the combustion technique. The metal nitrates corresponding to the stoichiometric proportion were mixed thoroughly in a porcelain dish and urea ($CO(NH_2)_2$) slowly added while stirring. In this process as an example in the preparation of the $Cd_{0.5}Ni_{0.5}Fe_2O_4$ oxide the decomposition reactions of metal nitrates that may be taking place are

$$\frac{1}{2}Cd(NO_3)_2.6H_2O + \frac{1}{2}Ni(NO_3)_2.6H_2O + 2Fe(NO_3)_3.9H_2O \qquad (4.2.5)$$
$$+\text{urea} \rightarrow Cd_{0.5}Ni_{0.5}Fe_2O_4 + (\text{gases} + \text{water}).$$

The decomposition of urea given by equation (4.2.8) is an exorthermic reaction [85]. The energy released helps the decomposition of nitrate salts into desired products at faster rate. The amount of urea used was such that the oxidizer (nitrate) to reducing reactant (urea) ratio was unity. This allows maximum energy to be released for the reaction, following the concepts of propellent chemistry [15, 30]. The solution was then heated on a hot plate until the ignition point was reached. At the ignition point a large amount of gases more likely to be NH_3, HNCO, O_2 and NO [37] are given off. Hence it was necessary to perform the synthesis under a fume cupboard. The combustion reaction is exothermic and therefore it is self–sustained once it has started. After the reaction was completed, the synthesized oxide was recovered and homogenised.

The oxides produced by combustion technique were used to investigate the effect of the pelletizing pressure (green density) during sample preparation. Each sample was divided into small portions which were pelletized under different pressures (400 MPa to 1200 MPa). The pellets were finally sintered at 1210 ^{o}C or 1250 ^{o}C for 6 hours.

4.3 X–ray diffraction

In section 4.2 we have introduced the techniques used to produce our samples. The intension was to produce good quality samples with easily reproducible

properties. In order to determine the quality of the samples and the ease of the formation of the desired phase, powder X–ray diffraction (XRD) was used. The technique is able to confirm if the sample produced is in single phase or not. In the present series of compounds this was achieved by indexing all the principal peaks in the XRD pattern with respect to the known Miller indices (hkl) of the cubic spinel structure [61]. From the analysis of the XRD pattern information of grain sizes, lattice constants, X-ray densities and porosity can be obtained.

XRD is based on the diffraction of a monochromatic beam of X–rays by lattice planes of atoms in a crystal. The position of the diffraction peaks in the XRD spectra is determined by Bragg's law

$$n\lambda = 2dsin\theta \tag{4.3.1}$$

where n is the order of the diffraction, λ is the X–ray wavelength, d is the perpendicular distance between adjacent planes of atoms and θ is the Bragg angle. In a cubic spinel structure, the size of the unit cell (lattice constant, a) is related to d by [62]

$$a = d\sqrt{h^2 + k^2 + l^2}. \tag{4.3.2}$$

Our XRD measurements were performed on a Phllips type PW1710 diffractometer. A monochromatic beam of Co (K_α) radiation of average $\lambda = 1.7903$ $\mathring{A}$ was used in the measurements. A typical sample size used in the XRD measurements was 0.20 grams.

4.4 Density measurements

The bulk density of a substance is defined as the mass per unit volume of the substance. Its accurate determination depends on how well both mass and volume are obtained. The measurement of mass tends to be easy and straightforward. It can be measured with high precision using electronic balances some

of which are readily available in a standard Chemistry or Physics laboratory. Some of the best balances have a precision of at least 0.00001 grams.

Apart from relatively large objects and those having regular geometry, volume determination tends to be more complicated. Direct measurement of volume tends to be impractical and hence the reason to resort to indirect methods. The basic commercial instruments to measure density are called pycnometers. There are various types, which tend to be distinguished by the technique used to measure volume. Many pycnometers are based on the Archimedes principle of fluid displacement or the technique of gas expansion. Unfortunately, the best pycnometers and related equipment such as porosimeter are expensive, and outside a Chemistry laboratory are rare. They also have a limitation on the sample size. For example the Quanta chrome Instruments Ultra Foam pycnometer has a specification of sample size of 0.1 to 135 cm^3 [63].

However, there is a simpler and readily available solution to the problem of density measurement based on the actual determination of the buoyant force on an object that is completely submerged in a liquid. This relies on mass measurement, which can be achieved with high precision even on small fragments. The buoyant force F_B, is equivalent to the weight of the displaced fluid,

$$F_B = V_0 \rho_f g \tag{4.4.1}$$

where V_0 is the volume of the object, ρ_f is the density of the fluid and g is the acceleration due to gravity. The left hand side of equation (4.4.1) depends on how F_B is being measured. If the mass is being weighed in air and then in the liquid, the apparent mass loss is

$$\Delta m = V_0 \rho_f. \tag{4.4.2}$$

The density of the object of mass m can easily be deduced to be

$$\rho_0 = \frac{m \rho_f}{\Delta m}. \tag{4.4.3}$$

Unfortunately, this is usually easier said than done especially if you want high precision in your measurements.

So far we have implicitly assumed that the balance is located above the mass along the supporting string [64]. This arrangement is typical of the Gouy system for measurement of susceptibilities [48]. However, the Gouy apparatus tends to be rare these days and when available, the balances used do not have the desired precision and are not as easy to operate as a modern electronic balance. Furthermore, a drastic modification of an old or new balance to suit the Gouy system is in many instances not an option.

Equation (4.4.1) can also be obtained if we measure the buoyant force directly. This is a good illustration of Newton's third law. Since the buoyant force is the force exerted by the liquid on the object, we measure the force exerted by the object on the liquid while it is suspended in the liquid by a supporting string secured to a stand. One can therefore take advantage of modern high precision balance with re-zeroing capability to monitor the apparent change in mass of the liquid and container when the object is lowered into the liquid. This procedure is usually not well known but it is conceptually straightforward.

Recent studies [15, 29] of Ni-Zn ferrites produced by the combustion technique, appear to show significant differences in the bulk density at the same nominal composition. Some criterion needs to be established to ensure reasonable reproducibility of results. Pressure or green density is expected to affect the properties of the sintered pellet, which would include its bulk density. Therefore accurate and reliable density determinations are essential.

Figure 4.2 shows a schematic diagram of the apparatus and experimental arrangement for density determination based on Archimedes principle. The plastic container with liquid is mounted on weighing platform of the balance. A small wire basket suspended by a nylon string was used to catch the solid fragments. A small copper plate was placed inside the basket. This helped the basket to sink easily and also to act as a base for solid pieces to settle on. The selection of the liquid was very critical in this experiment. Distilled water turned out to be unsuitable because the balance used was sensitive enough to

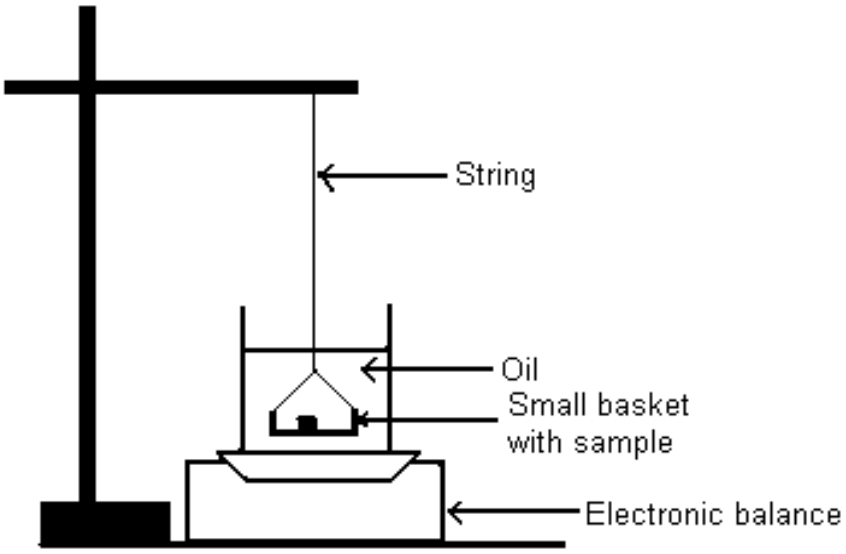

Figure 4.2: Bulk density determination based on Archimedes principle.

detect the rate of evaporation of water. Similarly glycerin alcohol from an old storage container was unsuitable as it showed continuous mass absorption from the atmosphere. For the third choice of liquid, we used a vegetable cooking oil which proved to be an excellent choice as it showed no detectable mass change when exposed to the atmosphere.

The density of the oil was determined by direct mass and volume measurements. Note that the above limitations in the choice of liquid do not apply in the Gouy type system for density determination based on Archimedes principle. Before mounting the container with oil on the balance, the masses of all the solid fragments were measured first. Once the container with the oil was on the balance, the basket was lowered into the oil until it was completely submerged. The balance reading was observed to increase due to the effect of buoyancy. One by one the fragments were dropped into the basket and each value of Δm noted. Using equation (4.4.3), the density of each fragment can be determined. In order to check the reliability of our density values, we also measured densities of pure metal chips (Si, Al, Cu, Zr, Sn, Pb, Cr and Fe) of known densities [65] and then used equation (4.4.3) to determine the density of the oil. The density of the vegetable cooking oil used in our measurements was

found to be 0.918 ± 0.004 g/cm^3 by direct mass and volume measurements. The value of the density of oil based on buoyancy on pure metals was found to be 0.923 ± 0.003 g/cm^3. The two values are in agreement. Hence all subsequent density calculations of the solid fragments were based on the density of oil of 0.923 ± 0.003 g/cm^3.

4.5 Mössbauer measurements

In a Mössbauer experiment a suitable radioactive source is used as a spectroscopic tool. This is achieved by changing the energy of the emission spectrum of the source with respect to that of the absorber (specimen) by moving the source towards and away from the absorber. This tunes the absorber in and out of resonance making it possible to scan through the different absorption lines and measure the hyperfine interactions.

The basic experimental set–up in transmission geometry consists of a Mössbauer source and a detector placed behind the specimen being measured. The γ ray–photons transmitted through the absorber are detected by a gas filled detector and the corresponding amplified pulses are put in different channels according to their energies. The pulses with same energy are put in the same channels. The Mössbauer spectrum develops with time as counts are accumulated as a function of the velocity of the source. The spectrum thus consists of 'dips' and high intensity counts. The 'dips' and high counts are at energies where resonant absorption and maximum transmission occur respectively.

There are different approaches used to measure γ–rays at different energies (velocities). In a constant velocity Mössbauer spectrometer, the transmitted photons in a fixed time interval are measured at constant velocity. The Mössbauer spectrum is accumulated as constant velocity is changed. In this way the spectrum is scanned stepwise one velocity at a time. The constant–velocity spectrometer consists of γ ray detection system, a timer and a scaler

for registering accumulated counts at each velocity. Although this is considered to be less expensive than velocity–sweep experiment, it is tedious to operate unless it is fully automated. Moving the source at constant velocity with high reproducibility and stability while restricted to small amplitude of movement is also not easy to achieve.

In the measurements presented in this thesis we have adopted the more common approach where the whole velocity range is rapidly scanned. By numerous repetitions of the velocity sweeps, data for individual velocities are accumulated simultaneously. The samples were measured from 79 K to 950 K. The measurements below 300 K were obtained using a Janis Research Mössbauer crysostat (VT–200). Measurements above 300 K were obtained using Wissel Mössbauer MBF–1100 furnace [66]. The experimental procedures during Mössbauer experiments are discussed in this section.

4.5.1 Furnace Mössbauer system

The experimental set–up for the Mössbauer system used to measure samples at temperatures above 300 K is shown in Figure 4.3. A 30 mCi ^{57}Co source sealed in rhodium matrix was mounted to a transducer operated at 6 Hz. The γ–photons transmitted through the sample were detected by a Xe,CO_2 LND proportional counter (tube type: 4546, operating voltage: 2176 V). The pulses from the detector were amplified by an ORTEC pre–amplifier (model 109 A) and then by the TENNELEC linear amplifier (TC202BLR).

The electromechanical drive system consisted of the Mössbauer driving unit (MDU) model MR–351, a multi channel scaling PCA2 card (supplied by Oxford Instruments) mounted in a computer and a pulse height analyzer (TN-7200). The MR–351 has a built–in function generator. The PCA2 card was used in conjunction with the pulse height analyzer (TN-7200). This was because the PHA mode which allows selection of the 14.41 keV energy peak on a PCA2 card was disfunctional. The Linear amplifier output signal was fed to the DIRECT input at the rear panel of the pulse height analyzer (PHA). The SCA output

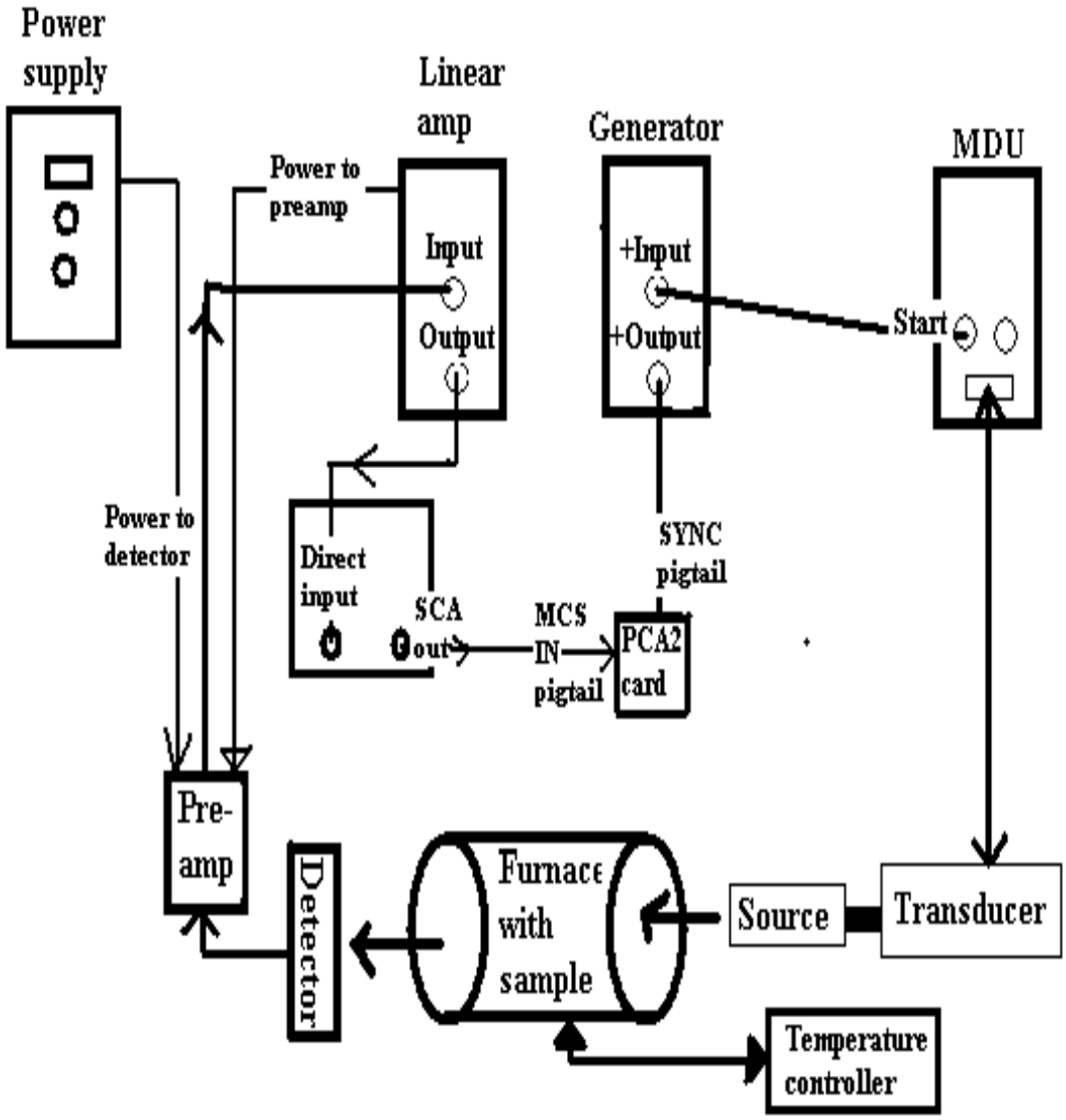

Figure 4.3: Experimental set–up for the Mössbauer furnace system.

of PHA was connected to the MCS pig–tail of the PCA2 card. In this way the 14.41 keV energy peak used in a Mössbauer experiment could be selected in PHA mode. The corresponding energy signal is then applied to the PCA2 card set in MCS mode. The START signal of the MDU was connected to the SYNC pig–tail of the PCA2 card.

The Mössbauer furnace (MBF1100) shown in Figure 4.4 was used to achieve sample measuring temperatures above 300 K. The sample was 'sandwiched' between two B_4N disks and secured at the center inside the furnace. The γ–photons from the source therefore pass through the furnace mylar windows and a heat screen (which absorbes less than 5 % of radiation) before hitting the sample.

The MBF–1100 is equiped with gas inlet and outlet pipes which can be used to evacuate, fill or create a continuous gas flow during measurements. The sample can therefore be measured in flowing or static gas. The inlet and outlet pipes can also be simply left open for measurements in air. The heater of the furnace is coiled on the outer surface of the quartz tube. The maximum power rating of the heater is 50 V DC and 3 A current. The heating of the furnace was controlled by an electronic temperature controller (TR–55). The controller has a temperature display, auto–tune and alarm functions. The furnace is set to operate at maximum temperature of 900 ^{o}C. An alarm function is activated that switches off the power to the heater if this temperature is exceeded. However, it is advisable to operate the furnace below the maximum set temperature to increase the longevity of the furnace.

During the operation of the furnace the desired sample measuring temperature is set on the controller. The controller supplies the neccessary power to the heater inputs of the furnace in order to heat it up to the set temperature. The temperature sensor (Chromel–Alumel thermo–couple) inside the furnace measures the sampe temperature (sample is in thermal contact with thermo–couple) the and provides a feedback voltage signal corresponding to the sample measuring temperature to the controller sensor input of the TR–55. The tem-

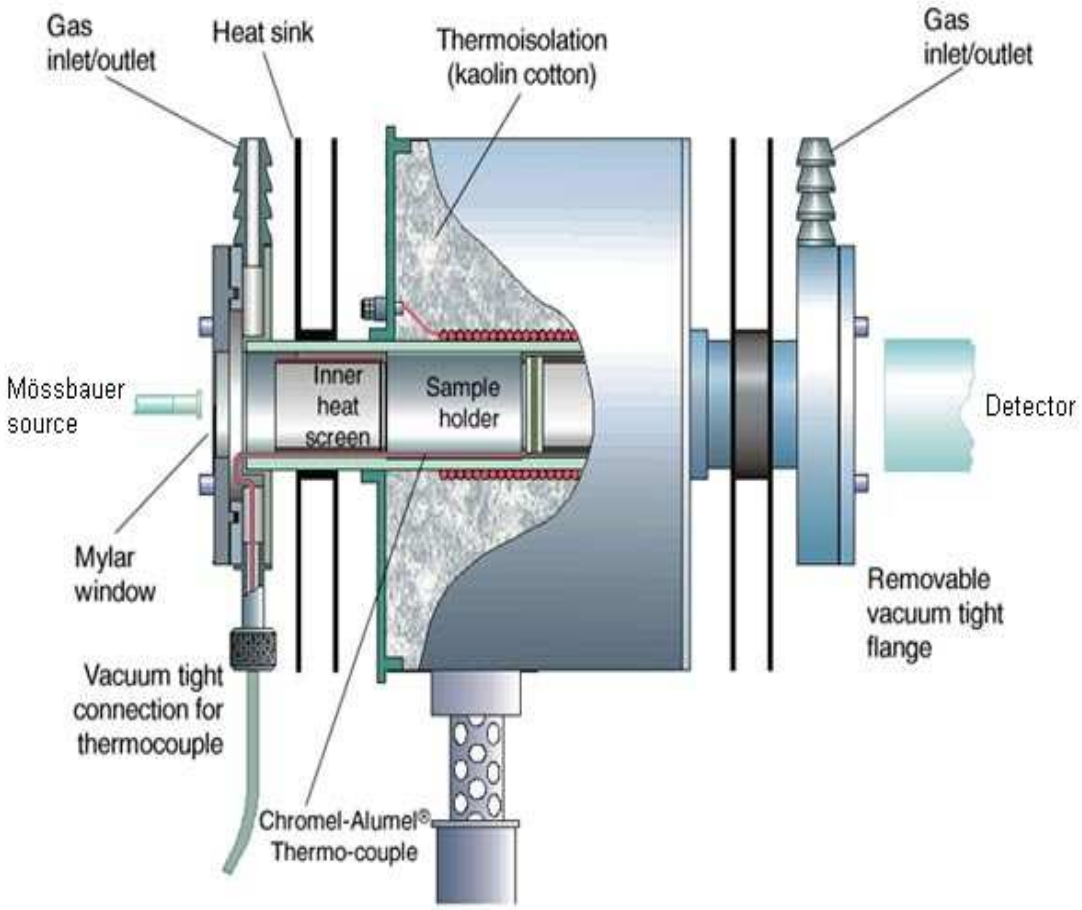

Figure 4.4: MBF–1100 Mössbauer furnace [66].

perature display thus displays both set–temperature and the sample measuring temperature. The measurements were started when the measuring temperature had stabilized (after about five minutes).

4.5.2 Cryostat Mössbauer system

The experimental set–up for Mössbauer measurements below 300 K is shown in Figure 4.5. The electromechanical drive system consists of the Mössbauer driving unit (MDU) model MR–350, Function Generator model FG 351 and a multi channel scaling MCS32 card (supplied by ORTEC). The γ–rays transmitted through the sample were detected by a Xe,CO_2 LND proportional counter (tube type: 45431, operating voltage: 1789 V). The pulses from the detector were amplified by a model 109 A pre–amplifier and then by a CANBERRA linear amplifier (model 2011). The linear amplifier output was connected to the MCS32 card through the SCA IN pig–tail. The START and CHA outputs of the function generator were respectively connected to START IN and CHN ADV IN pig–tails of the MCS card. The Analog and TRIG outputs of the FG 351 were respectively connected to Analog and Trig inputs of the MDU. The Function Generator was therefore communicating with both the MCS card and Mössbauer drive unit. The frequency at which the source motion was repeated is selected on the Function Generator. When a triangular wave output is selected, the source moves at constant acceleration. Varying acceleration is also possible by selecting the sinusoidal wave output. A feed–back voltage signal from the transducer drive coil which is proportional to velocity of the source is applied to the MDU. This signal is compared to the initial signal and corrected by the MDU to ensure that source motion is repeated at the frequency selected on the Function Generator. Since this is the frequency at which the START signal is applied to the MCS card, the Mössbauer source vibrates at the frequency proportional to the frequency of channel stepping in the MCS card. The active channel of the MCS card is therefore a linear function of the source velocity (energy). This results in all the detected transmitted amplified pulses

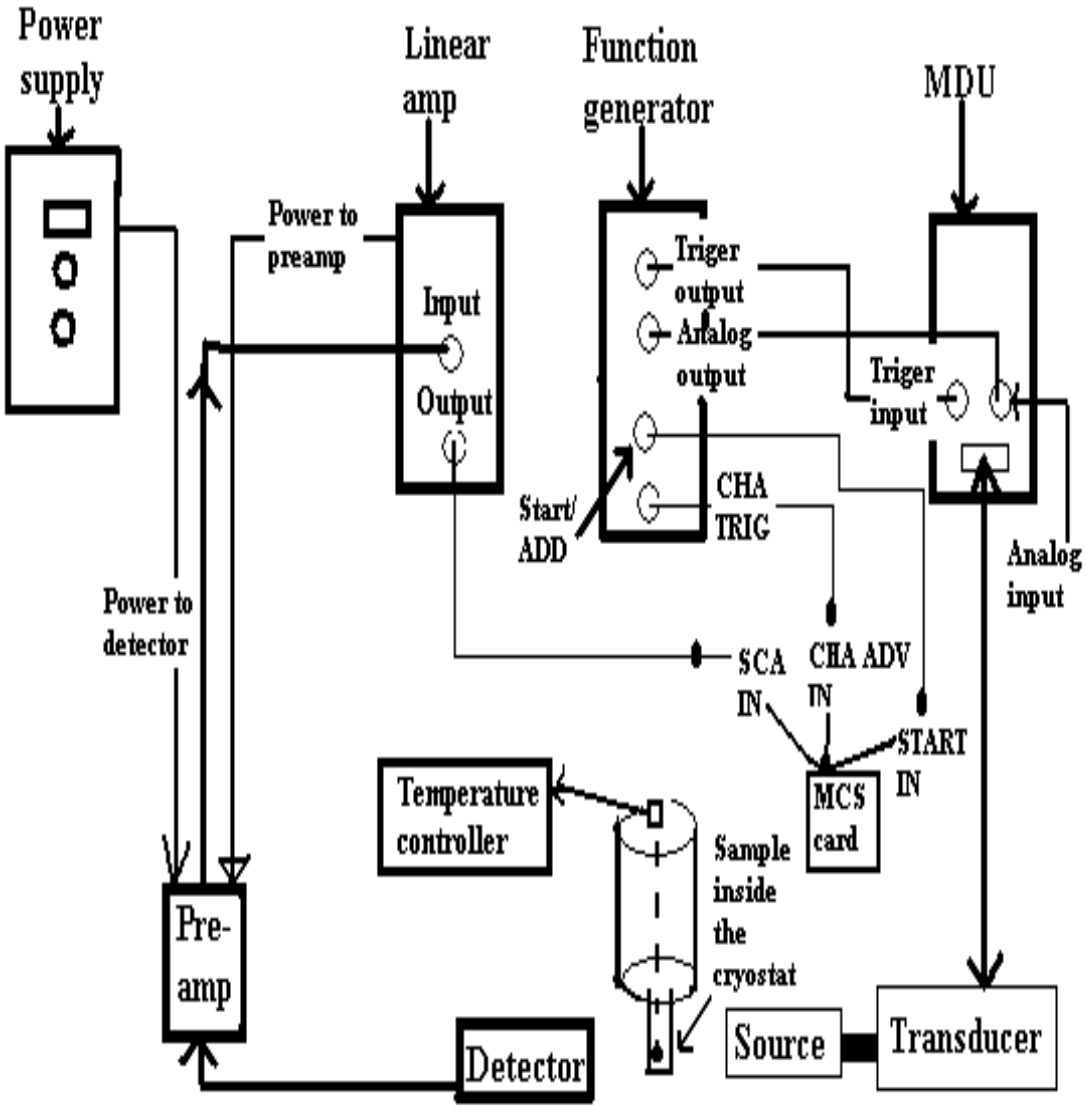

Figure 4.5: Experimental set–up for the Mössbauer cryostat system.

being stored in particular channels according to their energies. The Mössbauer spectrum develops with time. The longer the counting time, the better is the accumulated spectrum. This is however limited by the long term stability of the apparatus.

A Janis exchange gas Mössbauer cryostat (VT–200) shown in Figure 4.6 was used for measurements below 300 K. The Dewar body of the cryostat has a welded stainless steel inner 3 L liquid helium reservoir. This is surrounded by an outer 5 L liquid nitrogen reservoir. Both reservoirs can be accessed through fill and vent tubes at the top of the Dewar and are surrounded by interconnected vacuum jackets, isolating them from ambient temperature.

The VT–200 is equipped with a safety pressure relief valve located at the helium reservoir pumping arm. This protects the vacuum jacket in case of internal leaks. Such leaks would result in cryogen entering the vacuum jacket and warming it up to room temperature. This can cause high pressure to build up in the vacuum jacket which can be seen by frosting on the dewar outer surface. The safety valve opens and vents out the leaking gas when the pressure in the vacuum jacket is 14 kPa higher than atmospheric pressure. There is also a provision for thermocouple vacuum gauge at the exchange gas arm. This pressure gauge is important to monitor the vacuum level in the dewar body.

The Variable temperature insert includes a sample positioner assembly with a heater and temperature sensors, an exchange gas sample tube, outer vacuum tail, crown with exchange gas valve, pressure gauge and safety pressure relief valve. The header of the temperature insert consist of hermetic feed–throughs for electrical connections to the sample. The temperature insert is clamped at the Dewar body top flange. This suspends the sample positioner at the tail of the Dewar lying between the Mössbauer source and detector.

In an exchange gas cryostat the sample is put in an environment of helium gas. This gas cools down as it comes in contact with the copper wall of the sample tube passing through the cryogen reservoir. The helium gas therefore

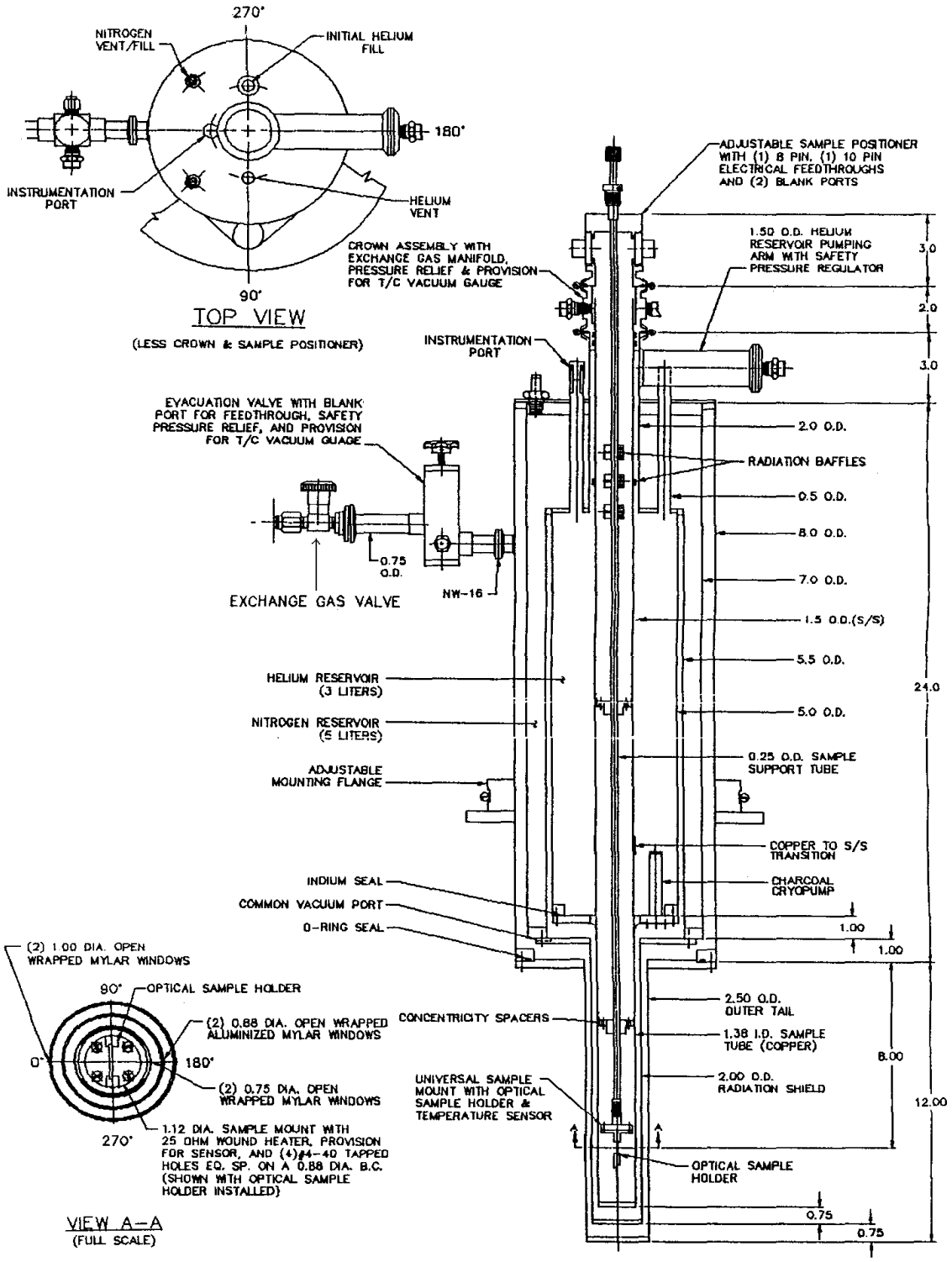

Figure 4.6: Janis exchange gas Mössbauer cryostat (model VT–200).

provides thermal link between the cryogen and the sample. The strength of this thermal link depends on the pressure of the exchange gas within the sample tube.

A heater attached to the sample holder makes it possible to vary the sample temperature above the cryogen boiling point to room temperature. An external automatic temperature controller supplies the necessary power to the heater attached to the sample holder once the desired temperature is selected. This heat input is transmitted into the cryogen with which it is in thermal contact. The temperature sensor at the sample mount senses the measuring temperature which is conveniently displayed.

In our measurements both the helium and the nitrogen reservoirs were filled with liquid nitrogen. The lowest sample temperature achieved was 78.8 K which is close to the boiling point (77 K) of liquid nitrogen. The sample holder was screwed to the bottom of the sample mount on the sample positioner assembly of the temperature insert. The insert was lowered into the sample tube of the cryostat and the header of the sample positioner was clamped firmly.

The vacuum jacket surrounding the cryostat reservoirs was pumped (using a diffusion pump) for about 5 hours. This was sometimes pumped overnight to achieve long cryogen holding periods. We were able to reach vacuum pressure of 59 μm Hg. Once the vacuum pressure reached the lowest value, the evacuation valve was closed. This is important because if the Dewar evacuation valve is kept open while transferring cryogen into the Dewar, cryopumping may pump back oil vapors into the vacuum jacket. This would contaminate the jacket and result in poor Dewar performance. Liquid nitrogen was loaded into the Dewar reservoir through fill ports at the top. This was achieved using a funnel and a pressurized storage tank. After transferring cryogen into the reservoir, the plugs were reinserted into the reservoir fills. This prevents air and moisture from entering the reservoirs. The vacuum pressure was observed to drop to about 55 μm Hg when the cryogen was admitted. The diffusion pump was

connected to the exchange gas valve and exchange gas tube was evacuated for at least 5 minutes and then sealed. Helium gas was admitted into the exchange gas tube when the temperature dropped to about 100 K. The helium gas was then flushed in and out of the exchange gas tube for at least 3 times. Finally the helium gas pressure was set to 20 mm Hg. The Mössbauer measurements were commenced when the temperature had stabilised to the desired value.

In the case where the temperature above liquid nitrogen was required, an automatic temperature controller was connected through feed–throughs for electrical connections on the cryostat sample positioner. After the desired temperature and the ramp rate were selected, we waited for about 5 minutes for the temperature to stabilize. When changing the sample during measurements, the exchange gas pressure was first noted. Helium gas was admitted into the sample tube until atmospheric pressure was reached. The temperature insert was unclamped and removed from the Dewar while helium was still flowing into the Dewar. The helium flow was cut–off and a cap quickly placed over the open sample tube to prevent air and moisture from condensing inside the exchange gas tube. The sample mount was then warmed by a heater and the sample replaced. The exchange gas tube was re–evacuated to the same level as noted earlier. To shut down the cryostat, the power of the temperature controller was simply turned off.

4.6 Magnetization measurements

A vibrating sample magnetometer (VSM) is a commonly used instrument in the study of magnetic properties of materials. It measures the magnetization of the sample as a function of the applied magnetic field and temperature. Measurement of magnetization with a VSM is described in reference [67]. The present set–up for magnetization measurements was commissioned recently [68] and is based on a Lakeshore model 735 VSM. It was calibrated against a nickel specimen and set up according to the manual specifications.

Chapter 5

Magnetic properties of bulk and nanosized $NiFe_2O_4$ oxides

5.1 Introduction

The magnetic properties of ferrites are dependent on the type of cations involved and their distribution amongst the tetrahedral (A) and octahedral (B) sites. Cation distribution changes when the particle size is reduced to nanometer scale. This results in nanosized oxides having properties that are drastically different from their bulk counterparts. As an example Zn atoms which are known to have preference for A sites in bulk compounds were found to migrate to B sites with reduction in grain size of $ZnFe_2O_4$ oxide [44]. This led to the enhancement of magnetic ordering temperature from 10 K to about 115 K [44, 45]. Below a critical grain size the domain structure of the particles changes from multidomain to single domain behavior [35] resulting into interesting magnetic properties [41, 69].

In general, upon reduction in grain size G, ferromagnetic materials become magnetically harder and exhibit increased coercivity. However, below a certain grain size, the coercivity is observed to decrease and soft magnetization begins to prevail. This appears to be a common feature for ferrites [40, 41, 69] and Fe–based alloys [70]. In Fe–based mechanically alloyed nanocrystalline materials,

the coercive field, H_C is found to follow a G^6–power law relation [70]. Different grain size dependences of H_C are observed in ferrites [41, 69].

We were interested in investigating the effects of grain size reduction on properties of ferrites and establish quantitatively the evolution of such properties with G. The measurements of coercive fields are particularly interesting. H_C can be obtained in a very reliable way because it does not depend on demagnetising field or poor calibration of magnetization on a magnetometer.

Measurements of hyperfine fields, $B_{hf}(T)$ as a function of temperature have been routinely obtained using Mössbauer spectroscopy in previous works [4–7, 9–12, 34, 38, 71–76] and in the current work. However, the temperature analysis of the hyperfine fields have not been exhaustive [4–7, 9–12, 34, 38, 71, 72, 74, 76]. We therefore intend to present a more detailed account of the dependence of $B_{hf}(T)$ on temperature.

The bulk $NiFe_2O_4$ oxide is a well established inverse spinel [34]. In this case, unlike Zn ions in normal spinel $ZnFe_2O_4$ oxide, the divalent Ni ions occupy B sites. Half of the trivalent Fe ions are distributed among A sites and the other half occupies B sites. In the study of mechanically milled $Zn_xNi_{1-x}Fe_2O_4$ fine powder, Sepelák et al [76] reported a decrease of the X-ray diffraction intensity ratio of the (220) to (222) diffraction lines which implied a redistribution of cations at A and B sites. In a similar study of $NiFe_2O_4$ by Chinnasamy et al [34], no significant change in the population of the cations amongst A and B sites was observed. Therefore unlike for the inverse spinel $ZnFe_2O_4$ oxide, this suggests that there is no change in the magnetic ordering temperature with reduction in grain size. This is one of the reasons we need a more systematic study to investigate the effect of grain size reduction on various properties. We have therefore made $NiFe_2O_4$ and $(Zn, Cd, Cu)_{0.5}Ni_{0.5}Fe_2O_4$ oxides in the bulk form using solid state reaction. The grain size has been reduced to nanometer scale using high energy ball milling after selected milling times for 1, 2, 4, 6, 12, 18, 24, 30, 40, and 50 hours.

The investigations of the magnetic properties of $(Zn, Cd, Cu)_{0.5}Ni_{0.5}Fe_2O_4$

compounds are presented in chapter 6. This chapter is concerned with the results and discussions on the magnetic properties of $NiFe_2O_4$ oxides.

5.2 X–ray diffraction results

In Figure 5.1 we show the variation of X-ray diffraction patterns of $NiFe_2O_4$ with milling time. The bulk oxide (0 h) was produced using solid state reaction. The most significant lines were successfully indexed using the XRD data of magnetite which has cubic spinel structure [2, 61]. This confirms the predominance of single-phase cubic spinel formation in the samples.

The lattice parameter for the bulk sample, deduced from XRD data (using equation (4.4.2)) was 8.34 ± 0.02 $\mathring{A}$. The bulk density ρ_B measurement was performed on a small mass fragment using Archimedes principle and found to be 3.49 ± 0.02 g/cm^3. This value is similar to 3.66 ± 0.03 g/cm^3 found in the preliminary work [4] for the cobalt ferrite ($CoFe_2O_4$). The X–ray density ρ_X was computed from the value of the lattice parameter by using the formula [31, 77]

$$\rho_X = \frac{8M}{N_A a^3} \tag{5.2.1}$$

where 8 represents the number of atoms in a unit cell of the spinel lattice, M is the molecular weight of the sample, a is the lattice parameter, and N_A is the Avogadro's number. The X–ray density was calculated to be 5.37 ± 0.03 g/cm^3. A larger value of X–ray density compared to that of bulk density is expected in principle because X–ray density reflects only the packing of atoms in a unit cell.

The percentage porosity (P_o) of the bulk sample can be calculated from the X–ray density and bulk density using the formula [77]

$$P_o(\%) = \left(1 - \frac{\rho_B}{\rho_X}\right) \times 100. \tag{5.2.2}$$

We have found the porosity to be 34.99 ± 0.04% for the $NiFe_2O_4$ compound. Porosity indicates vacant spaces in a material.

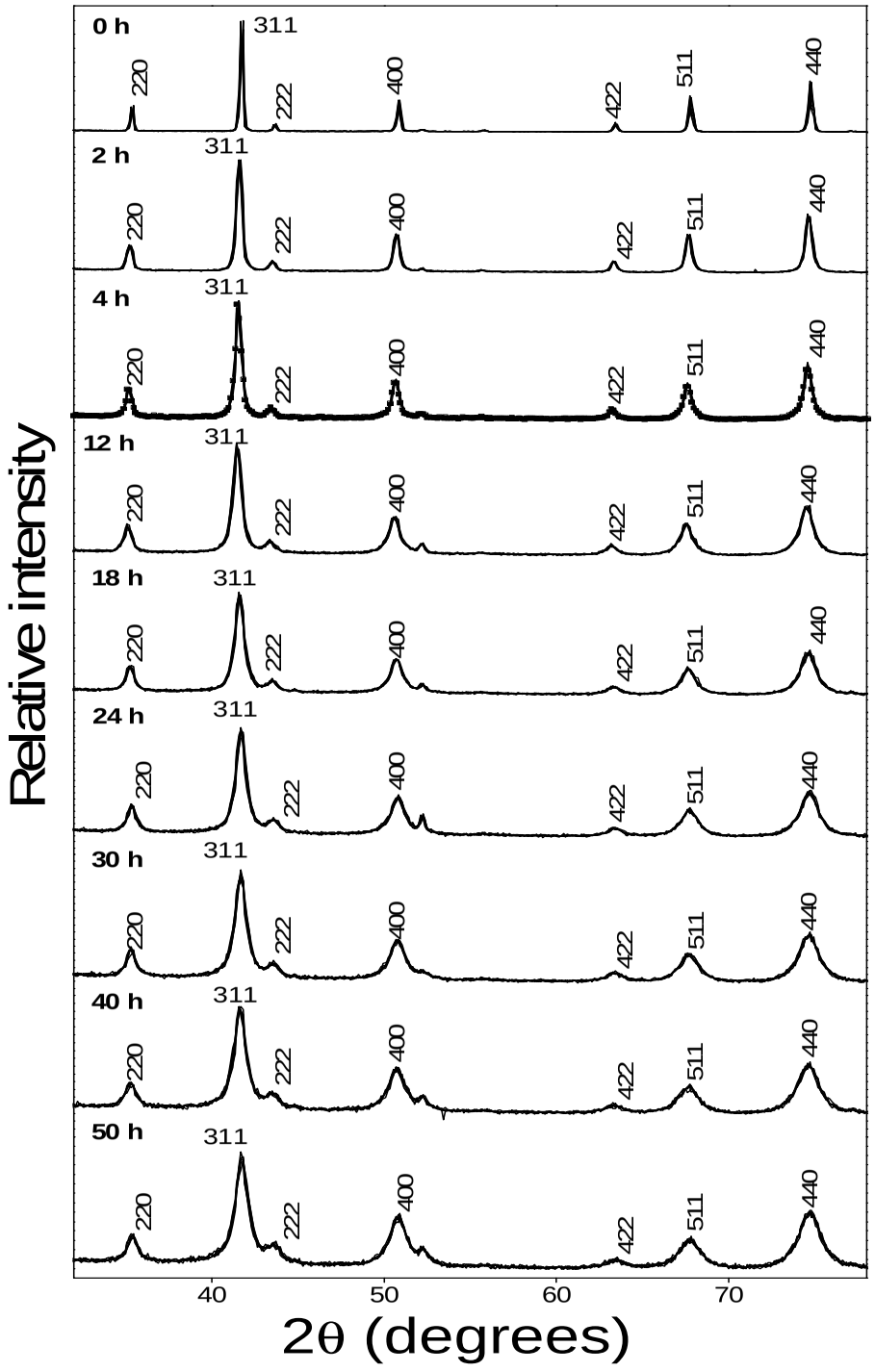

Figure 5.1: Variation of XRD patterns for $NiFe_2O_4$ with milling time.

The broadening of the XRD peaks with milling time (see Figure 5.1) indicates reduction in grain size. The crystallite size can be estimated from the width at half maximum of the of the (311) X–ray diffraction line (w_{311}) using the Scherrer formula [15, 35, 44]

$$G = \frac{0.9\lambda}{w_{311} cos\theta}. \tag{5.2.3}$$

Calculation of w_{311} and $cos\theta$ are obtained by fitting a Lorentzian or Gaussian fits to the (311) peaks using Origin 6.0 graphics software. The variation of grain sizes and lattice constants with milling time are shown in Table 5.1. The grain sizes are plotted in Figure 5.2. An initial sharp reduction in grain size with milling up to about 30 hours of milling occurs. The grain sizes appear to saturate after milling for more than about 30 hours. This can be attributed to grain sizes approaching the dimensions of the unit cell. The minimum grain size can also depend on the grinding limit which is determined by sample size, rate of rotation of grinding vials and presence of any additives such as acetone to the sample.

5.3 Mössbauer results

The typical Mössbauer spectra for the bulk sample measured at selected absorber temperatures are shown in Figure 5.3. The well resolved magnetic splitting in the spectra for $T \leq 300$ K may be attributed to the antiferomagnetic character in $NiFe_2O_4$ compound. The solid lines have been obtained by using Recoil Mössbauer spectral analysis software. The spectra were analysed using Lorentzian site analysis. The points correspond to experimental data. Below the magnetic ordering temperature T_C the spectra were resolved into sextets corresponding to the trivalent Fe ions in both tetrahedral (A) and octahedral (B) sites. Above T_C the data was fitted with two doublets. The sextets and doublets represent fractions of Fe ions on the A and B sites in ferrimagnetic and paramagnetic states respectively.

Table 5.1: Variation of grain size (G) and lattice parameters (a) with milling time (MT) for $NiFe_2O_4$ oxide.

MT (h)	G (nm)	a ($\mathring{A}$)
	$\pm$ 0.04	$\pm$ 0.01
0	55.05	8.34
1	33.40	8.31
2	26.51	8.33
4	23.88	8.36
6	24.65	8.34
12	17.61	8.35
18	15.14	8.35
24	14.61	8.33
30	12.68	8.33
40	13.37	8.34
50	12.58	8.32

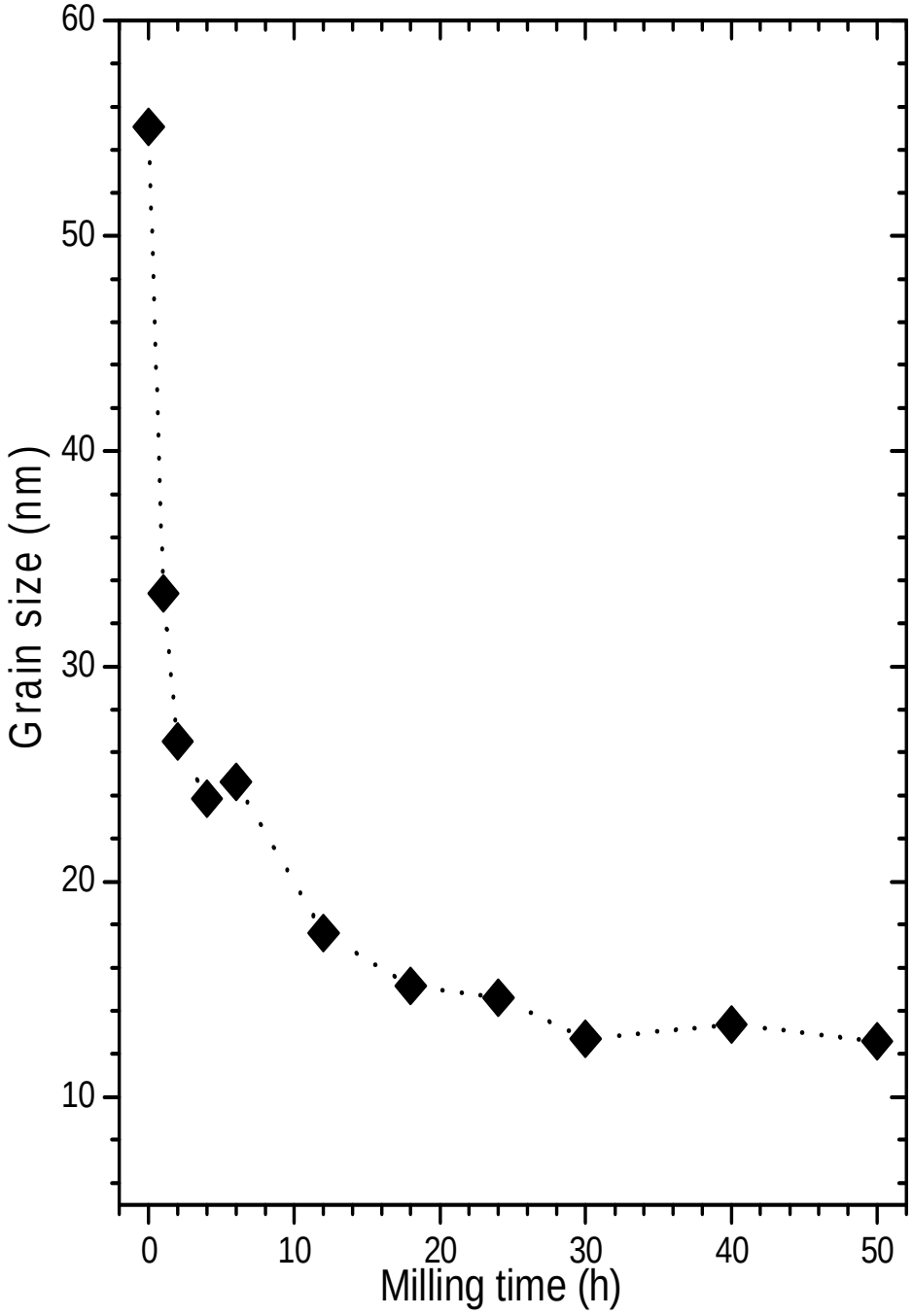

Figure 5.2: Variation of grain size of $NiFe_2O_4$ with milling time.

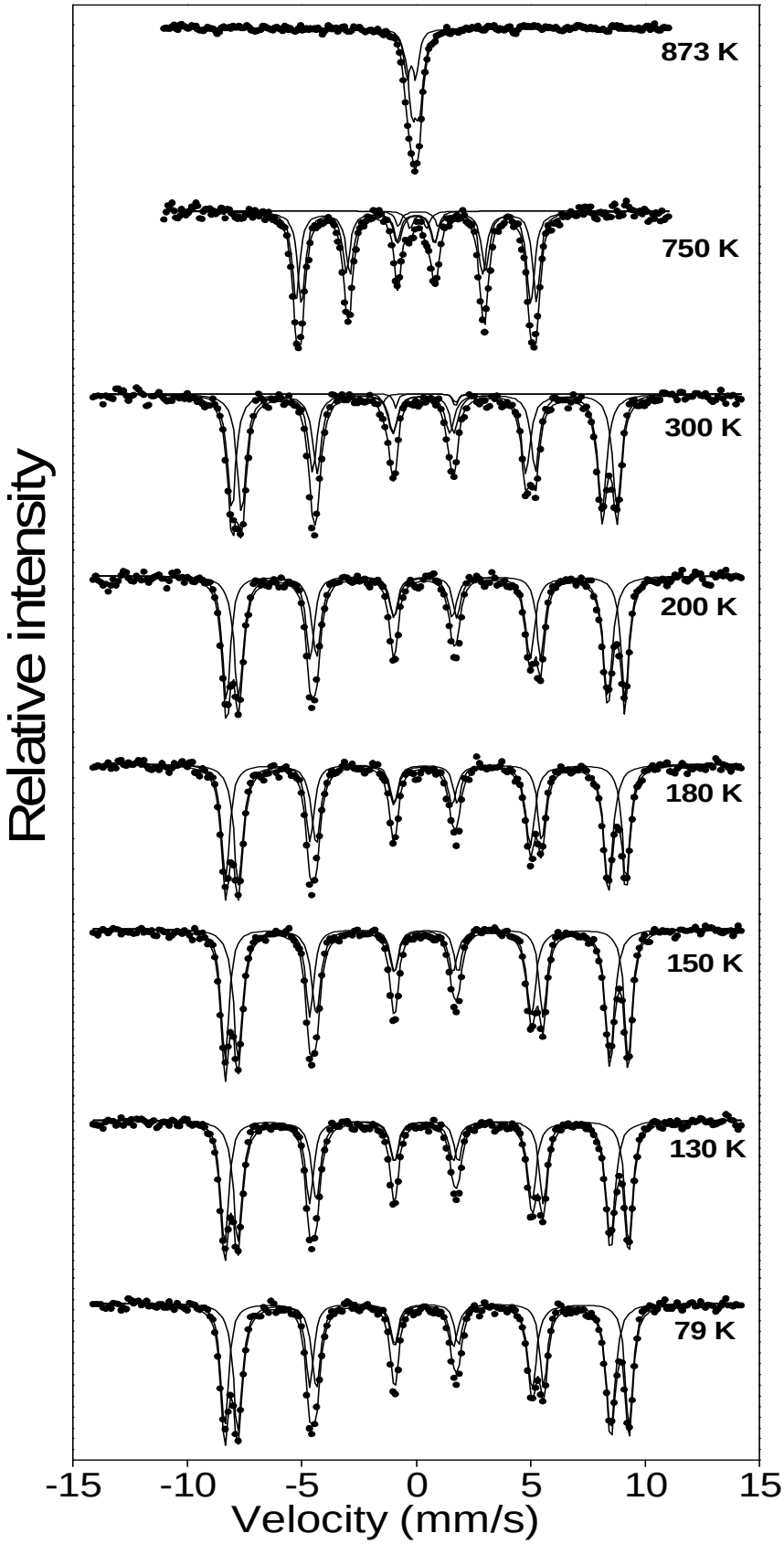

Figure 5.3: Variation of Mössbauer spectra for $NiFe_2O_4$ with temperature.

The magnetic ordering temperature was measured using the zero velocity Mössbauer technique in which the variation of transmitted γ–rays through an absorber sample with temperature is monitored. The rate of transmission is high through the magnetically ordered phase. As the temperature is increased thermal agitation causes spins to be become randomly oriented. Near magnetic transition temperature, the transmitted intensity of γ–rays drops significantly as shown in Figure 5.4. The Curie temperature T_C is taken at the discontinuity of rapid drop in transmitted intensity (low transmission rate edge). However, for the bulk $NiFe_2O_4$ oxide there is an anomalous increase in the count rate with increase in temperature beyond T_C. This behavior may indicate re-ordering of magnetic moments above the Curie point. An increase in magnetization above the Curie temperature with increasing measuring temperature has been observed in references [19, 20, 49]. Similar behavior has been observed by Read et al [78] in a sputtered $Fe_{0.91}Zr_{0.09}$ amorphous alloy. We suspect that this might be a consequence of the existence of significant negative exchange interactions in the compounds. The data for hyperfine fields, isomer shifts and quadrupole splitting deduced from Mössbauer fits are shown in Table 5.2. The criterion used to assign sextets or doublet to tetrahedral (A) and octahedral (B) sites was based on the fitted results of isomer shifts deduced from Mössbauer fits. These are expected to be lower for A sites compared to B sites [31, 32, 79]. Lower isomer shift on A site is due to high covalency of the Fe–O bond on the tetrahedral site. The cubic symmetry at A site also results in low electric field gradient compared to trigonal symmetry on B site. The quadrupole splitting is therefore also expected to be lower on the tetrahedral (A) site [31, 79]. In our samples the values of quadrupole splitting were within the experimental error and could not be used to assign sextets or doublets to A or B sites. Similar results have been observed in $CuFe_2O_4$ oxide [14].

A systematic decrease in hyperfine fields with increasing temperature shown in Figure 5.5 indicates weakening of the magnetic coupling between the Fe ions. The internal hyperfine fields of B site ^{57}Fe nuclei are higher than for

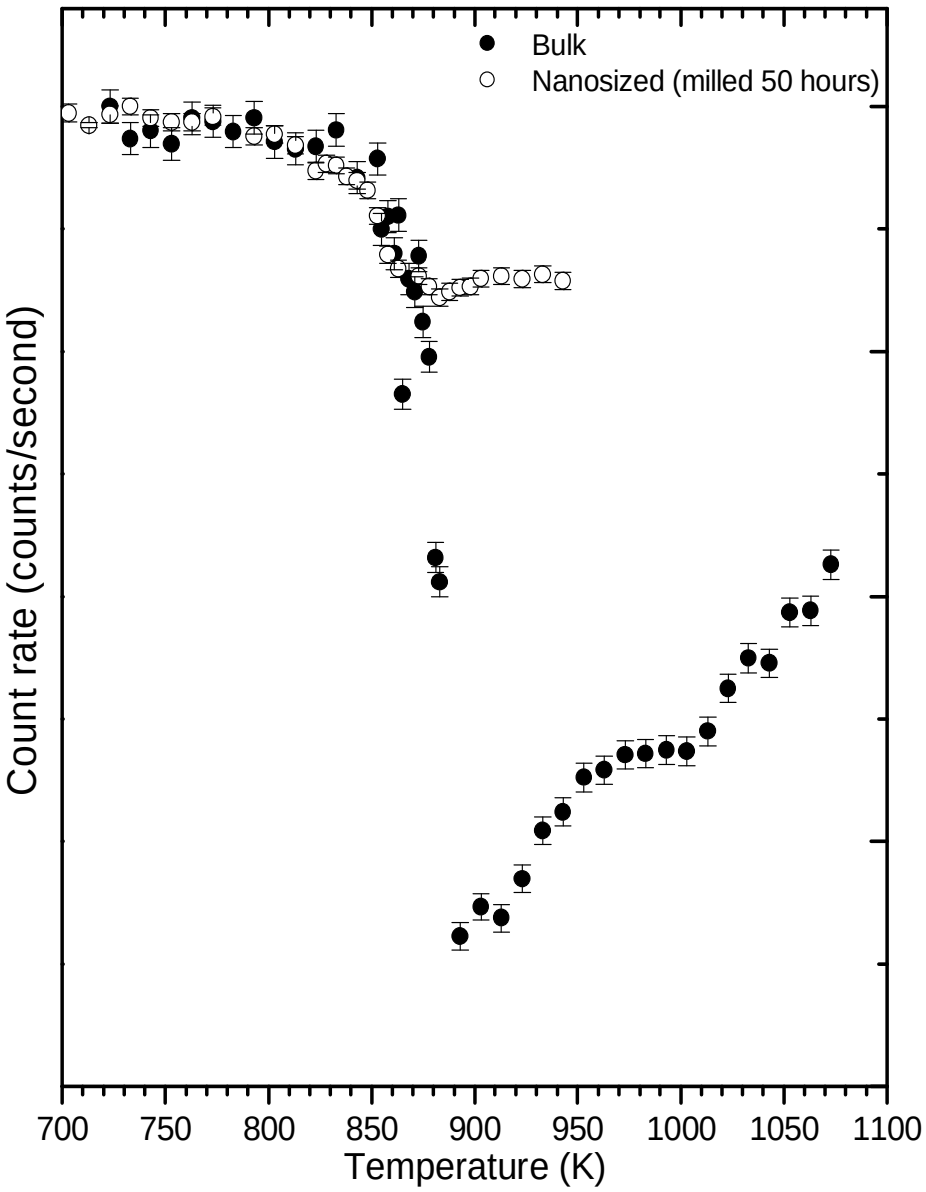

Figure 5.4: Variation of count rate in $NiFe_2O_4$ with temperature.

Table 5.2: Variation of isomer shift (IS), quadrupole splitting (QS) and hyperfine fields (B_{hf}) of $NiFe_2O_4$ with temperature.

	IS (mm/s)		QS (mm/s)		B_{hf} (kOe)	
Temp. (K)	$(IS)_A$	$(IS)_B$	$(QS)_A$	$(QS)_B$	$(B_{hf})_A$	$(B_{hf})_B$
	± 0.01	± 0.01	± 0.01	±0.01	± 0.8	±0.8
79	0.35	0.46	0.00	0.00	505.0	547.5
100	0.34	0.45	0.00	0.00	504.7	547.2
130	0.33	0.45	0.01	0.01	503.4	546.0
150	0.32	0.43	0.01	-0.00	503.0	544.5
180	0.31	0.42	0.01	-0.00	500.9	542.3
200	0.30	0.40	-0.01	0.00	499.9	539.6
230	0.28	0.39	0.01	0.01	498.1	536.5
300	0.24	0.34	0.01	0.01	488.4	521.7
350	0.20	0.32	-0.01	-0.02	482.0	507.7
400	0.19	0.28	-0.00	-0.01	471.3	495.8
450	0.17	0.25	0.00	-0.01	459.7	482.0
600	0.08	0.12	-0.00	-0.00	405.1	422.6
750	0.00	-0.01	-0.00	0.01	310.5	325.9

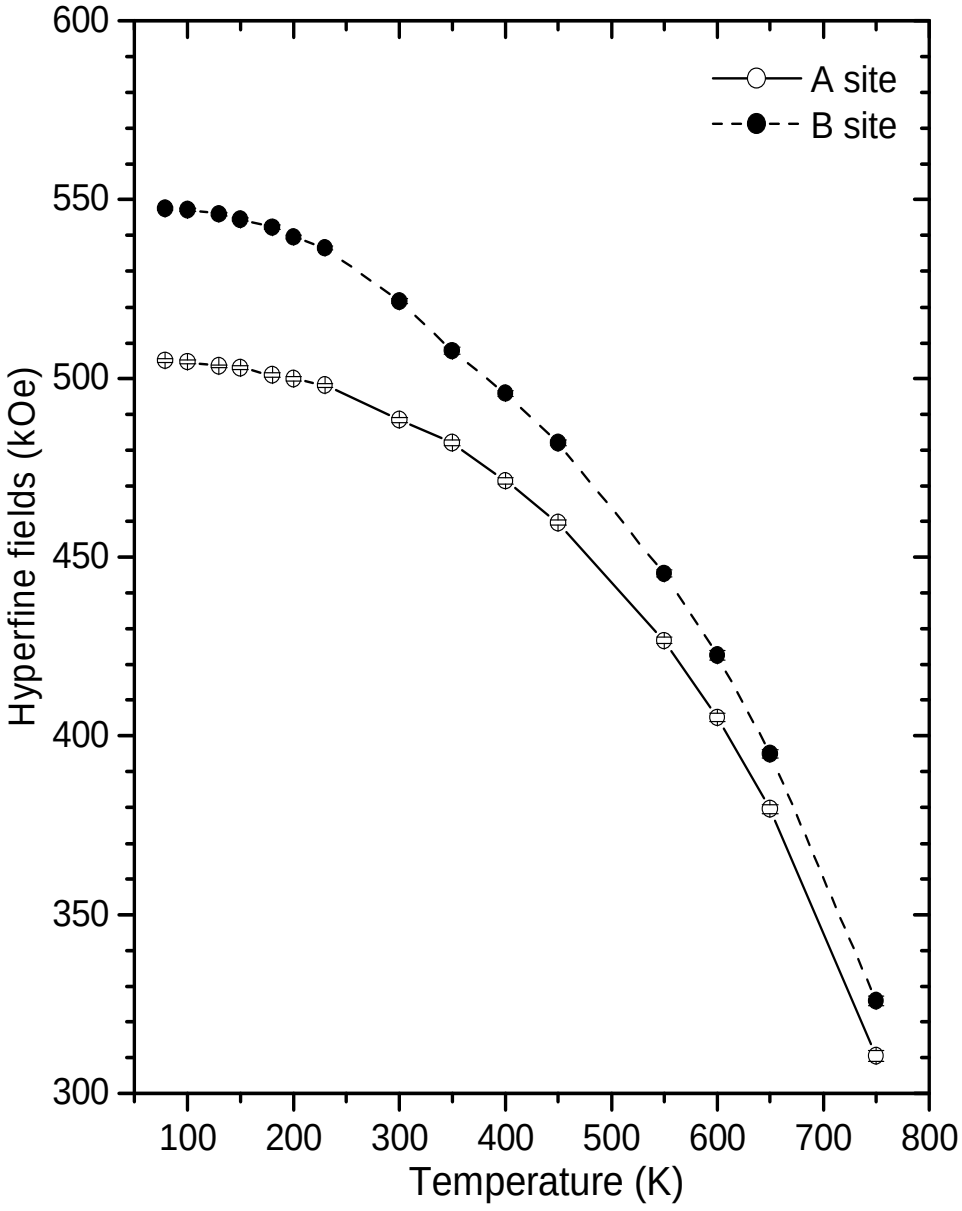

Figure 5.5: Variation of hyperfine fields of $NiFe_2O_4$ with temperature.

those on A sites. Since the hyperfine fields are associated with the strength of the magnetic coupling, the high hyperfine fields on B sites are consistent with the fact that $NiFe_2O_4$ is an inverse spinel (B sites are occupied by Ni ions which have strong magnetic moments). This is also in agreement with previous results [9, 14, 38, 75]. The high values of hyperfine fields below 300 K are consistent with the 3+ oxidation state of Fe [9]. It is reasonable to assume that the hyperfine field is directly proportional to the local magnetization of the sample i.e. $B_{hf}(T) \propto M(T)$ [1, 50, 52]. Hence the temperature dependence of B_{hf} can be expected to follow that of $M(T)$. From the Ginzburg–Landau theory equation (2.3.23) can be deduced [56]. Hence the hyperfine field can be assumed to vary as

$$B_{hf}(T) = B_{hf}(0)\left[1 - \frac{T}{T_C}\right]^{\beta_1} \tag{5.3.1}$$

where β_1 is a critical exponent. Equation (5.3.1) has been used to fit the temperature dependence of hyperfine fields in a wide range of compounds. For example equation (5.3.1) has been used to fit hyperfine field data for Sn–doped Cr_2O_3 and $(FeCr)_2O_3$ [73]. Linearizing equation (5.3.1) gives

$$\ln B_{hf}(T) = \ln B_{hf}(0) + \beta_1 \ln\left[1 - \frac{T}{T_C}\right]. \tag{5.3.2}$$

A graph of $\ln B_{hf}(T)$ versus $\ln\left[1 - T/T_C\right]$ for A and B sites hyperfine fields is shown in Figure 5.6 for $NiFe_2O_4$ compound. A similar plot based on published data of $CuFe_2O_4$ [14] is shown in Figure 5.7. The good fits (see correlation coefficients (R^2) in Table 5.3) to the data occurs only at higher temperatures nearer to T_C. This indicates that equation (5.3.1) fails at lower temperatures because T is much lower than T_C. The slopes of the fits to the data give the values of β_1 as shown in Table 5.3. In Table 5.3 we have included results of the analysis of published data of $CuFe_2O_4$ [14]. Any significant differences in the results of the analysis between $NiFe_2O_4$ and $CuFe_2O_4$ oxides can be attributed to differences in the basic magnetic interaction between magnetic moments. Ni and Cu have different electronic structure.

The temperature dependence of magnetization can also be investigated on

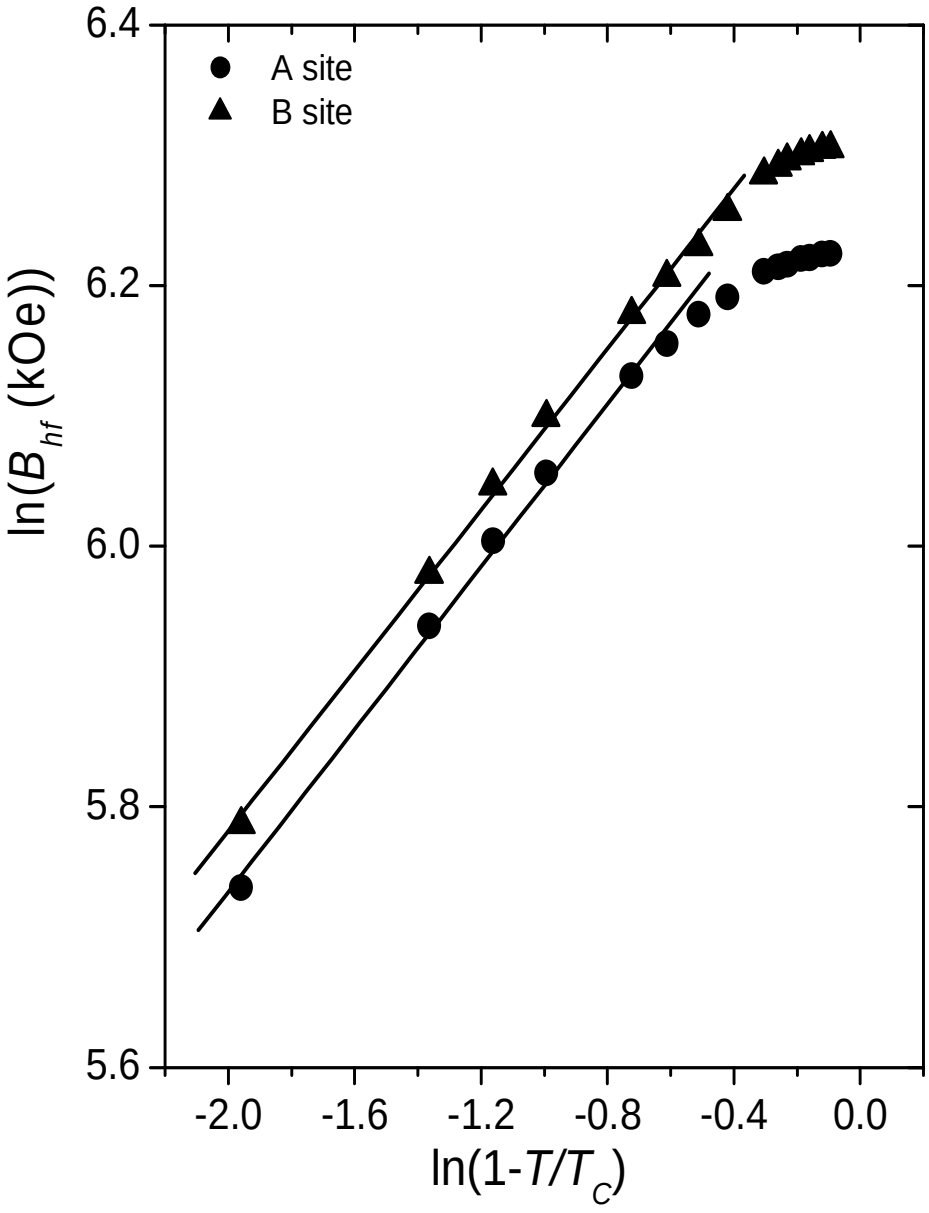

Figure 5.6: A graph of $\ln B_{hf}(T)$ versus $\ln[1 - T/T_C]$ for the $NiFe_2O_4$ oxide.

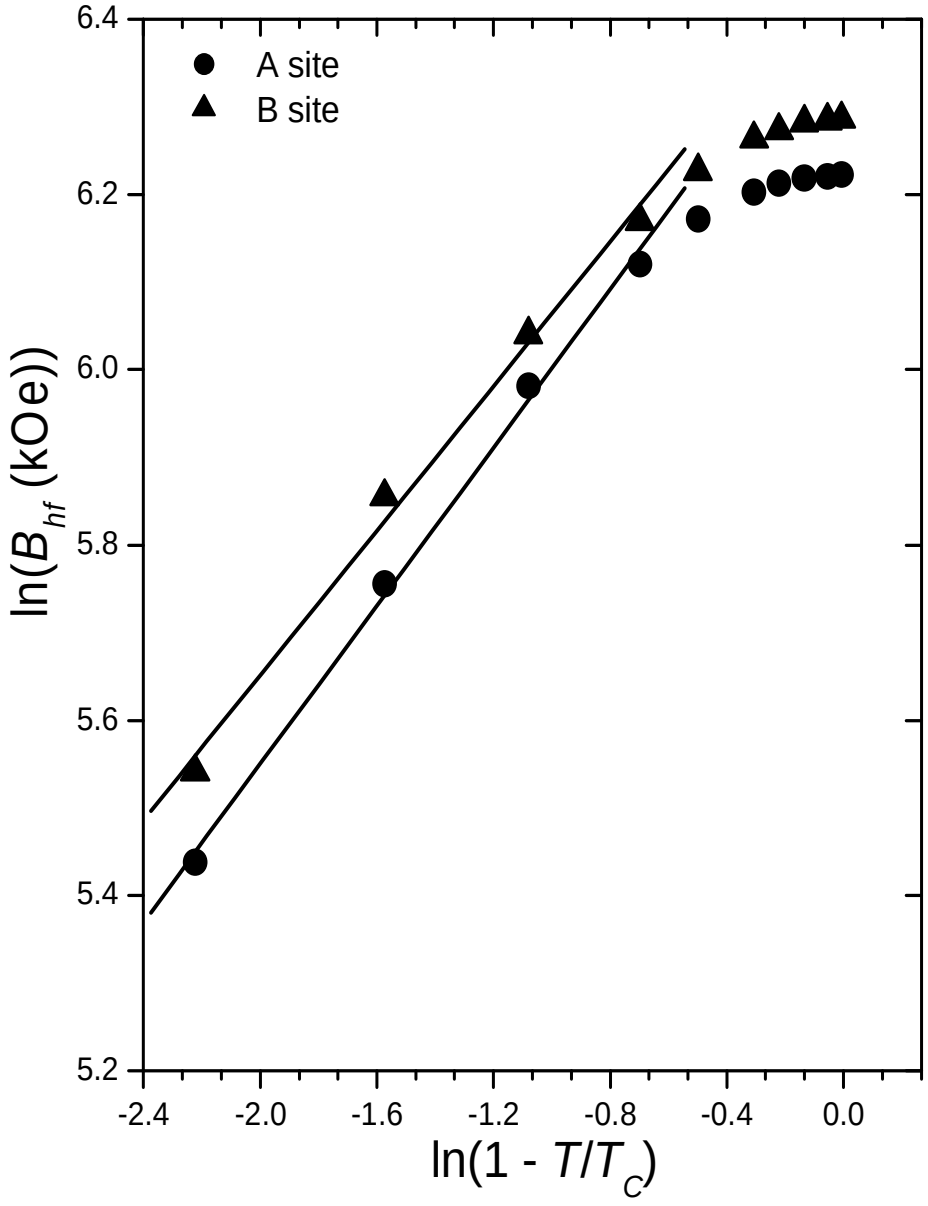

Figure 5.7: A graph of $\ln B_{hf}(T)$ versus $\ln[1 - T/T_C]$ for the $CuFe_2O_4$ oxide based on data in reference [14].

Table 5.3: Values obtained from a graph of (a) $\ln B_{hf}(T)$ versus $\ln[1 - T/T_C]$ and (b) $\ln B_{hf}$ versus $\ln\left[1 - (T/T_C)^2\right]$ for the $NiFe_2O_4$ and $CuFe_2O_4$ oxides.

	R^2		β_i i =1, 2		$B_{hf}(0)$ (kOe)	
	A	B	A	B	A	B
$NiFe_2O_4$ (a)	0.998	0.997	0.31 ± 0.01	0.31 ± 0.01	577 ± 1	601 ± 1
$NiFe_2O_4$ (b)	0.999	0.999	0.37 ± 0.01	0.40 ± 0.01	508 ± 1	550 ± 1
$CuFe_2O_4$ (a)	0.998	0.997	0.45 ± 0.02	0.41 0.02	634 ± 2	649 ± 1
$CuFe_2O_4$ (b)	0.998	0.999	0.49 ± 0.01	0.46 ± 0.01	512 ± 1	542 ± 2

the basis of the Stoner theory. The collapse of magnetization due to Stoner excitation is expressed by equation (2.3.29). Since magnetization is proportional to hyperfine fields, the temperature dependence can be assumed to be

$$B_{hf}(T) = B_{hf}(0)\left[1 - \left(\frac{T}{T_C}\right)^2\right]^{\beta_2}. \tag{5.3.3}$$

In linear form equation (5.3.3) can be expressed by

$$\ln B_{hf}(T) = \ln B_{hf}(0) + \beta_2 \ln\left[1 - \left(\frac{T}{T_C}\right)^2\right]. \tag{5.3.4}$$

Plots of $\ln B_{hf}(T)$ versus $\ln\left[1 - (T/T_C)^2\right]$ are shown in Figures 5.8 and 5.9 for $NiFe_2O_4$ and $CuFe_2O_4$ oxides. Unlike equation (5.3.1), equation (5.3.3) appear to fit the data well over a much wider temperature range.

The hyperfine fields for the $ErFe_{12-x}Nb_x$ compounds have been reported by Wang et al [74] to vary with temperature as

$$B_{hf}(T) = B_{hf}(0)\left[1 - b\left(\frac{T}{T_C}\right)^2\right] \tag{5.3.5}$$

where the constant $b = 0.46$. The T^2 dependence of hyperfine fields was associated with suppression of the magnetization by single–particle excitation mechanisms with increasing temperature [74, 80]. Clearly, the basis of equation (5.3.5) is equation (5.3.3) where $b = \beta_2$.

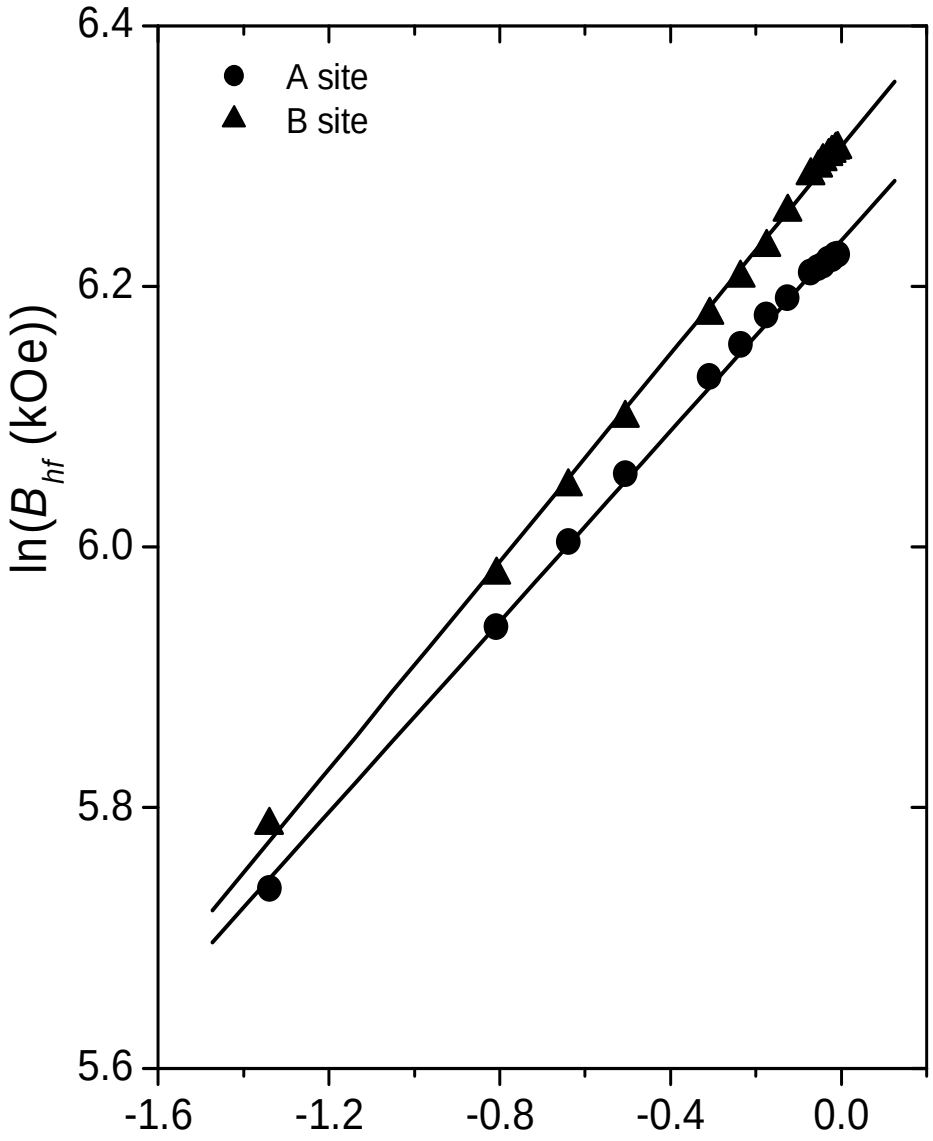

Figure 5.8: A graph of $\ln B_{hf}(T)$ versus $\ln\left[1-(T/T_C)^2\right]$ for the $NiFe_2O_4$ oxide.

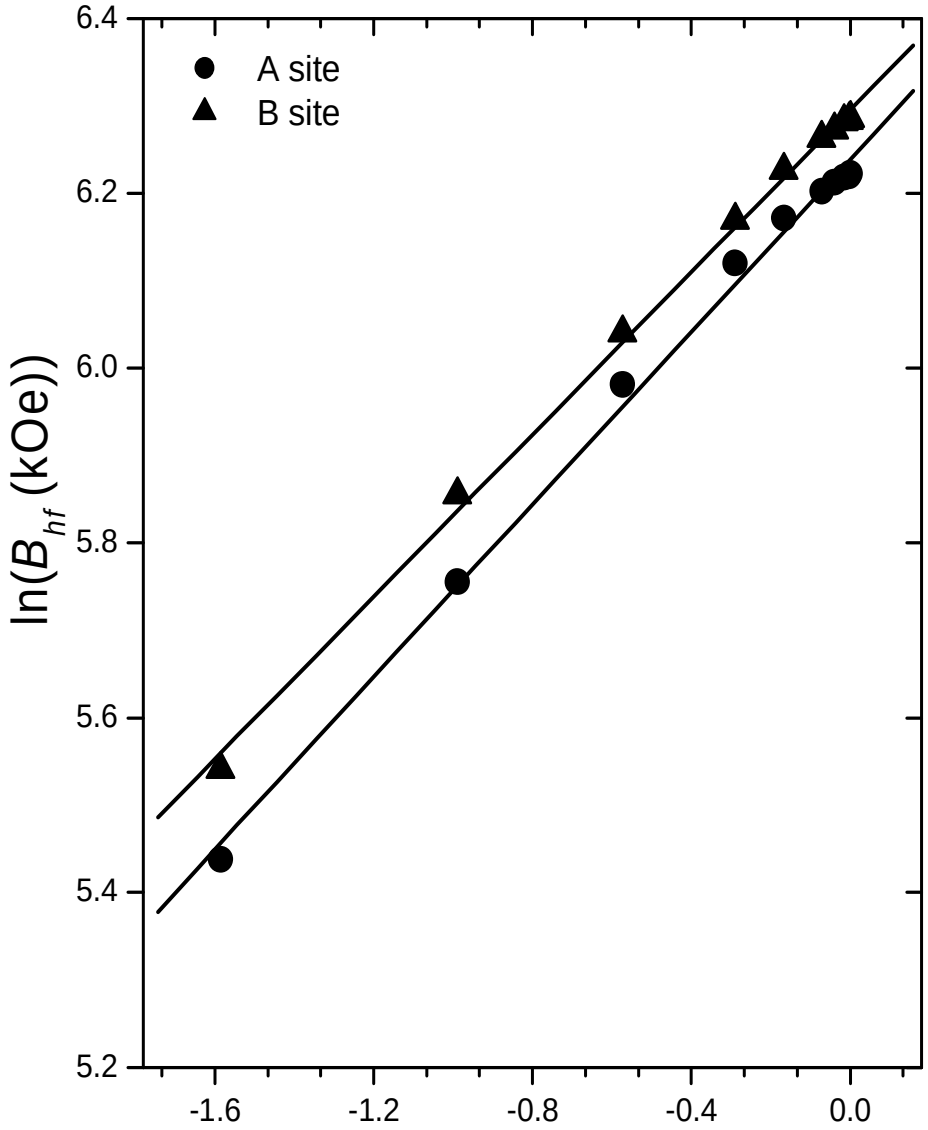

Figure 5.9: A graph of $\ln B_{hf}(T)$ versus $\ln\left[1-(T/T_C)^2\right]$ for the $CuFe_2O_4$ oxide based on data in reference [14].

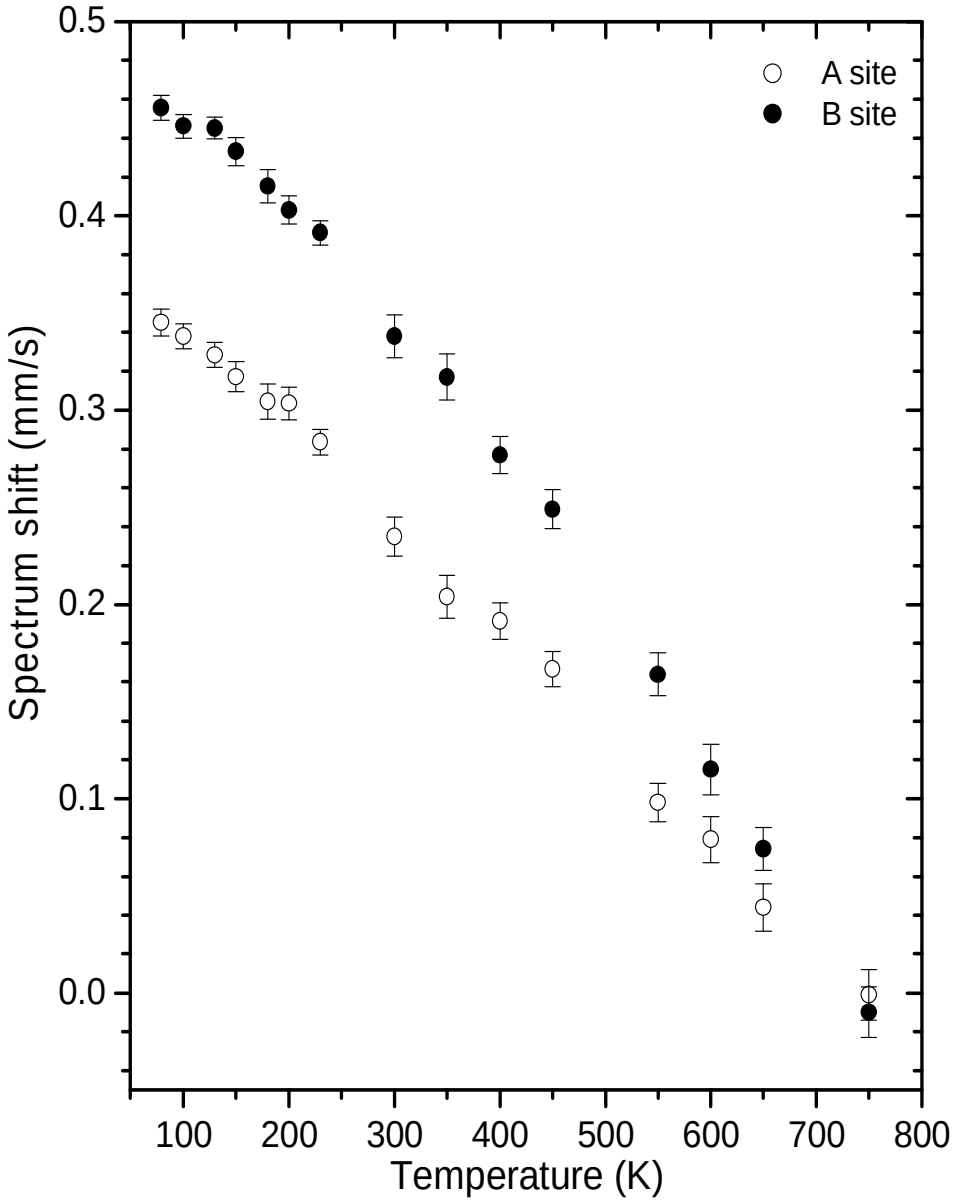

Figure 5.10: Variation of Mössbauer spectrum shifts of $NiFe_2O_4$ with temperature.

In Figure 5.10 we show the variation of Mössbauer spectrum shift from zero velocity with increasing sample measuring temperature. The shift in the Mössbauer spectrum consists of isomer shift and second–order Doppler shift resulting from the relative motion of the emitting ^{57}Co nuclei [75]. The isomer shift does not depend on temperature because the emitting or absorbing atom oscillates about its mean position at high frequency (10^{12} Hz) such that the average displacement is zero during the Mössbauer event [59]. The second–order Doppler shift is proportional to the vibrational energy of the ^{57}Fe nuclei. The decrease in spectrum shift is therefore attributed to the second order Doppler shift.

The variation of Mössbauer spectra with milling time (reduction in grain size) is shown in Figure 5.11. The spectra were fitted by three sextets and two doublet. The two sextets are attributed to Fe ions on A and B sites. An additional sextet was required to get better fit to the data for samples milled for at least 12 hours. The average hyperfine fields corresponding to the third sextets (B_{3rd}) in Table 5.4 is 306 $\pm$ 16 kOe. The origin of this sextet is attributed to the likely onset of small Fe clusters induced by milling. We note that the values of B_{3rd} are close to the hyperfine field of 330 kOe at room temperature for the α–Fe calibration sample used in the present work. The percentages of sextets and doublets areas used to get good fits to the Mössbauer experimental data represent the Fe population in A and B sites. The increasing doublet area with milling (see Figure 5.12) indicates the developing paramagnetic phase. This can be explained on the basis of transformation from multidomains in bulk samples to single domains in fine powders and oxygen vacancies created by milling mechanism [35]. Distances between single domains are larger after milling. This results in weaker superexchange interactions between magnetic moments leading to disordered spin state. Oxygen vacancies also result in broken superexchange paths between spins on tetrahedral (A) and those on the octerhedral (B) sites. This weakens the intersublattice superexchange interactions (A–O–B) giving rise to paramagnetic state. The fraction of Fe ions on

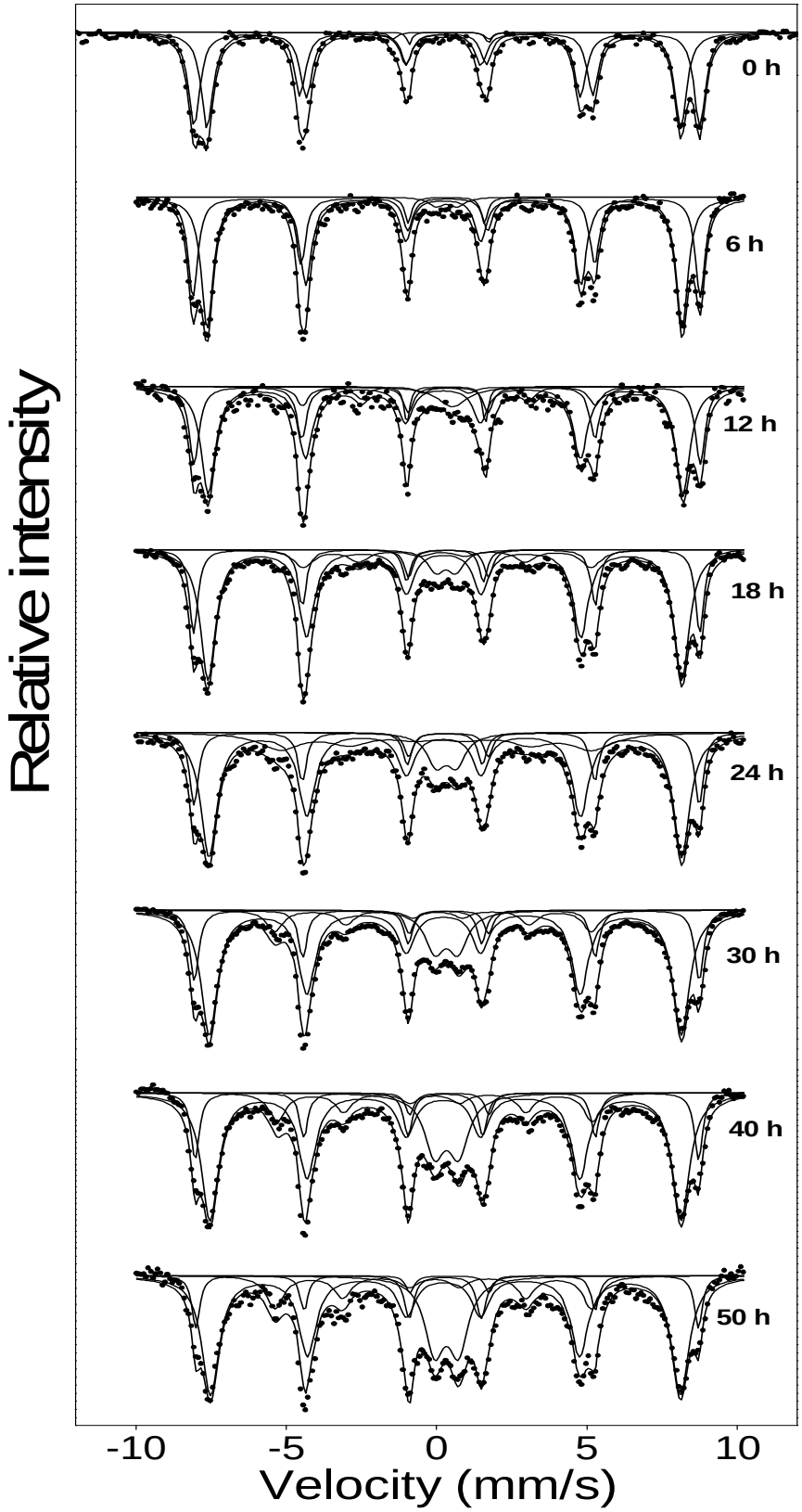

Figure 5.11: Variation of Mössbauer spectra for $NiFe_2O_4$ with milling time.

A site is not significantly affected by milling. The increasing doublet area in Figure 5.12 cannot be an artifact of the analysis. It is well known that Ni ions have preference for octahedral (B) sites and Fe ions are equally distributed at both tetrahedral (A) and octahedral sites in $NiFe_2O_4$. The effect of milling appears to suggest partial inversion of Ni ions from B to A sites. Evidence for this has also been provided by EXAFS studies [34] on bulk and milled Ni ferrites. Our results appear to provide further evidence of the transfer of Ni ions to A sites by milling. The magnetic order on B site weakens as a result of milling (as observed in Figure 5.12). Hence the doublet area can be expected to increase at the expense of weakening magnetic order on B sites.

The data deduced from Mössbauer spectra are shown in Tables 5.4 and 5.5. Our values compare well with those deduced spectra of similar compounds [38, 44]. A slight decrease in hyperfine fields (see Figure 5.13), indicating weakening of magnetic coupling, with milling is observed. This compares well with increasing paramagnetic component indicated by the growth of the doublet area with reduction in grain size. The magnetic coupling becomes weaker as some superechange paths are broken by milling. The variation of the isomer shift with milling time is shown in Figure 5.14. A slight general increase in isomer shift with milling occurs. This shows that the s–electron density is weakly affected by milling.

The magnetic ordering temperature was found to be 873 ± 3 K for the bulk and nanosized oxide. The anomalous change in magnetic ordering temperature observed in $ZnFe_2O_4$ [44, 45] with reduction in grain size is not observed in milled $NiFe_2O_4$ oxides. The increased Nèel temperature for the $ZnFe_2O_4$ fine powder can be explained by weakening of superexchange due to migration of Zn ions from A to B sites with milling. The $ZnFe_2O_4$ oxide is a normal spinel where all the Zn ions are on A sites and all Fe ions on B site. Since Zn is nonmagnetic, there are no superexchange intra–sublattice (J_{AA} (A–O–A)) or inter–sublattice (J_{AB} (A–O–B)) but only the J_{BB} (B–O–B) exchange interactions. This results in low magnetic ordering temperature. If the Fe ions on B sites are replaced

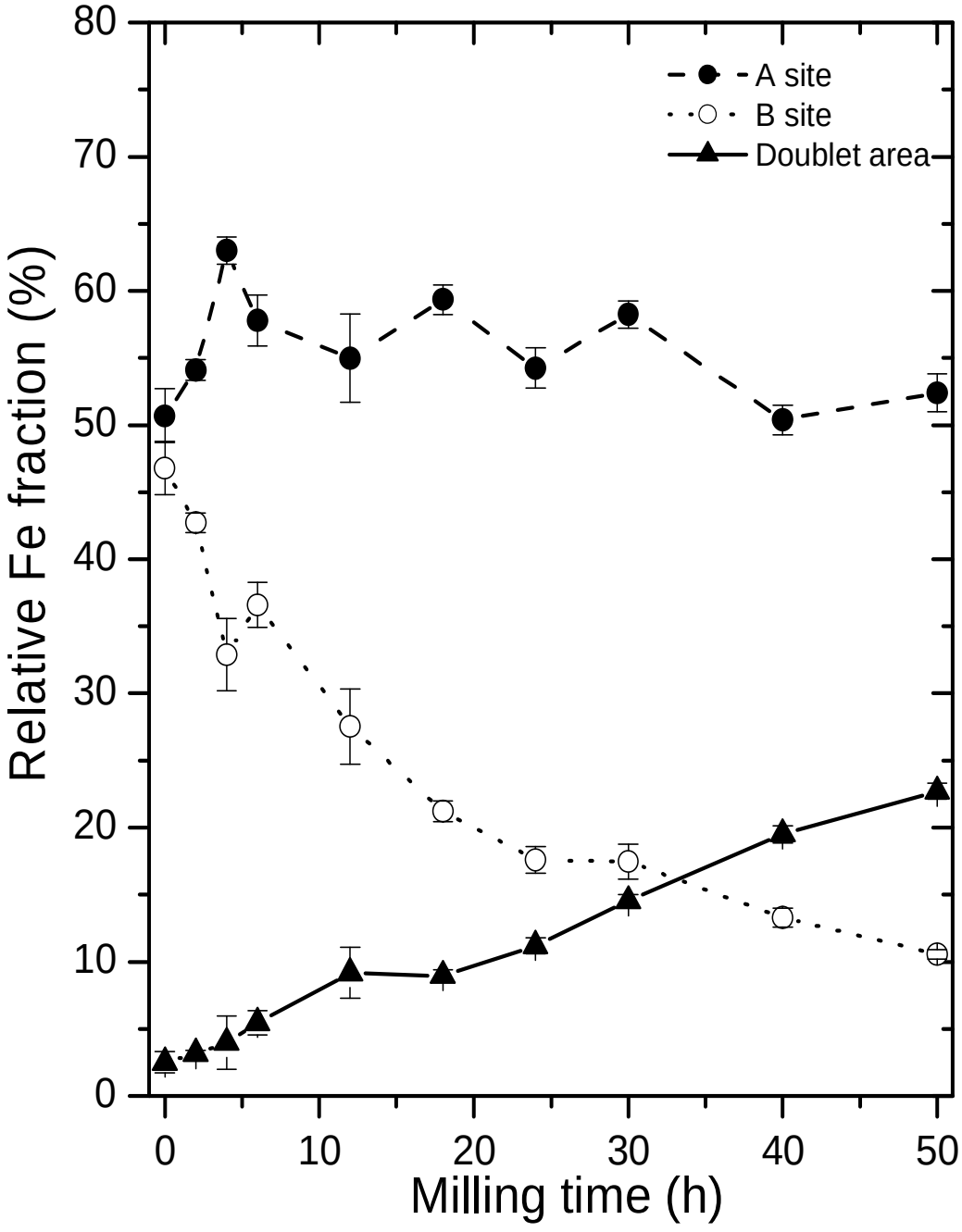

Figure 5.12: Variation of Fe fractions in $NiFe_2O_4$ with milling time.

Table 5.4: Variation of isomer shift (IS), quadrupole splitting (QS) and hyperfine fields (B_{hf}) of $NiFe_2O_4$ with milling time. B_{3rd} is the hyperfine field corresponding to the third sextet observed only for at least 12 hours of milling.

	IS (mm/s)		QS (mm/s)		B_{hf} (kOe)		
MT (h)	$(IS)_A$	$(IS)_B$	$(QS)_A$	$(QS)_B$	$(B_{hf})_A$	$(B_{hf})_B$	B_{3rd} (kOe)
	± 0.01	± 0.01	±0.01	± 0.01	± 0.8	±0.8	±5
0	0.24	0.34	0.01	0.01	488.4	521.7	
2	0.25	0.36	0.02	-0.01	490.0	522.7	
4	0.25	0.37	0.03	-0.01	491.6	522.8	
6	0.25	0.35	0.02	-0.02	489.7	523.3	
12	0.26	0.37	0.04	-0.02	489.6	522.1	302
18	0.26	0.37	0.02	-0.03	488.6	522.0	297
24	0.27	0.37	0.03	-0.03	487.4	521.1	322
30	0.26	0.38	0.03	-0.04	486.8	520.7	281
40	0.26	0.39	0.03	-0.04	485.7	519.2	325
50	0.27	0.39	0.03	-0.04	486.0	519.3	326

Table 5.5: Variation of isomer shift (IS), quadrupole splitting (QS) and line wdth (LW) of $NiFe_2O_4$ (deduced from doublets) with milling time.

	IS (mm/s)		QS (mm/s)		LW (mm/s)	
MT (h)	$(IS)_A$	$(IS)_B$	$(QS)_A$	$(QS)_B$	$(LW)_A$	$(LW)_B$
	± 0.03	± 0.02	±0.01	± 0.01	± 0.02	±0.01
0	0.32	0.37	0.15	0.10	0.15	0.10
2	0.31	0.35	2.33	0.50	0.12	0.22
4	0.31	0.38	2.32	0.68	0.15	0.32
6	0.33	0.34	2.54	0.71	0.13	0.29
12	0.32	0.39	2.58	0.70	0.11	0.31
18	0.28	0.37	2.56	0.66	0.16	0.33
24	0.28	0.34	2.49	0.67	0.18	0.37
30	0.28	0.37	2.34	0.75	0.17	0.37
40	0.29	0.34	2.48	0.80	0.18	0.40
50	0.29	0.33	2.40	0.79	0.19	0.39

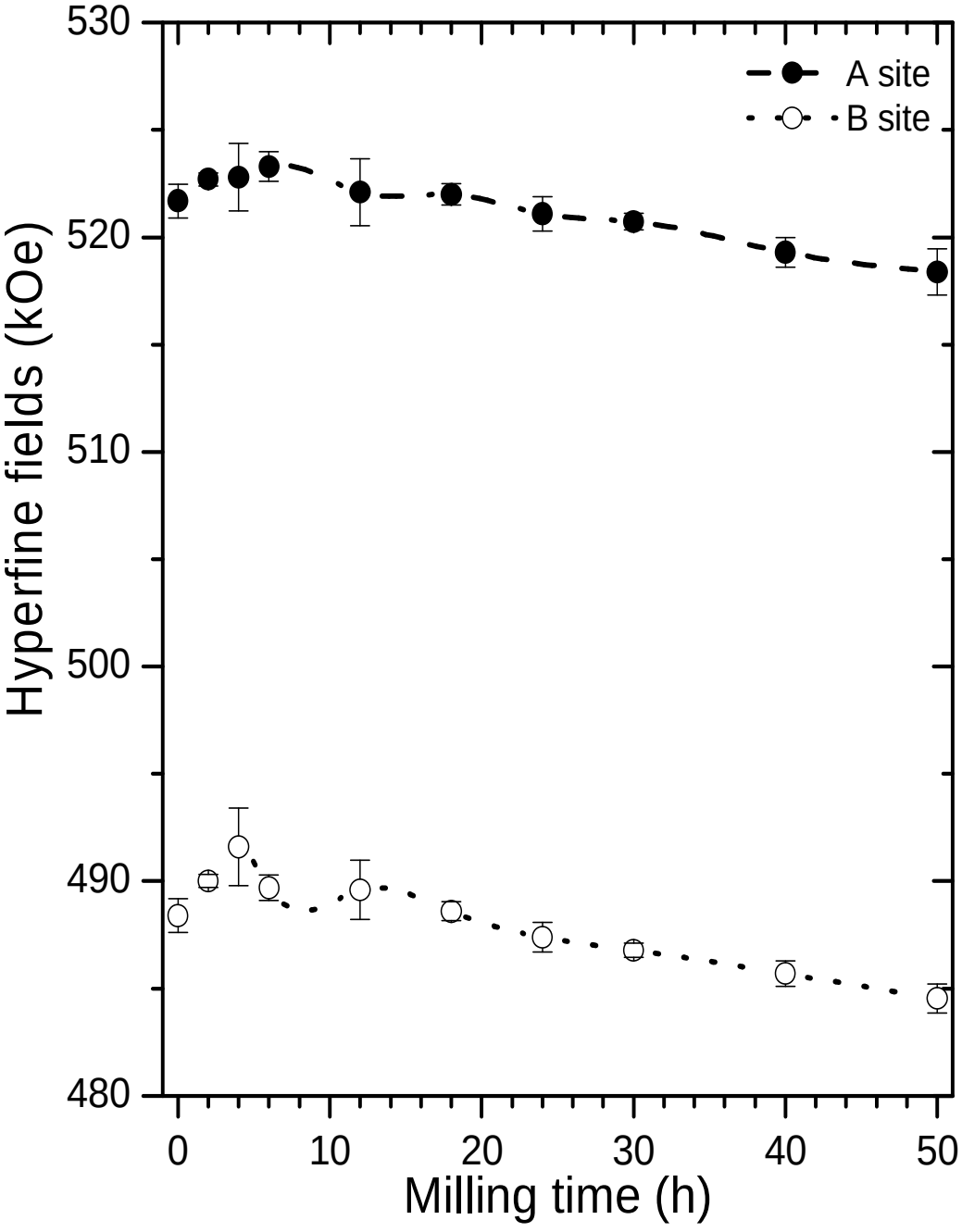

Figure 5.13: Variation of hyperfine fields of $NiFe_2O_4$ with milling time.

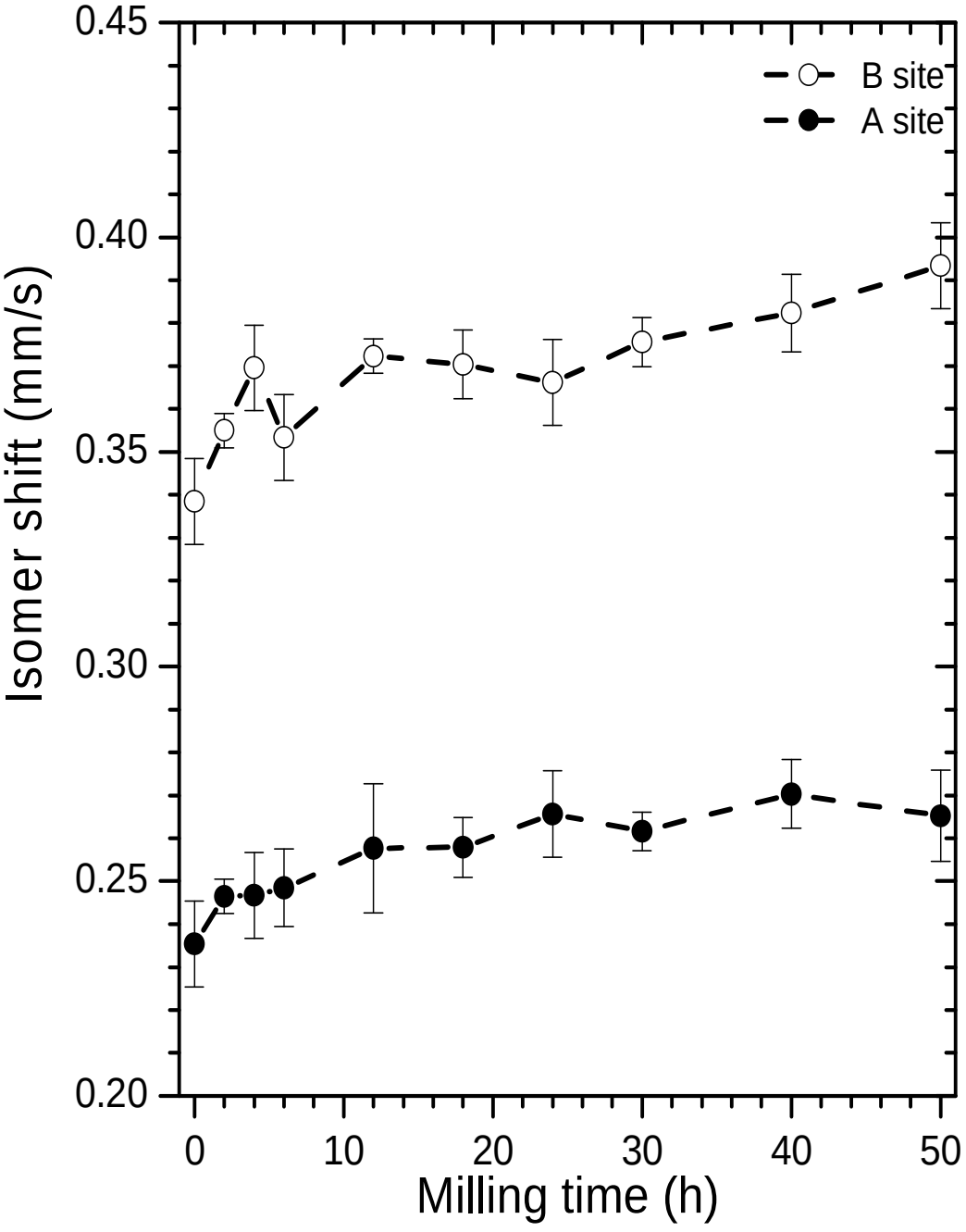

Figure 5.14: Variation of isomer shift of $NiFe_2O_4$ with milling time.

by Zn ions, J_{AB} (antiferromagnetic interaction) can become stronger than J_{AA} or J_{BB} and this can be seen as higher magnetic ordering temperature. On the other hand, in $NiFe_2O_4$ the Ni ions are magnetic. Therefore the strong inter–sublattice superexchange interactions (A–O–B) exist which are weakly affected by milling. Hence no significant change in the magnetic transition temperature is observed with milling $NiFe_2O_4$ oxides.

In general superexchange integrals can be determined from hyperfine fields and magnetic moment [9, 14]. However, the total spontaneous magnetization near the Curie (or Nèel) temperature can not be correctly determined under the effect of an external magnetic field due to induced magnetization near the Curie temperature. The data that are not affected by external field are therefore required in order to correctly extract information on superexchange interactions. The data of magnetic hyperfine fields at ^{57}Fe nuclei on A and B sites measured without external fields using Mössbauer spectroscopy can be used to determine the exchange integrals [9, 14]. From Néel theory of ferrimagnetism [14], the intersublattice exchange constant J_{AB} can be related to the Curie (or Nèel) temperature by the equation

$$J_{AB} = -\frac{g^2 T_C k_B}{12Q}. \tag{5.3.6}$$

Q can be can be calculated from the molecular field coefficients α and β defined in reference [14]. The intrasublattice super exchange constants

$$J_{AA} = -\frac{3}{2}\alpha J_{AB} \tag{5.3.7}$$

and

$$J_{BB} = -2\beta J_{AB} \tag{5.3.8}$$

can be deduced from the knowledge of coefficients α and β.

5.4 Magnetization results

Isothermal magnetization measurements presented here were performed at room temperature using a recently commisioned Lakeshore vibrating sample

magnetometer [68]. Hysteresis loops of the samples in powder forms (about 0.05 g) were obtained in the applied field range: -6 < B_0 <6 kOe. The variation of hysteresis loops for different milling times is shown in Figure 5.15. From a hysteresis loop information about saturation magnetization, remanance and coercive field can be deduced. These results are presented in Table 5.5.

The saturation magnetization was taken as the magnetization at the highest applied field. This is a reasonable estimate if we are interested in elucidating the trends in the properties with milling. The values of saturation magnetization and remanance are also subject to corrections for demagnetizing effects which are ignored in the present analysis. The saturation magnetization reduces from about 48 emu/g to 32 emu/g with reduction in grain size after milling for 50 hours as shown in Table 5.6. An increase in saturation magnetization with increasing grain size has been observed in reference [72]. The reduction in saturation magnetization is attributed to weakening of magnetic coupling between moments. This compares well with the evolution of the paramagnetic phase in the Mössbauer spectra with decreasing grain size. The remanent magnetization appears to attain a maximum value and then reduces with further milling (see Figure 5.16). This trend is expected to be closely related to the change in magnetic hardness of the samples.

The coercive (H_C) data derived from the hysteresis loops are more reliable because they are not affected by the calibration of the magnetization and demagnetizing effects. H_C is determined when the magnetization $M(B_0) = 0$. The coercive field data therefore deserve a more detailed analysis. The coercive field is also a useful parameter in providing information about the internal microstructure of a material and its relation to domain wall movements.

The bulk $NiFe_2O_4$ oxide has a small coercive field. Similar results have been observed in other ferrites [15, 81]. The variation of the coercive field with milling time is shown in Figure 5.17. The coercive field H_C initially increases rapidly due to milling. This relates well with the initial fast decrease in grain size with milling (see Figure 5.2). After about 40 hours of milling no significant

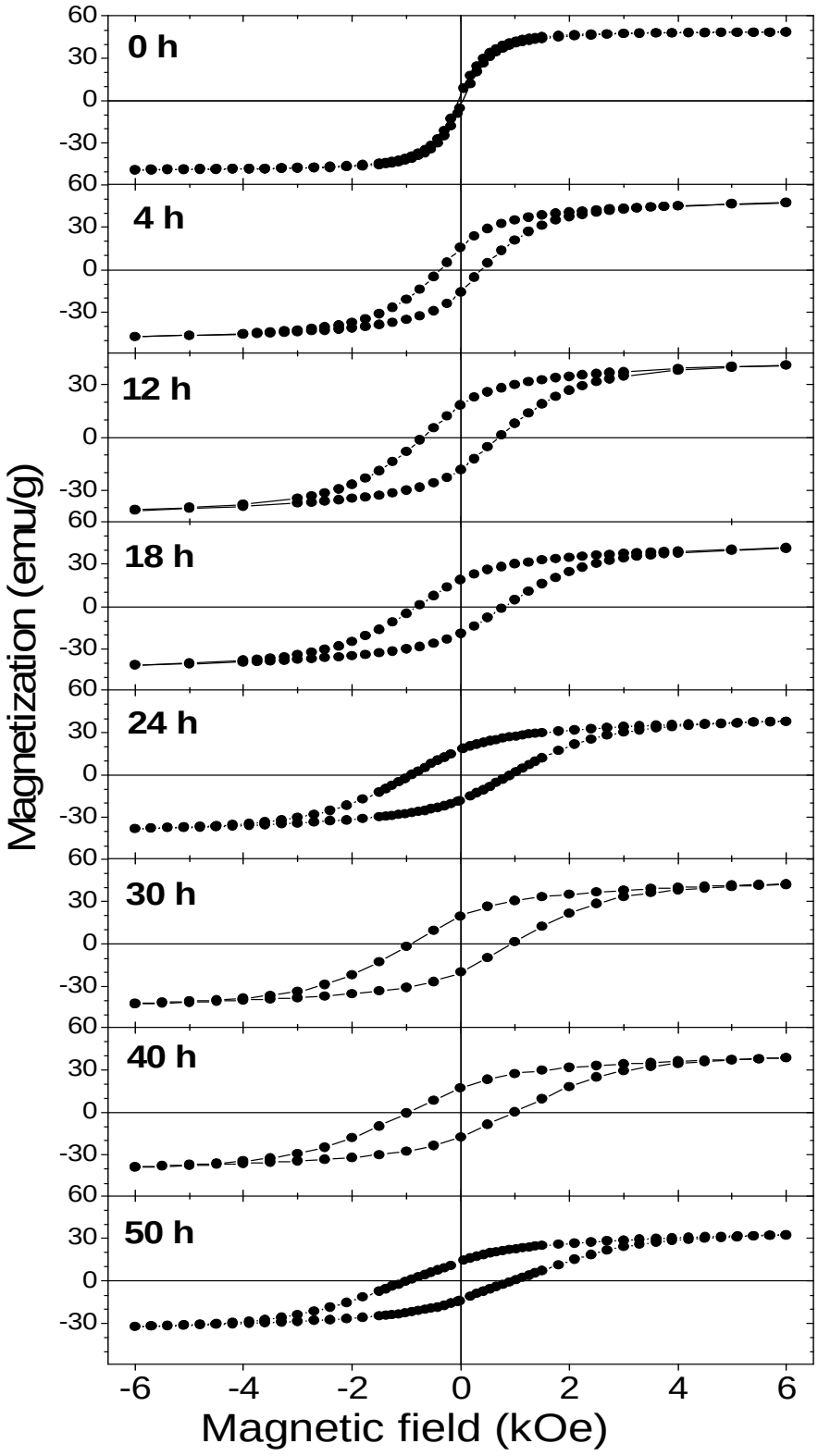

Figure 5.15: Variation of hysteresis curves for $NiFe_2O_4$ with milling time.

Table 5.6: Variation of saturation magnetization (M_S), remanence (M_R) and coercivity (H_C) with milling time (MT) for $NiFe_2O_4$ oxide.

MT (h)	M_S (emu/g)	M_R (emu/g)	H_C (kOe)
		$\pm$ 0.4	$\pm$ 0.01
0	48.3	3.4	0.04
4	14.5	14.5	0.39
12	41.3	17.9	0.70
18	41.4	18.4	0.81
24	37.9	17.7	0.91
30	42.3	18.6	0.93
40	38.4	16.0	0.97
50	32.4	13.6	0.98

change occurs with further grinding. This also compares well with the saturation in grain sizes observed after milling for about 30 hours. The coercive field is closely related to processes that limit the motion of domain walls in a material. In the present system of compounds we assume that this arises due to an increased number of grain boundaries with milling [70]. The milling process increases the number of multidomain particles. For multidomain particles the coercive field can be expected to increase with reduction in particle size G according to the relation [69]

$$H_C = a + \frac{b}{G} \tag{5.4.1}$$

where a and b are constants. In Figure 5.18 we have plotted the coercive field H_C with $1/G$. A good linear fit (correlation coefficient 0.9896) to the data is obtained. The constants a and b are found to be -0.23 $\pm$ 0.06 kOe and 15 $\pm$ 1 nm kOe respectively. The high coercive fields of the fine powders also show that although the particles are in the nanometer scale, superparamagnetic regime

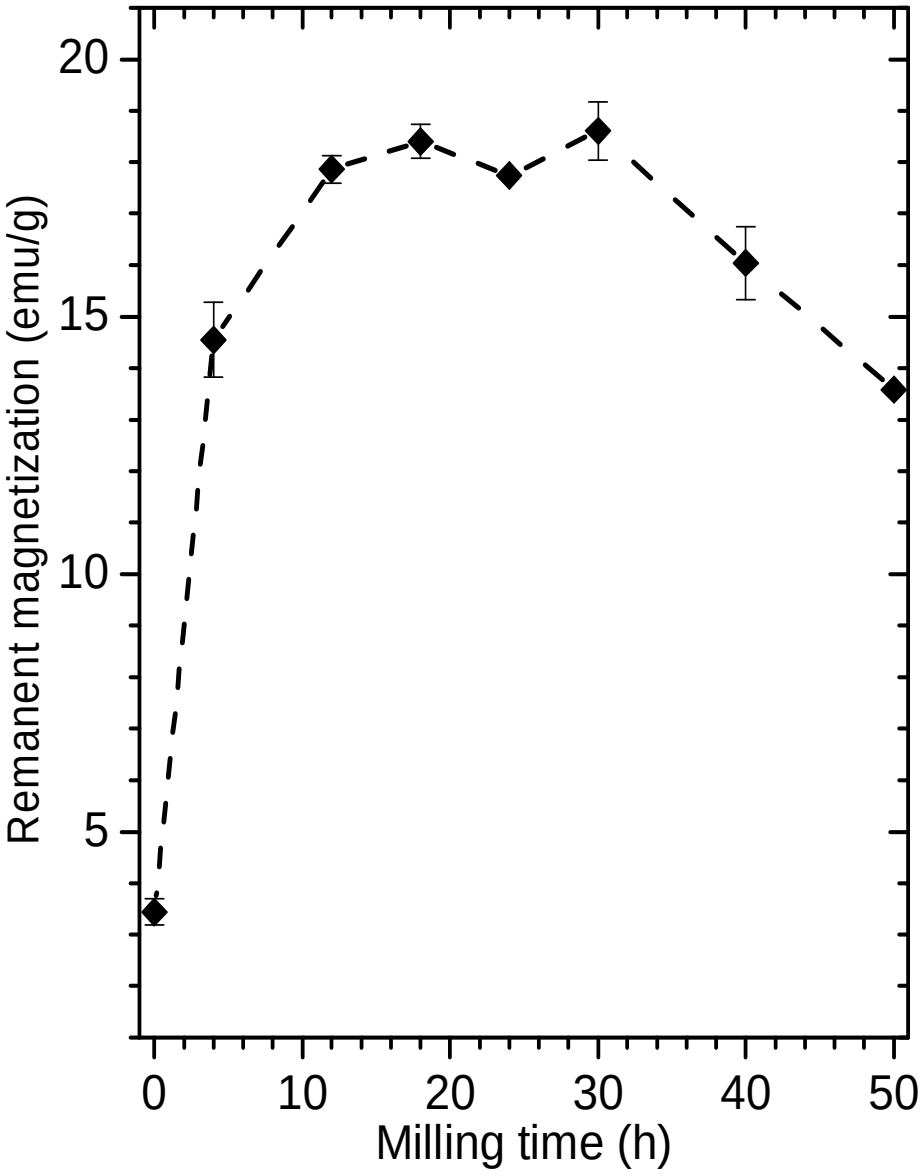

Figure 5.16: Variation of remanent magnetization for $NiFe_2O_4$ with milling time.

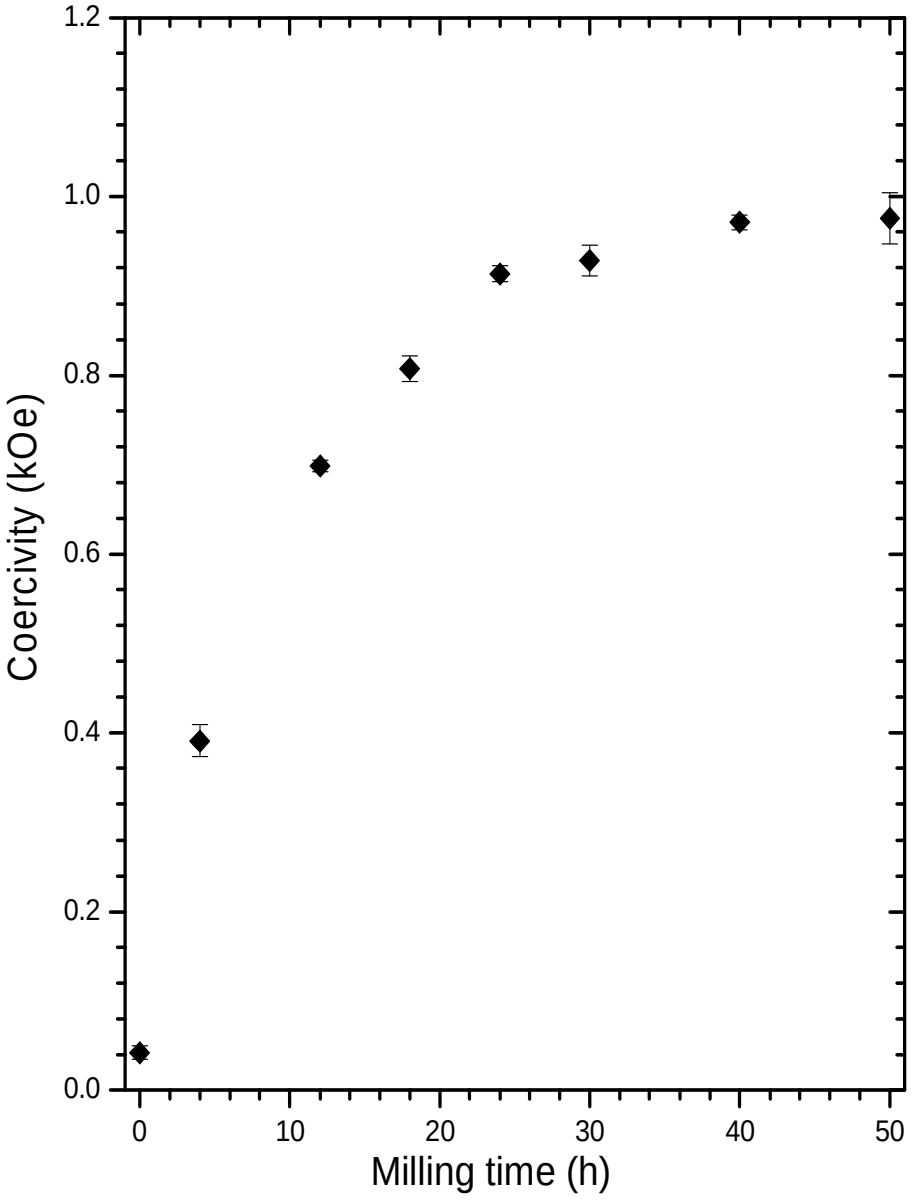

Figure 5.17: Variation of coercive fields for $NiFe_2O_4$ with milling time.

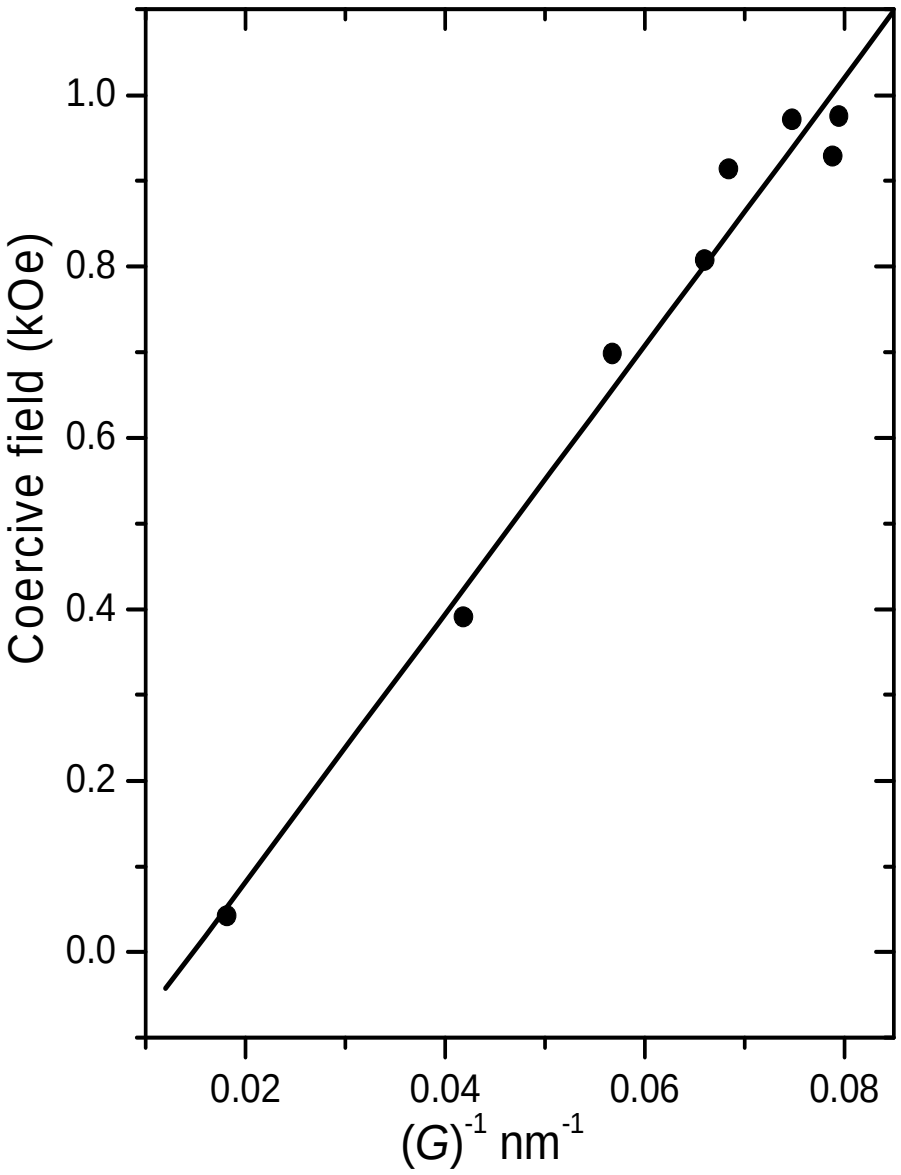

Figure 5.18: Variation of coercive fields for $NiFe_2O_4$ with $1/(G)$.

was not reached in the present measurements. Moumen et al [**?**] obtained a superparamagnetic state after the particle size of $CoFe_2O_4$ was reduced to about 5 nm.

5.5 Conclusions

The temperature dependence of hyperfine fields bulk $NiFe_2O_4$ and $CuFe_2O_4$ oxides appear to be well described by Stoner theory of single particle excitations according to the equation (5.3.3).

The Mössbauer spectra of fine powders of $NiFe_2O_4$ oxides indicate the existence of both ferrimagnetic and paramagnetic phases. Good correlation between reduction in grain size and coercive field has been observed. The coercive fields of $NiFe_2O_4$ oxides have been found to increase with reduction in grain size according to the equation (5.4.1). This indicates the presence of multidomain particles. Quantitative values of the constants a and b have been obtained which can be compared to other compounds. No significant change in the distribution of cations with reduction in grain size has been observed. This is in agreement with the results in reference [34].

Chapter 6

Magnetic properties of bulk and nanosized $(Zn, Cd, Cu)_{0.5}Ni_{0.5}Fe_2O_4$ oxides

6.1 Introduction

A study of grain size effects on the magnetic properties of the spinel $NiFe_2O_4$ oxides has been presented in Chapter 5. Apart from the grain size, the distribution of cations amongst the tetrahedral (A) and octahedral (B) sites are dependent on the type of cations involved. This chapter is concerned with grain size effects on the diluted magnetic phase of $NiFe_2O_4$ oxide. The Zn–Ni substituted ferrites have many applications in the electronics industry (see chapter 1). In particular the magnetic properties of the compound with a nominal composition of $Zn_{0.5}Ni_{0.5}Fe_2O_4$ has been studied by many authors [15, 17, 47] and shows many interesting properties. The Cd ion has larger size (0.097 nm) than Zn (0.074 nm) or Cu (0.072 nm) ions and the atomic size for Ni is 0.069 nm. While Zn and Cd atoms have full outer s orbital electrons, Cu has a single unpaired electron in its outer orbital. It is therefore interesting to investigate how the properties are affected by changes of atomic size and electronic

configurations of atoms diluting the $NiFe_2O_4$ compound.

In the previous works [4, 5] we have investigated the effect of atomic size difference between Cd and Zn on the magnetic properties and structure of $(Zn, Cd)_xCo_{1-x}Fe_{2-x}Al_xO_4$ and $(Cd, Zn)_xCo_{0.9}Fe_{1.7-x}Ti_{0.4}O_4$ compounds. Contraction of the unit cell was observed when bigger atoms were replaced by smaller ones. Deviation from this expected behavior was also observed at high concentration of Zn and Cd ions. Mössbauer spectroscopy did not reflect significant changes on the magnetic properties associated with size difference between Cd and Zn atoms. However, Mössbauer spectroscopy studies alone do not give full information of the magnetic behavior of materials.

In this chapter we investigate the structural and magnetic properties of $(Zn, Cd, Cu)_{0.5}Ni_{0.5}Fe_2O_4$ oxides using X–ray diffraction, Mössbauer spectroscopy and magnetization measurements. Bulk samples of $(Zn, Cd, Cu)_{0.5}Ni_{0.5}Fe_2O_4$ oxides were produced by solid–state reaction. Nanosized compounds were obtained by systematically grinding the bulk samples using a Retsch high energy ball mill.

6.2 X-ray diffraction results

In Figures 6.1 and 6.2 we show the variation with milling time of X–ray diffraction patterns of $(Zn, Cd, Cu)_{0.5}Ni_{0.5}Fe_2O_4$ compounds. The most significant peaks were successfully indexed with respect to cubic spinel structure in all the samples. The broadening of the X–ray diffraction lines with milling time indicates a reduction in grain sizes.

In Figure 6.3 we have plotted the lattice constant with atomic size of Zn, Cd and Cu. There is a good correlation between atomic size and lattice constant of the compounds. The larger lattice parameter of $Cd_{0.5}Ni_{0.5}Fe_2O_4$ compared to that of $(Cu, Zn)_{0.5}Ni_{0.5}Fe_2O_4$ compounds (see Table 6.1) is due to the larger size of the Cd compared to Zn or Cu atoms as shown in Table 6.2. The lattice parameter for the Zn–based compound is comparable to that of the Cu–based

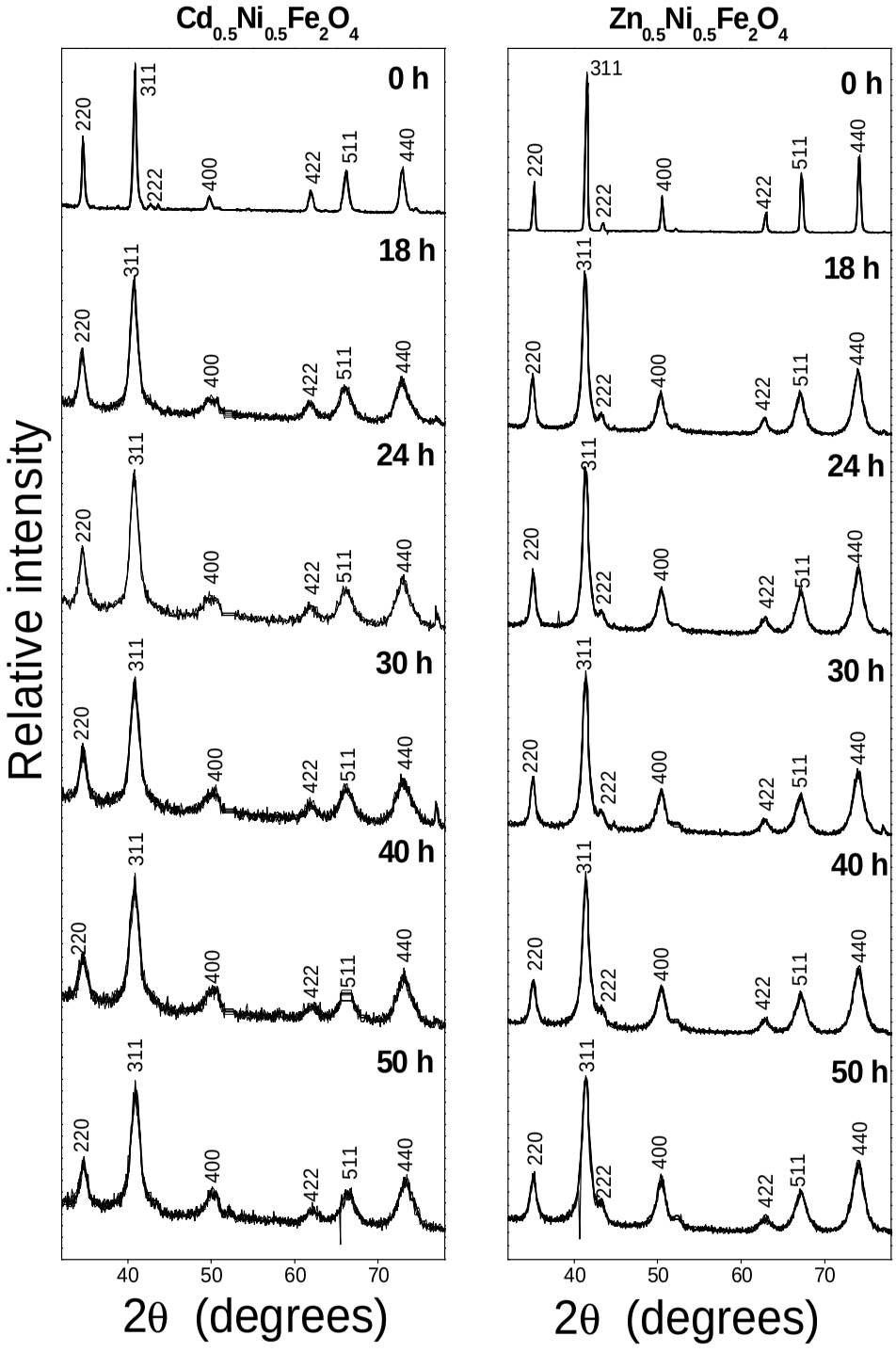

Figure 6.1: Variation of XRD patterns for (Zn, Cd)$_{0.5}$Ni$_{0.5}$Fe$_2$O$_4$ with milling time.

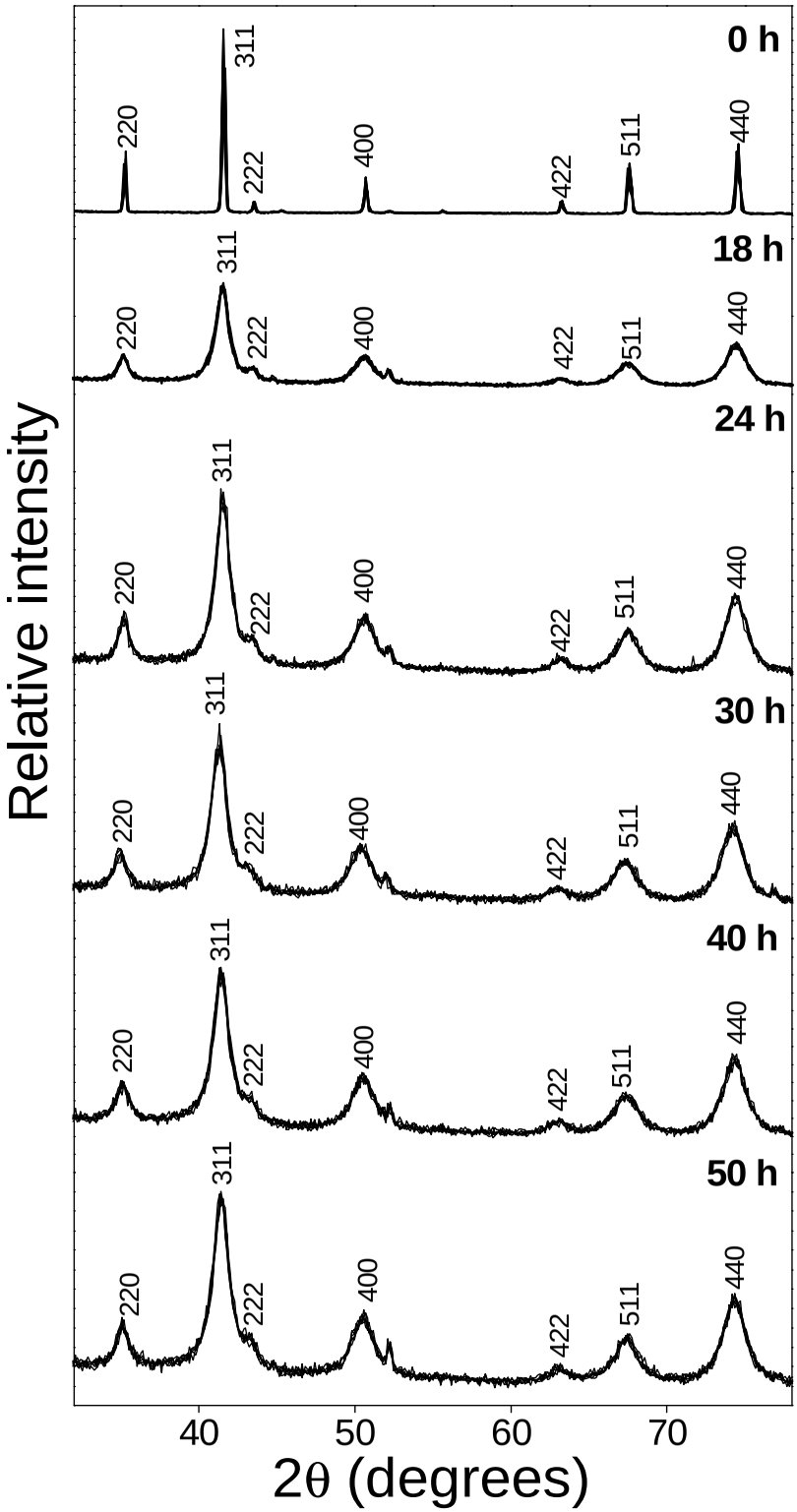

Figure 6.2: Variation of XRD patterns for $Cu_{0.5}Ni_{0.5}Fe_2O_4$ with milling time.

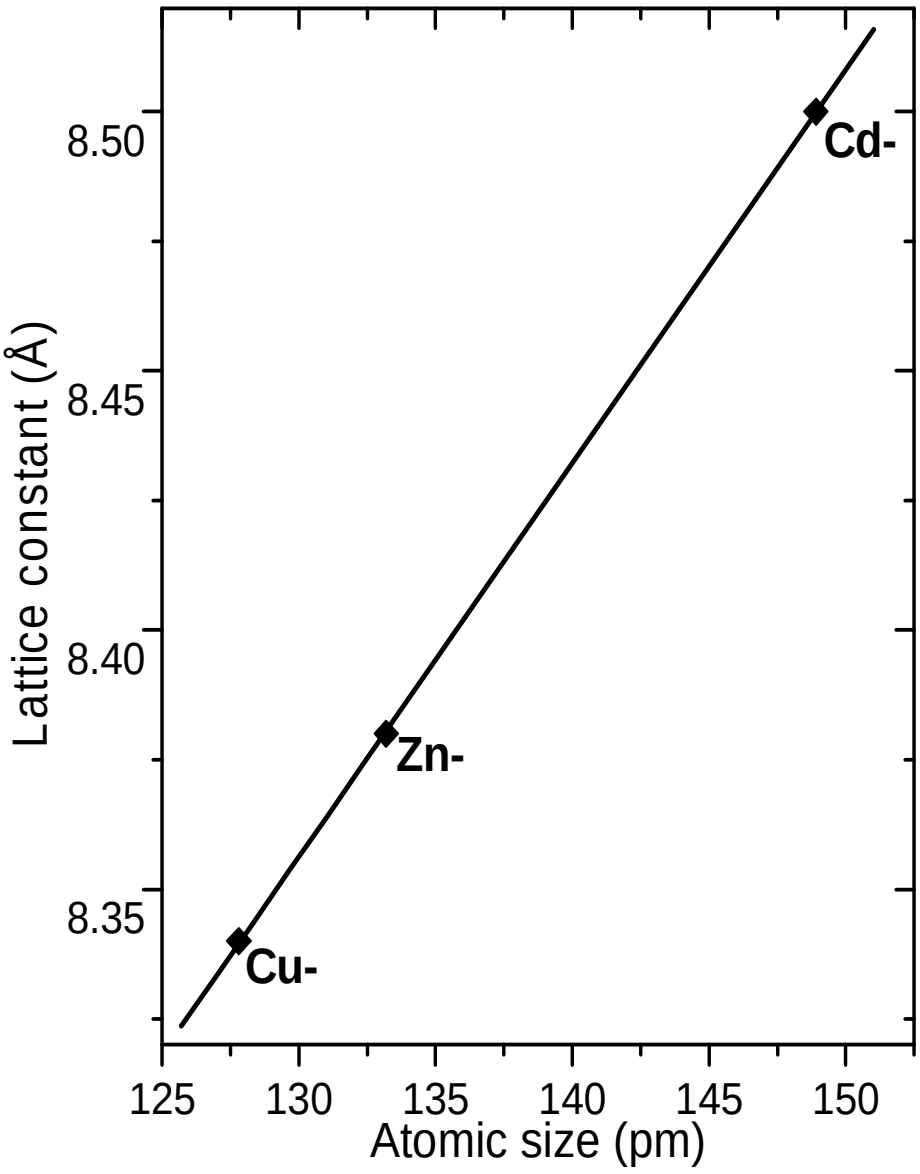

Figure 6.3: Variation of lattice parameters for bulk (Zn, Cd, Cu)$_{0.5}$Ni$_{0.5}$Fe$_2$O$_4$ with atomic size.

Table 6.1: Bulk (ρ_B) and X–ray (ρ_X) densities, porosity (P_o) and lattice parameter (a) for (Zn, Cd, Cu)$_{0.5}$Ni$_{0.5}$Fe$_2$O$_4$ oxides.

Oxide	ρ_B (g/cm^3)	ρ_X (g/cm^3)	G ($\mathring{A}$)	P_o (%)	a ($\mathring{A}$)
	$\pm$ 0.02	$\pm$ 0.03	$\pm$ 1	$\pm$ 0.04	$\pm$ 0.02
$Cu_{0.5}Ni_{0.5}Fe_2O_4$	4.43	5.36	445	17.42	8.37
$Zn_{0.5}Ni_{0.5}Fe_2O_4$	5.11	5.35	480	4.70	8.39
$Cd_{0.5}Ni_{0.5}Fe_2O_4$	5.17	5.63	451	8.17	8.51

Table 6.2: Atomic radii values [71].

Atom	Cd	Zn	Cu
Radius (pm)	148.9	133.2	127.8

oxide. This relates well with the similar ionic sizes between Zn^{2+} (0.074 nm) and Cu^{2+} (0.072 nm) ions.

The bulk densities deduced by Archimedes principle from small mass fragments are also shown in Table 6.1. The larger bulk density of the Cd– compared to that of Zn– and Cu–based oxides is also attributed to the larger size of Cd atoms. Our value of the bulk density of Zn–based oxide is close to 5.01 g/cm^3 reported earlier by Costa et al [15] for the same compound made by combustion technique. The X–ray densities were computed from the values of lattice parameters using equation (5.2.1). These densities are larger compared to the bulk densities. This is expected in principle because X–ray densities reflect the way atoms are packed in a unit cell. Our values compare well with those reported previously [82] for similar compounds.

The percentage porosity (P_o) of the samples were deduced from the X–ray density (ρ_X) and bulk density (ρ_B) data using equation (5.2.2). The porosity

for the Zn–based oxide is the lowest. A porosity of as low as 1.96 % has been reported previously for the $Cu_{0.7}Cd_{0.3}Fe_2O_4$ oxide [82]. The porosity in ferrite materials is generally between 2 % and 30 % [82, 83]. The bulk density and porosity are dependent on the sintering temperature. A decrease in porosity with increasing sintering temperature (see Table 6.3) has been observed previously for the $Zn_{0.5}Ni_{0.5}Fe_2O_4$ oxide [30]. In the current work, the samples were sintered at 1100 ^oC.

Bulk (Zn, Cd, Cu)$_{0.5}Ni_{0.5}Fe_2O_4$ compounds were milled for 50 hours in order to reduce the grain sizes (G) to nanometer scale. G was estimated from the broadening of the 311 XRD peak using equation (5.2.3). The values of G are shown in Table 6.4 and plotted in Figure 6.4 as a function of milling time. The initial grain sizes are largest for the Cu–based oxide and least for the Cd–based oxide. Smaller sized atoms are associated with bigger grains. The inter–atomic interactions are expected to be weaker between bigger atoms. The saturation of grain sizes observed after milling for about 30 hours may be attributed to grain sizes approaching the dimensions of the unit cell or the limit of grinding by the available set of balls. Yu et al [47] obtained a minimum G of about 10 nm after 100 hours of milling a $Zn_{0.5}Ni_{0.5}Fe_2O_4$ bulk sample. The reduction of G seems to be associated with the formation of structural defects and deformation of the unit cell. This is more significant for Cd–based oxide as shown in Figure 6.5. A contraction of unit cell from 8.51 $\pm$ 0.01 $\mathring{A}$ to 8.43 $\pm$ 0.01 $\mathring{A}$ is observed for the Cd–based oxide after about 50 hours of grinding (see Table 6.5). The redistribution of Cd and Fe ions may be causing the contraction of the unit cell. It is also interesting to note that the Cd–based sample has the smallest grain size (9.89 $\pm$ 0.04 nm) compared to that of the Zn–based (11.87 $\pm$ 0.06 nm) and Cu–based (10.21 $\pm$ 0.04 nm) samples obtained after milling for 50 hours. This indicates that it is easier to achieve finer particles when grinding samples that incorporate larger atoms.

Table 6.3: Variation of bulk density (ρ_B) and porosity (P_0) for $Zn_{0.5}Ni_{0.5}Fe_2O_4$ with annealing temperature (T_A) [30].

T_A (^{o}C)	ρ_B (g/cm^3)	P_0 (%)
1150	4.25	22.5
1250	4.55	17.0
1350	4.73	13.7

Table 6.4: Variation of grain size with milling time (MT) for (Cu, Zn, Cd)$_{0.5}$Ni$_{0.5}$Fe$_2$O$_4$ oxides.

	Cu–based	Zn–based	Cd–based
MT (h)	G (nm)	G (nm)	G (nm)
	$\pm$ 0.05	$\pm$ 0.06	$\pm$ 0.05
0	60.40	33.53	26.75
2	45.42	29.45	22.09
4	26.34	24.78	20.08
12	14.43	19.29	12.65
18	11.91	15.98	10.82
24	10.82	14.61	10.31
30	10.09	13.72	9.22
40	10.36	12.36	9.57
50	10.21	11.87	9.89

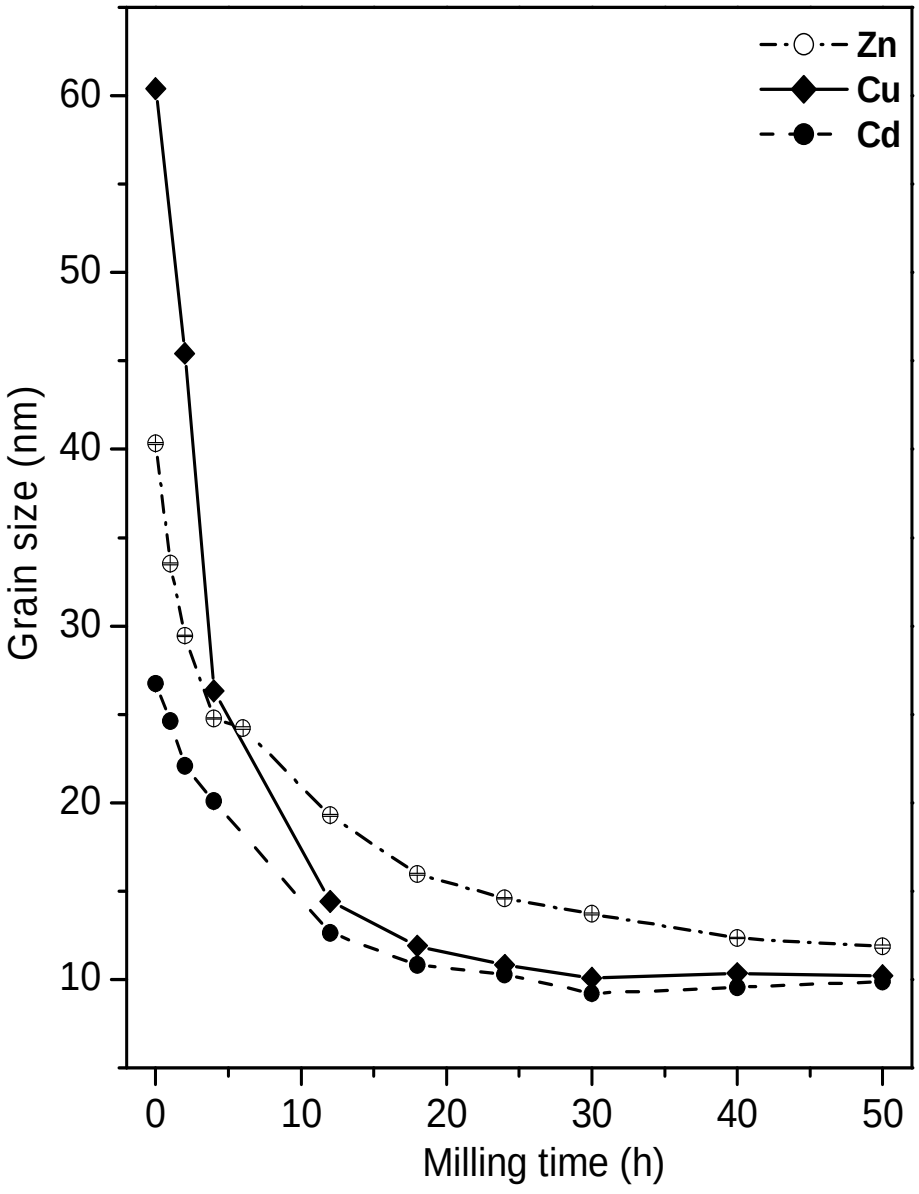

Figure 6.4: Variation of grain sizes for (Zn, Cd, Cu)$_{0.5}$Ni$_{0.5}$Fe$_2$O$_4$ with milling time.

Table 6.5: Variation of lattice constants (a) with milling time (MT) for (Cu, Zn, Cd)$_{0.5}$Ni$_{0.5}$Fe$_2$O$_4$ oxides.

	Cu–based	Zn–based	Cd–based
MT (h)	a ($\mathring{A}$)	a ($\mathring{A}$)	a ($\mathring{A}$)
	$\pm$ 0.01	$\pm$ 0.01	$\pm$ 0.01
0	8.34	8.39	8.51
2	8.35	8.40	8.53
4	8.38	8.40	8.53
12	8.37	8.40	8.52
18	8.38	8.40	8.52
24	8.35	8.40	8.52
30	8.39	8.40	8.49
40	8.38	8.40	8.49
50	8.37	8.38	8.43

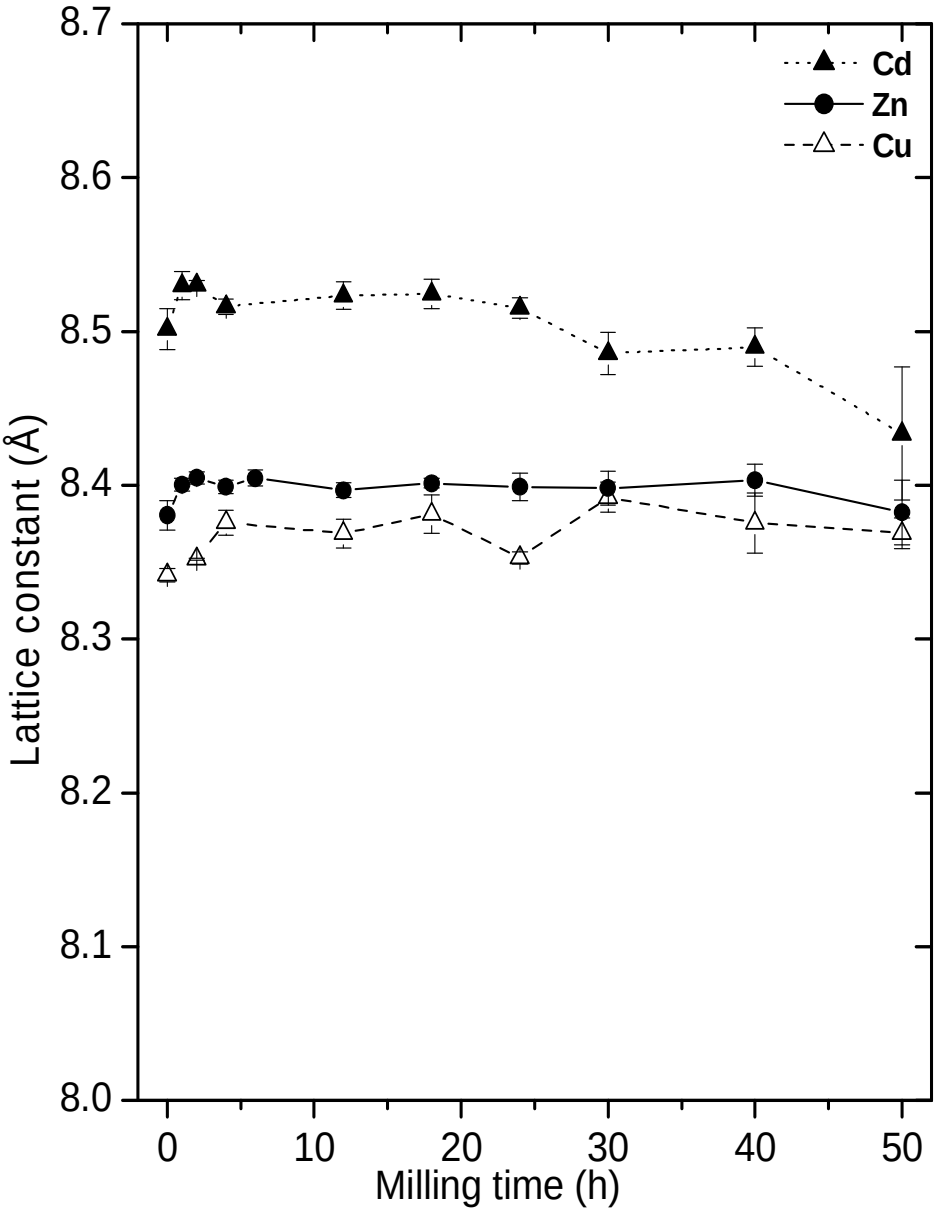

Figure 6.5: Variation of lattice parameters for (Zn, Cd, Cu)$_{0.5}$Ni$_{0.5}$Fe$_2$O$_4$ with milling time.

6.3 Mössbauer spectroscopy results

The temperature dependence of the Mössbauer spectra for (Zn, Cd)$_{0.5}$Ni$_{0.5}$Fe$_2$O$_4$ and Cu$_{0.5}$Ni$_{0.5}$Fe$_2$O$_4$ compounds are shown in Figures 6.6 and 6.7. The points are the experimental data and solid lines are the results of the computer fits using Recoil Mössbauer spectral analysis software. The spectra for the Cd– and Zn–based oxides are closely related. This is attributed to the similar electronic configurations between Zn ([Ar]4s^{2}3d^{10}) and Cd ([Kr]5s^{2}3d^{10}) ions. This behavior was observed in the preliminary work [4, 5] when the Mössbauer studies of (Cd, Zn)$_x$Co$_{1-x}$Fe$_{2-x}$Al$_x$O$_4$ and (Cd, Zn)$_x$Co$_{0.9}$Fe$_{1.7-x}$Ti$_{0.4}$O$_4$ (where $0 \leq x \leq 1.0$, x in steps of 0.1 or 0.05) were carried out. Well resolved magnetic splitting in the spectra for Cu–based oxide is observed. This shows antiferromagnetic character in this compound.

The magnetic phase changes from ordered to paramagnetic spin states with increasing temperature. This is evident from transformation of the six line Mössbauer spectra to quadrupole doublets. Between 79 K and 300 K the spectra were decomposed into two Zeeman sextets and two quadrupole doublets. Above the magnetic transition temperature spectra were fitted by two quadrupole doublets. Sextets and doublets respectively represent Fe ions in ferrimagnetic and paramagnetic states. The criterion used to assign sextets or doublet to tetrahedral A and octahedral B sites was based on the fitted results of isomer shifts deduced from Mössbauer spectra which are expected to be lower for A sites compared to B sites [31, 32] as discussed in chapter 5.

The data of hyperfine fields, isomer shifts and quadrupole splitting of the ^{57}Fe nuclei at the A and B sites are shown in Tables 6.7, 6.8 and 6.9. In Figure 6.8 we show the variation of hyperfine fields with sample measuring temperature. In the Zn– and Cd–based oxides the hyperfine fields at A site are higher than those at B site. This is in agreement with previous results [4, 5]. However for the Cu–based oxide, hyperfine fields at A site are lower. This agrees with results reported by Roumaih et al [75] for the Cu$_{1-x}$Ni$_x$FeMnO$_4$ oxides. The

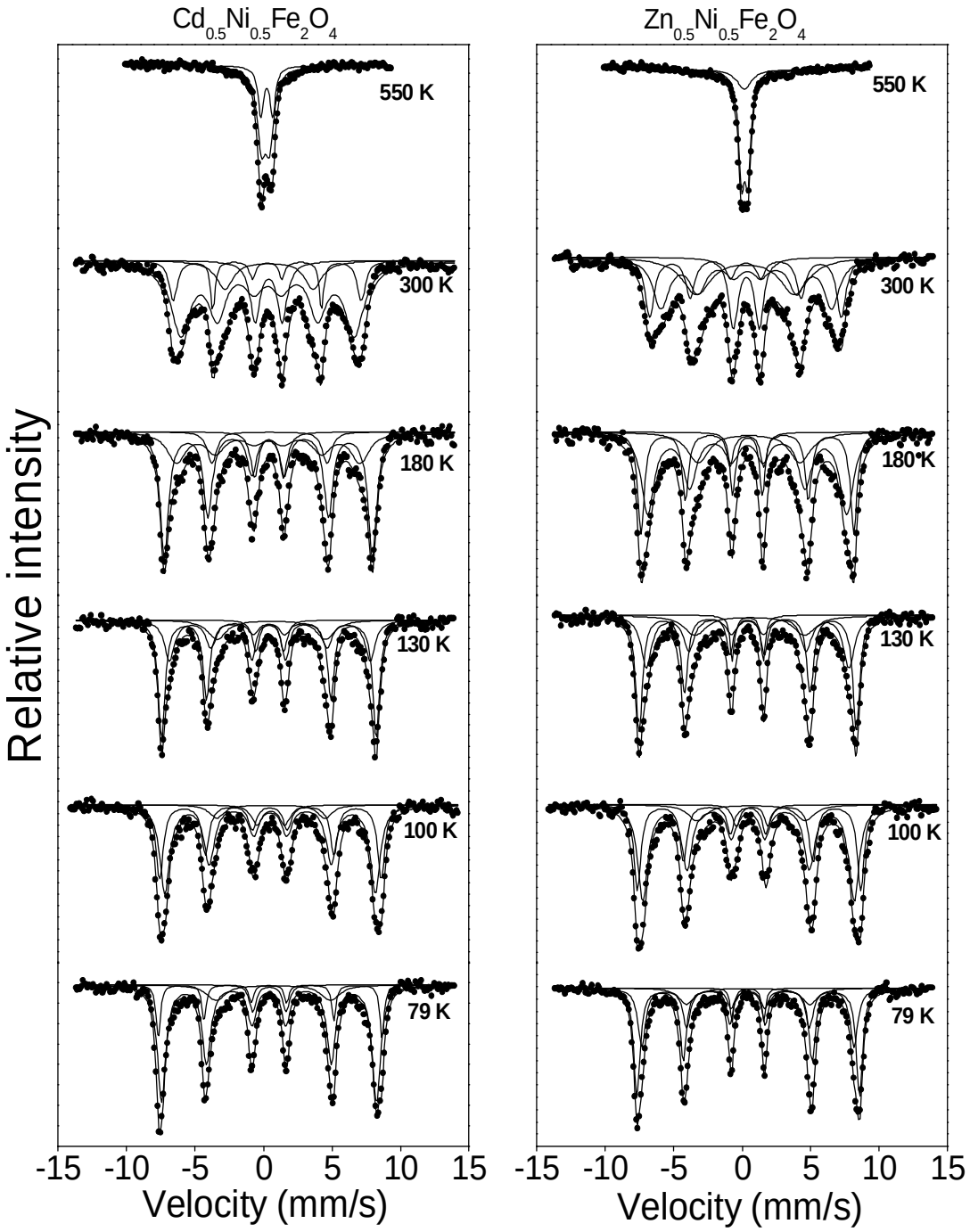

Figure 6.6: Variation of Mössbauer spectra for (Zn, Cd)$_{0.5}$Ni$_{0.5}$Fe$_2$O$_4$ with temperature.

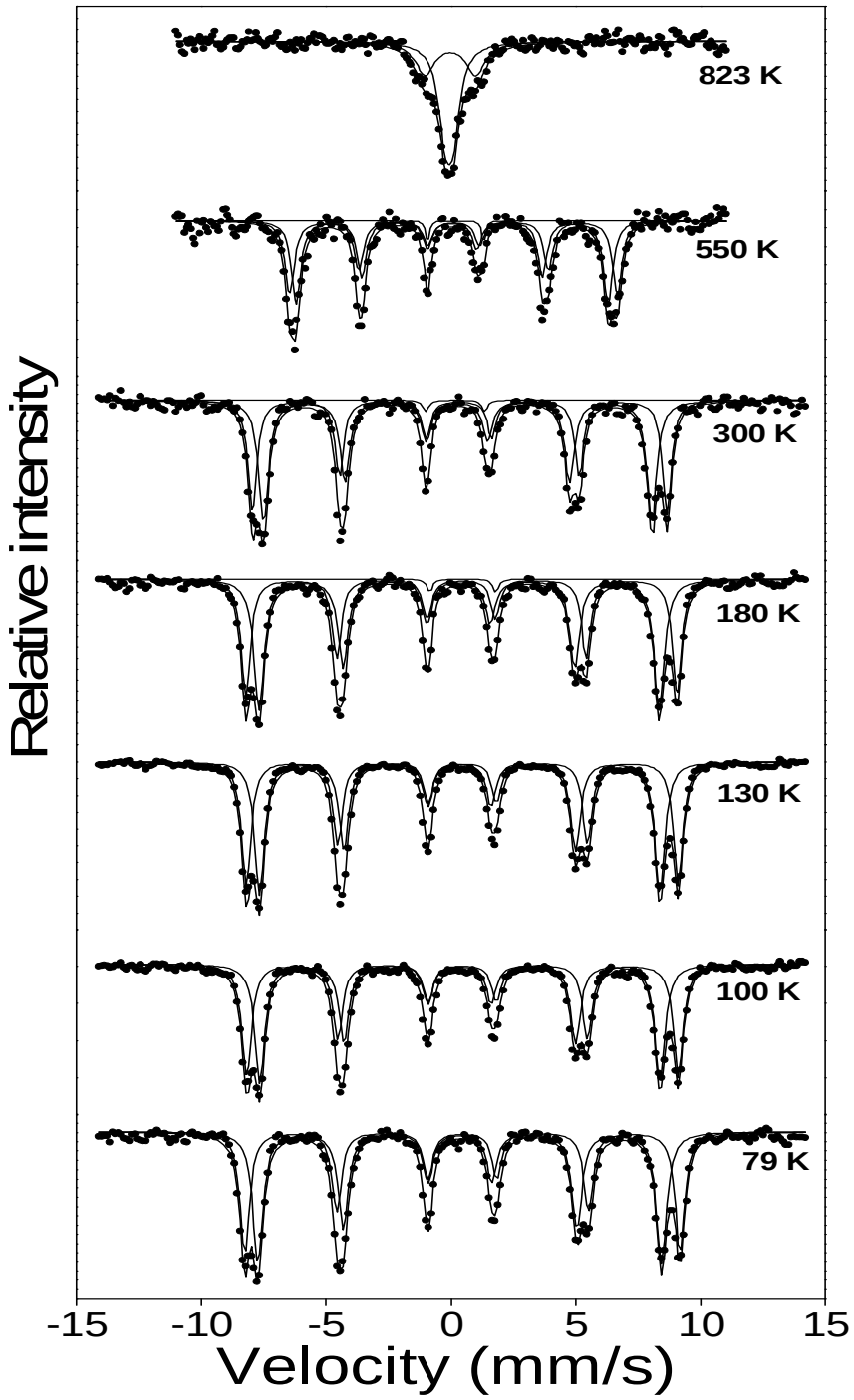

Figure 6.7: Variation of Mössbauer spectra for $Cu_{0.5}Ni_{0.5}Fe_2O_4$ with temperature.

Table 6.6: Variation of isomer shift (IS), quadrupole splitting (QS) and hyperfine fields (B_{hf}) of $Zn_{0.5}Ni_{0.5}Fe_2O_4$ with temperature.

	IS (mm/s)		QS (mm/s)		B_{hf} (kOe)	
T (K)	$(IS)_A$	$(IS)_B$	$(QS)_A$	$(QS)_B$	$(B_{hf})_A$	$(B_{hf})_B$
	± 0.02	± 0.04	± 0.02	±0.05	± 2	±4
79	0.43	0.43	0.01	-0.01	504	480
130	0.39	0.41	0.01	0.00	492	459
180	0.37	0.39	0.01	-0.01	482	451
230	0.34	0.43	0.02	-0.03	466	427
300	0.27	0.34	-0.01	-0.04	434	387
350	0.25	0.29	0.01	-0.05	420	365
400	0.18	0.26	-0.00	-0.02	394	326

Table 6.7: Variation of isomer shift (IS), quadrupole splitting (QS) and hyperfine fields (B_{hf}) of $Cd_{0.5}Ni_{0.5}Fe_2O_4$ with temperature.

	IS (mm/s)		QS (mm/s)		B_{hf} (kOe)	
T (K)	$(IS)_A$	$(IS)_B$	$(QS)_A$	$(QS)_B$	$(B_{hf})_A$	$(B_{hf})_B$
	± 0.02	± 0.05	±0.02	± 0.04	±2	± 4
79	0.40	0.44	0.04	-0.03	505	485
130	0.38	0.42	0.00	0.03	487	455
180	0.36	0.37	0.02	-0.05	470	414
230	0.34	0.34	0.00	-0.00	457	417
300	0.28	0.30	0.00	0.00	426	393
350	0.22	0.26	0.01	0.02	411	373
400	0.19	0.20	0.03	0.04	385	343

Table 6.8: Variation of isomer shift (IS), quadrupole splitting (QS) and hyperfine fields (B_{hf}) of $Cu_{0.5}Ni_{0.5}Fe_2O_4$ with temperature.

	IS (mm/s)		QS (mm/s)		B_{hf} (kOe)	
T (K)	$(IS)_A$	$(IS)_B$	$(QS)_A$	$(QS)_B$	$(B_{hf})_A$	$(B_{hf})_B$
	± 0.01	± 0.01	±0.01	±0.01	± 1	± 1
79	0.36	0.46	-0.01	-0.01	501	540
100	0.35	0.46	0.00	-0.00	497	536
130	0.35	0.46	0.00	-0.01	497	536
150	0.33	0.44	0.00	-0.00	498	537
180	0.32	0.42	-0.01	-0.00	497	535
200	0.31	0.41	0.00	-0.00	494	533
300	0.26	0.34	0.01	0.01	482	515
400	0.21	0.29	-0.01	-0.01	462	490
500	0.10	0.15	-0.00	-0.00	402	425
550	0.05	0.11	0.00	-0.00	387	407
600	0.04	0.09	0.01	0.00	365	384

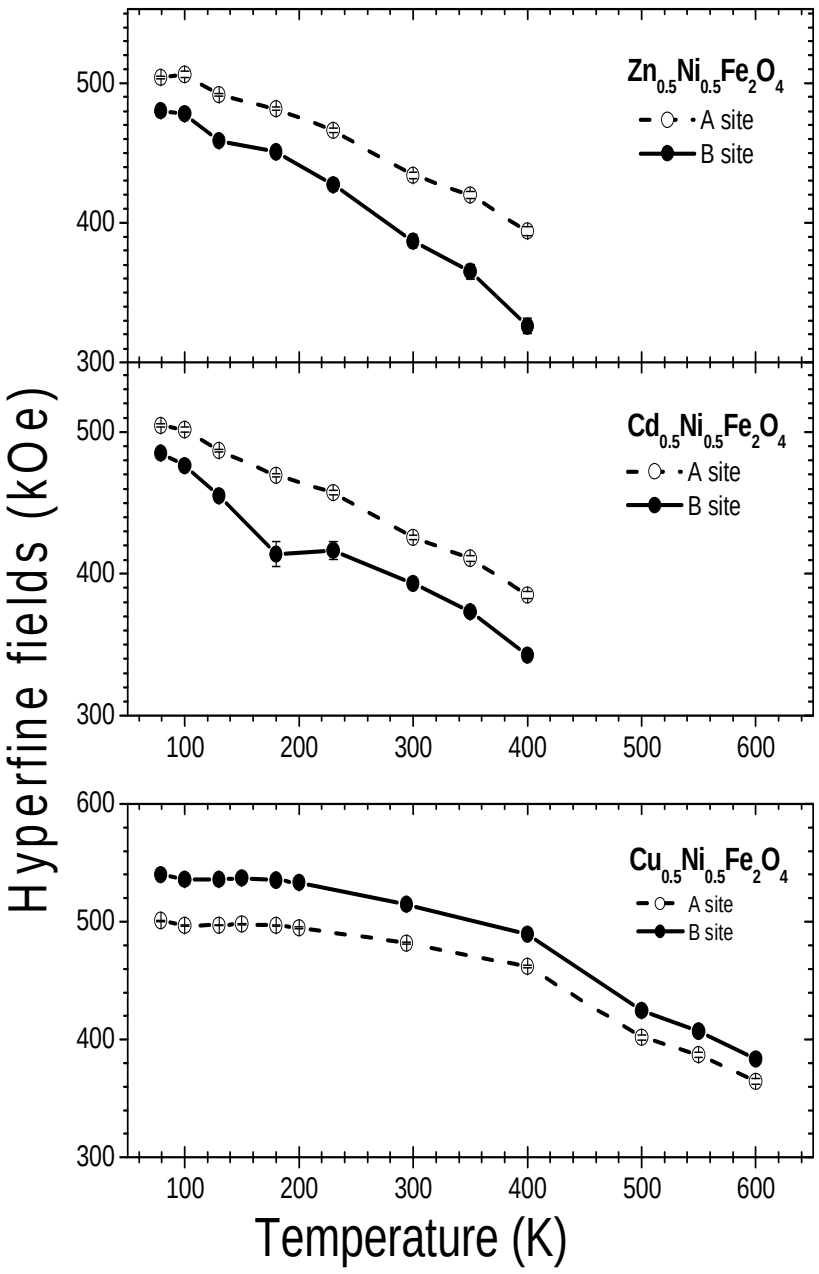

Figure 6.8: Hyperfine fields with temperature for (Zn, Cd, Cu)$_{0.5}$Ni$_{0.5}$Fe$_2$O$_4$.

internal magnetic field is associated with the degree of covalent bonding in the A or B site cation sublattices. The lower hyperfine field on A site indicates high degree of covalent bonding [75]. The difference between magnitudes of hyperfine fields can be explained in terms of differences in electronic configurations between Zn, Cd and Cu atoms. Zn and Cd atoms are known to have preference for A sites [7, 31, 79] and have full outer s orbitals. On the other hand Cu atoms have preference for B sites [6] and have an unpaired electron in the outer shell. In the Cu–based oxide the magnetic moments may also interact through the unpaired electrons by RKKY interactions in addition to superexchange interactions. This results in stronger magnetic coupling. The systematic decrease in hyperfine fields with temperature is attributed to the weakening of the magnetic coupling resulting in a paramagnetic state at higher temperature. The hyperfine fields for Zn–based and Cd–based samples decrease more rapidly with increase in temperature compared to those of the Cu–based ferrite. This further suggests stronger magnetic interaction between spins in the Cu–based oxide. For the Sn–doped Cr_2O_3 and $(FeCr)_2O_3$ oxides the hyperfine fields were found to vary with temperature according to the equation [73]

$$B_{hf}(T) = B_{hf}(0)\left[1 - \frac{T}{T_C}\right]^{\beta_1} \tag{6.3.1}$$

as observed in chapter 5. The log form of equation (6.3.1) is given by equation (5.3.2). We have plotted $\ln B_{hf}(T)$ versus $\ln\left[1 - T/T_C\right]$ for A and B sites for the Cu–, Zn–, and Cd–based oxides in Figures 6.9–6.11. The plots were fitted with linear fits in order to test the validity of equation (6.3.1). The values of β_1 and β_2 from equations (5.3.3) and (5.3.4) respectively deduced from the fits are shown in Table 6.9. The correlation coefficients (R^2) indicating the quality of the linear fits are also shown in Table 6.9. For the Cu–based sample the graph of $\ln B_{hf}(T)$ versus $\ln\left[1 - T/T_C\right]$ appears to be non–linear for both A and B sites (see Figure 6.9). The hyperfine fields therefore do not vary according to equation (6.3.1). For the Zn–based oxide a linear fit could be fitted over the entire temperature range. Both A and B site hyperfine fields therefore decrease

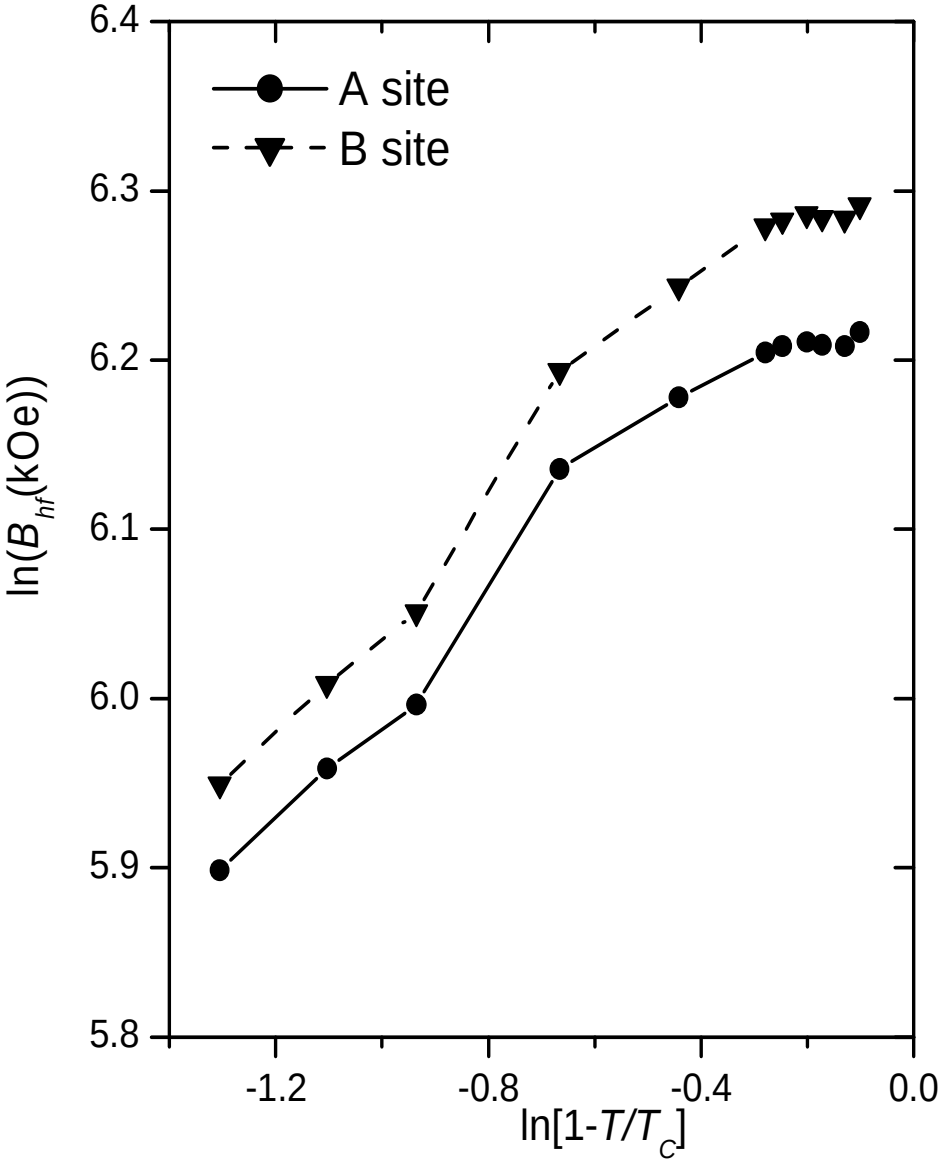

Figure 6.9: A graph of $\ln B_{hf}(T)$ versus $\ln[1 - T/T_C]$ for the $Cu_{0.5}Ni_{0.5}Fe_2O_4$ oxide.

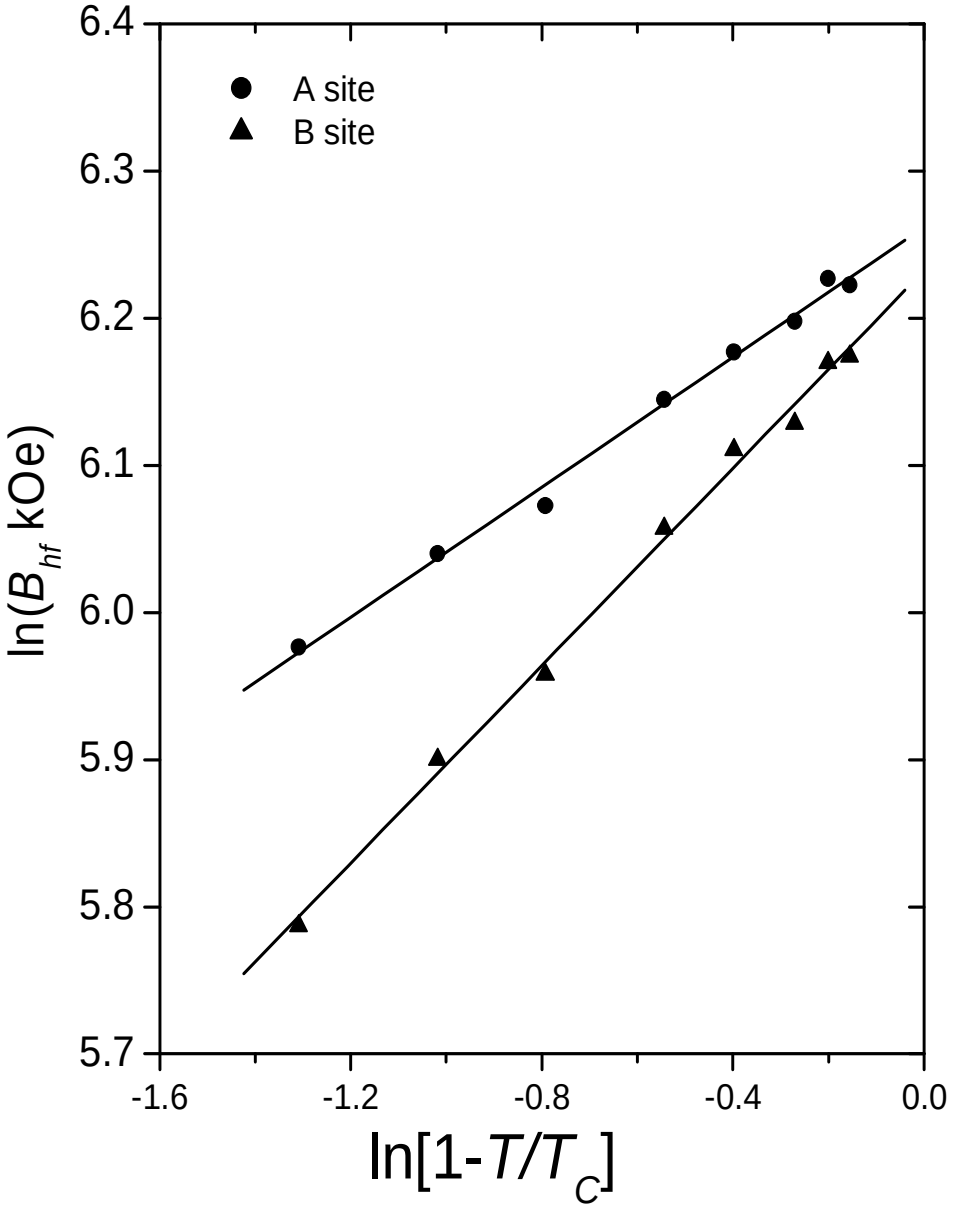

Figure 6.10: A graph of $\ln B_{hf}(T))$ versus $\ln[1 - T/T_C]$ for the $Zn_{0.5}Ni_{0.5}Fe_2O_4$ oxide.

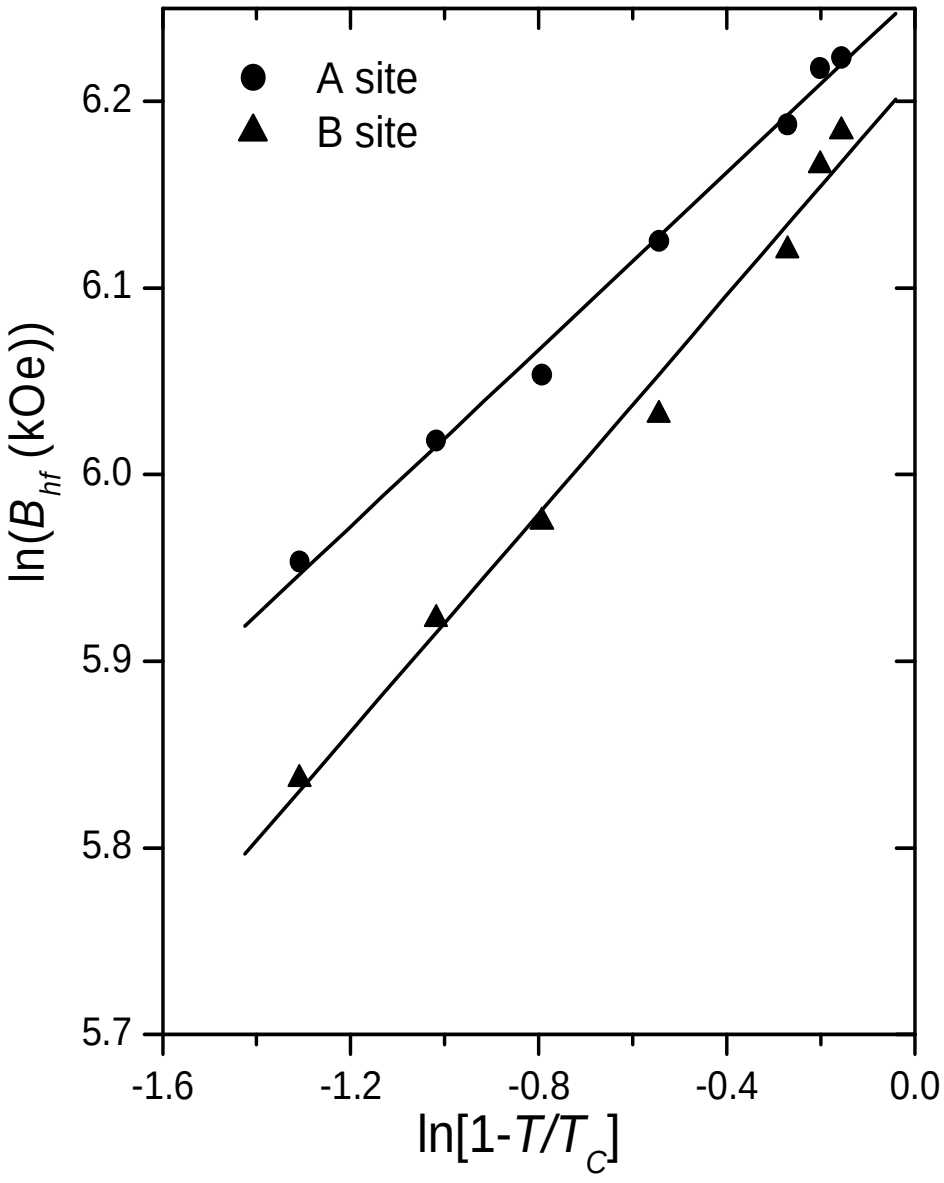

Figure 6.11: A graph of $\ln B_{hf}(T)$ versus $\ln[1 - T/T_C]$ for the $Cd_{0.5}Ni_{0.5}Fe_2O_4$ oxide.

Table 6.9: β_1 and β_2 values obtained from a graph of $\ln B_{hf}(T)$ versus $\ln[1 - T/T_C]$ and $\ln B_{hf}(T)$ versus $\ln\left[1 - (T/T_C)^2\right]$ for the (Zn, Cd, Cu)$_{0.5}$Ni$_{0.5}$Fe$_2$O$_4$ oxides.

	R^2		β_i (i = 1, 2)	
	A	B	A	B
			± 0.02	± 0.03
Cu– (β_2)	0.993	0.994	0.44	0.48
Zn– (β_1)	0.997	0.998	0.22	0.34
Zn– (β_2)	0.988	0.994	0.34	0.52
Cd– (β_1)	0.996	0.972	0.24	0.28
Cd– (β_2)	0.982	0.950	0.36	0.43

with temperature according to equation (6.3.1) where $\beta_1 = 0.22 \pm 0.01$ (A site) and $\beta_1 = 0.34 \pm 0.01$ (B site). For the Cd–based oxide $\ln B_{hf}(T)$ also varies linearly with $\ln[1 - T/T_C]$ for A site.

On the basis of the Stoner theory the hyperfine fields vary with temperature according to equation (5.3.3). We have plotted a graph of $\ln B_{hf}(T)$ versus $\ln\left[1 - (T/T_C)^2\right]$ in Figures 6.12, 6.13 and 6.14 in order to test the validity of equation (5.3.3) in ferrites. The β_2 values deduced from these graphs are also shown in Table 6.9. For the Cu–based oxide, hyperfine fields decrease with increase in temperature according to equation (5.3.3) where β_2 are 0.44 ± 0.02 and 0.48 ± 0.02 for A and B sites respectively. These constants are close to β_2 = 0.5 in equation (6.3.2) and $\beta_2 = 0.46$ found for the ErFe$_{12-x}$Nb$_x$ compounds by Wang et al [74]. The (Zn, Cd)$_{0.5}$Ni$_{0.5}$Fe$_2$O$_4$ also obeys equation (5.3.3). The R^2 values in Table 6.9 for linear fits for $\ln B_{hf}(T)$ versus $\ln[1 - T/T_C]$ are higher than those for linear fits in of $\ln B_{hf}(T)$) versus $\ln\left[1 - (T/T_C)^2\right]$. This shows that the temperature dependence of hyperfine fields for the Zn– and Cd–based oxides are better fitted by equation (6.3.1) than by (5.3.3).

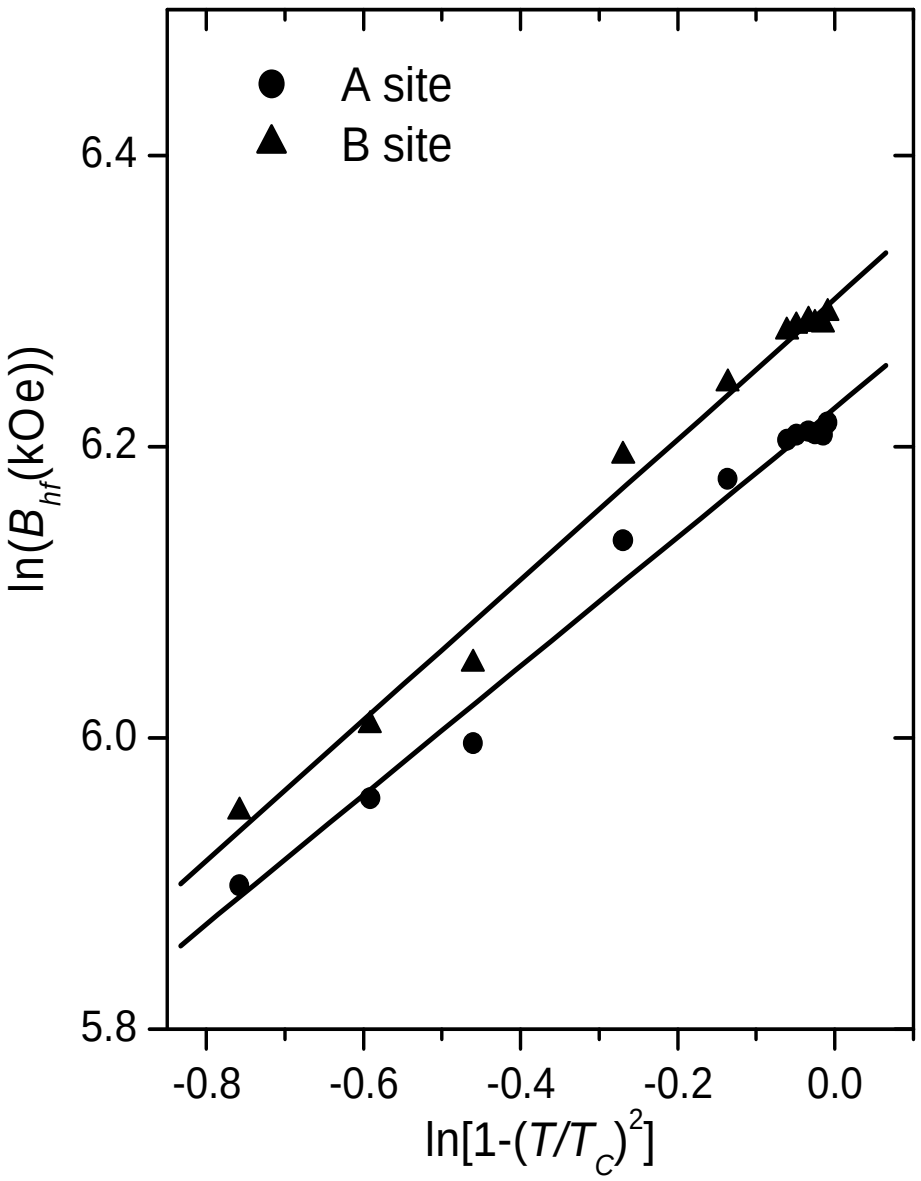

Figure 6.12: A graph of $\ln B_{hf}(T)$ versus $\ln\left[1-(T/T_C)^2\right]$ for the $Cu_{0.5}Ni_{0.5}Fe_2O_4$ oxide.

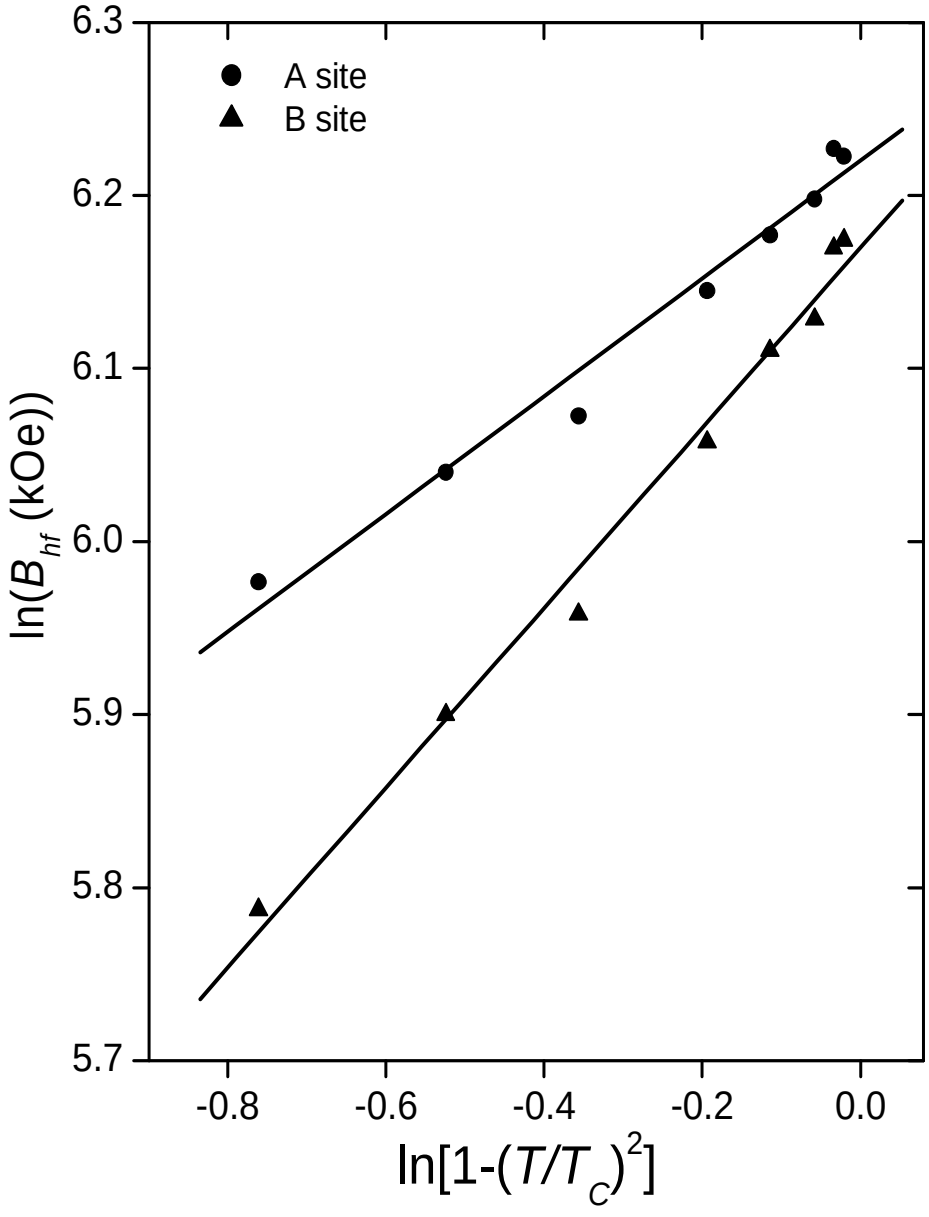

Figure 6.13: A graph of $\ln B_{hf}(T)$ versus $\ln\left[1-(T/T_C)^2\right]$ for the $Zn_{0.5}Ni_{0.5}Fe_2O_4$ oxide.

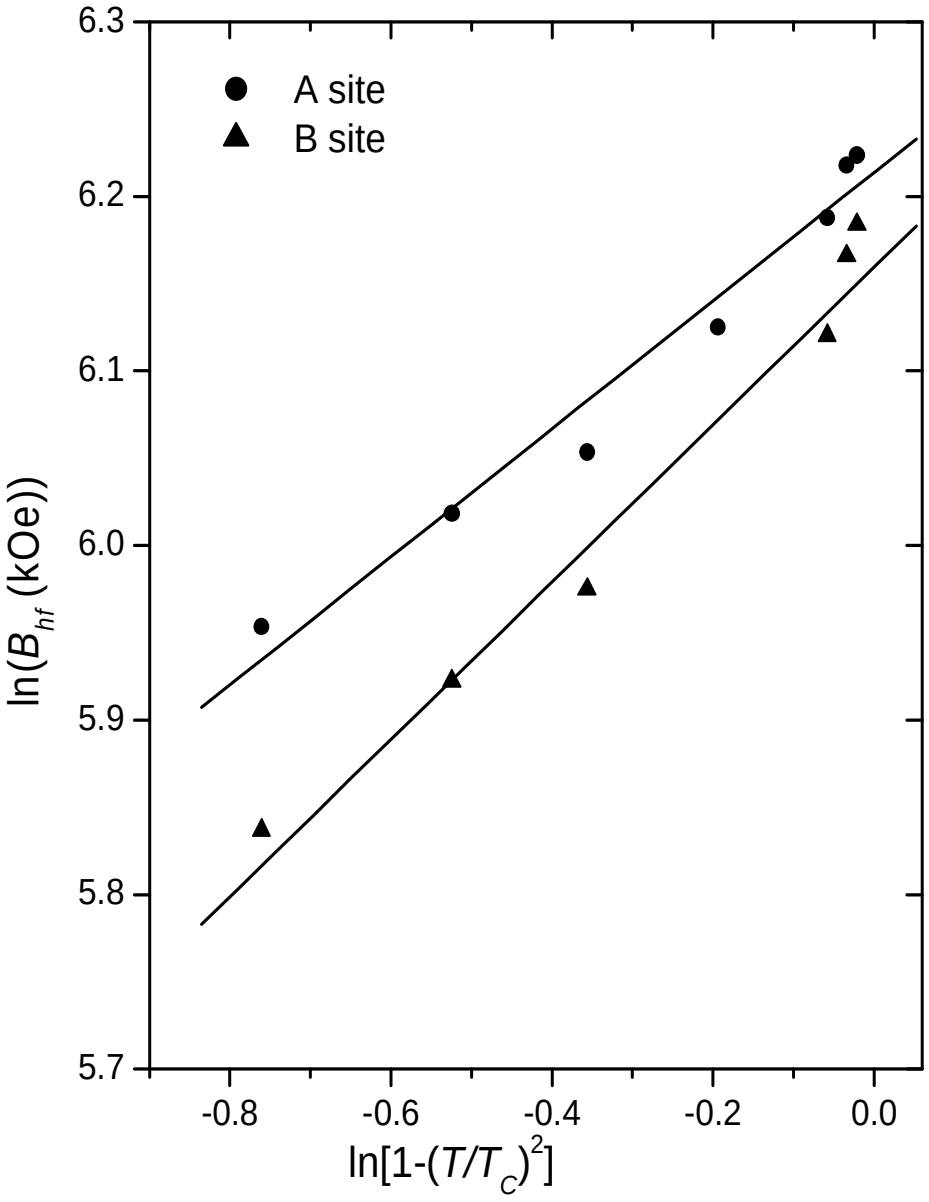

Figure 6.14: A graph of $\ln B_{hf}(T))$ versus $\ln\left[1-(T/T_C)^2\right]$ for the $Cd_{0.5}Ni_{0.5}Fe_2O_4$ oxide.

In Figure 6.15 we show the variation of Mössbauer spectrum shifts with temperature. The shift of the centroid of Mössbauer spectra from zero velocity consists of isomer shift and second–order Doppler shift as discussed in chapter 5. A decrease in the centroid shift with temperature observed is due to the second order Doppler shift.

The variations of Mössbauer spectra with milling time are shown in Figures 6.16 and 6.17. The increase in the central doublet with milling time (reduction in grain size) indicates the presence of paramagnetic phase, which increases with milling. In the nanometer scale, the samples have both ferrimagnetic and paramagnetic components. The paramagnetic component can be explained on the basis of transformation of multidomain particles in bulk samples to single domain particles in fine powders and oxygen vacancies created by milling mechanism [35]. Distances between single domains will tend to be larger compared to multi–domains. This results in weaker superexchange interactions between magnetic moments inducing disordered spin orientations. Oxygen vacancies also result in broken superexchange paths between spins on A and those on B sites. This weakens the intersublattice superexchange interactions and induces the paramagnetic state.

The magnetic transition temperatures (T_C) shown in Table 6.10 were obtained using the zero velocity Mössbauer technique. The critical point is taken at the discontinuity of the rapid drop in the transmitted intensity. The typical variations of transmitted intensities with temperature are shown in Figure 6.19. The Curie points for the bulk (Zn, Cd)$_{0.5}$Ni$_{0.5}$Fe$_2$O$_4$ oxides were found to be similar.

This reflects similar magnetic interactions between magnetic moments in Cd– and Zn–based compounds. This behavior is attributed to the similar electronic configuration between the Zn and Cd ions. It also shows that the size difference between Cd and Zn weakly affects the magnetic coupling between the magnetic moments. The magnetic transition temperature for the Cu$_{0.5}$Ni$_{0.5}$Fe$_2$O$_4$ oxide is significantly higher than for a Cd– or Zn–based com-

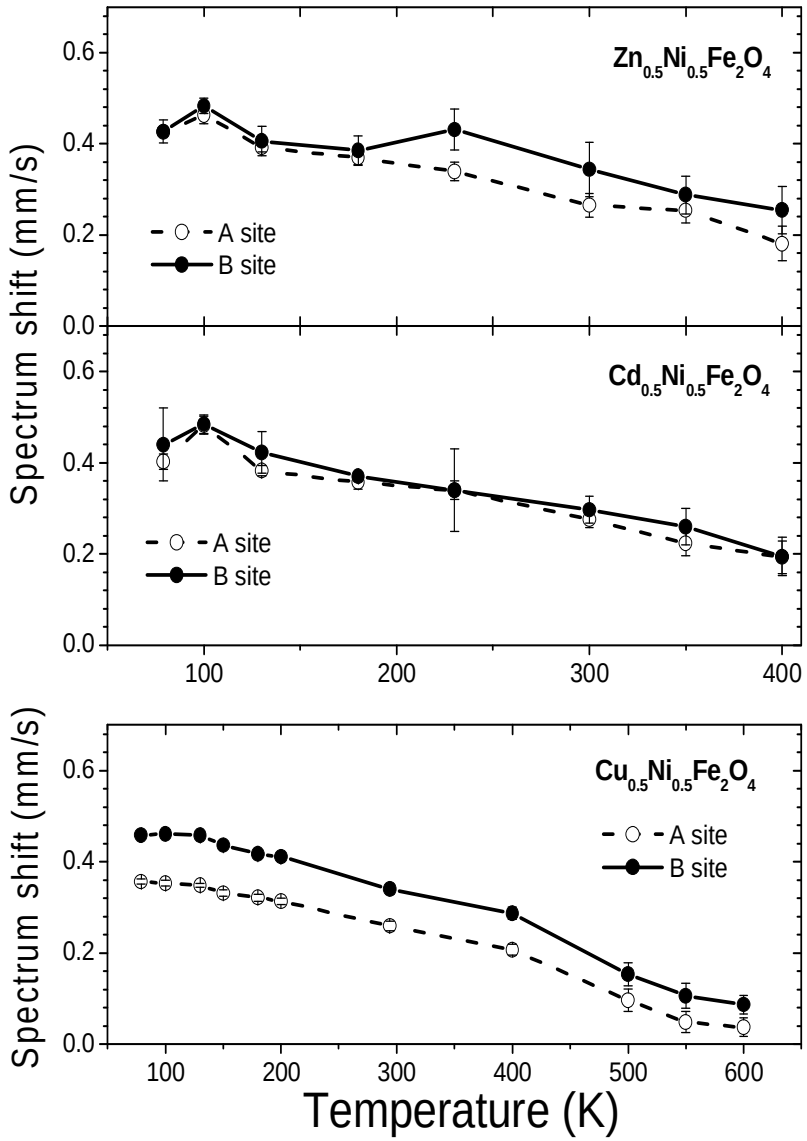

Figure 6.15: Isomer shift with temperature for (Zn, Cd, Cu)$_{0.5}$Ni$_{0.5}$Fe$_2$O$_4$ oxides.

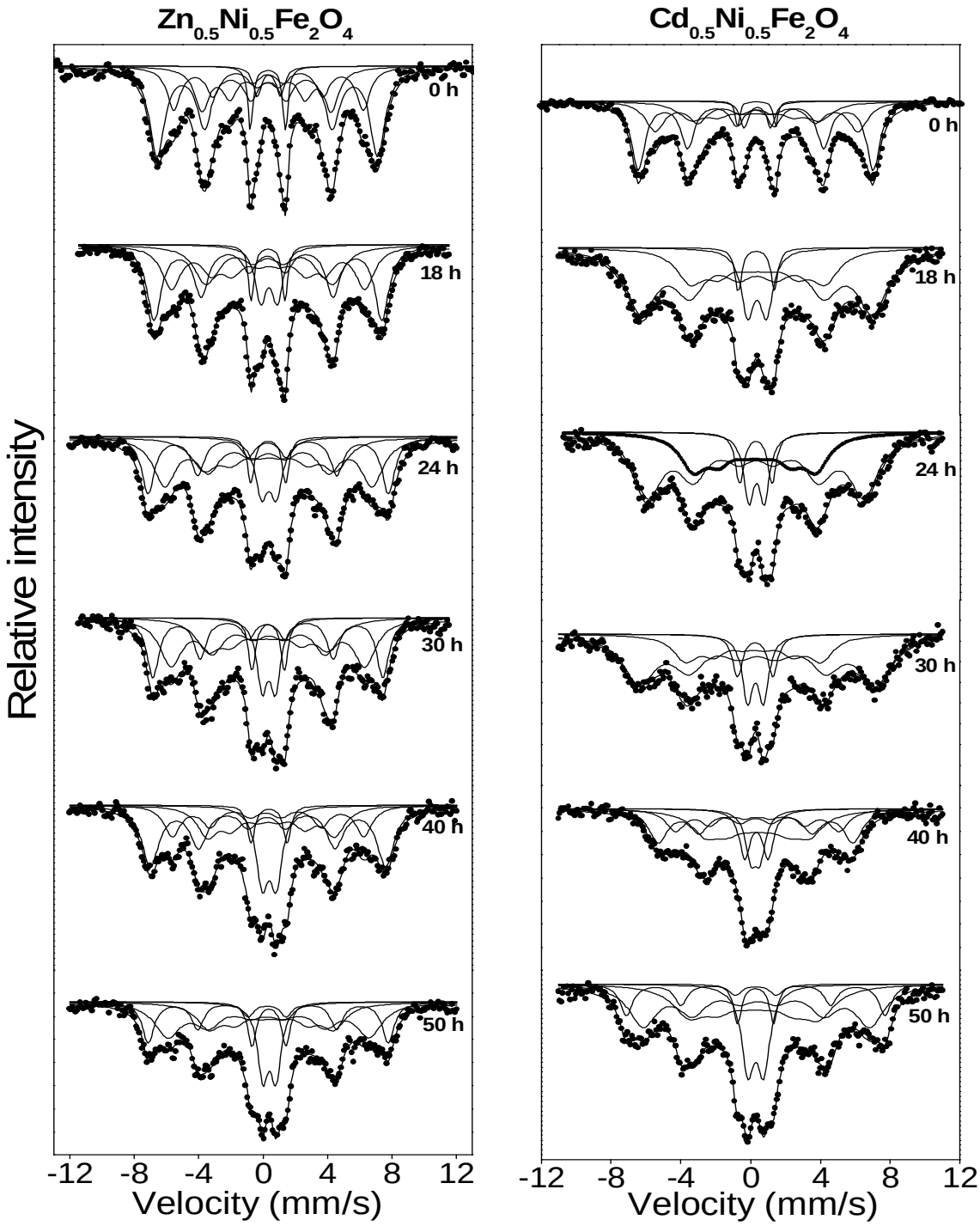

Figure 6.16: Variation of Mössbauer spectra for (Zn, Cd)$_{0.5}$Ni$_{0.5}$Fe$_2$O$_4$ with milling time.

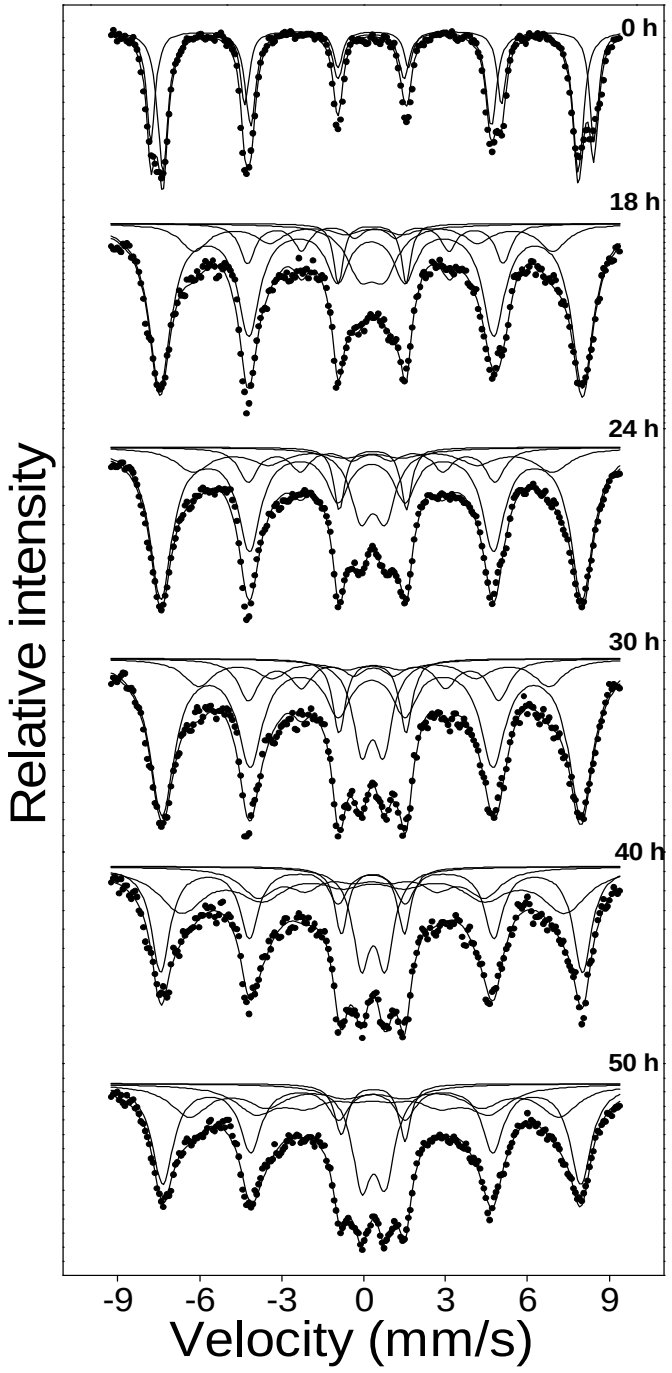

Figure 6.17: Variation of Mössbauer spectra for $Cu_{0.5}Ni_{0.5}Fe_2O_4$ with milling time.

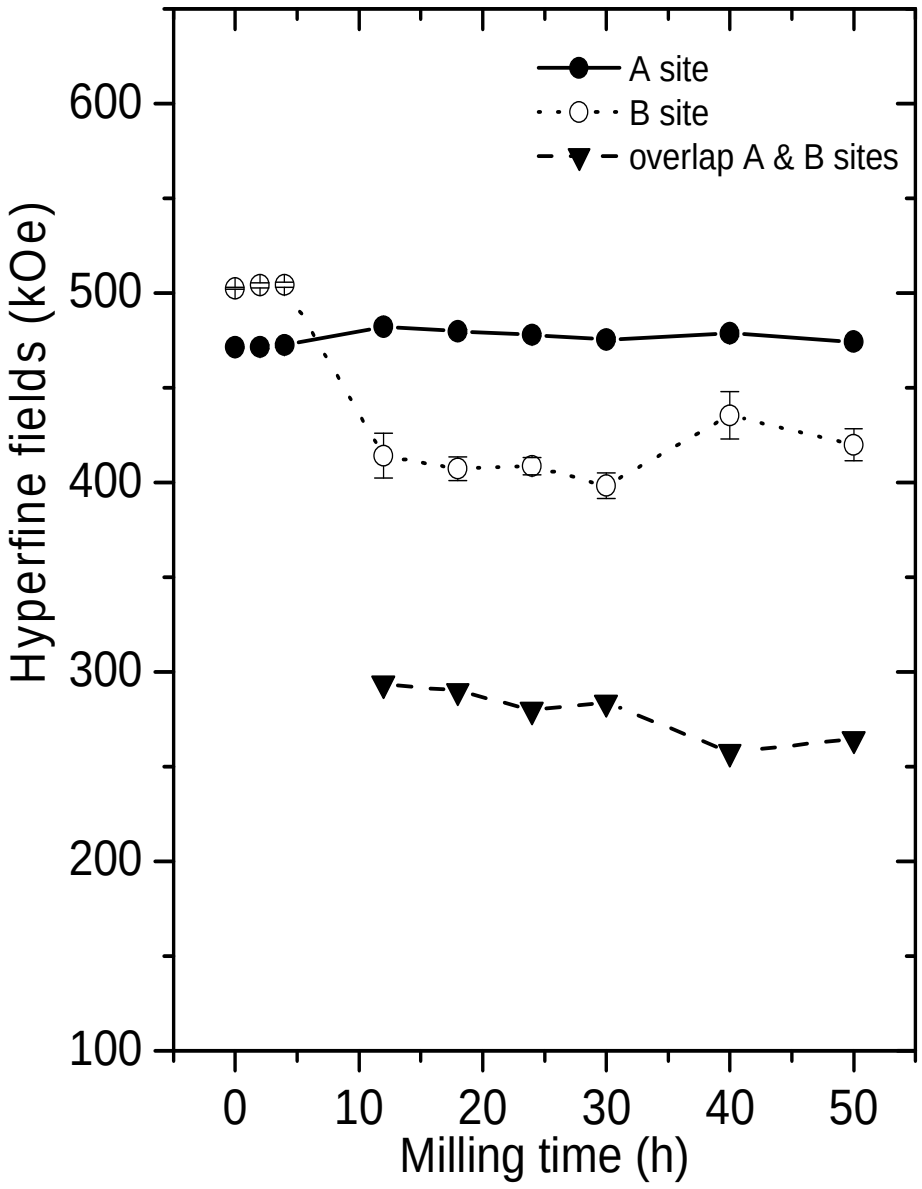

Figure 6.18: Variation of hyperfine fields for $Cu_{0.5}Ni_{0.5}Fe_2O_4$ with milling time.

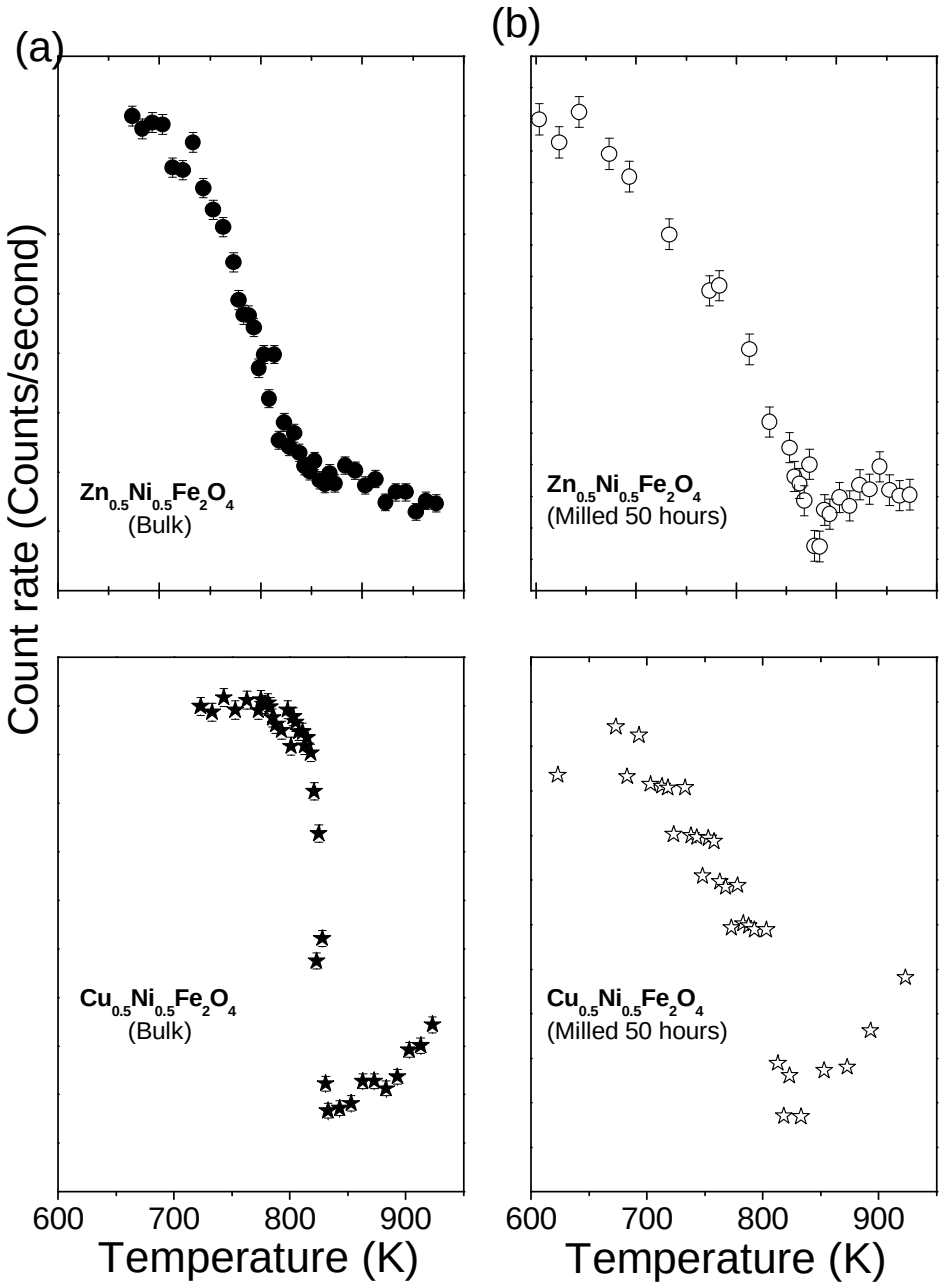

Figure 6.19: Zero–velocity transmission intensities as a function of temperature for (a) bulk and (b) nanosized (milled for 50 hours) (Zn, Cu)$_{0.5}$Ni$_{0.5}$Fe$_2$O$_4$ oxides.

Table 6.10: Magnetic transition temperatures.

	Bulk	Nanosize
Oxide	T_C (K)	T_C (K)
	± 3	± 3
$Cu_{0.5}Ni_{0.5}Fe_2O_4$	828	823
$Zn_{0.5}Ni_{0.5}Fe_2O_4$	548	583
$Cd_{0.5}Ni_{0.5}Fe_2O_4$	548	478

pounds. This reveals stronger magnetic coupling between the magnetic moments in the Cu–based oxide. The value of the magnetic transition temperature for the Cu–based oxide is similar to 820 ± 2 K reported by Woo et al [9] for the compound with the same nominal composition.

The Curie point for the Cu–based compound is weakly affected by decreasing grain size. This further reveals strong magnetic interactions in this compound. An anomalous increase in Curie temperature for the $Zn_{0.5}Ni_{0.5}Fe_2O_4$ oxide with decreasing grain size is observed. This can be explained by migration of Zn ions from A to B sites with reduction in grain size [44, 46, 84]. In bulk ferrites Zn ions are distributed amongst the A sites only where their 4s,p and 5s,p electrons respectively form covalent bonds with six 2p electrons of oxygen ions [7, 31, 79]. Since Zn is nonmagnetic, there are no superexchange interactions between magnetic moments in the A sublattice (A–O–A) or between the A and B sites moments (A–O–B). Superexchange interactions are only present on the B sublattice (B–O–B) where there are magnetic atoms (Ni and Fe). Hence a small amount of heat energy would be required to thermally agitate the spins into paramagnetic phase. This shows as a lower value of Curie point for the bulk samples of $(Zn, Cd)_{0.5}Ni_{0.5}Fe_2O_4$. If Zn ions migrate to B sites (some of magnetic Fe ions migrate to A sites) with milling a strong inter–sublattice

superexchange interactions (A–O–B) can be induced. This may be responsible for the observed increase in T_C due to milling for the $Zn_{0.5}Ni_{0.5}Fe_2O_4$ sample.

6.4 Magnetization results

The magnetization measurements of the compounds at about 300 K were performed by using a Lakeshore vibrating sample magnetometer. The isothermal magnetization curves are shown in Figure 6.20. A general decrease in saturation magnetization with reduction in grain size is observed. This is attributed to the weakening of the magnetic coupling between ions. The reduction in saturation magnetization can also be explained by structural distortions in the surface of fine powders compared to that of bulk compounds [85]. The Zn–based sample has the highest and the Cu–based oxide the lowest saturation magnetization. This behavior seems to be associated with site preferences for Cd, Zn and Cu atoms in a spinel structure. Both Zn and Cd atoms have preferences for A sites, while Cu has strong preference for B site as observed in chapter 1. The central doublet indicates a paramagnetic state which is more prominent in the Cu–based sample. This is in agreement with the low saturation magnetization in this oxide.

The values of saturation magnetization and coercive fields are shown in Table 6.11. The bulk oxides have small coercive fields. In Figure 6.21 we show the variation of coercive fields with milling time. The coercive fields H_C increase rapidly to a maximum at a critical grain size and then decrease with further reduction in grain size. This behavior is attributed to transformation from multidomain to single domain particles. Similar trends have been reported for the $CoFe_2O_4$ oxide [40, 41] and $CoAl_xFe_{2-x}O_4$ [69] compounds. The decrease in H_C beyond a critical grain size is more evident for Cu– and Cd–based oxides. For the Cu–based oxide a sharp increase in coercivity to a maximum value about 0.75 kOe occurs. This is compatible with a sharp decrease in grain size due to milling observed in Figure 6.4. The coercive field then decreases to

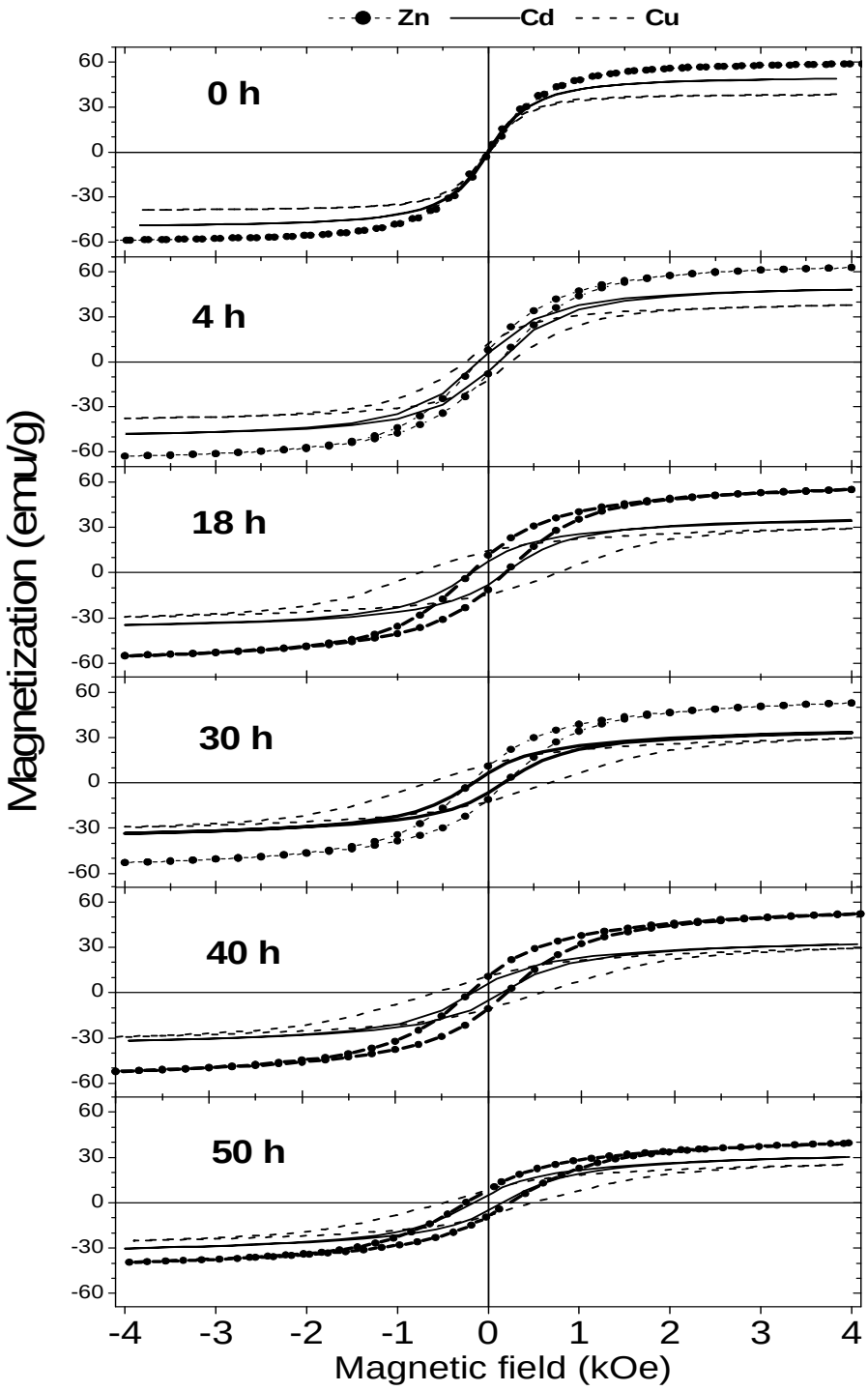

Figure 6.20: Variation of hysteresis curves for (Zn, Cu, Cd)$_{0.5}$Ni$_{0.5}$Fe$_2$O$_4$ with milling time.

Table 6.11: Variation of coercive field (H_c) and saturation magnetization (M_S) with milling time (MT) for (Zn, Cd, Cu)$_{0.5}$Ni$_{0.5}$Fe$_2$O$_4$ oxides.

	Zn		Cd		Cu	
MT (h)	H_C (kOe)	M_S (emu/g)	H_C (kOe)	M_S (emu/g)	H_C (kOe)	M_S (emu/g)
	± 0.01	± 0.5	± 0.01	±0.5	±0.02	±0.5
0	0.02	59.0	0.01	49.3	0.02	38.7
4	0.12	63.7	0.11	50.5	0.26	36.6
12	0.20	57.9	0.21	43.3	0.69	29.0
18	0.19	56.3	0.19	37.3	0.75	30.5
24	0.23	49.1	0.19	38.2	0.74	27.9
30	0.21	54.2	0.16	37.1	0.65	30.7
40	0.20	53.8	0.16	36.5	0.58	30.7
50	0.24	39.2	0.15	31.3	0.49	26.8

about 0.5 kOe after milling for 50 hours. For the Cd–based oxide the coercive field also attains a maximum value after milling the sample for about 12 hours and then slowly decreases with further milling. The variation in coercive fields with milling time can be explained on the basis of a crossover from multidomain to single domain behavior at a critical grain size. In the multidomain region the coercive field is expected to increase with reduction in grain size according to the equation [69]

$$H_C = a_m + \frac{b_m}{G} \tag{6.4.1}$$

where a_m and b_m are constants. In Figures 6.22 and 6.23 we have plotted H_C with $1/G$ for the oxides in order to determine values of a_m and b_m. On fitting a linear fit to the data we obtained the constants shown in Table 6.12.

The constants a_m and b_m obtained for the Cu–based oxide (see Table 6.12) are similar to a_m = -0.23 ± 0.06 kOe and b_m = 15 ± 1 nm kOe obtained for the

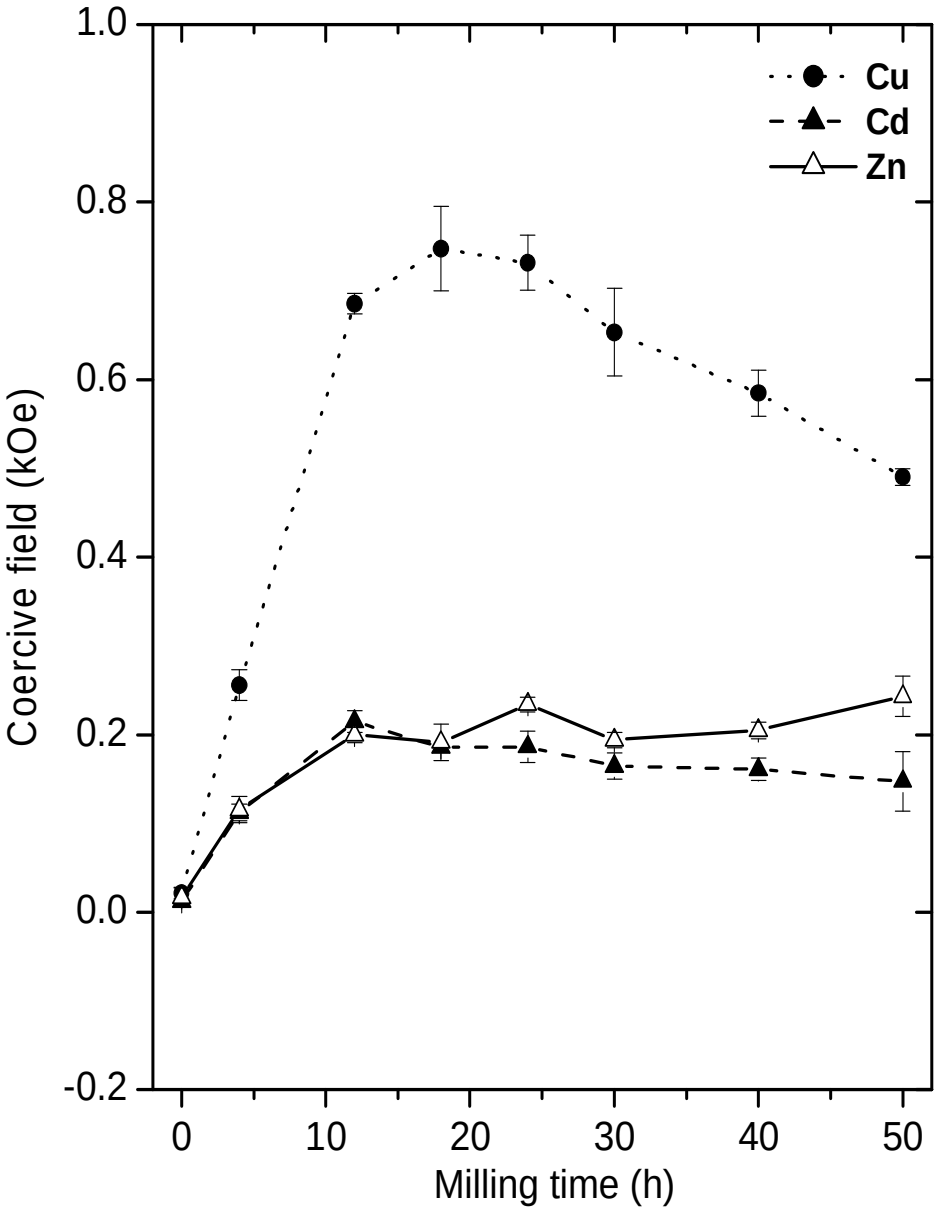

Figure 6.21: Variation of coercive fields for (Zn, Cd, Cu)$_{0.5}$Ni$_{0.5}$Fe$_2$O$_4$ with milling time.

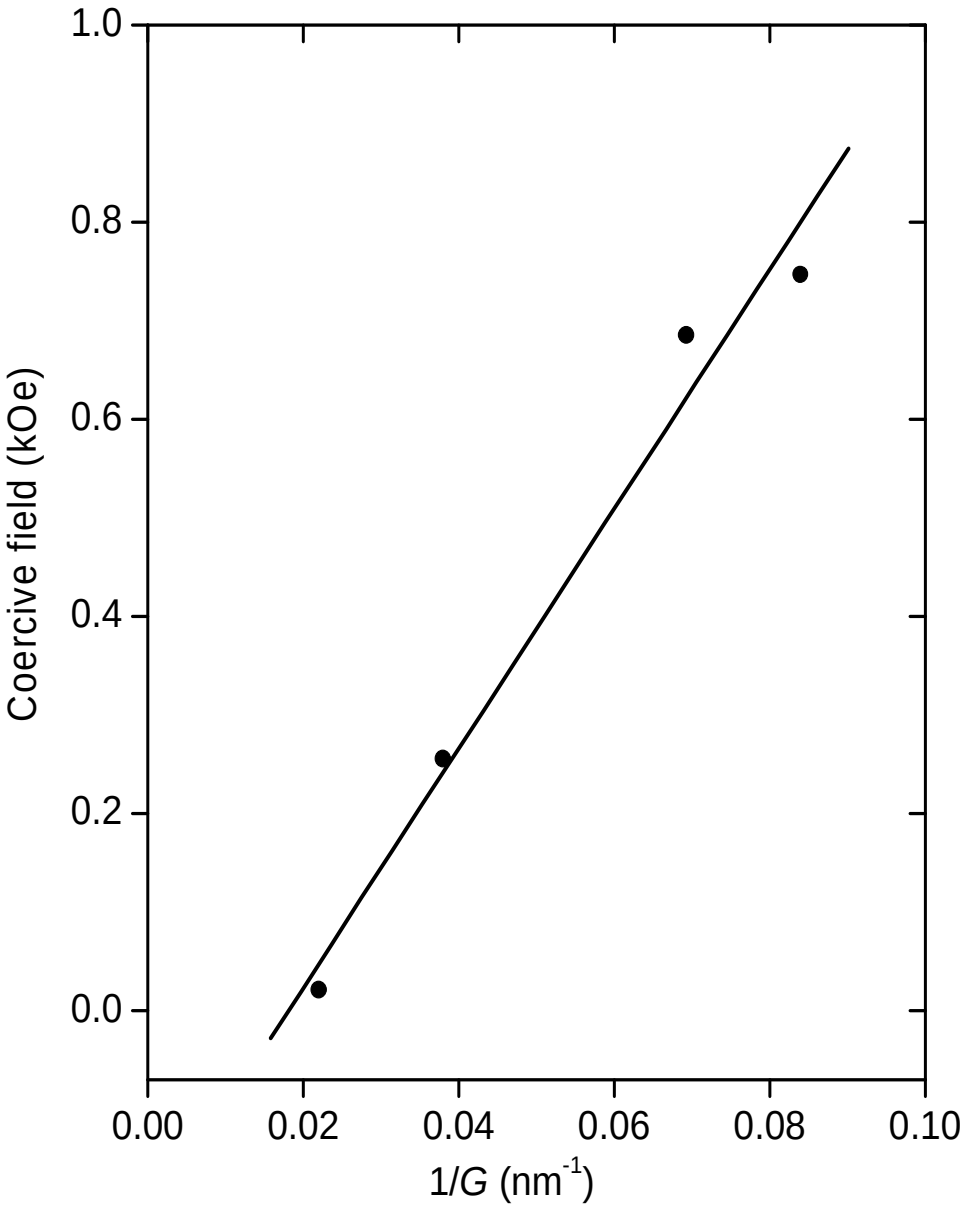

Figure 6.22: Variation of coercive fields for $Cu_{0.5}Ni_{0.5}Fe_2O_4$ with $1/G$.

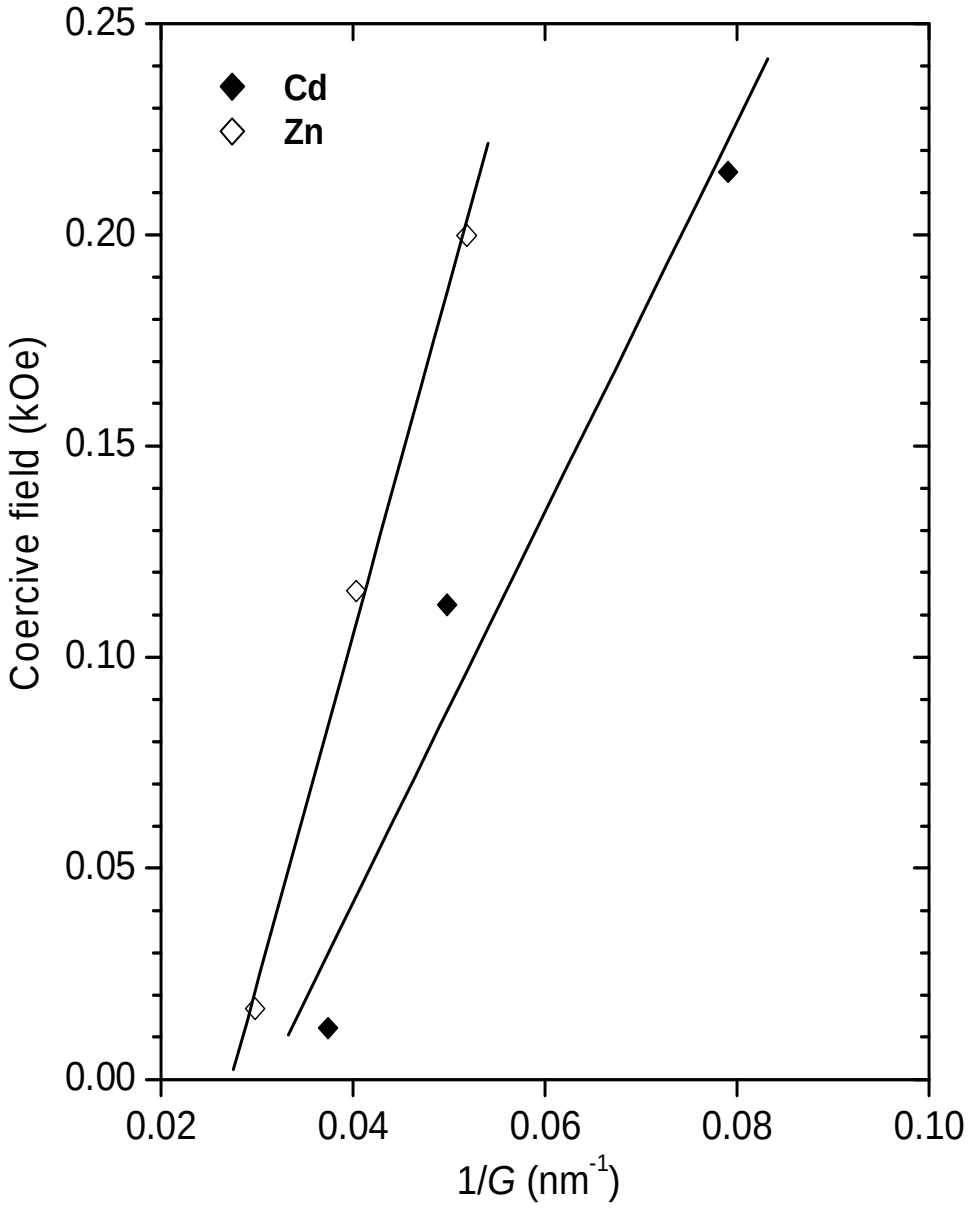

Figure 6.23: Variation of coercive fields for (Cd, Zn)$_{0.5}$Ni$_{0.5}$Fe$_2$O$_4$ with $1/G$.

Table 6.12: Constants a_m, b_m, a_s and b_s in equations (6.4.1) and (6.4.2) for (Cu, Zn, Cd)$_{0.5}$Ni$_{0.5}$Fe$_2$O$_4$ oxides.

	a_m (kOe)	b_m (nm kOe)	R^2
$NiFe_2O_4$	-0.23 ± 0.01	15 ± 1	0.998
$Cu_{0.5}Ni_{0.5}Fe_2O_4$	-0.22 ± 0.01	12 ± 1	0.989
$Zn_{0.5}Ni_{0.5}Fe_2O_4$	-0.23 ± 0.02	8.3 ± 0.5	0.997
$Cd_{0.5}Ni_{0.5}Fe_2O_4$	-0.14 ± 0.06	5 ± 1	0.975
	a_s	b_s	R^2
$Cu_{0.5}Ni_{0.5}Fe_2O_4$	2.6 ± 0.3	-220 ± 34	0.997
$Cd_{0.5}Ni_{0.5}Fe_2O_4$	0.27 ± 0.01	-9 ± 1	0.998

$NiFe_2O_4$ oxide (see chapter 5). Both $Cu_{0.5}Ni_{0.5}Fe_2O_4$ and $NiFe_2O_4$ compounds have strong magnetic coupling between the magnetic moments as reflected by Mössbauer results. Unlike antiferomagnetic $Cu_{0.5}Ni_{0.5}Fe_2O_4$ and $NiFe_2O_4$, the (Zn, Cd)$_{0.5}$Ni$_{0.5}$Fe$_2$O$_4$ oxides exhibit ferrimagnetic behavior. The constant b_m (slope of the graph of H_C versus $1/G$) might be related to the magnetic order in these compounds.

At a critical particle size multidomains become single domain particles. In single domain region the coercivity decreases with reduction in grain size as

$$H_C = a_s - \frac{b_s}{G^2}. \tag{6.4.2}$$

The graphs of H_C versus $1/G^2$ for the single domain regions in the Cu– and Cd–based oxide are shown in Figures 6.24 and 6.25. The linear fit (correlation coefficient 0.997) confirms single domain particles. The a_s and b_s values are also shown in Table 6.12 and can be compared to similar compounds.

The variation of coercive fields with reducing grain size may also have contribution from surface effects (anisotropy of the crystal) and development of domain walls in the nanoparticles [41, 69]. The initial increase in coercive fields

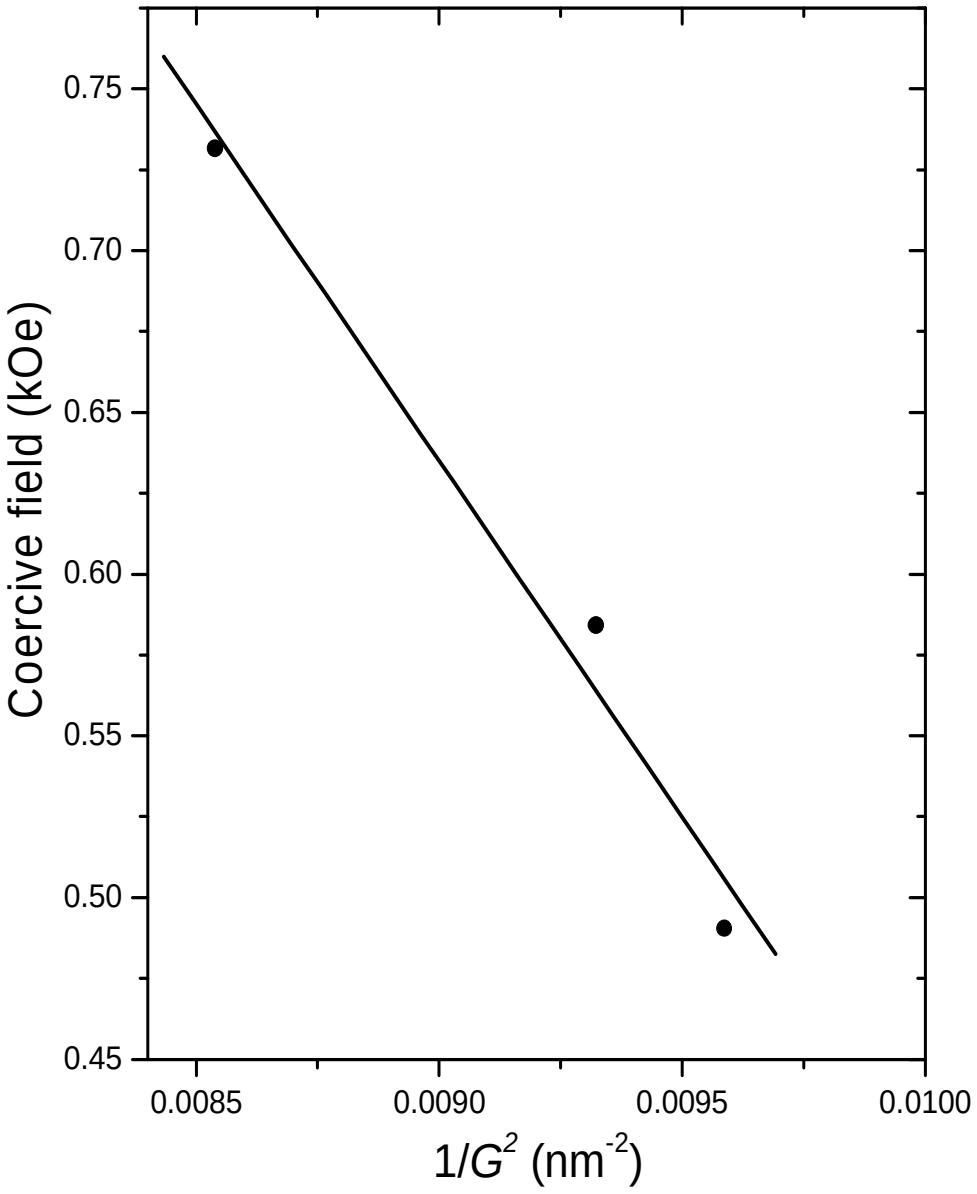

Figure 6.24: Variation of coercive fields for $Cu_{0.5}Ni_{0.5}Fe_2O_4$ with $1/G^2$.

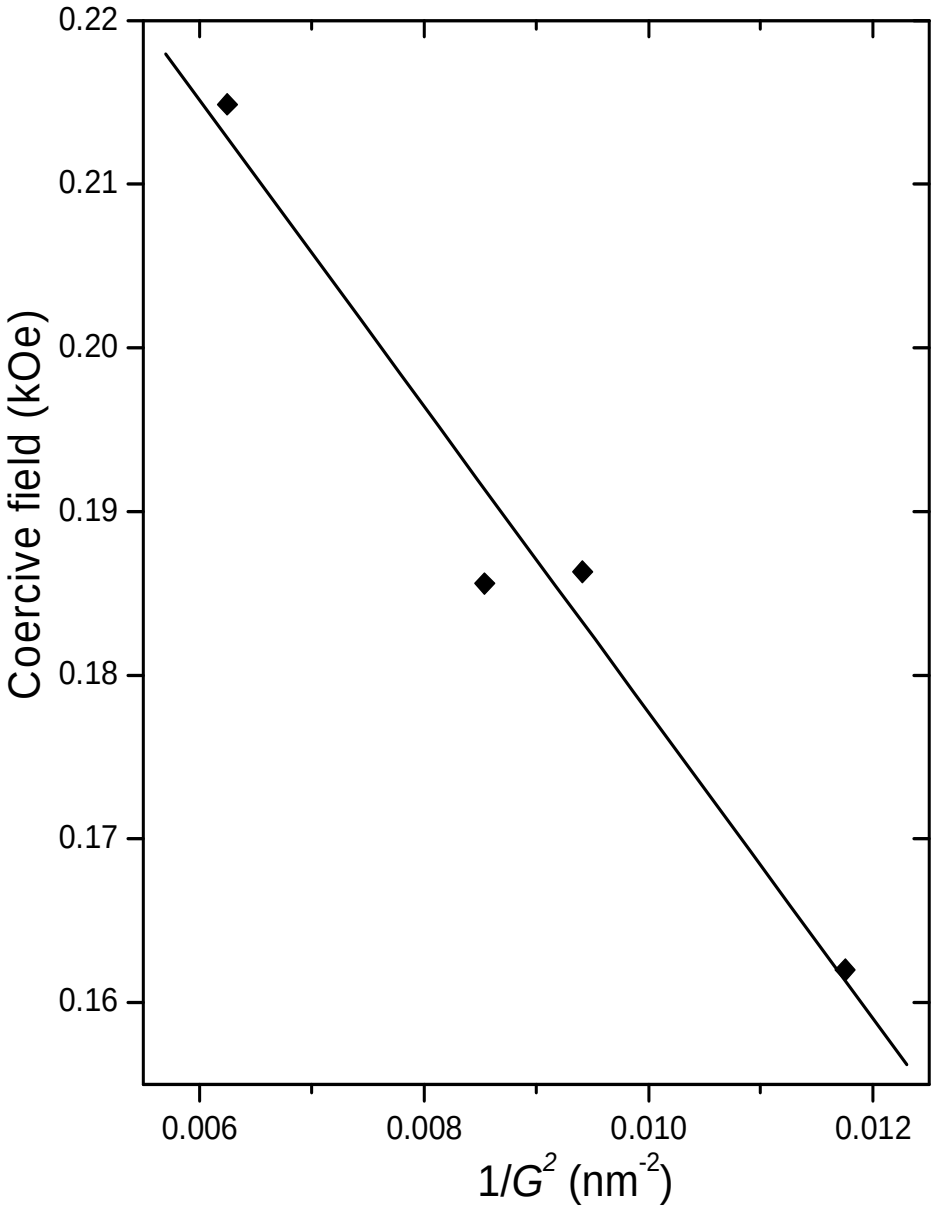

Figure 6.25: Variation of coercive fields for $Cd_{0.5}Ni_{0.5}Fe_2O_4$ with $1/G^2$.

is due to the enhanced surface anisotropy as the grain size is reduced. At a minimum grain size the anisotropy energy becomes comparable to the thermal energy. This leads to the thermally assisted jumps over the anisotropy barriers. The number of domain walls also increases with reducing grain sizes. Since the magnetization or demagnetization due to domain wall movement requires less energy than that needed for domain rotation, larger grains would be expected to have low coercive field. Hence a decrease in coercive field occurs beyond a critical grain size [41, 69].

6.5 Conclusions

The effects of grain size reduction, ionic size and electronic configuration differences between Zn, Cd and Cu atoms have on the magnetic properties have been investigated. The Mössbauer spectra for Cd and Zn–based oxide were closely related. This behavior is attributed to similar electronic configuration of Zn and Cd atoms.

While Zn and Cd–based oxides have low Curie temperature, the Cu–based oxide has high Curie temperature. The stronger magnetic coupling in the Cu–based oxide has been explained by existence of RKKY interaction in addition to the superexchange interactions. The hyperfine fields of the Cu–based compound appear to follow a T^2 dependence which is associated with single particle excitations. In Cd– and Zn–based oxides the hyperfine fields follow T dependence. Evidence of change from multidomain to single domain particles at critical grain sizes has been observed.

Chapter 7

Green density effects on the structural and magnetic properties of $(Zn, Cd)_{0.5}Ni_{0.5}Fe_2O_4$ ferrites

7.1 Introduction

Zn–Ni ferrites are amongst some of the well-studied and used ferrites. They are characterized by soft magnetic properties and high resistivity. The desired phase is easy to form and materials produced have the advantage of high stability and low cost. This accounts for the wide use of Zn–Ni ferrites in magnetic and electrical applications. The research interest in these materials is aimed at improving the quality, reliability and consistency in the material properties. A good understanding of the evolution of properties imposed by the methodology and sample preparation conditions is therefore critical. The techniques used to arrive at the final product are known to influence the properties. However, it is expected that better techniques for sample preparation in different places under similar conditions should produce samples with greater consistency because

of the use of common raw materials of similar or identical purity.

The conventional technique used to produce ferrites is the ceramic technique, which involves at least two stages of grinding of the starting oxides. Here the final level of homogeneity depends on the type and duration of grinding process and the initial particle size of the oxides. Hence the same level of homogeneity every time and in different places is harder to achieve when samples are produced by mechanical methods. There is also greater chance of contamination and sample loss during milling operations [15]. Prolonged heating of the samples at high temperature also gives rise to further mass loss.

In materials produced by wet chemical methods a higher degree of homogeneity of the starting solution can be achieved. The samples produced by these techniques should therefore demonstrate a higher degree of consistency. Unfortunately, this appears not to be the case when two sets of data were compared in two recent reports [15, 29]. It is therefore important to develop firm criteria that can be used to compare properties of samples from different sources.

We have employed the combustion technique to produce samples of high quality from a well-homogenized mixture of starting nitrates and urea. The main interest was to investigate the extent to which material properties evolve from samples prepared from the same homogenized and ignited mixture under different conditions of applied pressure (related to the green density) in the production of sample pellets. The effect of totally replacing Zn^{2+} by the larger Cd^{2+} ions in the $Zn_{0.5}Ni_{0.5}Fe_2O_4$ compound was also investigated.

7.2 X–ray diffraction results

Two sets of data were produced by combustion technique. In order to investigate the effect of pelletizing pressure (green density) during synthesis on the properties of ferrite materials, the recovered powders after combustion were divided into small portions which were pelletized under different pressure from

about 300 MPa to 1400 MPa. The first set of pellets (set 1) was sintered at 1250 ^{o}C and the second set at 1210 ^{o}C (set 2). Both sets of pellets were sintered for six hours.

The variations of X-ray diffraction patterns with pelletizing pressure for set 1 and 2 samples are shown in Figures 7.1 and 7.2. Virtually all the significant peaks are indexed. Hence all the pellets sintered at slightly lower temperature (1210 ^{o}C) crystallized with single phase cubic spinel structure. The spectra are consistent with the spectrum published by Costa et al [15] on similar compounds produced by the combustion technique. The X–ray diffraction data of set 1 samples indicated that single phase formation of the Cd–based samples was not achieved. The higher sintering temperature (1250 ^{o}C) appears to adversely affected single phase formation. Complete single phase formation was obtained for set 2 samples. This also shows that Zn–based samples form easily compared to the Cd–based samples. The Zn atoms have been reported to promote single phase formation [15].

The average bulk density of a sample after sintering is an important parameter that measures the average coordination of the atoms in the entire sample. This parameter has information of the average compaction of the atoms and also includes the effects of the empty spaces (a measure of porosity). The bulk densities (ρ_B) were measured using Archimedes principle. In Tables 7.1 and 7.2 we present results of X-ray and bulk densities, grain size (G), porosity (P_o) and lattice parameters (a) as a function of applied pressure (P). Slight but definite changes with pressure are observed.

The results of bulk density measurements are plotted in Figure 7.3. Apparent anomalies in the variation of the bulk density with pressure are observed. Initially a slight increase in bulk density occurs for set 2 and Zn–set 1 samples. The bulk density decreases with further increase in pressure. The anomalous reduction in bulk density is more evident for the Cd–based samples. In principle a pellet subjected to high pressure would be expected to have higher bulk density. It is interesting that the reduction in bulk density with pressure was

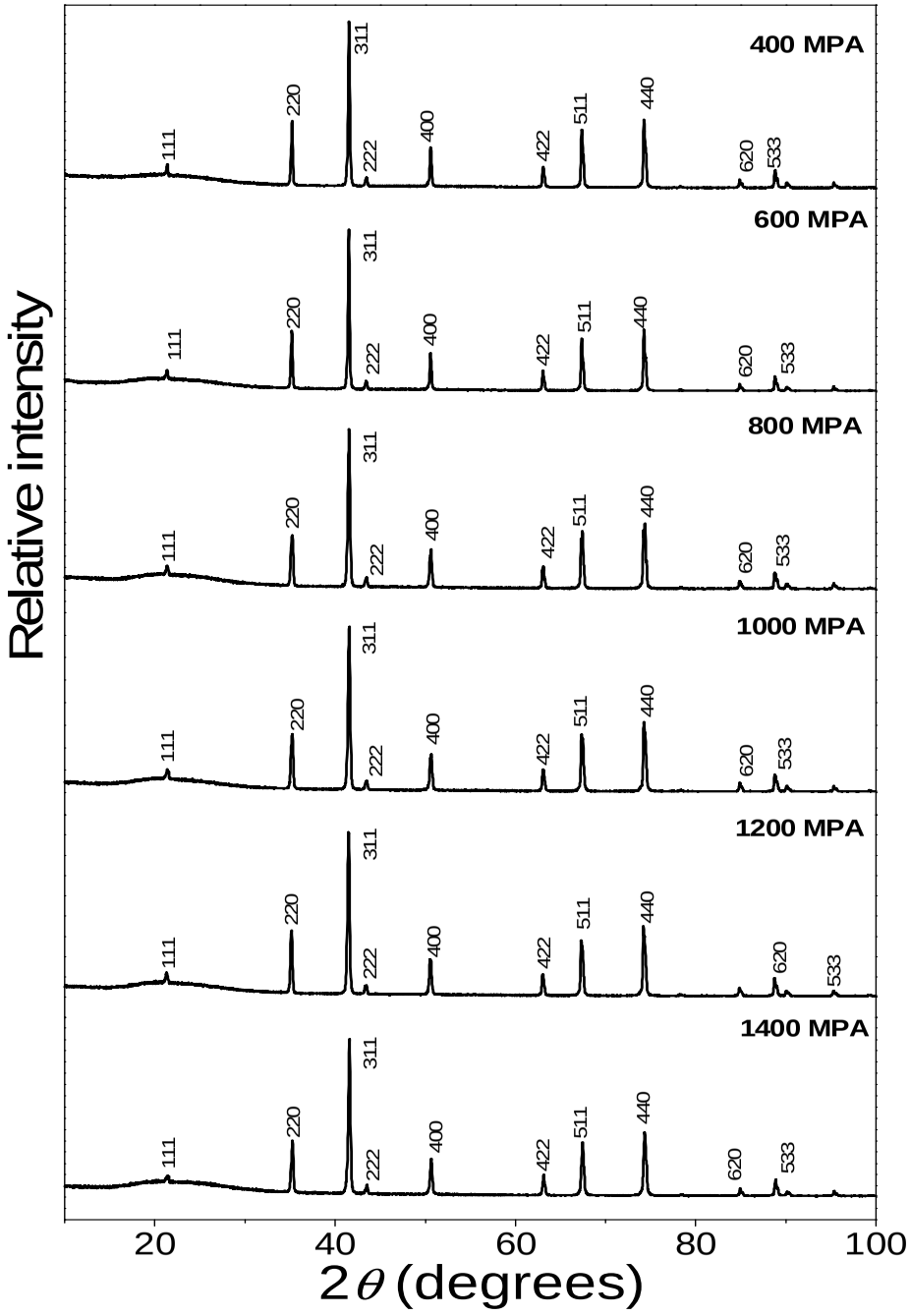

Figure 7.1: Variation of XRD patterns for $Zn_{0.5}Ni_{0.5}Fe_2O_4$ oxide sintered at 1250 ^oC with pelletizing pressure.

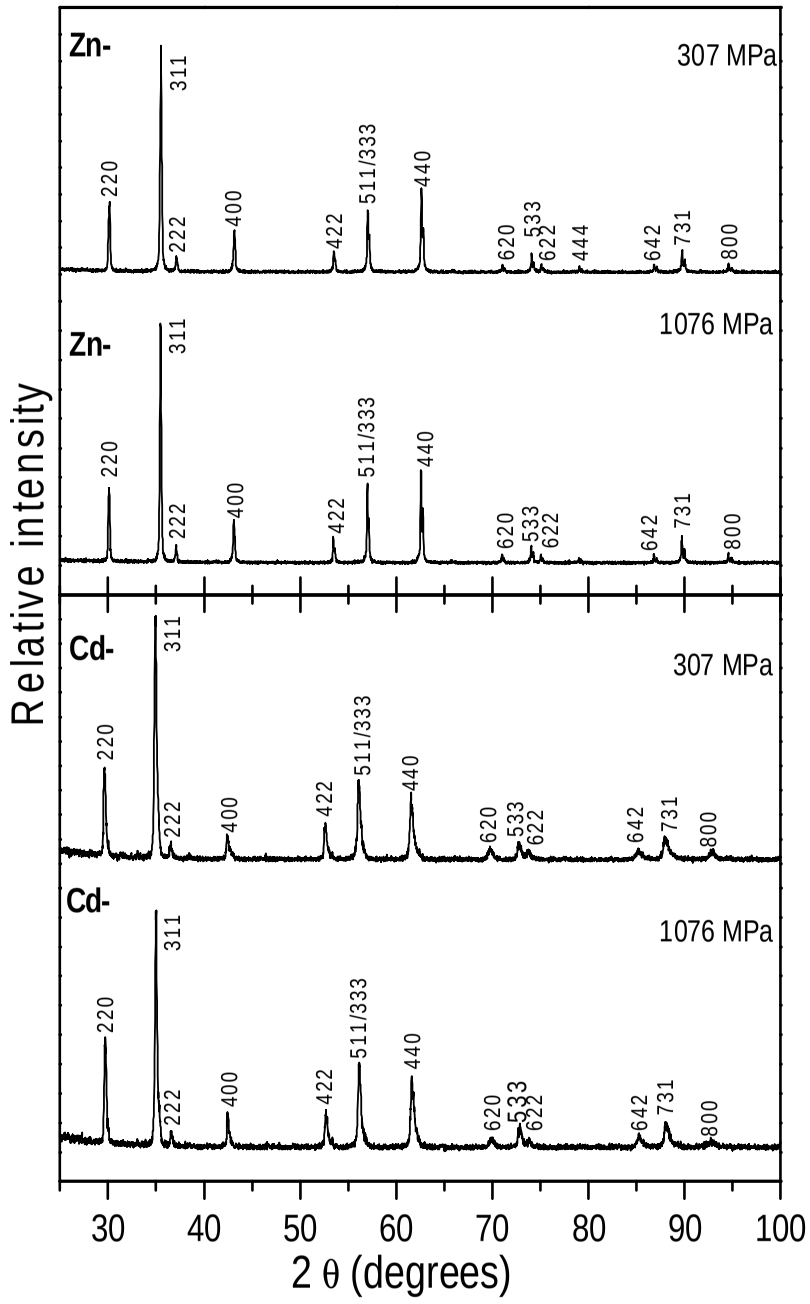

Figure 7.2: Variation of XRD patterns for (Zn, Cd)$_{0.5}$Ni$_{0.5}$Fe$_2$O$_4$ oxides sintered at 1210 ^{o}C with pelletizing pressure.

Table 7.1: Variation of bulk (ρ_B) and X-ray (ρ_X) densities, grain size (G), porosity (P_o) and lattice constant (a) for $Zn_{0.5}Ni_{0.5}Fe_2O_4$ sintered at 1250 ^oC with pressure (P).

P (MPa)	ρ_B (g/cm^3)	ρ_X (g/cm^3)	G(nm)	P_o(%)	a ($\AA$)
	$\pm$ 0.02	$\pm$ 0.02	$\pm$ 0.1	$\pm$ 0.1	$\pm$ 0.01
400	5.09	5.38	48.3	11.9	8.37
600	5.12	5.37	50.1	13.5	8.38
800	5.12	5.40	39.4	15.9	8.36
1000	5.05	5.39	39.9	19.4	8.37
1200	5.06	5.35	41.6	20.7	8.39
1400	4.97	5.40	41.3	21.1	8.36

reproduced in the second set of pellets. We believe that these results can be explained on the basis of a significant amount of trapped porosity. The pelletizing pressure can interfere with escape routes of excess gases from a pellet during the sintering process. The average bulk and X-ray densities for the Zn–based oxide were 5.07 $\pm$ 0.02 g/cm^3 and 5.38 $\pm$ 0.02 g/cm^3 respectively. The bulk density of the Zn–based oxide compares well with 5.00 g/cm^{-3} reported in reference [15] for the sample made by combustion method but at a pre–sintering pressure of 392 MPa. These values are also similar to ρ_B = 5.11 $\pm$ 0.02 g/cm^3 and ρ_X = 5.35 $\pm$ 0.03 g/cm^3 found for the sample with similar composition made by solid state reaction.

The porosity of the sample can be calculated from the knowledge of bulk density and X-ray density deduced from the size of the unit cell (using equation 5.2.2). The variation of porosity with pressure is shown in Figure 7.4 (a). An increase in porosity with pelletizing pressure relates well with reduced grains on samples pelletized under high pressures. The increase in porosity appears

Table 7.2: Variation of bulk (ρ_B) and X-ray (ρ_X) densities, grain size (G), porosity (P_o) and lattice constant (a) for $Zn_{0.5}Ni_{0.5}Fe_2O_4$ sintered at 1210 ^{o}C.

	P (MPa)	ρ_B (g/cm^3)	ρ_X (g/cm^3)	G (nm)	P_o(%)	a ($\mathring{A}$)
		$\pm$ 0.017	$\pm$ 0.008	$\pm$ 0.7	$\pm$ 0.05	$\pm$ 0.0005
Zn	307	4.952	5.356	45.6	7.57	8.3848
	461	4.993	5.357	49.1	6.83	8.3849
	615	5.018	5.356	49.5	6.37	8.3837
	769	4.964	5.345	51.2	7.15	8.3905
	922	4.8964	5.340	51.7	8.37	8.3929
	1076	5.019	5.361	48.8	6.40	8.3823
Cd	307	4.94	5.693	32.1	12.04	8.516
	461	4.98	5.919	39.4	11.79	8.504
	615	4.83	5.758	28.2	15.09	8.482
	769	4.67	5.706	30.9	17.17	8.508
	1076	4.63	5.711	35.7	17.87	8.505

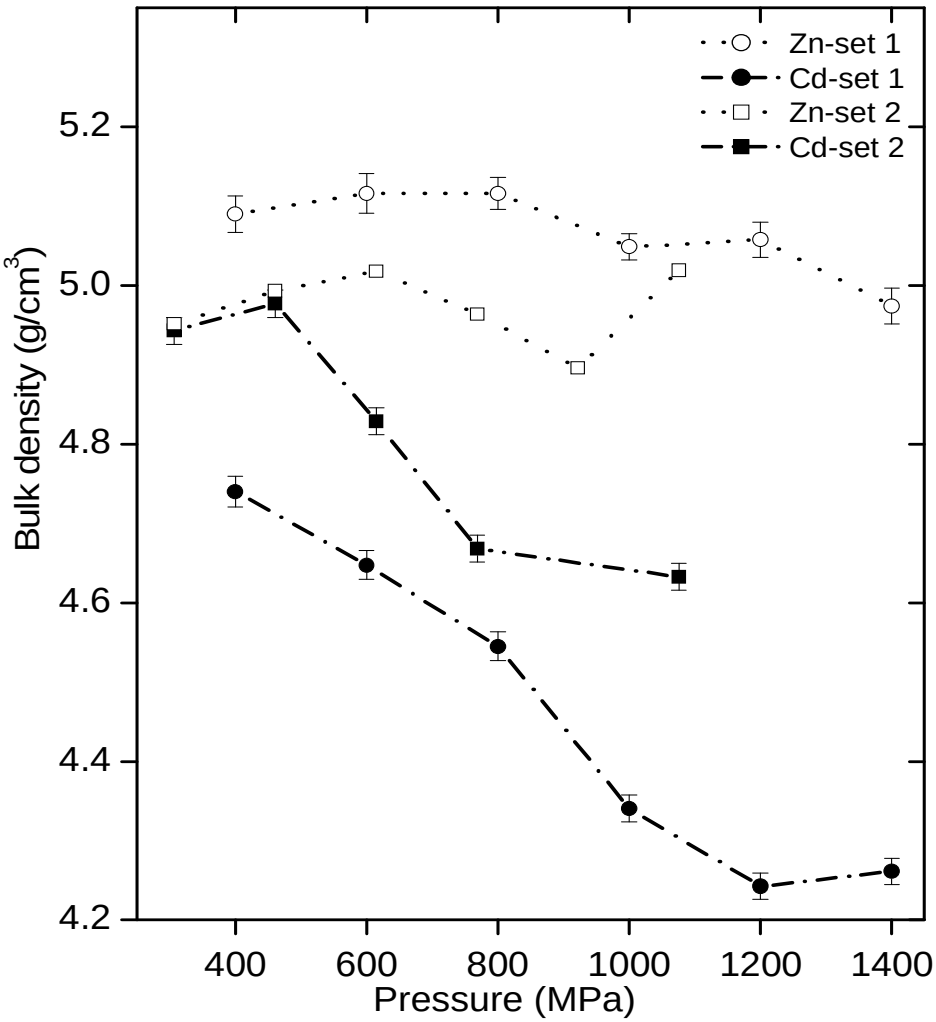

Figure 7.3: Variation of bulk (ρ_B) densities for (Zn, Cd)$_{0.5}$Ni$_{0.5}$Fe$_2$O$_4$ with pelletizing pressure.

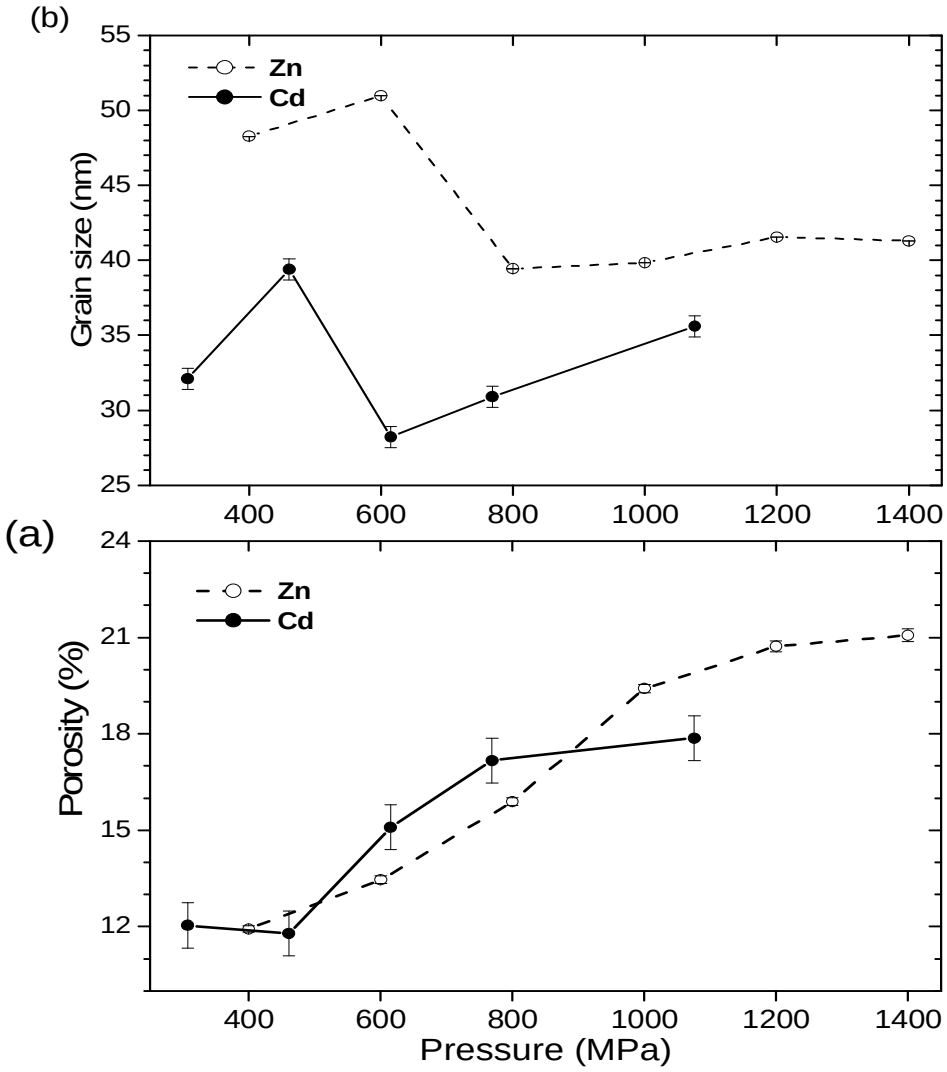

Figure 7.4: Variation of (a) porosity and (b) grain sizes for $Zn_{0.5}Ni_{0.5}Fe_2O_4$ with pelletizing pressure.

to be associated with inreasing pressure used to form pellets.

In Figure 7.4 (b) we show the variation of grain size for (Zn, Cd)$_{0.5}$Ni$_{0.5}$Fe$_2$O$_4$ oxides with pelletizing pressure. The grain sizes are larger for Zn–based compounds reflecting the well–known tendency of Zn to enhance the desired phase formation. The grain sizes are lower in Cd–based samples. We attribute this to the larger ionic size of Cd atoms. Larger atoms would tend to weaken inter–ionic interactions resulting in smaller crystallites. For the samples made under pressure of 400 MPa and 600 MPa the grain sizes were 48.3 ± 0.1 nm and 50.1 ± 0.1 nm respectively. These values compare well with the grain size of 48.0 ± 0.2 nm obtained for Zn–based sample presented in chapter 6 made by solid state reaction. On increasing the pressure to 800 MPa the grain sizes reduced to about 39 nm and then slowly increased to about 42 nm when pelletizing pressure was increased to 1200 MPa. Nanosized oxide (sample with grains less than 20 nm) could therefore not be made by combustion technique. Similar results have been observed in reference [15]. This may be due to the high sintering temperature (1250 ^{0}C) used to form single phase spinel structure. In the future it will be important to investigate if complete crystallization of sample made by combustion technique can not be achieved at lower sintering temperatures.

The size of the unit cell also did not change significantly with pressure as shown in Tables 7.1 and 7.2. The average lattice parameters were respectively 8.37 ± 0.01 $\mathring{A}$ and 8.503 ± 0.001 $\mathring{A}$ for the Zn– and Cd–based oxides. These values also compare well with the lattice constants of 8.39 ± 0.02 $\mathring{A}$ (Zn–based) and 8.51 ± 0.01 $\mathring{A}$ (Cd–based) obtained for samples produced by solid state reaction in chapter 6.

7.3 Mössbauer results

Mössbauer measurements were performed at room temperature. Typical spectra are given in Figures 7.5 and 7.6, which show ordered magnetic phase at

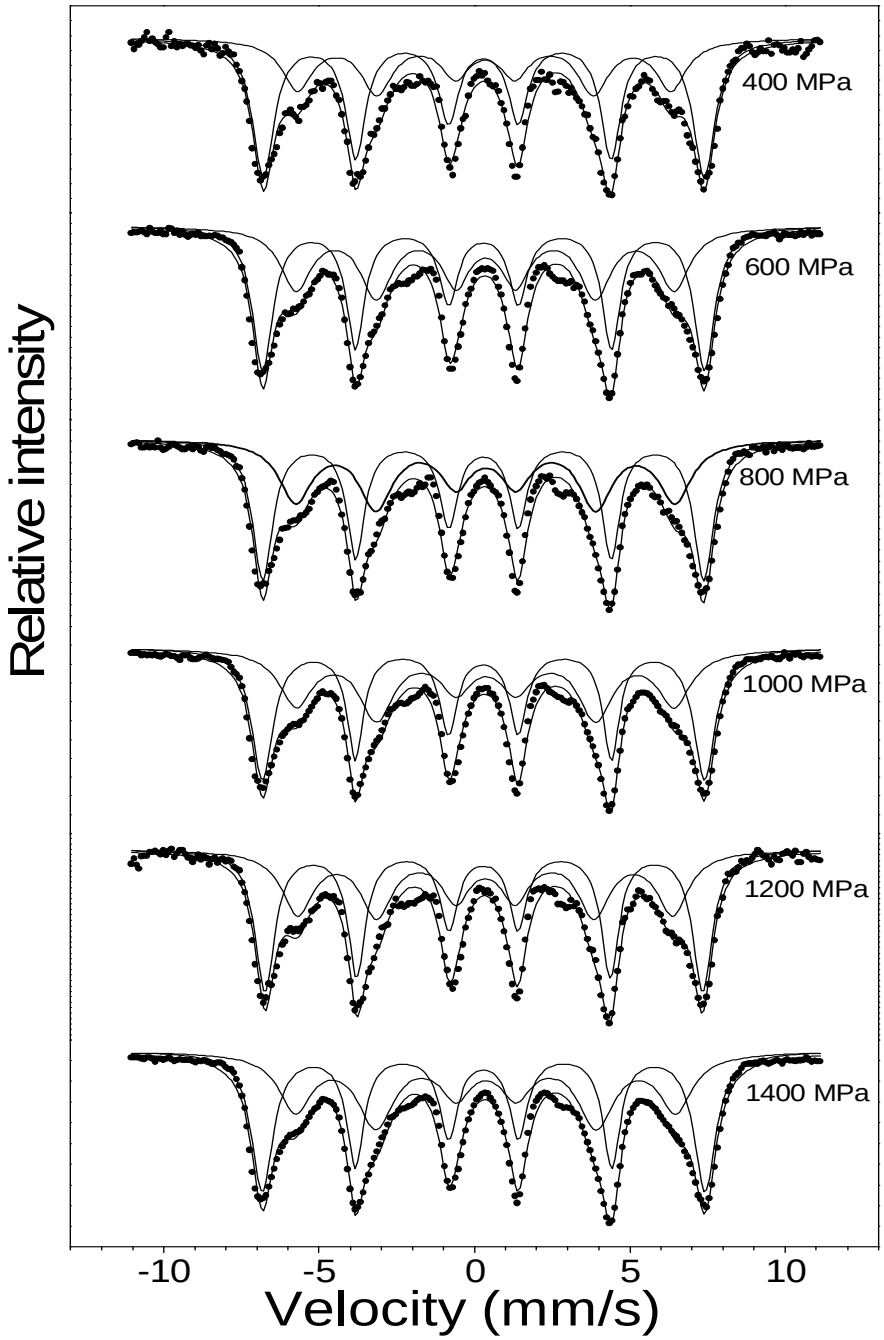

Figure 7.5: Variation of Mössbauer spectra for $Zn_{0.5}Ni_{0.5}Fe_2O_4$ sintered at 1250 ^oC with pelletizing pressure (set 1).

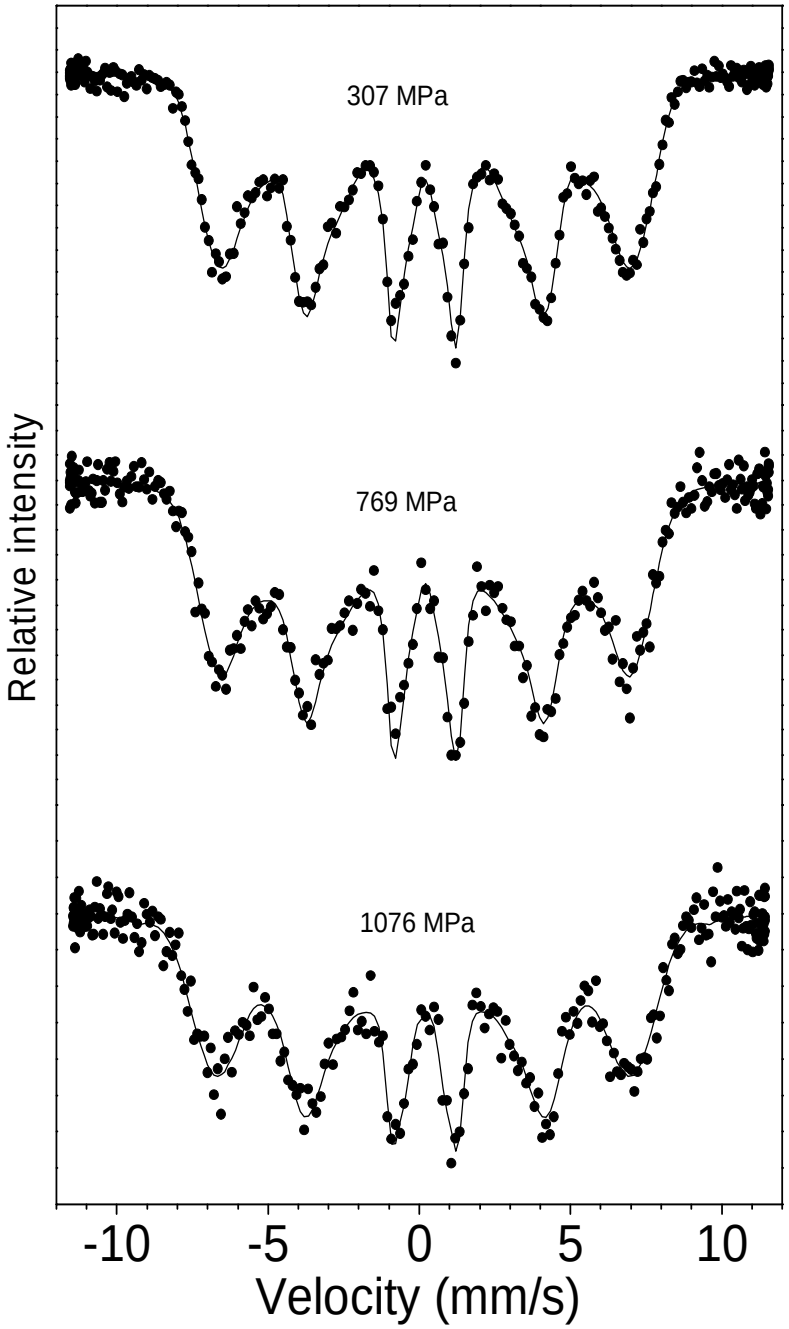

Figure 7.6: Typical Mössbauer spectra for $Cd_{0.5}Ni_{0.5}Fe_2O_4$ sintered at 1210 ^oC with pelletizing pressure (set 2).

room temperature. The spectra are characterized by broad peaks, which indicate a range of hyperfine fields. The appropriate analysis is therefore to deduce hyperfine field distributions from the spectra. Such distributions are shown in Figure 7.7. The plots clearly show systematic change of the hyperfine field distributions as a function of pelletizing pressure (green density). We can also identify four principle gaussian peaks that make up the hyperfine field distribution as illustrated in Figure 7.8.

In Figure 7.5 we have fitted the Mössbauer spectra with two sextets to represent the ions in A and B sites. The sextets were assigned A or B sites based on the fitted results of isomer shifts. The A site isomer shifts are expected to be lower as discussed in chapter 5. The data deduced from Mössbauer fits are shown in Table 7.3. The isomer shift and hyperfine fields were weakly affected by pelletizing pressure. The average isomer shifts on A site was 0.29 $\pm$ 0.01 mm/s. On B site the average isomer shift was 0.35 $\pm$ 0.01 mm/s. These values compare well with 0.27 $\pm$ 0.02 mm/s (A site) and 0.34 $\pm$ 0.04 mm/s (B site) obtained for the bulk sample with same nominal composition made by solid state reaction. The A site and B site average hyperfine fields were 440 $\pm$ 5 kOe and 376 $\pm$ 3 kOe respectively. These values are also in agreement with 434 $\pm$ 2 kOe (A site) and 387 $\pm$ 2 kOe (B site) obtained for the samples produced by solid state reaction. The Curie temperatures deduced by zero velocity Mössbauer technique as discussed in chapter 5 were also not significantly affected by the pelletizing pressure. The average Curie point was 554 $\pm$ 4 K (set 1).

7.4 Magnetization results

The isothermal magnetization measurements were performed at room temperature in the field range: -9 kOe $\leq B_0 \leq$ 9 kOe. Typical magnetization curves are shown in Figures 7.9 and 7.10. The results show very little hysteresis loss at room temperature. In Table 7.4 we show the data of coercive field and

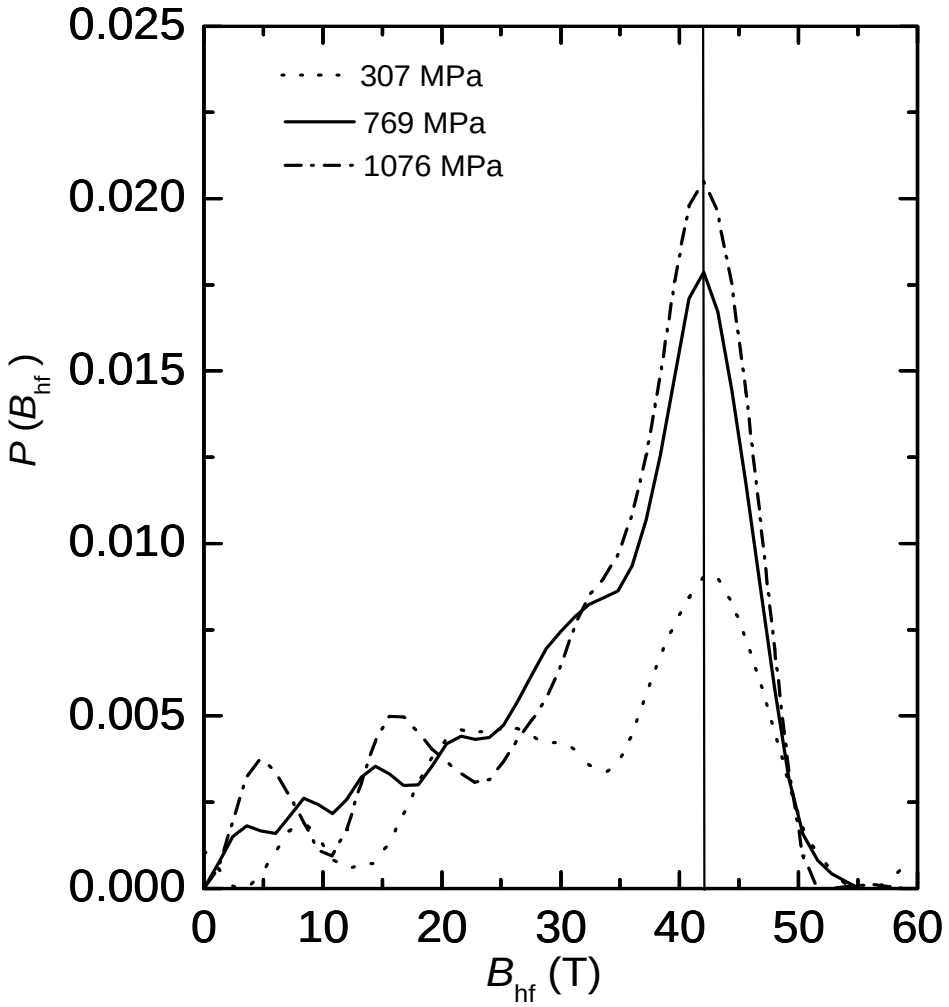

Figure 7.7: Hyperfine field distributions for $Cd_{0.5}Ni_{0.5}Fe_2O_4$ oxides sintered at 1210 ^{o}C (set 2).

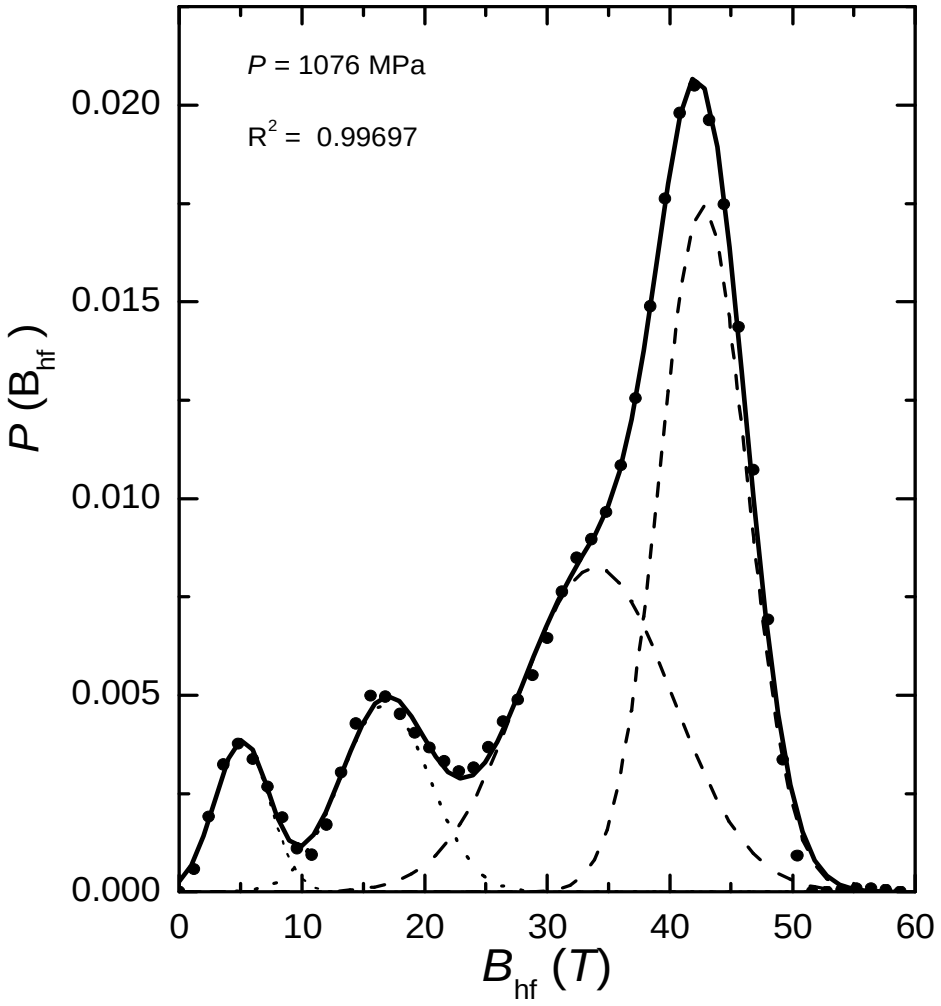

Figure 7.8: Gaussian fits to the hyperfine field distributions for $Cd_{0.5}Ni_{0.5}Fe_2O_4$ oxide (set 2).

Table 7.3: Variation of isomer shift (IS), quadrupole splitting (QS) and hyperfine fields (B_{hf}) of $Zn_{0.5}Ni_{0.5}Fe_2O_4$ with pelletizing pressure.

P (MPa)	IS (mm/s)		QS (mm/s)		B_{hf} (kOe)	
	$(IS)_A$	$(IS)_B$	$(QS)_A$	$(QS)_B$	$(B_{hf})_A$	$(B_{hf})_B$
	± 0.005	±0.01	±0.01	±0.01	± 5	±3
400	0.293	0.33	0.01	-0.02	440	373
600	0.290	0.35	0.00	0.02	441	377
800	0.286	0.36	0.03	0.03	440	379
1000	0.287	0.36	-0.01	0.01	441	376
1200	0.294	0.35	0.04	0.02	437	374
1400	0.294	0.26	0.01	0.02	442	379

saturation magnetization as function of pressure. There appears to be a slight correlation between coercive and bulk density. Lower coercive field seems to be associated with higher bulk density in Zn–based sample. A slight increase in saturation magnetization was observed after pelletizing under pressure above 600 MPa. The saturation magnetization then remained almost constant with further increase in pressing pressure.

7.5 Conclusions

Our results show a significant influence of the green density on the final bulk density of (Zn, Cd)$_{0.5}Ni_{0.5}Fe_2O_4$ ferrites investigated. The bulk density measurements are important because they can provide information of the quality of the materials and how their properties are influenced by the sample preparation conditions such as the pre-sintering green density. Our results show that a maximum bulk density can be obtained for a pressure of about 600 MPa. Samples produced from different states of green density appear to be

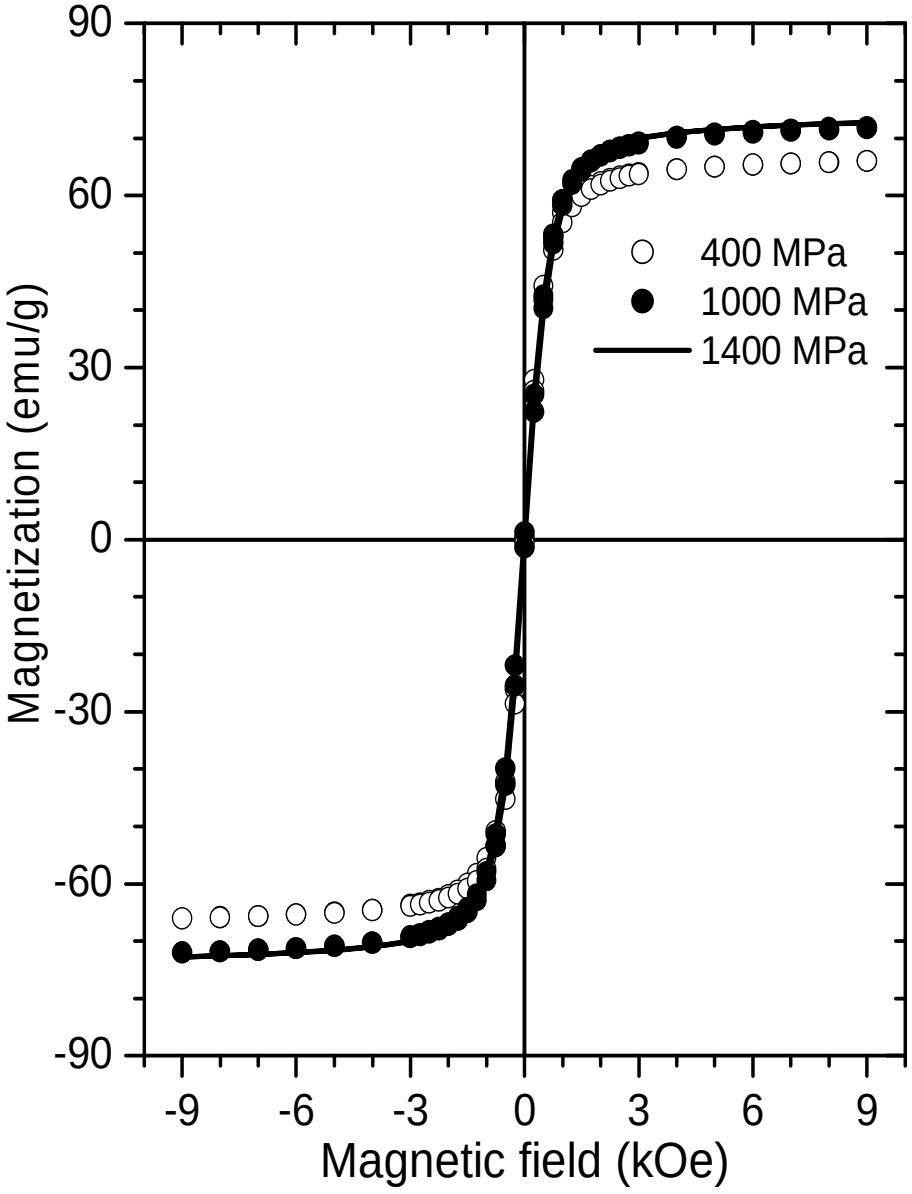

Figure 7.9: Magnetization curves for $Zn_{0.5}Ni_{0.5}Fe_2O_4$ oxide (pelletized at 400 MPa, 1000 MPa and 1400 MPa) sintered at 1250 ^{o}C.

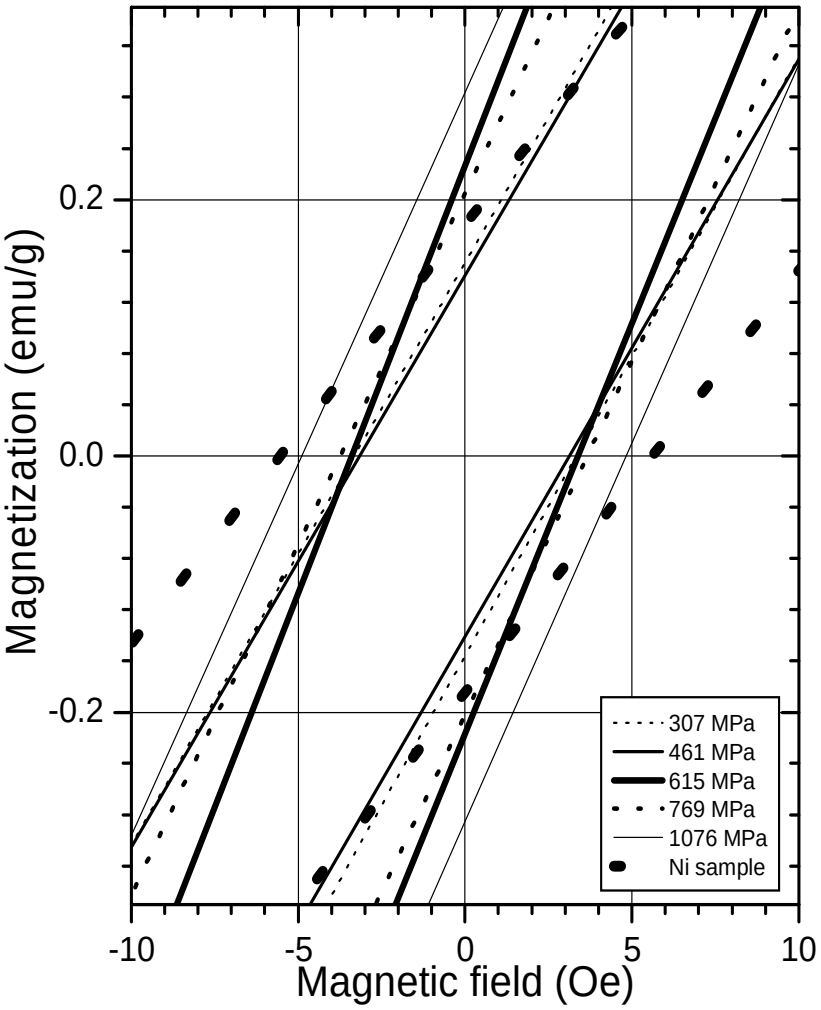

Figure 7.10: Magnetization curves in low fields for $Cd_{0.5}Ni_{0.5}Fe_2O_4$ oxide (pelletized at different pressures) sintered at 1210 ^{o}C and Ni sample.

Table 7.4: Coercive field (H_C) and saturation magnetization (M_S) as a function of applied pressure for (Zn, Cd)$_{0.5}$Ni$_{0.5}$Fe$_2$O$_4$ sintered at 1210 ^{o}C (set 2).

	P (MPa)	H_C(Oe)	M_S (emu/g)
	± 10	± 0.5	± 0.2
Zn	307	3.7	74.2
	461	1.9	72.8
	615	2.2	73.5
	769	0.6	75.1
	922	4.5	74.1
	1076	2.7	75.3
Cd	307	3.4	56.1
	461	3.2	56.0
	615	3.4	56.9
	769	3.8	58.0
	1076	4.9	57.9

easily distinguished by hyperfine field distributions as shown in Figure 7.7. The parameters like lattice constants, grain sizes, porosity, coercive fields and saturation magnetization are less significantly affected by the pelletizing pressure.

Chapter 8

Synthesis and magnetic properties of $(Cd, Cu)_{0.5}Ni_{0.5}Fe_2O_4$ nanoparticles by glycothermal and hydrothermal processes

8.1 Introduction

Apart from the type of metal cations and their distribution amongst the tetrahedral (A) and octahedral (B) sites, the magnetic properties of ferrites also depend on the sample preparation methodology. Samples produced from different laboratories and by different techniques can show differences in properties [17, 37]. Solid state reaction has the disadvantage of prolonged heat treatments at high temperatures. This can lead to evaporation of some of the constituent metal oxides or phase changes e.g. Fe_3O_4 to α–Fe_2O_3 or γ–Fe_2O_3 [16]. This can also lead to final products with modified stoichiometric compositions or samples with unreproducible properties. Using wet chemical methods, single

phase samples can be formed at low sintering temperatures. Since the starting materials are nitrates or chlorides mixed at molecular level, the possibility of contamination is also lower and a higher level of homogeneity of the starting solutions can be achieved before formation of the desired compound.

In this chapter we present the results and discussions of the effects of synthesis and preparation conditions on the structural and magnetic properties of nanosized (Cu, Cd)$_{0.5}$Ni$_{0.5}$Fe$_2$O$_4$ oxides made by hydrothermal and glycothermal techniques. The reaction temperature and pressure during sample preparation were changed in order to investigate the ease of phase formation. The nanosized compounds were annealed at different temperatures until complete single phase spinel structure was formed. The properties of the samples produced by glycothermal and hydrothermal processes are compared to samples produced by solid state reaction, combustion and milling presented in chapters 6 and 7.

8.2 X–ray diffraction results

8.2.1 $Cu_{0.5}Ni_{0.5}Fe_2O_4$ oxides

The nanosized $Cu_{0.5}Ni_{0.5}Fe_2O_4$ oxides were made by glycothermal and hydrothermal reactions. The main difference between these techniques was the reaction conditions (temperature and pressure). During hydrothermal method the sample was reacted in deionised water. During glycothermal process the reaction took place in ethelyne glycol solution. The boiling point of ethelyne glycol solution is 200 ^{o}C and thus the reaction took place under higher temperature. The glycothermal reaction was carried out in a pressure vessel. The temperature was slowly increased to 200 ^{o}C and the gauge pressure rose to 690 kPa. During hydrothermal reaction the sample was boiled in deionised water (zero gauge pressure).

In Figure 8.1 (a) and (b) we show the X–ray diffraction patterns for the

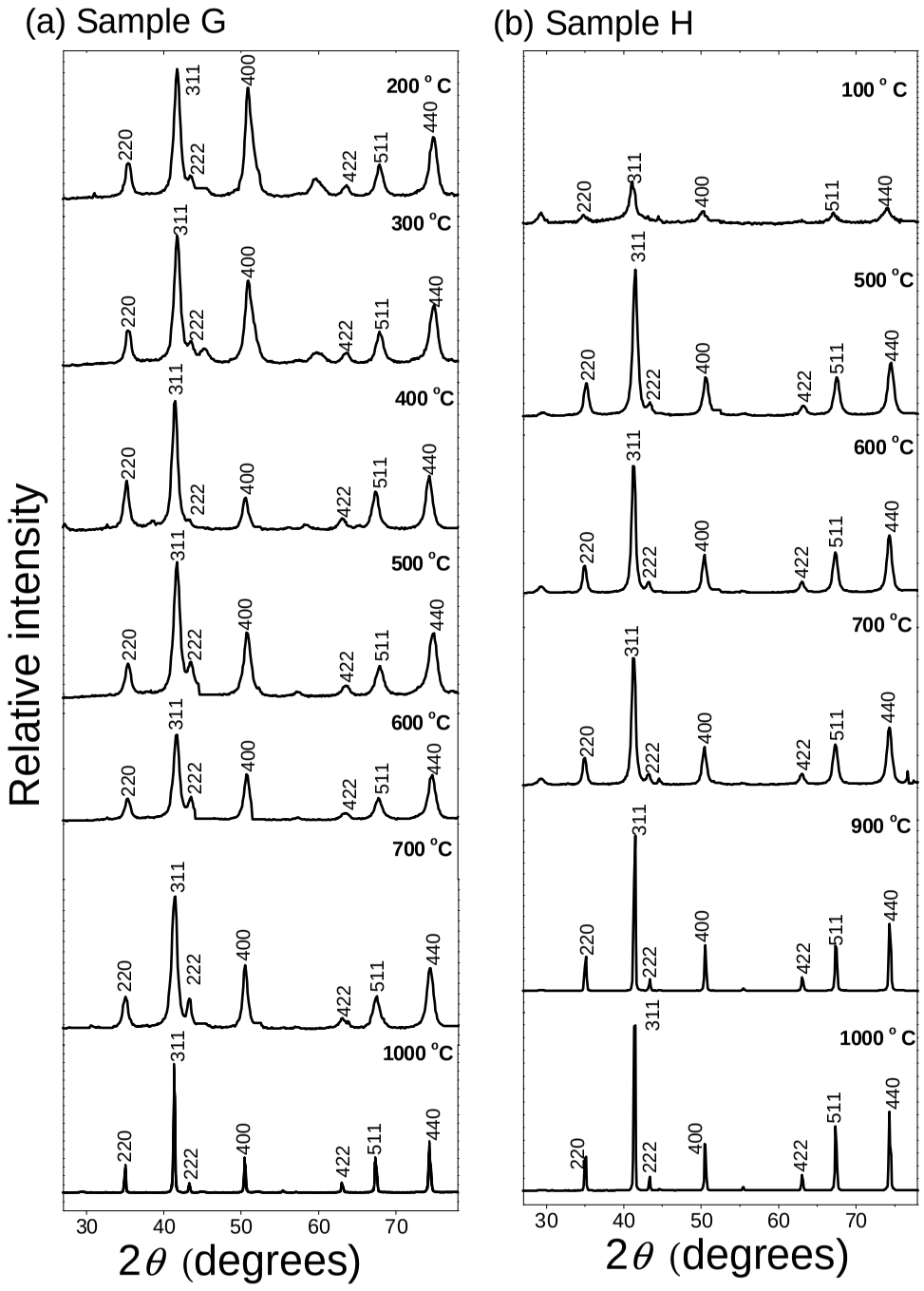

Figure 8.1: Variation of XRD patterns for $Cu_{0.5}Ni_{0.5}Fe_2O_4$ oxides with sintering temperature.

$Cu_{0.5}Ni_{0.5}Fe_2O_4$ oxides made by glycothermal (sample G) and hydrothermal (sample H) processes respectively. Both samples G and H were sintered at different temperatures until complete cubic spinel phase was formed. Except for the XRD peak at $2\theta = 59^o$ corresponding to the α-Fe_2O_3 phase [19], the majority of the XRD peaks of sample G were indexed to the cubic spinel phase. This impurity peak disappears after sintering at 600 ^{o}C. Complete spinel phase formation was therefore achieved after annealing sample G at 600 ^{o}C. This sintering temperature is low compared to high temperature heat treatments (1100 ^{o}C to 1400 ^{o}C [7, 15, 38]) used during solid state reaction.

The XRD patterns for the samples produced by hydrothermal process (sample H) show that single phase formation was almost achieved at 100 ^{o}C. Almost all the intensity peaks are indexed except for a small impurity peak at $2\theta = 30^o$. The impurity peak dissapears after annealing sample H at 900 ^{o}C. This sintering temperature (900 ^{o}C) is again lower than the usual sintering temperatures for sample prepared by solid state reaction. Sample preparation by hydrothermal and glycothermal appear to enhance the movement of atoms to stable positions in order to form the crystal structure. The main apparatus that are required during hydrothermal technique are the heating mantle, round bottom flask and condenser. The sample preparation method is clearly a cheap way to make ferrite materials because it does not require the use of an expensive pressure reactor.

The narrowing of the X–ray diffraction lines with increasing sintering temperature observed in Figure 8.1 reflects increasing grain size. The grain sizes were estimated from the broadening of the 311 XRD peak using equation (5.2.3). The grain sizes as a function of sintering temperature are shown in Table 8.1 and plotted in Figure 8.2. The grain sizes for sample H increase continuously with increase in sintering temperature. For sample G (sintered between 600 ^{o}C and 700 ^{o}C), the grain size fluctuates between 10 nm and 12 nm. We have therefore successfully made nanosized $Cu_{0.5}Ni_{0.5}Fe_2O_4$ oxide by glycothermal technique. A similar grain size (10.82 ± 0.05 nm) for the sample

Table 8.1: Variation of grain size (G) with sintering temperature for Cu–based (G and H) and Cd–based (A and B) samples.

	sample G	sample H	sample A	sample B
T (^{o}C)	G (nm)	G (nm)	G (nm)	G (nm)
	$\pm$ 0.04	$\pm$ 0.04	$\pm$ 0.04	$\pm$ 0.05
100		12.04	12.54	
200	10.28			
300	10.48		12.81	
400	12.04		13.14	
500	10.20	16.50	13.01	5.78
600	10.95	19.90	13.35	7.75
700	11.04	25.14	13.10	8.89
1000	44.78	53.64	42.56	35.54

with the same nominal composition was obtained after milling the bulk oxide for 24 hours (see Table 6.4). After annealing sample G at 1000 ^{o}C, the grain size increased to 44.8 $\pm$ 0.1 nm. This compares well with the grain size of about 45.5 nm for the bulk $Cu_{0.5}Ni_{0.5}Fe_2O_4$ sample made by solid state reaction presented in chapter 6. This is also comparable to $G = 48.3 \pm 0.1$ nm for the Zn–based sample with similar composition made by combustion technique presented in chapter 7. This compares well with similar ionic sizes between Zn and Cu atoms. The average lattice parameter of sample G and that of sample H were 8.36 $\pm$ 0.03 $\mathring{A}$ and 8.37 $\pm$ 0.03 $\mathring{A}$ respectively. These values are in agreement with lattice constant of 8.37 $\pm$ 0.03 $\mathring{A}$ obtained for the bulk sample produced by solid state reaction.

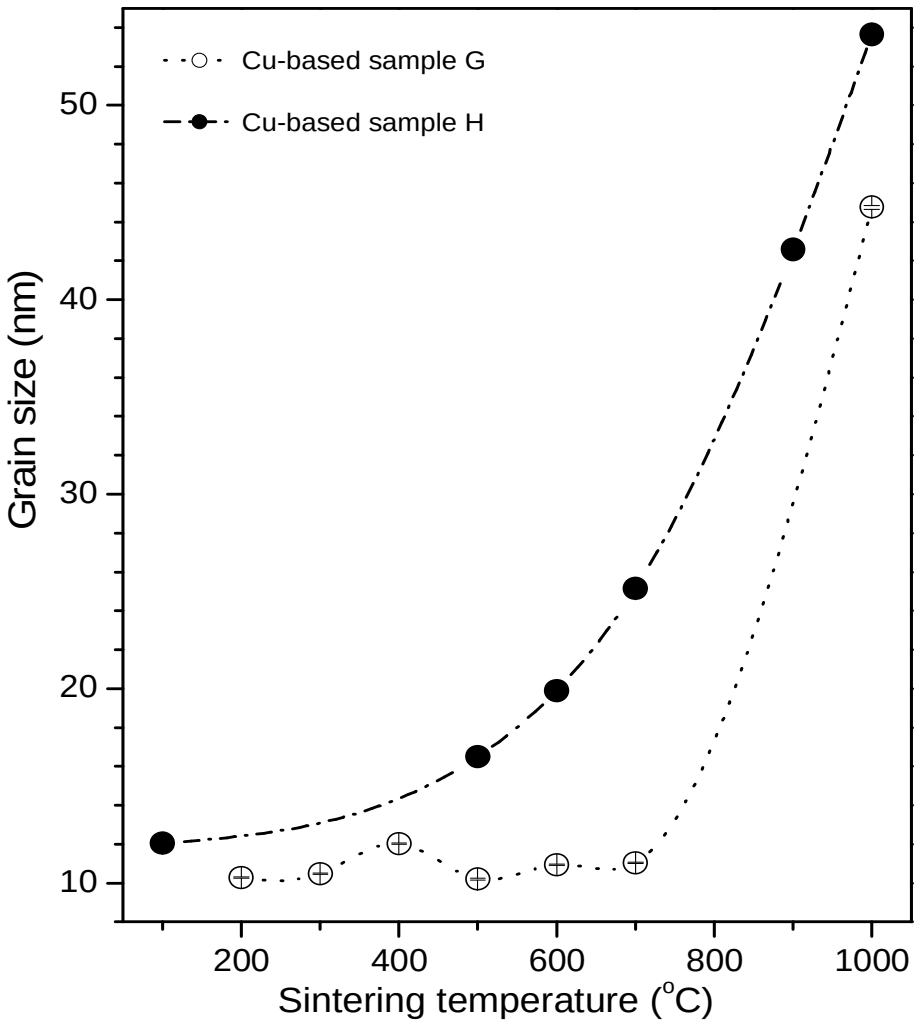

Figure 8.2: Variation of grain size for $Cu_{0.5}Ni_{0.5}Fe_2O_4$ oxides with sintering temperature.

8.2.2 $Cd_{0.5}Ni_{0.5}Fe_2O_4$ oxides

Two $Cd_{0.5}Ni_{0.5}Fe_2O_4$ samples were also made by hydrothermal processes under slightly different reaction conditions. The first sample (A) was reacted in distilled water at 100 ^{o}C under a gauge pressure of 345 kPa in a pressure reactor. The second sample (B) was boiled in deionised water under atmospheric pressure. The synthesis time in both cases was 6 hours. The synthesized fine powders of the samples were sintered at different temperatures in order to establish when formation occured.

The variations of XRD patterns are shown in Figure 8.3. The majority of the XRD lines for the sample made under pressure (A) were indexed to cubic spinel structure. This shows that the structure was almost formed at a reaction temperature of 100 ^{o}C. Some impurity peaks are observed in the spectra which reduce with sintering temperature. These reduce with increasing sintering temperature. We suspect that the use of distilled water instead of deionised water is partly responsible for adversely affecting phase formation in this case. For sample B the XRD peaks for the raw sample produced at 100 ^{o}C could not be indexed to cubic spinel phase. Single phase formation was enhanced with increasing sintering temperature. By about 900 ^{o}C single phase cubic spinel structure was finally formed.

In Figure 8.4 we show the variation of grain size for $Cd_{0.5}Ni_{0.5}Fe_2O_4$ oxide made under pressure (A) and zero pressure (B). For sample A the grain size of 35.5 $\pm$ 0.1 nm was obtained after annealing sample at 1000 ^{o}C. The grain size of sample B annealed at 1000 ^{o}C was 42.6 $\pm$ 0.1 nm. These values are lower than the average grain size of about 50 nm for the Cu–based sample with same nominal composition made by glycothermal and hydrothermal reactions. This further shows good correlation between grain size and ionic size of constituent atoms. Larger ions appear to be associated with samples having smaller grain sizes.

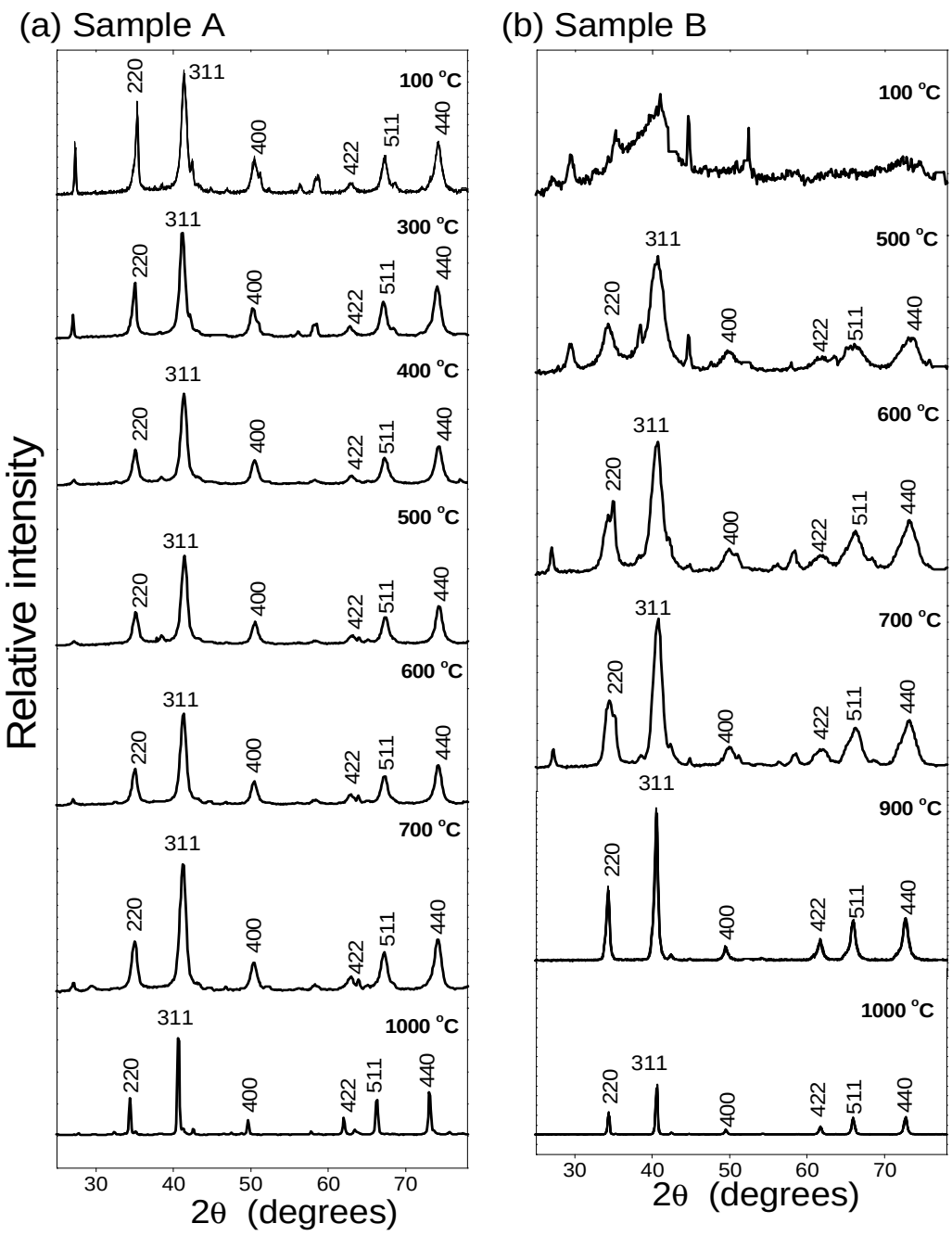

Figure 8.3: Variation of XRD patterns for $Cd_{0.5}Ni_{0.5}Fe_2O_4$ oxides with sintering temperature.

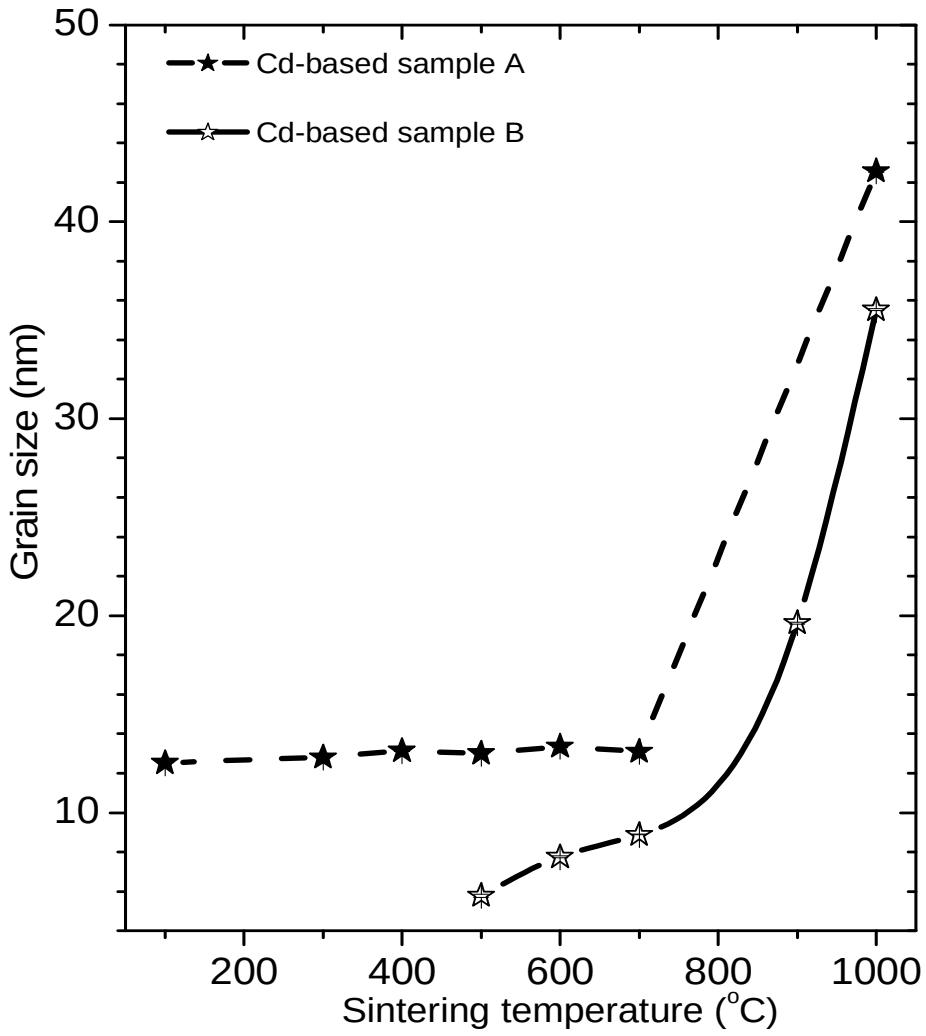

Figure 8.4: Variation of grain size for $Cd_{0.5}Ni_{0.5}Fe_2O_4$ oxides with sintering temperature.

8.3 Mössbauer results

In Figure 8.5 we show the Mössbauer spectra for the $Cu_{0.5}Ni_{0.5}Fe_2O_4$ oxides made by hydrothermal (sample H) and glycothermal (sample G) respectively, sintered at 600 ^oC and 700 ^oC and 1000 ^oC. The well–resolved six line Mössbauer spectra of sample H indicates ferrimagnetic phase. The additional central doublet and broad Mössbauer peaks in the spectra for sample G indicate superparamagnetic relaxation. The spectra for sample H could be fitted by two sextets and two doublets. The sextets and doublets represent trivalent Fe ions in ordered and paramagnetic phases respectively at A and B sites. Three sextets and two doublets were required to get a good fit to the experimental data of sample G. The criterion used to assign sextets and doublets at A and B sites was based on the fitted results of isomer shifts, which are expected to be lower due to cubic symmetry on A site.

The data deduced from fitted results of Mössbauer spectra are shown in Tables 8.2 and 8.3. Figure 8.6 shows the variation of hyperfine fields with sintering temperature. There was no significant change in the hyperfine fields of ^{57}Fe nuclei at A and B sites with increasing annealing temperature for sample H. The average hyperfine fields at A and B sites of sample H were 486.0 $\pm$ 0.4 kOe and 519.5 $\pm$ 0.4 kOe respectively. These values compare well with 482 $\pm$ 1 kOe (A site) and 515 $\pm$ 1 kOe (B site) found for the bulk sample prepared by solid-state reaction. For sample G there is a general increase in hyperfine fields with sintering temperature. After sintering at 1000 ^oC hyperfine fields increased to 484.9 $\pm$ 0.5 kOe and 519.0 $\pm$ 0.6 kOe on A and B sites respectively. Sintering above 600 ^oC seems to have little effect on hyperfine fields of samples produced by hydrothermal process. Hyperfine fields are higher for hydrothermal samples than for glycothermal samples. The difference appears to be due to bigger grain size in hydrothermal samples at a particular sintering temperature. The isomer shifts were weakly affected by sintering temperature. This shows that the s electron charge distribution was not significantly affected by

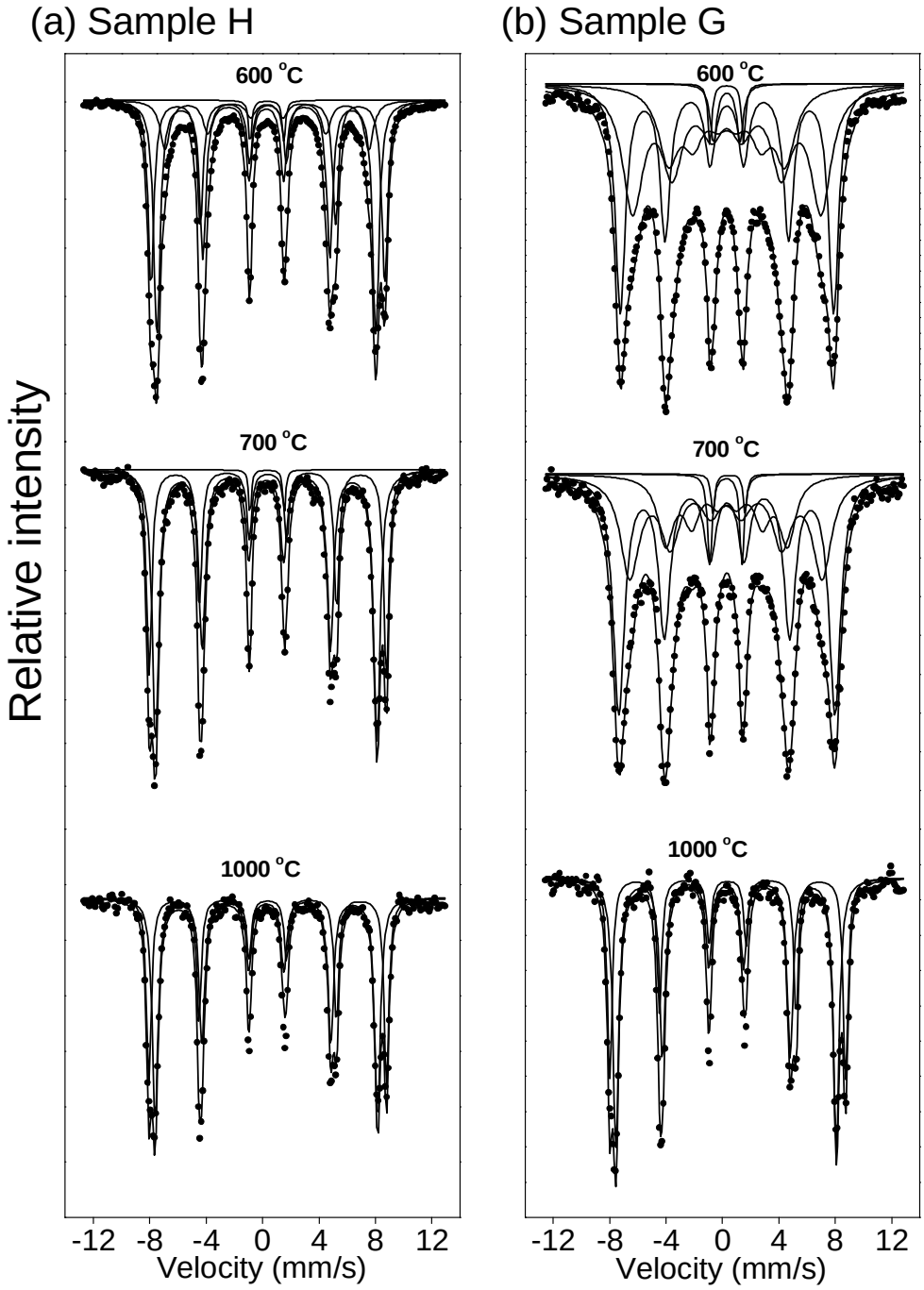

Figure 8.5: Variation of Mössbauer spectra for $Cu_{0.5}Ni_{0.5}Fe_2O_4$ oxides with sintering temperature.

Table 8.2: Variation of isomer shift (IS), quadrupole splitting (QS) and hyperfine fields (B_{hf}) of $Cu_{0.5}Ni_{0.5}Fe_2O_4$ made under zero pressure (sample H) with annealing temperature.

	IS (mm/s)		QS (mm/s)		B_{hf} (kOe)	
Temp. (^{o}C)	$(IS)_A$	$(IS)_B$	$(QS)_A$	$(QS)_B$	$(B_{hf})_A$	$(B_{hf})_B$
	± 0.009	± 0.006	±0.008	± 0.004	± 4	±0.4
600	0.269	0.379	-0.005	-0.002	482	514.1
700	0.266	0.378	-0.007	-0.005	487	521.5
1000	0.264	0.366	0.004	0.002	489	522.7

Table 8.3: Variation of isomer shift (IS), quadrupole splitting (QS) and hyperfine fields (B_{hf}) of $Cu_{0.5}Ni_{0.5}Fe_2O_4$ made under pressure (sample G) with annealing temperature.

	IS (mm/s)		QS (mm/s)		B_{hf} (kOe)	
Temp. (^{o}C)	$(IS)_A$	$(IS)_B$	$(QS)_A$	$(QS)_B$	$(B_{hf})_A$	$(B_{hf})_B$
	± 0.05	± 0.01	±0.03	± 0.01	± 4	±1
200	0.28	0.33	-0.01	-0.01	415	472
300	0.32	0.37	-0.01	-0.01	406	477
400	0.30	0.31	-0.02	0.01	405	460
500	0.32	0.33	0.01	0.01	415	468
600	0.31	0.32	0.02	0.00	414	469
700	0.25	0.32	0.01	-0.01	423	475
1000	0.27	0.37	-.01	0.01	485	519

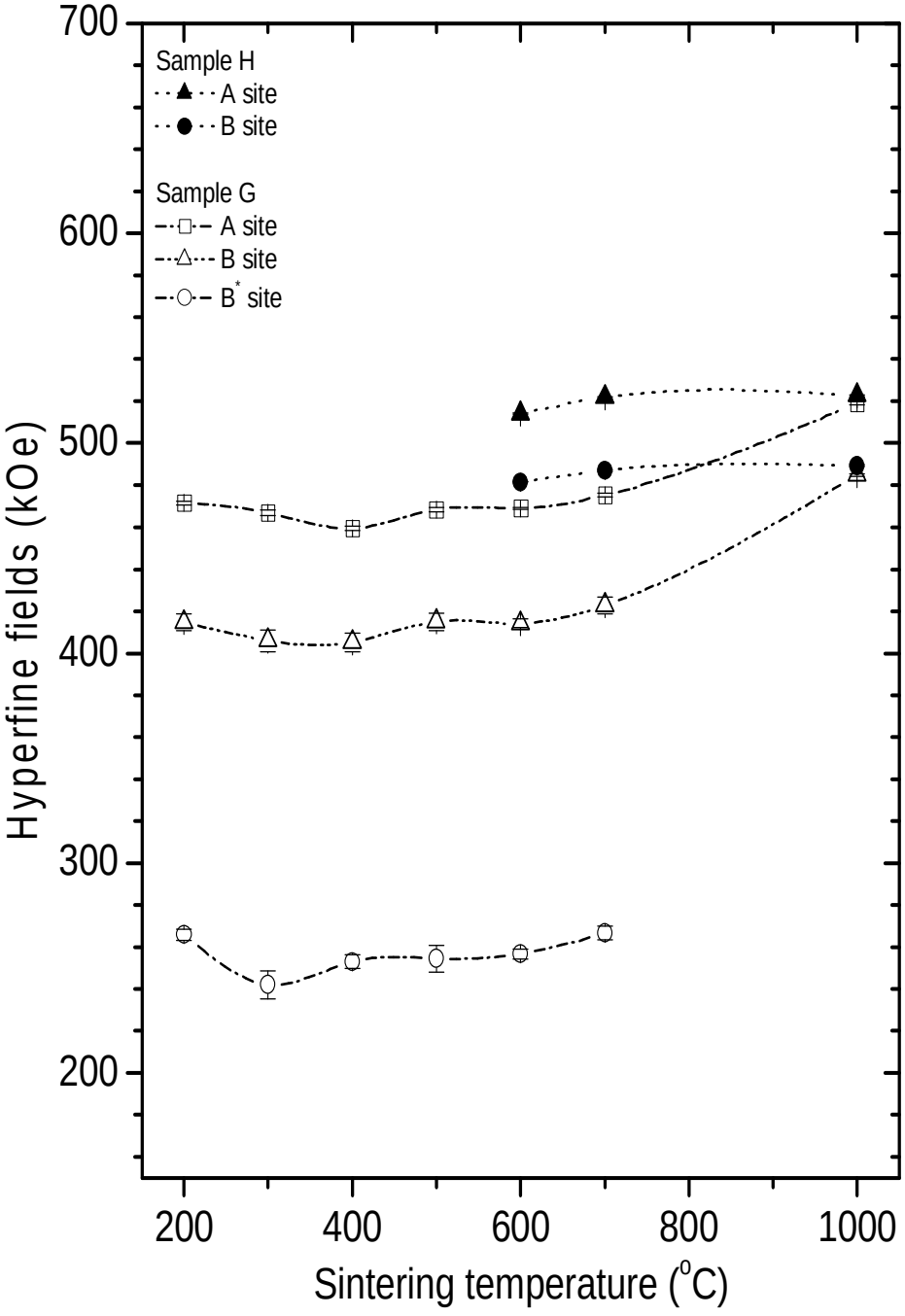

Figure 8.6: Variation of hyperfine fields for $Cu_{0.5}Ni_{0.5}Fe_2O_4$ oxides with sintering temperature.

sintering temperature. The average isomer shifts at A and B sites were 0.266 ± 0.009 mm/s and 0.374 ± 0.009 mm/s respectively. These values compare well with the A site (0.26 ± 0.01 mm/s) and B–site (0.34 ± 0.01 mm/s) isomer shifts obtained for the bulk sample made by solid state reaction.

The Mössbauer spectra for the Cd–based sample sintered at 600 ^{o}C, 700 ^{o}C and 1000 ^{o}C are presented in Figure 8.7. The Mössbauer spectrum for the sample sintered at 600 ^{o}C was decomposed into two doublets. This differs from the ordered magnetic phase (see Figure 8.5 (a)) observed in the Cu–based sample prepared under the same conditions. The values of isomer shifts, quadrupole splitting and hyperfine fields are shown in Table 8.4. A slight increase in A site hyperfine fields is observed. While the B site hyperfine fields are not significantly affected by increasing sintering temperature. The isomer shift values are also comparable to the $Cd_{0.5}Ni_{0.5}Fe_2O_4$ sample made by standard ceramic process presented in chapter 6.

8.4 Magnetization results

The results of magnetization measurements are shown in Figure 8.8. The sample H, which was sintered at 600 ^{o}C has a coercive field of 72 Oe. The coercive field increased to 133 Oe when the sample was annealed at 700 ^{o}C and dropped to 11 Oe after sintering the sample at 1000 ^{o}C. This behavior may be related to the change in domain structure with increase in grain size. At a critical grain size single domain particles can be expected to transform to multidomain particles with increase in grain size. Similar behavior has been observed due to the effect of high energy ball milling on coercive fields as grain sizes reduce (see chapter 6). The sample G appears to exhibit super-paramagnetic character (with very small coercive fields). Bae et al [25] have obtained similar behavior in $Co_xNi_{1-x}Fe_2O_4$ samples prepared by glycothermal process. This relates well with broadened Mössbauer peaks and a central doublet, which indicate super-paramagnetic relaxation.

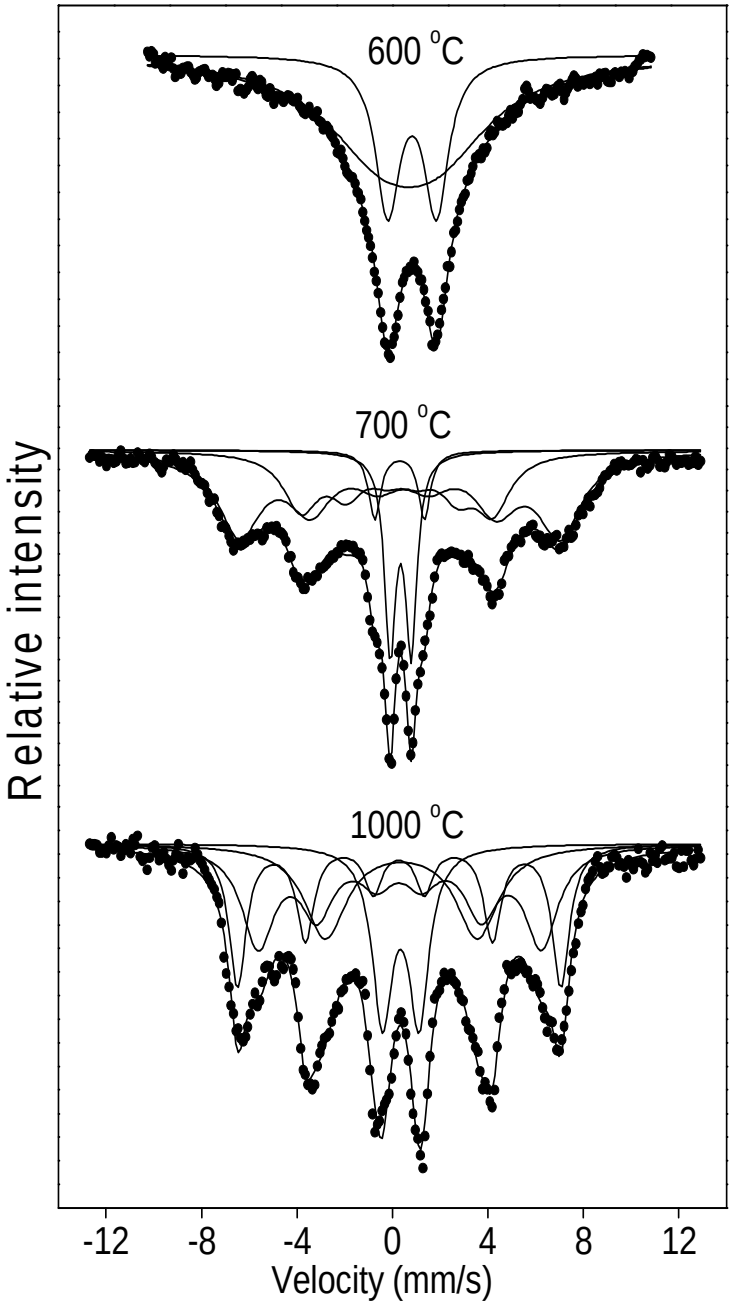

Figure 8.7: Variation of Mössbauer spectra for $Cd_{0.5}Ni_{0.5}Fe_2O_4$ (sample A) with sintering temperature.

Table 8.4: Variation of isomer shift (IS), quadrupole splitting (QS) and hyperfine fields (B_{hf}) of $Cd_{0.5}Ni_{0.5}Fe_2O_4$ (sample A) with annealing temperature.

	IS (mm/s)		QS (mm/s)		B_{hf} (kOe)	
Temp. (^{o}C)	$(IS)_A$	$(IS)_B$	$(QS)_A$	$(QS)_B$	$(B_{hf})_A$	$(B_{hf})_B$
	± 0.09	± 0.06	±0.04	±0.05	± 5	±2
600	0.30	0.36	0.87	1.01		
700	0.29	0.38	-0.11	-0.07	249	416
900	0.32	0.34	-0.03	-0.03	244	415
1000	0.30	0.28	0.02	0.01	368	420

In Figure 8.9 the variation of s magnetization measured at 9 kOe with sintering temperature is shown. For the sample H, the magnetization increases with increasing sintering temperature (grain size). This trend is expected in principle, as bulk ferrites tend to have stronger magnetic interactions. For the sample G, the magnetization drops as the spinel phase forms. After sintering at 700 ^{o}C the complete spinel phase forms (as indicated by X-ray diffraction results) and saturation magnetization increases with further increase in sintering temperature. Typical magnetization curves for the $Cd_{0.5}Ni_{0.5}Fe_2O_4$ samples are shown in Figure 8.10. For samples A and B the coercive field was about 29.6 Oe and 5.5 Oe respectively. The smaller values of coercive fields reflect the superparamagnetic character of the samples prepared by hydrothermal process. The saturation magnetization for samples A and B were respectively 53.36 emu/g and 51.38 emu/g. These compare well to values of about 51 emu/g observed for the bulk sample made by solid state reaction.

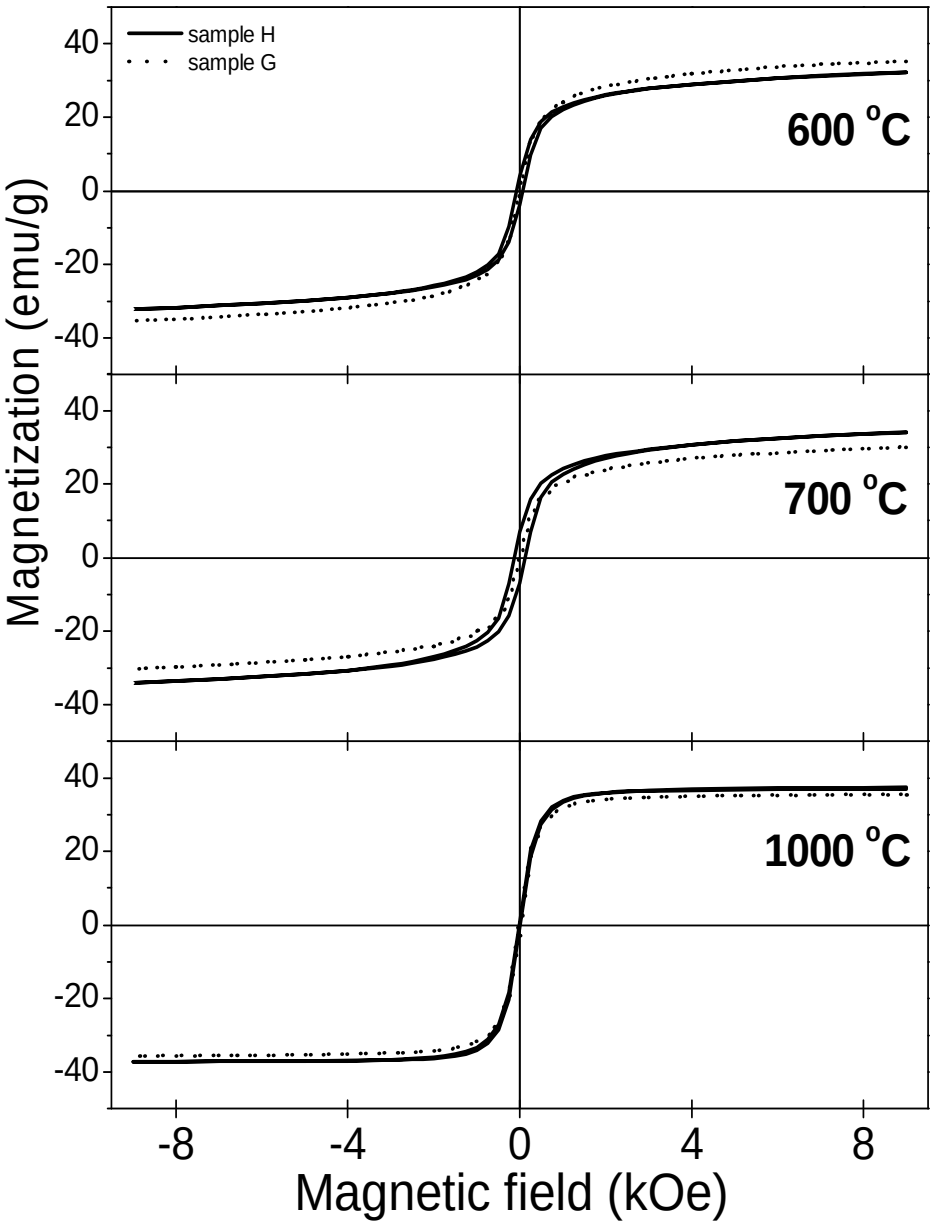

Figure 8.8: Variation of magnetization curves for $Cu_{0.5}Ni_{0.5}Fe_2O_4$ oxides with sintering temperature.

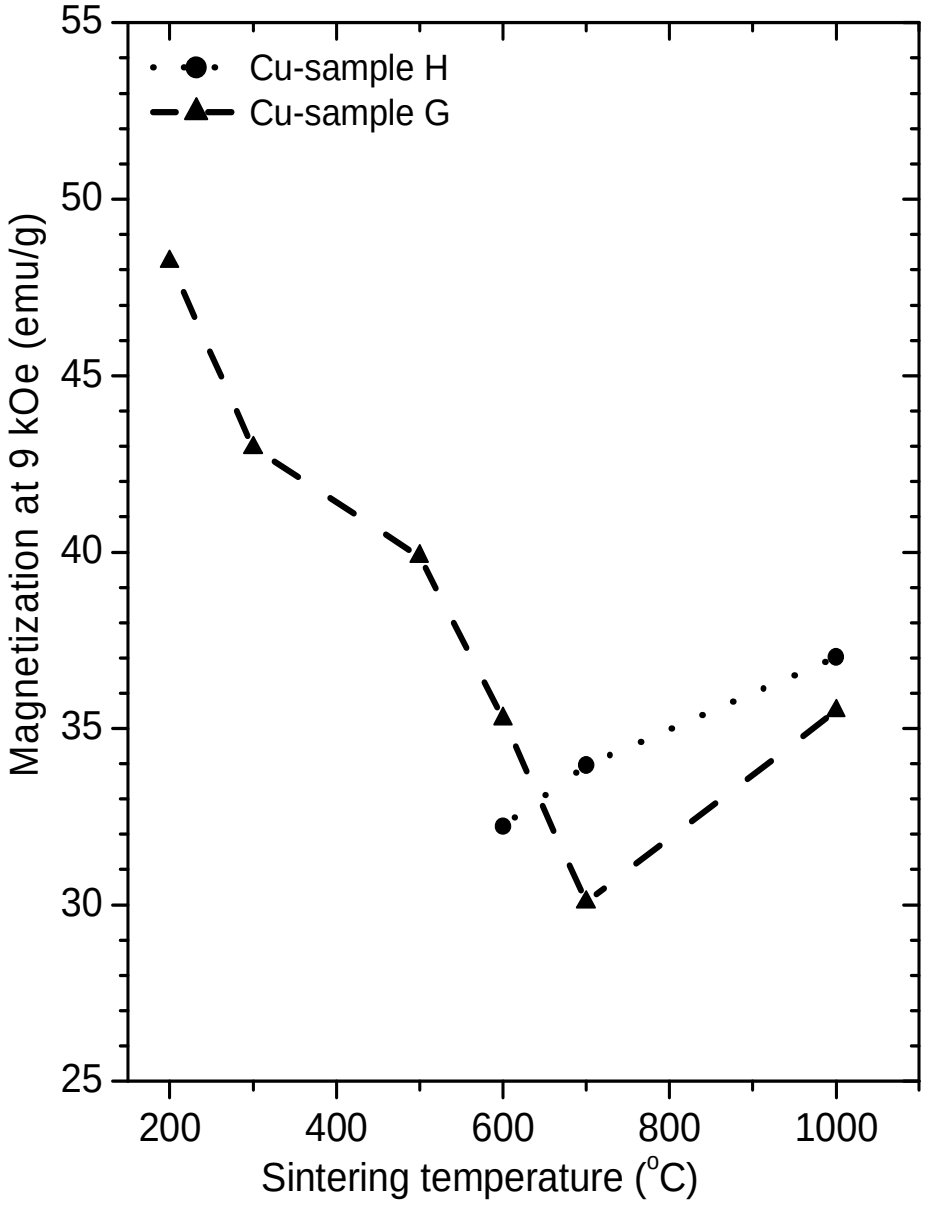

Figure 8.9: Variation of magnetization measured at 9 kOe for $Cu_{0.5}Ni_{0.5}Fe_2O_4$ oxides with sintering temperature.

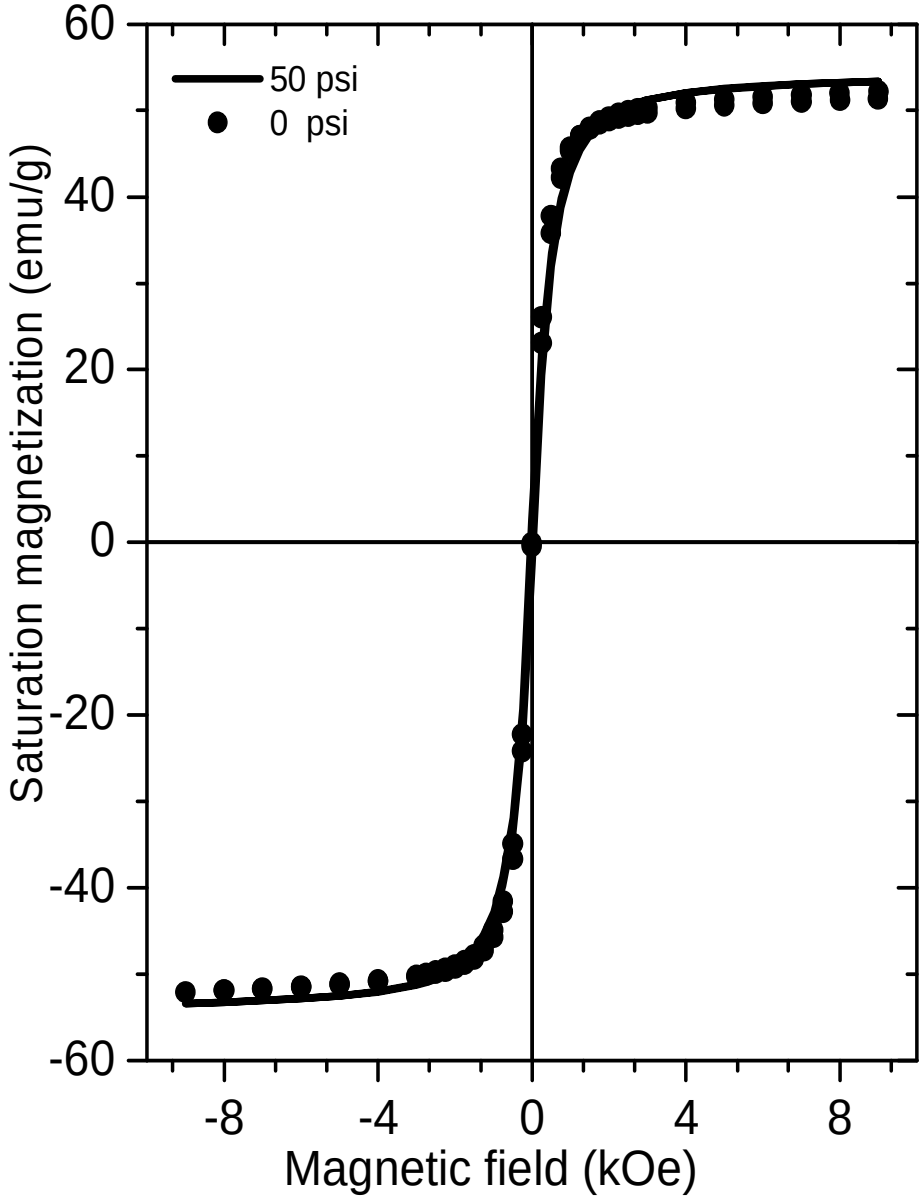

Figure 8.10: Magnetization curves for $Cd_{0.5}Ni_{0.5}Fe_2O_4$ oxides made under pressure (50 psi, sample A) and zero pressure (0 psi, sample B) sintered at 1000 ^oC.

8.5 Conclusions

We have successfully made (Cu, Cd)$_{0.5}$Ni$_{0.5}$Fe$_2$O$_4$ compounds by hydrothermal and glycothermal reactions. Single-phase cubic spinel structure formed after sintering samples at lower temperature than in solid-state reaction. Nanosized samples with grain sizes of about 11 nm were obtained after sintering the glycothermal samples between 500 ^{o}C and 700 ^{o}C. The samples produced through hydrothermal process have larger grain size compared to those produced by glycothermal process. With increased sintering temperature, the samples begin to adopt characteristics of bulk materials. Evidence of transformation from single domain to multidomain structure can be deduced from isothermal magnetization measurements on hydrothermal samples.

Chapter 9

Conclusions

We have investigated the structural and magnetic properties of bulk and nanosized (Zn, Cd, Cu)$_{0.5}$Ni$_{0.5}$Fe$_2$O$_4$ and NiFe$_2$O$_4$ compounds using X–ray diffraction (XRD), Mössbauer spectroscopy and magnetization measurements. The compounds studied were produced by solid state reaction, combustion, hydrothermal and glycothermal methods. The nanosized oxides were obtained by high energy ball milling of bulk samples and by direct synthesis using hydrothermal and glycothermal processes. Single phase formation of the spinel structure was easier to achieve in samples prepared by wet chemical methods because of lower sintering temperatures ($T < 1000$ ^{o}C) required. In the Cu$_{0.5}$Ni$_{0.5}$Fe$_2$O$_4$ sample prepared by hydrothermal process, single phase formation as indicated by XRD was almost complete at the initial synthesis temperature of 100 ^{o}C.

In the (Cd, Zn)$_{0.5}$Ni$_{0.5}$Fe$_2$O$_4$ ferrites prepared by the combustion technique we investigated the effect of the pelletizing pressure (related to green density) on properties before sintering the samples. An anomalous reduction in bulk density with increasing pressure was observed. We suspect that this may be related to blocked escape routes of gas out of the pellets during phase formation and hence contributing to trapped porosity in the samples. Not much significant effect on structural and magnetic properties were observed due to the effect of green density. However, analysis of Mössbauer spectra shows signifi-

cant and systematic changes in the hyperfine field distribution with increased pelletizing pressure. The distribution of the internal hyperfine fields appears to be related to the changing synthesis temperature until ignition at about 600 ^{o}C.

One of the objectives of the current work was to study the effect of ionic size differences between Cu–, Zn– and Cd–based samples on the properties. The lattice parameters of (Cu, Zn, Cd)$_{0.5}$Ni$_{0.5}$Fe$_2$O$_4$ were found to be larger than for NiFe$_2$O$_4$ oxide. This is consistent with the smaller ionic size of Ni. A good correlation between the lattice parameters of the Cu–, Zn–, and Cd–based oxides and their atomic sizes was also observed. The larger lattice parameter for the Cd–based oxide (8.51 $\pm$ 0.02 $\mathring{A}$) compared to that of the Zn–based oxide (8.39 $\pm$ 0.02 $\mathring{A}$) and that of the Cu–based oxide (8.37 $\pm$ 0.02 $\mathring{A}$) relate well to atomic (or ionic) size differences. The lattice parameters for Zn– and Cu–based samples were not significantly affected by high energy ball milling. However, a contraction of the unit cell for the Cd–based oxide from 8.50 $\pm$ 0.04 $\mathring{A}$ to 8.43 $\pm$ 0.04 $\mathring{A}$ was observed after 50 hours of milling. The sample with larger sized atoms seems to be more sensitive to milling.

The milling process leads to a significant reduction in grain sizes as deduced from XRD. The smallest grain size (9.89 $\pm$ 0.04 nm) was obtained for the Cd–based sample compared to 11.87 $\pm$ 0.06 nm and 10.21 $\pm$ 0.04 nm for the Zn– and Cu–based samples respectively. These values of grain sizes are comparable to those obtained by glycothermal process after sintering at about 600 ^{o}C. Changes in grain sizes due to milling and sintering are associated with changes in coercive fields (H_C). With reduction in grain sizes due to milling H_C was observed to increase according to equation (5.4.1) associated with multidomain behavior. This trend was observed in all the milled (Cu, Zn, Cd)$_{0.5}$Ni$_{0.5}$Fe$_2$O$_4$ and NiFe$_2$O$_4$ samples. For the Cd– and Cu–based samples, beyond a critical grain size, the coercive field decreases with further reduction in grain size according to equation (6.4.2). This equation is associated with single domain behavior. In Zn$_{0.5}$Ni$_{0.5}$Fe$_2$O$_4$ and NiFe$_2$O$_4$ compounds the crossover from mul-

tidomain to single domain was not observed. The crossover effect is more likely to be achieved in these compounds by slightly wetting the samples and milling for longer times. Sample with smaller grain size can also be obtained by force hydrolysis technique. In a recent report [86] Zn–substituted cobalt ferrites were synthesized by forced hydrolysis and average grain size of about 3.0 nm was obtained.

The coercive field of the $Cu_{0.5}Ni_{0.5}Fe_2O_4$ sample made by hydrothermal method under zero pressure and sintered at 600 ^{o}C was about 70 Oe. On sintering the sample at 700 ^{o}C, the coercive field attained a maximum value of about 130 Oe and then reduced to 10 Oe after sintering at 1000 ^{o}C. This behavior can be explained as due to transformation from single domain to multidomain structure with increasing grain size.

The Curie temperatures (T_C) were measured using zero velocity Mössbauer technique. An anomalous increase in T_C from about 548 K to 583 K for the $Zn_{0.5}Ni_{0.5}Fe_2O_4$ oxide was observed with reduction in grain size. A similar enhancement of T_C has been reported in milled $ZnFe_2O_4$ compound [44, 45] and can be explained by redistribution of Zn atoms in both A and B sites with milling.

The Mössbauer spectra for the bulk $NiFe_2O_4$ and $Cu_{0.5}Ni_{0.5}Fe_2O_4$ oxides have been found to have similar characteristics with well resolved magnetic splitting and high Curie temperatures. The spectra for the $Zn_{0.5}Ni_{0.5}Fe_2O_4$ and $Cd_{0.5}Ni_{0.5}Fe_2O_4$ oxides are similar to each other. This can be attributed to similar electronic configuration between Zn and Cd atoms. The temperature dependence of the hyperfine fields at the tetrahedral (A) and octahedral (B) sites have been found to vary as

$$B_{hf}(T) = B_{hf}(0)\left(1 - \left(\frac{T}{T_C}\right)^n\right)^{\beta_n} \tag{9.0.1}$$

where $n = 1$ or 2. For $n = 1$, equation (9.0.1) expresses the variation of hyperfine fields based on the Landau–Ginzburg theory. This is valid relatively close to T_C. For $n = 2$, equation (9.0.1) expresses the variation of hyperfine

fields based on single particle excitations and is valid over a wider temperature range below T_C.

The present study has provided us with useful information on the synthesis, structural and magnetic properties of spinel oxides [87–91]. The study of the temperature dependence of the magnetization is not presented in this thesis. This is left to a future project as the vibrating sample magnetometer still needs to be re-commissioned in the School of Physics at the Westville Campus of the University of KwaZulu–Natal.

Bibliography

[1] S. Chikazumi and S. H. Charap, *Physics of magnetism*, John Wiley and Sons, New York, 1964, p. 29–33.

[2] R. S. Tebble and D. J. Craik, *Magnetic materials*, John Wiley and Sons, London, 1969, p. 252–257.

[3] A. R. Shitre, V. B. Kawade, G. K. Bichile and K. M. Jadhav, Mater. Lett. 56 (2002) 188.

[4] J. Z. Msomi, T. Moyo and K. Bharuth-Ram, Hyperfine Interactions (C), 5 (2002) 181.

[5] T. Moyo, J. Z. Msomi, and K. Bharuth-Ram, Hyperfine Interactions 136 3 (2002) 579.

[6] B. S. Trivedi and R. G. Kulkarni, J. Mater. Sci. 35 (2000) 5523.

[7] V. T. Thanki, K. H. Jani, B. S. Trivedi, Kunal B. Modi and H. H. Joshi, Mater. Lett. 37 (1998) 236.

[8] A. Ray, R. N. Bhowmik, R. Ranganathan, A. Roy, J. Ghose and S. Chaudhury, J. Magn. Magn. Mater. 223 (2001) 39.

[9] W. C. Kim, S. J. Kim and C. S. Kim, J. Magn. Magn. Mater. 239 (2002) 82.

[10] S. C. Bhargawa, A. H. Morrish, H. Kunkel and Z. W. Li, J. Phys. Condens. Matter. 12 (2000) 9667.

[11] A. M. Abdeen, O. M. Hemeda, E. E. Assem and M. M. El–Sehly, J. Magn. Magn. Mater. 238 (2002) 75.

[12] O. M. Hemeda and M. M. Barakat, J. Magn. Magn. Mater. 223 (2001) 127.

[13] A. Roy, J. Ghose, A. Ray and R. Rangathan, J. Magn. Magn. Mater. 202 (1999) 359.

[14] H. N. Oak, K. S. Baek and S. J. Kim, Phys. Stat. Sol. B 208 (1998) 249.

[15] A. C. F. M. Costa, E. Tortella, M. R. Morelli and R. H. G. A. Kiminami, J. Magn. Magn. Mater. 256 (2003) 174.

[16] S. Dey, A. Roy, D. Das and J. Ghose, J. Magn. Magn. Mater. 270 (2004) 224.

[17] L. Wang and F. S. Li, J. Magn. Magn. Mater. 223 (2001) 233.

[18] C. Upadhyay, D. Mishra, H. C. Verma, S. Anand and R. P. Das, J. Magn. Magn. Mater. 260 (2003) 188.

[19] C. Rath, K. K. Sahu, S. Anand, S. K. Date, N. C. Mishra and R. P. Das, J. Magn. Magn. Mater. 202 (1999) 77.

[20] A. P. Guimaraes, I. S. Oliveira, *Magnetism and Magnetic Resonance in Solids*, John Willey and Sons INC. New York, 1989.

[21] F. X. Liu and T. Z. Li, Mater. Lett. 59 (2005) 194.

[22] S. Verma, P. A. Joy, Y. B. Khollam, H. S. Potdar and S. B. Deshpande, Mater. Lett. 58 (2004) 1092.

[23] D. Mishra, S. Anand, R. K. Panda and R. P. Das, Mater. Lett. 56 (2002) 873.

[24] T. J. Gillepsie, C. H. Marshall, M. Contrelas, J. Keane, E. Wolski, W. Wolski, P. Piszora, M. Pietrusik, J. Subrt, T. Grygar and M. Nejezchleba, Int. J. Inorg. Mat. 1 (1999) 187.

[25] D. Bae, S. Kim, H. Lee and K. Han, Mater. Lett. 57 (2003) 1997.

[26] A. Verma, T. C. Goel, R. G. Mendiratta and R. G. Gupta, J. Magn. Magn. Mater. 192 (1999) 271.

[27] R. N. Panda, J. C. Shih and T. S. Chin, J. Magn. Magn. Mater. 257 (2003) 79.

[28] W. F. Pong, M. H. Su, M. H. Tsai, H. H. Hsieh, Y. K. Chang, K. C. Kou, P. K. Tseng, J. F. Lee, S. C. Chang, C. I. Chen, K. L. Tseng and C. T. Chen, Phys. Rev. B 54 (1996) 16641.

[29] R. V. Mangalaraja, S. Ananthakumar, P. Mahohar and F. D. Gnanam, Mater. Lett. 57 (2003) 1151.

[30] R. V. Mangaraja, S. Ananthakumar, P. Mahohar, F. D. Gnanam and M. Awano, Mater. Lett. 58 (2004) 1593.

[31] J. Smith and H. Wijn, *Ferrites*, Cleaver–Hume Press, London, 1959, p. 140–154.

[32] T. C. Gibbs, *Principles of Mössbauer spectroscopy*, Chapman and Hall, London, 1976, p. 22–43, 159–180.

[33] M. A. Amer and O. M. Hemeda, Hyperfine Interactions 96 (1995) 99.

[34] C. N. Chinnasamy, A. Narayanasamy, N. Ponpandian, K. Chattopadhyay, K. Shonoda, B. Jeyadefan, K. Tohji, K. Nakatsuka, T. Furubayashi and I. Nakatan, Phys. Rev. B 63 (2001) 184108.

[35] X. Liu, W. Zhong, S. Yang, Z. Yu and B. Gu, Y. Du, J. Magn. Magn. Mater. 238 (2002) 207.

[36] K. A. Singh, A. Verma, O. P. Thakur, C. Pracash, T. C. Goel and R. G. Mendiratta, Mater. Lett. 57 (2003) 1040.

[37] Y. Fu, K. Pan and C. Lin, Mater. Lett. 57 (2002) 291.

[38] B. Parvatheeswara Rao, P. S. V. Subba Rao, G. V. S. Murthy and K. H. Rao, J. Magn. Magn. Mater. 268 (2004) 315.

[39] R. N. Bhowmik and R. Ranganathan, Phys. Rev. B 68 (2003) 134433.

[40] M. Grigorova, H. J. Blythe, V. Blaskov, V. Rusanov, V. Petkov, V. Masheva, D. Nihtianova, LI. Martinez, J. S. Munõz and M. Mikhov, J. Magn. Magn. Mater. 183 (1998) 163.

[41] K. Maaz, A. Mumntaz, S. K. Hasain and A. Ceylan, J. Magn. Magn. Mater. 308 (2007) 289.

[42] I. Hilger, R. Hergt, W. A. Kaiser, J. Magn. Magn. Mater. 293 (2005) 314.

[43] M. Mozaffari and J. Amighian, J. Magn. Magn. Mater. 260 (2003) 244.

[44] F. S. Li, L. Wand, J. B. Wang, Q. G. Zhou, X. Z. Zhou, H. P. Kunkel and G. Williams, J. Magn. Magn. Mater. 268 (2004) 332.

[45] G. F. Goya and H. R. Rechenberg, J. Magn. Magn. Mater. 196–197 (1999) 191.

[46] V. A. Brabers, Phys. Rev. Lett. 68 (1992) 3113.

[47] L. Yu, J. Zhang, Y. Liu, C. Jing and S. Chao, J. Magn. Magn. Mater. 288 (2005) 54.

[48] J. Crangle, *The Magnetic Properties of Solids*, Edward Arnold, London, 1977.

[49] H. P. Myers, *Introductory Solid State Physics*, Second Edition, Taylor and Francis Ltd., London, 1997, p. 321–379.

[50] N. W. Ashcroft and N. D. Mermin, *Solid State Physics*, Holt, Rinehart and Winston, 1976, p. 643–658, 694–734.

[51] G. Burns, *Solid State Physics*, Academic Press, London, 1985, p. 564–594, 599–603.

[52] S. R. Elliott, *The Physics and Chemistry of Solids*, John Wiley and Sons, England, 1998, p. 608–614, 624–640.

[53] C. Kittel, *Introduction to Solid State Physics*, 8th edition, John Wiley and Sons, 2005, p. 299, 352.

[54] C. M. Hurd, Contemp. Phys. 23 (1982) 469.

[55] D. I. Uzunov, *Introduction to the Theory of Critical Phenomena*, World of Science Publishing Co. Pte. Ltd, USA, 1993, p. 1–428.

[56] M. F. Collins, *Magnetic Critical Scattering*, Oxford University Press, New York, 1989, p. 3–164.

[57] H. Ibach and H. Lüth, *Solid–State Physics*, Springer–Verlag, 1993.

[58] T. Môriya, *Spin Fluctuations in Itinerant Electron magnetism*, Springer Series in Solid–State Sciences 56, Germany, 1985, p. 20.

[59] N. N. Greenwood and T. C. Gibbs, *Mössbauer spectroscopy*, Chapman and Hall, London, 1971, p. 1–25, 46–52.

[60] Q. Zeng, Y. F. Xiao, S. Z. Dong, X. B. Liu, B. Q. Qiu, Z. Y. Zhang and R. Wang, J. Magn. Magn. Mater. 192 (1999) 321.

[61] Mineral Powder Diffraction File, JCPDS, USA, 1980, p. 590.

[62] R. H. Jenkins and B. de Vries, *Worked examples in X–ray spectrometry*, Macmillan, London, 1970, p. 124–126.

[63] www.quantachrome.com.

[64] D. C. Giancoli, *Physics Principles and Applications*, Prentice Hall, 5 th Edition, 1998, p. 284.

[65] D. R. Lide and H. P. R. Frederikse, *CRC Handbook of Chemistry and Physics*, 78 th Edition, 1997–1998, p. 4–1.

[66] www.wissel–instruments.de.

[67] D. Jiles, *Introduction to Magnetism and Magnetic Materials*, Chapman and Hall, London, 1991, p. 50–52.

[68] T. B. Doyle, School of Physics, Howard Colledge campus, University of KwaZulu–Natal.

[69] S. Singhal and S. K. Barthwal and Kailash Chandra, J. Magn. Magn. Mater. 306 (2006) 233.

[70] T. D. Shen, R. B. Schwarz and J. D. Thompson, Phys. Rev. B. 72 (2005) 014431.

[71] www.periodic.lanl.gov.

[72] V. Šepelák, D. Baabe, D. Mienert, D. Schultze, F. Krumeich, F. J. Litterst and K. D. Becker, J. Magn. Magn. Mater. 257 (2003) 377.

[73] F. J. Berry, Ö. Helgason, T. Moyo and X. Ren, Mater. Lett. 59 (2005) 3241.

[74] J. L. Wang, S. J. Campbell, J. M. Cadogan, O. Tegus and A. V. J. Edge, J. Phys. Condens. Matter 17 (2005) 3689.

[75] K. Roumaih, R. A. Manapov, E. K. Sadykov and A. V. Pyataev, J. Magn. Magn. Mater. 288 (2005) 267.

[76] V. Šepelák, A. Buchal, K. Tkacova and K. D. Becker, Mat. Sci. Forum 16 (1998) 862.

[77] D. Ravinder and T. Alivelumanga, Mater. Lett. 49 (2001) 1.

[78] D. A. Read, T. Moyo, Suad Jassim, R. A. Dunlap and G. C. Hallam, J. Magn. Magn. Mater. 82 (1989) 267.

[79] M. R. Singh and S. C. Bhargawa, J. Phys. Condens. Matter 7 (1995) 8183.

[80] M. Venkatesan, U. V. Varadaraju and K. V. S. Rama Rao, Phys. Rev. B. 64 (2001) 94427.

[81] V. Masheva, M. Grigorova, N. Valkov, H. J. Blythe, T. Midlarz, V. Blaskov, J. Geshev and M. Mikhov, J. Magn. Magn. Mater. 196–197 (1999) 128.

[82] M. ul–Islam, T. Abbas and M. A. Chaudhry, Mater. Lett. 53 (2002) 30.

[83] T. Pannaparayil, R. Marande and R. Komameni, J. Appl. Phys. 69 (8) (1991) 5349.

[84] P. J. van der Zaag, A. Noordemeer, M. T. Johnson and P. F. Bongers, Physical Rev. Lett. 68 (1992) 3112.

[85] A. Franco, E. C. de Oliveira Lima, M. A. Novak and P. R. Wells, J. Magn. Magn. Mater. 308 (2007) 198.

[86] G. V. Duong, R. S. Turtelli, N. Nanh, P. V. Linh, M. Reissner, H. Michor, J. Fidler, G. Wiesinger and Grössinger, J. Magn. Magn. Mater. 307 (2006) 313.

[87] J. Z. Msomi, K. Bharuth-Ram, V. V. Naicker and T. Moyo, Hyperfine Interactions 158 (2004) 151.

[88] J. Z. Msomi, T. Moyo and T. B. Doyle, J. Magn. Magn. Mater. 310 (2007) 2534.

[89] J. Z. Msomi and T. Moyo, J. African Phys. Rev. (submitted for publication, 2007).

[90] J. Z. Msomi and T. Moyo, J. African Phys. Rev. (submitted for publication, 2006).

[91] T. Moyo, P. R. Silva, H. Saitovitch and J. Z. Msomi, J. African Phys. Rev. (submitted for publication, 2006).